Northumbria University
NEWCASTLE

Synthesis and Characterisation of Piezoelectric Composites for Sensing and Actuation Applications

Pakinam Eltouby

PhD

2023

Synthesis and Characterisation of Piezoelectric Composites for Sensing and Actuation Applications

Pakinam Eltouby

A thesis submitted in partial fulfilment of the requirements of the University of Northumbria at Newcastle for the degree of Doctor of Philosophy

Research undertaken in the Faculty of Engineering and Environment

July 2023

Abstract

The need for high-performance dielectric ceramic-polymer composites is growing day after day. These composites are characterised by their functional properties and find their applications in various fields of current modern technology. Amongst the various factors influencing the performance of these composites, the morphology of the incorporated ceramic fillers within the polymeric matrix has proven to have a significant impact. Achieving the desired morphology is highly dependent on the synthesis process employed. This work has therefore implemented the response surface methodology approach (RSM) within the widely employed molten salt synthesis (MSS) framework to systematically explore the intricate parameter space associated with MSS and to develop predictive mathematical models that can capture the morphology of future molten salt synthesised two-dimensional (plate-like) particles. With bismuth sodium titanate (BNT) as a case study, this work has focused primarily on the optimisation of two-dimensional plate-like particles' production, intended for subsequent incorporation in a polymeric matrix (Epoxy) to attain high performance dielectric composites. The main and combined interaction effects of the various molten salt synthesis parameters, i.e., synthesis temperature, holding time and heating rate, on the morphology of the resulting powder such as the area, thickness, Feret's diameter, particle size, and aspect ratio of particles, have been investigated. The models for the aspect ratio and particle size were found to be insignificant in this study, with P-values of more than 0.05. Three predictive models depicting the area, thickness, and Feret's diameter of the synthesised powder particles as a function of the affecting synthesis parameters were developed, optimised, and validated. Using the optimised synthesis conditions, optimally synthesised large BNT plate-like particles with an average area of approximately 157 μm^2, an average platelet thickness of approximately 1.5 μm, and an average Feret's diameter of approximately 17 μm were synthesised using the NBiT precursor particles. Since the alignment of the filler particles within the matrix is also amongst the various factors influencing the performance of dielectric composites, this study has further explored a mechanical alignment approach to align optimally synthesised plate-like particles into a chain-like quasi 1-3 structure, offering a cost-effective and straightforward alternative approach to existing alignment methods and anticipating resulting in improved dielectric constant and energy storage properties of the aligned composites. In comparison to composites made with non-

optimally synthesised BNT particles, composites made with optimally synthesised particles showed superior degrees of alignment with observable chain-like structure similar to that achieved in dielectrophoretically aligned composites. The dielectric, piezoelectric, ferroelectric and energy storage properties of the developed BNT-Epoxy composites were also investigated throughout this work. A remarkable dielectric constant of 52 was achieved at a 35% BNT volume content in the composite, surpassing values reported in literature for other two-phasic similar composites. The piezoelectric performance seemed to be affected by the poling direction, in which composites poled parallel to the applied electric field exhibited greater piezoelectric charge coefficients, d_{33} values, compared to those poled in a perpendicular direction, with a maximum value of 4.5 pC/N at 35% BNT. The piezoelectric voltage coefficient, g_{33}, increased linearly with BNT volume content, peaking at 3.5 mV.m/N at 35% BNT. At this volume content, a remarkably high discharge energy density of 3.7 J/cm^3 was achieved under a maximum breakdown electric field of 1267 kV/cm, which up to our knowledge also surpasses the value of other two-phasic similar systems. The herein developed models, along with the results of the studied multi-objective optimisation provide means to customise and regulate the size and shape of the particles according to specific application requirements. The developed BNT-Epoxy composites with improved dielectric and energy storage properties compared to state-of-the-art, hold promise for diverse dielectric applications, including capacitors.

Table of Contents

List of Figures

List of Tables

List of Acronyms

Acronyms	Description
P-E loop	Polarisation-Electric Field Loop
PZT	Lead Zirconate Titanate
BT/BTO	Barium Titanate/Barium Titanium Oxide
BNT/NBT	Bismuth Sodium Titanate
NBiT	Bismuth Sodium Titanate Precursor
KNN	Potassium Sodium Niobate
MPB	Morphotropic Phase Boundary
SSR	Solid-State Reaction
MSS	Molten Salt Synthesis
TMC	Topochemical Microstructure Conversion
PMMA	Polymethyl Methacrylate
PVC	Polyvinyl Chloride
PA	Polyamide/Nylon
PC	Polycarbonate
PE	Polyethylene
PP	Polypropylene
PS	Polystyrene
PTFE	Polytetrafluoroethylene
PVDF	Polyvinylidene Fluoride
PVP	Polyvinylpyrrolidone
SEM	Scanning Electron Microscopy
SE	Secondary Electrons
BSE	Backscattered Electrons
XRD	X-Ray Diffraction
EDS	Energy-Dispersive X-Ray Spectroscopy
LIGA	Lithography Galvano-forming and Plastic Molding
FDM	Fused Deposition Modeling
ABS	Acrylonitrile Butadiene Styrene
DEP	Dielectrophoresis

PT	Platinum
BN	Boron Nitride
PDMS	Polydimethylsiloxane
BHF	Barium Hexaferrite
TPU	Thermoplastic Polyurethane
CNT	Carbon Nanotube
SC	Single Crystal
DOE	Design of Experiments
RSM	Response Surface Method
CCD	Central Composite Design
ANOVA	Analysis of Variance
SS	Sum of Squares
MS	Mean Square
df	Degree of Freedom
AR	Aspect Ratio
GA	Genetic Algorithm
R1	Response 1
R2	Response 2
R3	Response 3
R4	Response 4
R5	Response 5
RM	Roller Mixer
MS	Magnetic Stirring
LCP	Liquid Crystalline Polymer
PEI	Polyetherimide
PEEK	Polyether Ether Ketone
CBT	Cyclic Butylene Terephthalate

List of Symbols

Symbol	Description	Unit
ε_r	Relative dielectric constant	
ε_c	Dielectric constant of ceramic phase	
ε_p	Dielectric constant of polymeric phase	
tanδ	Dielectric loss tangent	
ε_0	Permittivity of free space ($8.85418782 \times 10^{-12}$)	F/m
E	Electric field	kV/cm
Emax	Maximum applied electric field	kV/cm
E_c	Coercive electric field	kV/cm
P	Polarisation	$\mu C/cm^2$
P_s	Saturation polarisation	$\mu C/cm^2$
P_r	Remnant polarisation	$\mu C/cm^2$
D	Electric displacement	C/m^2
C	Capacitance	F
d_{33}	Longitudinal piezoelectric charge coefficient	pC/N
d_{15}	Shear piezoelectric charge coefficient	pC/N
d_{31}	Transverse piezoelectric charge coefficient	pC/N
g_{33}	Piezoelectric voltage coefficient	mVm/N
k	Electromechanical coupling factor	
U_e	Discharge energy density	J/cm^3
T_c	Curie Temperature	^oC
T_m	Melt Temperature	^oC
T_s	Sintering Temperature	^oC
φ / V_f	Volume fraction of the filler	%
n	Reciprocal of the depolarisation factor	
ip	Interparticle-distance	um
Y_c	Elastic modulus of the ceramic particles	GPa
Y_p	Elastic modulus of the polymer matrix	GPa
R	Ratio of average particle size to interparticle distance	
τ	Poling time	min
α	Poling ratio of the dispersed ceramic particles	
λ	Wavelength of the X-rays	Å

θ	Diffraction angle
d_{hkl}	Crystal lattice planes
Å	Angstrom (unit of length)
R^2	Coefficient of determination
Y	Predicted response variable
b_o	Constant coefficient
b_i	Linear coefficient
b_{ii}	Pure second order/quadratic effect
b_{ij}	Interaction coefficient
$x_{i/j}$	The design factors
∈	Random error term
Bi	Bismuth
Ti	Titanium
Na2CO3	Sodium carbonate
Cu	Cupper
$CaTiO_3$	Calcium Titanate
KCl	Potassium Chloride
NaCl	Sodium Chloride
Nb	Niobium
Na	Sodium
K	Potassium
O	Oxgen
ZnO	Zinc oxide
PT	Platinum

Acknowledgements

First of all, I am grateful to the almighty God for providing me with a goodwill health and patience to complete this thesis.

I would like to extend my deepest gratitude to my principal supervisor, *Dr. Jibran Khaliq*, for his unwavering support, invaluable guidance, and insightful comments throughout the course of this work. His patience, encouragement, and motivation have been instrumental in the successful completion of this thesis, and I am truly grateful to have had him as my supervisor. I would also like to express my deepest thanks to *Prof. Islam Shyha* for his enthusiasm, inspiration, valuable guidance, and skills during my research.

Special thanks are owed to *Dr. Pietro Maiello, Phil Donelley, Simon Neville*, and *Sam Hutchinson* for their training sessions and constant assistance during the experimental work. Special thanks to *Dr. Linzi Dodd* for her valuable assistance during the experimentation lab work.

I would also like to express my gratitude to all my colleagues at the Department of Mechanical Engineering and Construction for their collaboration, support, and insightful discussions throughout this journey. Furthermore, I am sincerely thankful to *Northumbria University* for funding this project and for provision of research facilities through RDF.

Moreover, I would like to thank my family, especially my mother, for supporting me spiritually throughout this journey. I am also thankful for my Newcastle family, *Rana, Yomna, Nahed, Hisham, Mayssa* and *Ramy* who have made Newcastle feel like home and whose presence has made even the toughest days pass by easily.

Finally, I am truly and incredibly thankful to my husband, *Hossam Eldessouky*, who has been always by my side during this PhD journey. I am thankful beyond words for all his continuous support, patience and all the sacrifices he made to help me complete this thesis. Without his consistent encouragement and his belief in my abilities, this accomplishment would not have been possible.

I dedicate this thesis to my son Moussa Eldessouky

whose arrival has brought infinite happiness into my life.

Declaration

I declare that the work contained in this thesis has not been submitted for any other award and that it is all my work. I also confirm that this work fully acknowledges opinions, ideas, and contributions from the work of others.

Any ethical clearance for the research presented in this thesis has been approved. Approval has been sought and granted by the Faculty Ethics Committee on 04 September 2019 under reference number 13751.

I declare that the Word Count of this Thesis is 47,728 words.

Name: Pakinam Eltouby

Chapter 1

1. Introduction

The rapid pace of the fast-growing technology is significantly increasing the demand for modern smart devices day after day [1,2]. Nowadays, smart devices seem to be an essential integral part of everyday life. These devices are characterised by their intelligent functional capabilities such as sophisticated sensing properties, data processing capabilities, energy conversion and storage capabilities as well as their superior interactive connectivity capabilities. These extraordinary capabilities have allowed their incorporation in a wide range of applications, including but not limited to, aerospace [3], automotive [4], electronics [5], biomedical [6] and wearable industries [7]. Notably, the utilisation of smart devices with low-energy consumption capabilities has seen a significant increase in recent years. As such, extensive research efforts have been devoted to exploring the integration of energy harvesters as a sustainable solution to power devices in extreme conditions [8]. These harvesters seem to be advantageous due to their environmentally sustainable nature, suitability for operation in extreme environments, potential for weight reduction, extended lifetime, and minimal maintenance requirements.

To meet the growing need for smart devices with outperforming capabilities, there is an ongoing quest for materials that can improve the functionality and performance of these devices. As such, several researchers have investigated the utilisation of functional ceramics as well as smart polymers for incorporation in modern smart devices. However, one promising approach was the combination of ceramics and polymers together to design and form ceramic-polymer composites [9]. These composites blend the distinct qualities of ceramics and polymers to produce a flexible platform for enhancing smart gadgets with cutting-edge functionality. These composites have proven to exhibit diverse potential properties which enable their applicability in a diverse range of applications, such as their piezoelectricity for sensors and energy harvesting applications, dielectric properties for capacitors and electronic components, and pyroelectric properties for thermal energy harvesting. Specifically, ceramic-polymer composites with dielectric properties, referred to as dielectric ceramic-polymer composites, have gained enormous attention due to their ability to exhibit highly reversible dipole [10], which enables their application in a wide range of energy system and energy storage-based applications.

Furthermore, over the past 20 years, several high-performance energy and power systems have been actively developed using dielectric ceramic-polymer composites that possess piezoelectric and ferroelectric properties as well [10]. This combination of functionalities has opened up new possibilities for the design and implementation of advanced sensing technologies and smart devices. Therefore, there is an ongoing quest to further enhance the dielectric and energy storage capabilities of dielectric ceramic-polymer composites to expand their potential applications. Researchers are actively exploring novel fabrication techniques and material combinations to optimise the performance of these composites based on specific applications.

1.1. Scope of the Thesis

To unlock the full potential of dielectric ceramic-polymer composites, careful consideration should be given to the factors that impact their performance in the first place. Generally, the performance of such composites is influenced by various factors, such as the fabrication technique, the functional nature of the selected constituents, i.e., ceramics and/or polymers, the distribution of the selected filler within the polymeric matrix, the morphology of the selected filler, and whether a third phase is added. These factors may be divided into seven distinct factors and are discussed in detail in chapter two of this thesis (see Figure 2.22).

Among these factors, the morphology of the incorporated ceramic filler within the polymeric matrix has proven to have a significant effect on the resulting properties of the composites. As such, the shape and size of these fillers may dictate the resulting electrical, mechanical, and thermal characteristics of the composites. By carefully controlling and optimising the morphology of these fillers, it becomes possible to tailor the properties of the composites to meet specific application requirements. One way to tailor the properties of these incorporated ceramic fillers, is to manipulate the synthesis process with which the ceramic filler was originally synthesised [11,12]. Amongst various ceramic synthesis methods, molten salt synthesis (MSS) has emerged as a promising synthesis technique that allows for precise control over the particle size and shape [13,14]. MSS has been widely employed in the synthesis of various lead-free ceramics such as barium titanate (BT), potassium sodium niobate (KNN) and bismuth sodium titanate (BNT) with varying shapes such as the production of spheroidal, plate-like shaped, or rod-like shaped structures and varying sizes, spanning from nanoscale to microscale dimensions [15–17].

To this end, several research endeavours have explored the effects of various individual molten salt synthesis parameters on the morphology of the resulting powder. These include reaction temperature, holding time, salt composition, reactant concentration, stirring rate, and heating rate. However, all these studies investigated the effect of the synthesis parameters through experimental trial and error and without any statistical analysis. Additionally, the specific combination of parameters required to determine the exact dimensions and shape of the product particles remains unclear. Furthermore, each parameter has been examined independently which may be time-consuming and may not provide a comprehensive understanding of the complex relationship between several parameters and the resulting powder properties.

Consequently, a more systematic and statistically rigorous investigation is needed to bridge this gap and provide a more comprehensive understanding of how the synthesis parameters interact and collectively affect the outcome. To the best of our knowledge no study has been conducted to 1) investigate the significance level of the main effects of the MSS parameters 2) the significance level of the simultaneous combined effect of these parameters, 3) identify the most significant parameter (s), as well as 4) propose predicted models to control size and shape of future molten synthesised two-dimensional particles and achieve desired morphology for specific applications, without the need for the time-consuming trial and error experiments.

Therefore, this study has implemented the Design of Experiments (DOE) based on the response surface methodology (RSM) approach to comprehensively investigate and identify the significance level of molten salt synthesis parameters and their combined interaction effect on the resulting shape and size of synthesised two-dimensional particles, with the ultimate aim of establishing predictive models for future MSS synthesis based on BNT as a case study. By employing RSM in MSS, researchers can navigate the complex parameter space of MSS, providing valuable insights into the optimal conditions required to achieve the desired particle size and shape.

Another crucial factor affecting the dielectric performance of the functional ceramic-polymer composites is the distribution and the alignment of the incorporated ceramic filler within the polymeric matrix. In this context, several researchers have investigated the effect of various alignment techniques on the resulting properties of the composites. As such the fabrication of quasi 1-3 composites using

dielectrophoresis have proven to show enhanced dielectric and piezoelectric properties compared to randomly dispersed 0-3 composites [18]. Generally, this quasi chain-like structure can be achieved via various alignment techniques such as dielectrophoresis, magnetic alignment, electromagnetic alignment, and injection moulding. However, these techniques can be challenging and time-consuming due to the precise control required during the alignment process. Moreover, they often necessitate specialised experimental setups and equipment, resulting in increased costs, especially for large-scale production. Therefore, this study proposes to mechanically align ceramic filler particles with plate-like structure in a quasi 1-3 structure by using the doctor blade, offering simplicity and cost reduction in comparison to other alignment methods.

1.2. Aims and Objectives

1.2.1. Aims

The **first aim** of this thesis is to meticulously develop and optimise predictive mathematical models that comprehensively depict the intricate shape and precise size of synthesised two-dimensional plate-like ceramic particles in the molten salt synthesis environment as a function of the variable synthesis parameters. Additionally, the thesis aims to perform multi-objective optimisation to refine the synthesis process parameters and achieve plate-like particles with optimised morphology intended for incorporation in subsequent ceramic-polymer composites.

The **second aim** of this thesis is to fabricate a quasi 1-3 ceramic-polymer composite using the optimally synthesised ceramic powder (achieved in aim 1), via a mechanical alignment technique (with preferred directionality) resulting in enhanced dielectric properties compared to the state-of-the-art two-phasic composite materials.

1.2.2. Objectives

The objectives outlined below are designed to achieve the aims of the thesis:

1. Comprehensively review literature to identify key factors affecting the performance of dielectric ceramic-polymer composites, as well as identify knowledge gaps in the MSS technique and fillers alignment techniques.
2. Study the influence of MSS parameters on the morphology of the synthesised ceramic particles based on bismuth sodium titanate (BNT) as a case study.

3. Develop an experimental design matrix using response surface methodology (RSM) to efficiently synthesise NBiT precursor with minimum possible trials. Collect data for various responses depicting the size and shape of synthesised particles using a combination of methods such as SEM, Image J and Mastersizer.
4. Determine the significance level of both the individual and combined effect of the MSS parameters and identify the most significant one(s) based on the ANOVA analysis utilising the Design Expert software.
5. Develop predictive mathematical models through regression analysis to accurately describe the shape and size of plate-like BNT particles. Perform multi-objective optimisation to obtain optimized particle synthesis and validate models.
6. Use mechanical alignment (doctor-blade technique) to align optimally synthesised BNT particles in BNT-Epoxy composites with various volume fractions of BNT.
7. Characterise and assess the dielectric, piezoelectric, ferroelectric and energy storage properties of the developed BNT-Epoxy composites using relative measurements such as dielectric constant, d_{33}, g_{33} measurements as well as P-E loop analysis and discharge energy density measurements.
8. Benchmark and compare the dielectric properties and energy storage capabilities of the developed BNT-Epoxy composites with those state-of-the-art composites of similar systems.

1.3. Thesis outline

This thesis is divided into nine chapters which present the research work conducted within the scope of a PhD programme. A schematic diagram showing an outline of the thesis structure is presented in Figure 1.1. Chapter 3 and 4 present the experimental work and the methodological framework of the implemented DOE approach. Chapter 5 presents the results of the statistical analysis along with the developed predictive mathematical models. Chapter 6 discusses the underlying reasons and mechanisms for parameter effects, presents phases analysis results, demonstrated optimal synthesis conditions, and validates models. Chapter 7 analyses morphological characteristics, discusses dielectric, piezoelectric, ferroelectric, and energy storage properties, compares results with state-of-the-art composites, and evaluates competitiveness for

energy storage applications. Chapters 8 and 9 present the conclusions and suggested recommendations for future work, respectively.

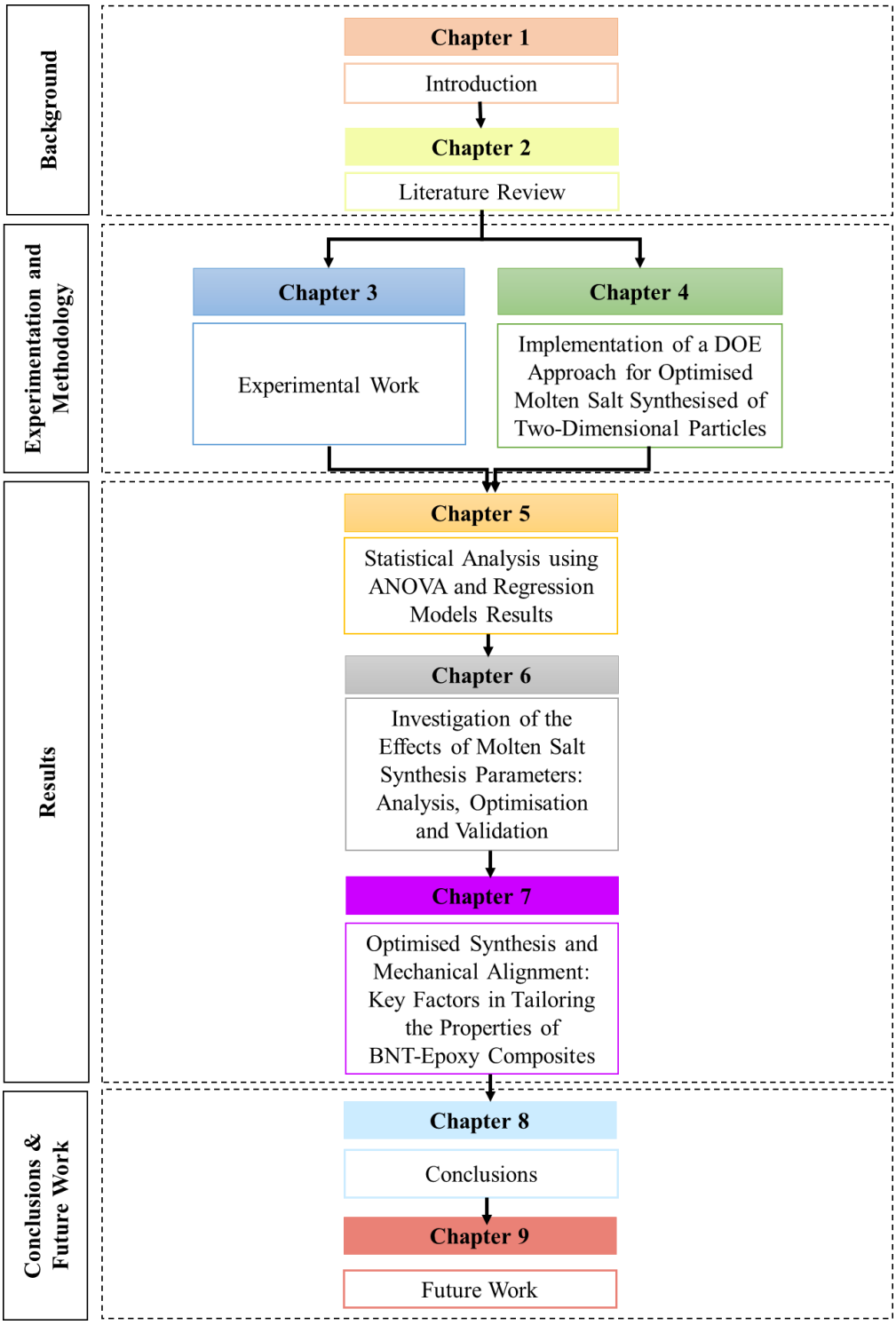

Figure 1.1: A schematic diagram showing the thesis structure outline.

Chapter 2

2. Literature Review

2.1. Introduction

The demand for smart electronic devices that can operate efficiently with minimal power consumption and extended battery life has seen a significant rise in recent years [19,20]. Therefore, significant research endeavors have been dedicated to exploring new materials, technologies, and design approaches to satisfy these needs and ensure the sustainability of smart electronic devices. One promising avenue for achieving the desired performance characteristics in electronic devices was the exploration of functional ceramics and their incorporation in various electronic energy-based devices [21–23]. This was due to the distinctive properties they provide such as, high dielectric constants, decreased dielectric loss, low electric conductivity, and remarkable insulation characteristics which may be vital in developing high-performance electronic components that are able to store and transmit electrical energy effectively [24]. In this context, this chapter provides a comprehensive overview of the fundamental principles and concepts related to functional ceramics such as dielectric, piezoelectric, and ferroelectric properties. The chapter further explores the various performance measurement parameters with which the functional characteristics can be assessed such as dielectric constant, piezoelectric charge, and voltage coefficient as well as energy storage potentials. Additionally, this chapter provides a thorough overview of the widely employed lead-based and lead-free ceramics along with an exploration of their unique properties. Besides, various polymeric materials and their corresponding characteristics have also been reviewed within this chapter. In order to overcome the disadvantages of both polymers and ceramics, and combine their advantages, ceramic-polymer composites have seemed to be a viable solution. This chapter primarily aims to conduct an analysis of the diverse factors that affect the performance of ceramic-polymer composites which are indented for use in numerous dielectric and piezoelectric applications. By examining these factors, researchers may gain insights into how to optimise the properties and enhance the overall performance of these composites for specific applications. Thus, the last section of this chapter presents the various factors affecting the overall performance of these composites.

2.2. An Overview of Dielectric, Piezoelectric and Ferroelectric Fundamentals

Dielectric materials are an integral component in a wide range of current modern technology ranging from energy harvesting and energy storage devices to sensor and actuation applications [25]. The scientific term “dielectric” is frequently employed in the domains of electrical engineering and physics [26]. It generally refers to a substance that possesses the ability to impede the flow of electric current, in other words, does not conduct electricity but rather exhibits insulating capabilities and support electrostatic fields [26,27]. The discovery and principal understanding of dielectric materials back to the 18th century when the Dutch scientist Pieter van Musschenbroek made one of the earliest important contributions to the science of dielectrics in 1745 [28]. He created the Leyden jar, a pioneering capacitor design that utilised glass as the dielectric medium. In his invention, he used a glass jar to store a high-voltage electric charge between two aluminum foil conductors on the inside and exterior of the jar [28]. This invention significantly affected the development of the field of electricity.

Hence, those materials possessing the unique property of storing electrical energy when an external field is applied are referred to as dielectric materials [29,30]. Generally, upon application of either direct or alternating current on any material, the movement of electric charges is typically promoted, however, in a dielectric material, this movement is restrained [29]. This restrained movement leads to the establishment of dipole moments between the charges, thereby inducing polarisation within the material. This polarisation creates an internal electric field that opposes the applied field and consequently, the dielectric material can sustain the presence of the electrostatic field without allowing significant charge flow or electrical current.

Dielectric materials are mainly categorised into ferroelectric and non-ferroelectric materials [31]. Based on the predominant polarisation mechanism, non-ferroelectric materials which are commonly referred to as paraelectric or normal dielectric, can be further classified into non-polar dielectrics, polar dielectrics, and dipolar dielectrics [31]. The first category, the non-polar dielectrics, consists of atoms of a single type, and their polarisation in an external electric field arises from the displacement of electric charge relative to the nucleus. The materials in the second group, known as polar dielectrics, are made up of molecules without a permanent dipole moment,

whereas the third group materials, the dipolar dielectrics, are made up of molecules that exhibit a permanent dipole moment [31].

On the other hand, the second main category of dielectric materials, namely ferroelectric materials, refers to those materials that exhibit spontaneous electric polarisation that is reversible and that may be altered by the application of either an electric field or stress. This phenomenon of spontaneous polarisation is observed within a specific temperature range, denoted as the spontaneous polarisation interval [32]. However, these materials can lose their spontaneous polarisation and exhibit a phase transition beyond a critical temperature known as the transition temperature or Curie temperature (T_c), turning the material into what is called paraelectric. This phase transition from the ferroelectric phase to the paraelectric phase is accompanied by notable changes in various physical properties and a transition in crystal structure from a lower symmetry configuration to a higher symmetry configuration [32]. Additionally, within the crystal, the alignment of electric dipoles can be localised to specific regions, while other regions may exhibit a reversed direction of spontaneous polarisation. These regions characterised by homogeneous uniform polarisation are commonly referred to as domains [33].

For a material to exhibit any of the above-mentioned properties such as ferroelectric, paraelectric, or even piezoelectric (which is explained below), the presence or absence of an inversion center which refers to the absence of a point within the crystal structure where all the atoms or ions can be perfectly mirrored, plays a pivotal role in determining their distinctive characteristics [34]. Consequently, properties such as ferroelectricity, paraelectricity, and piezoelectricity, which inherently exhibit asymmetry, can only manifest in crystals lacking a center of symmetry. Generally, crystals can be classified based on the number of rotational axes and reflection planes they exhibit, leading to a total of 32 crystal classes, out of which 11 classes exhibit symmetrical centers [34]. The remaining classes exhibit a non-centrosymmetric nature. However, among these 21 classes, one class possesses an inversion center, thereby forfeiting its non-centrosymmetric characteristic and resembling the crystal classes with center symmetry. Consequently, there are only 20 crystal classes that lack center symmetry and display inherent asymmetric properties. Crystals belonging to these 20 classes exhibit a remarkable property known as piezoelectricity [35]. This piezoelectricity describes a phenomenon where the application of mechanical stress

on a non-centrosymmetric crystal from these 20 classes results in the asymmetric displacement of ions within the crystal structure [31]. This displacement gives rise to the generation of electric polarisation. A piezoelectric material, on the other hand, experiences strain when an electric field is applied to it, causing the material to expand or contract depending on the direction of the field. It is possible to transform electrical energy into mechanical energy and vice versa thanks to the piezoelectric effect's bidirectional nature. Quartz, a highly utilised material in transducers, serves as a prominent example of a piezoelectric material. A subgroup of piezoelectric materials, containing 10 crystal classes that possess a distinctive polar axis are referred to as pyroelectric materials. These (pyroelectric) materials demonstrate a dependence on temperature, as they undergo changes in their spontaneous polarisation and unit cell dimensions with variations in temperature. As a result, their polarisation is temperature dependent. Pyroelectric materials can be further categorized into ferroelectric and non-ferroelectric materials whereas the former category (ferroelectric) denotes the capability to reverse the spontaneous polarisation when an electric field is applied.

Notably, piezoelectricity and pyroelectricity are intrinsic properties of a material. Ferroelectricity, in contrast, is a phenomenon that develops in pyroelectric materials as a result of the application of an external electric field.

Figure 2.1 demonstrates the classification of the 32 crystallographic point groups [36].

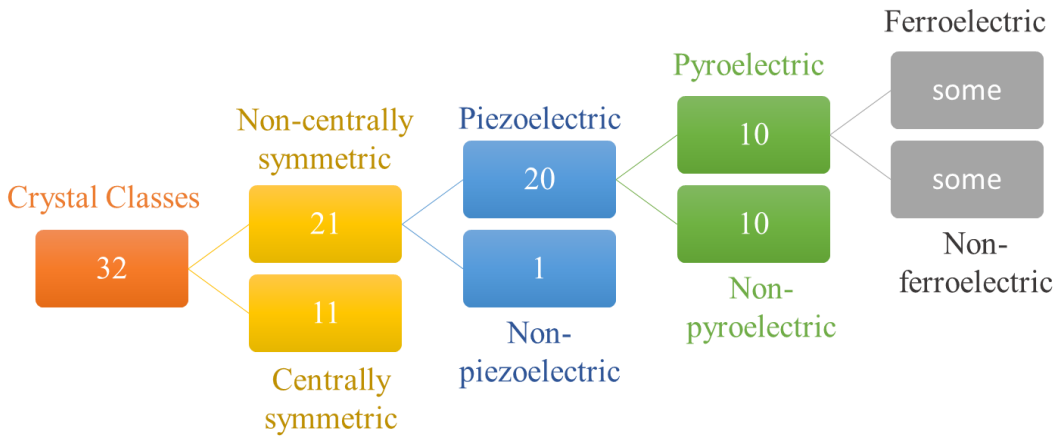

Figure 2.1: Classification of the 32 crystallographic structures into various categories (reproduced from [36])

To sum up, ferroelectric materials possess unique characteristics that include both pyroelectric and piezoelectric properties. A group of pyroelectric materials exhibiting

temperature-dependent polarisation falls within the category of piezoelectric materials [37]. On the other hand, piezoelectricity encompasses a broader range of materials that exhibit the ability to generate an electric polarization when subjected to mechanical stress or strain [37]. This relationship is further depicted in Figure 2.2 [37].

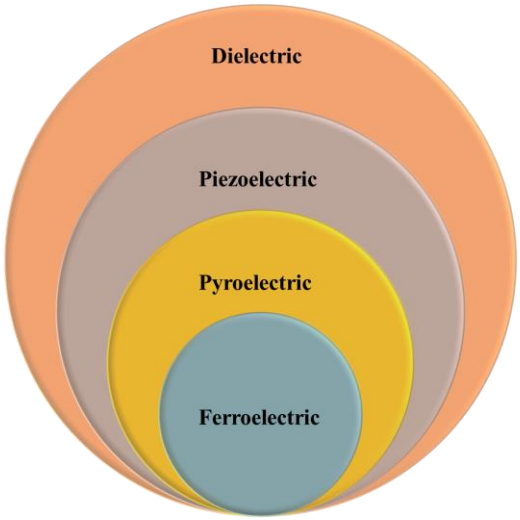

Figure 2.2: A schematic showing the interrelationship among different categories of dielectric materials [37]

2.3. Performance Measure Parameters

In the realm of ferroelectric, dielectric, and piezoelectric materials, each property is characterised by specific performance measures that quantify the extent of the property's manifestation. This section aims to provide a comprehensive understanding of these performance measures by delving deeper into their relevance and significance.

2.3.1. Dielectric Constant Properties

In the realm of dielectric materials, permittivity (often showed as dielectric permittivity and represented by symbol ε) is a fundamental property that elucidates the interaction between a material and an electric field [38] and characterises how it affects the distribution of electric charges within the material itself [37]. This characteristic can be determined by evaluating the ratio of the electric field (E) present within the material to the associated electric displacement (D), under conditions of constant stress (ε^{Tij}) or constant strain (ε^{sij}), where T and S denote stress and strain, respectively. This relationship is illustrated in Equation 2.1 [38].

$$\varepsilon_{ij} = \frac{D_i}{E_j} \qquad \text{(Equation 2.1)}$$

As was previously mentioned, a dielectric material experiences a phenomenon known as electric polarisation when it is exposed to an external electric field. During this process, the positive and negative charges inside the component atoms or molecules seek to separate. The electric polarisation vector (P) measures how much charge separation there is within the substance [39]. A schematic showing the electric polarisation upon application of an external electric field is shown in Figure 2.3 [40].

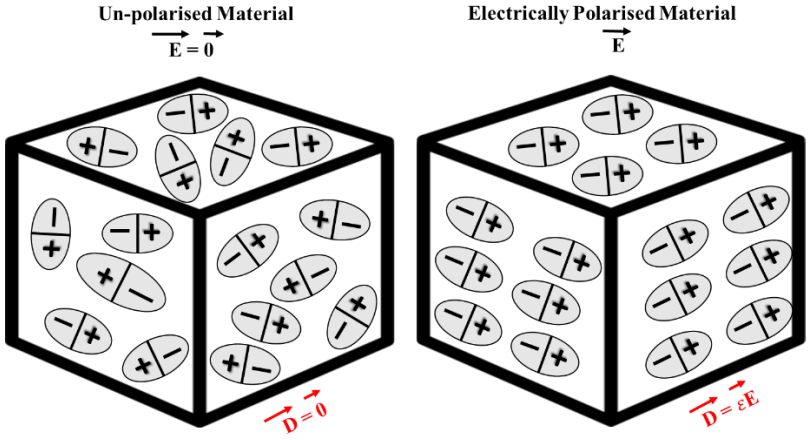

Figure 2.3: A schematic showing the dielectric polarisation in response to external electric field (inspired from [40])

The relationship between the exhibited polarisation (P), the electric field (E), and the corresponding electric displacement (D) may be explained by the formula shown in Equation 2.2, where ε_0 represents the permittivity of free space (8.85418782 × 10^{-12} F/m) [41–43]. Hence, by substituting the D in Equation 2.1 above, the dielectric constant or relative permittivity of a material (ε_r) , indicating how much a medium can withstand the passage of charge, may be defined as in Equation 2.3 [41–43].

$$D = \varepsilon_0 E + P \qquad \text{(Equation 2.2)}$$

$$\varepsilon_r = \frac{\varepsilon_0 E + P}{\varepsilon_0 E} = 1 + \frac{P}{\varepsilon_0 E} \qquad \text{(Equation 2.3)}$$

The dielectric constant or relative permittivity further describes the material's capacity to hold electrical energy. It can thus be represented by the ratio of the material's permittivity (ε_m) to that of free space as illustrated in Equation 2.4 [38]. A higher dielectric constant indicates an increased capability of the material to accommodate electric charge and exert influence on the behavior of an electric field.

$$\varepsilon_{r=\frac{\varepsilon_m}{\varepsilon_o}} \qquad \text{(Equation 2.4)}$$

For a parallel capacitor consisting of two plates with an area (A) and separated by a distance (d), the dielectric constant plays a crucial role in determining the behavior of the capacitor. The dielectric constant of the material inserted between the plates directly influences the capacitance (C) of the capacitor and thus dictates its energy storage capabilities [44]. This relationship can be depicted by the formula presented in Equation 2.5.

$$\varepsilon_r = \frac{C * d}{\varepsilon_o * A} \qquad \text{(Equation 2.5)}$$

It is worth noting that understanding and evaluating the dielectric constant is of paramount importance in the design and performance analysis of various electrical and electronic systems, such as capacitors, insulators, and dielectric materials used in numerous applications, including energy storage devices, communication systems, and electronic circuits.

2.3.2. Piezoelectric Charge Coefficient Properties

Section 2.1 of this chapter has provided an in-depth understanding of the crystal structure of various materials such as piezoelectric materials and highlighted their inherent lack of symmetry. The absence of a centre of symmetry in the crystal structure renders these materials anisotropic in nature [45]. As explained, piezoelectric materials exhibit the extraordinary phenomenon referred to as the direct piezoelectric effect, whereas electric charge or voltage is generated when subjected to mechanical stress or strain. When an external force is applied to a piezoelectric material a charge separation is exhibited which consequently generates an electric potential difference or voltage across the material [46]. In other words, mechanical energy is converted into electrical energy through the direct piezoelectric effect. In the converse piezoelectric effect, the application of an electric field induces a strain in the material that exhibits a linear relationship with the field strength. A schematic showing the direct and converse (inverse) piezoelectric effect is depicted in Figure 2.4 (a) and (b), respectively [47]. This linear connection suggests that the material's strain is directly proportional to the strength of the applied electric field and may be stated using tensor notation, as shown in Equation 2.6 [48], whereas the piezoelectric strain is referred to as S_{jk}, the applied electric field is E_i and the third rank tensor, denoted as d_{ijk}, represents the piezoelectric charge coefficients of the material; whereas the dipole polarisation direction or the applied electric field direction is depicted by the subscript ‘i’ and the

generated stress/strain is depicted by the superscript 'j'. The designated axes notations are shown in Figure 2.5.

$$S_{jk} = d_{ijk}E_i \qquad \text{(Equation 2.6)}$$

Further, the piezoelectric charge coefficient denoted as (d_{ij}) provides insights into the material's response to different types of deformation. Generally, this coefficient is influenced by the poling orientation, which determines the relative direction of the applied electric field and the resulting strain or deformation in the material. In this context, poling refers to the deliberate alignment of the material's internal electric dipoles along a preferred direction. This is achieved when the material is subjected to a strong electric field either during the fabrication process or through a subsequent poling treatment. Details on various poling techniques and alignment of the particles are explained in subsequent sections of this chapter.

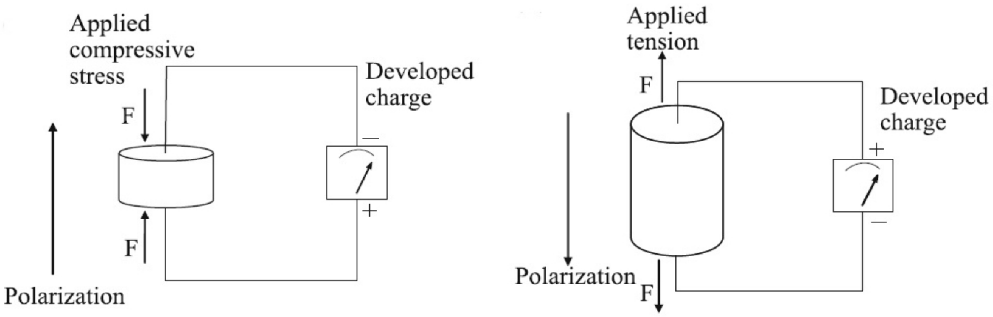

(a) Direct piezoelectric effect at applied compressive and tension stress

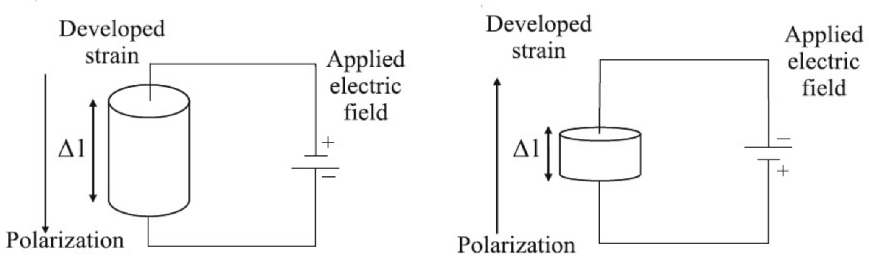

(b) Inverse piezoelectric effect at applied electric field

Figure 2.4: A schematic showing the direct and inverse (converse) piezoelectric effect [47]

Figure 2.5 illustrates the typical notations of a three-dimensional piezoelectric material's x, y, and z-axis are 1, 2, and 3, and the shear around them is 4,5 and 6, as per the IEEE standard on piezoelectricity [49]. Specifically, the longitudinal piezoelectric coefficient (d_{33}) occurs when the force applied is parallel to the direction

of the polarisation (both of them in direction 3), the shear piezoelectric coefficient (d_{15}) relates that the induced electric field is perpendicular to the polarisation direction and the corresponding strain is shear around the other perpendicular axis, and the transverse piezoelectric coefficients (d_{31} and d_{24}) indicate that the applied strain is in direction 1 perpendicular to the polarisation in direction 3 [49].

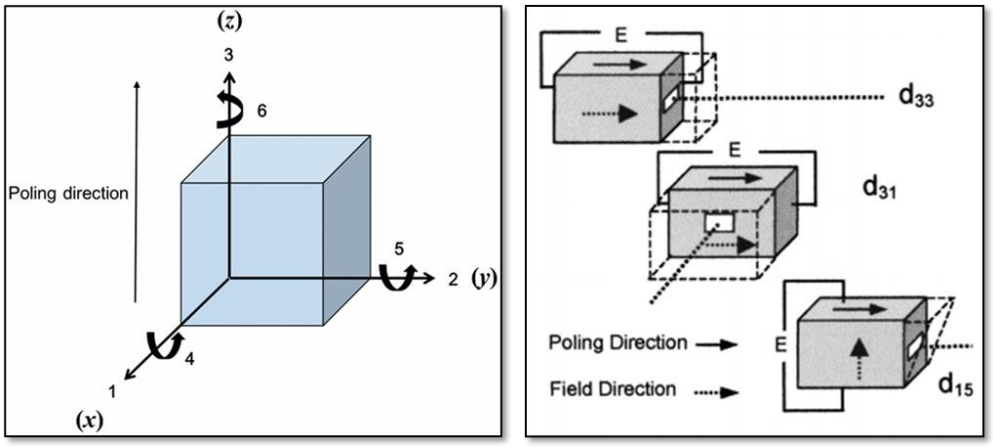

Figure 2.5: A schematic depicting the axes notation for the piezoelectric effect along with various piezoelectric coefficients and their respective poling directions [50]

To quantitatively evaluate the intrinsic piezoelectric effect (d_{ij}) and gain insights into the material's ability to generate an electric charge in response to mechanical stress or strain, direct measurements are performed using a quasi-static d_{33} meter which allows for the determination of the piezoelectric coefficient in units of picocoulombs per newton (pC/N). Additionally, the converse piezoelectric effect may be evaluated using the piezoelectric strain coefficient (d_{ij}*) which serves as a measure of domain wall motion and can be derived S-E by unipolar S-E curves (d_{ij}*)=(pm/V). This can be achieved by applying Equation 2.7 where S_{max} and E_{max} stand for maximal force and electric field, respectively [51].

$$dij* = \frac{Smax}{Emax} \qquad \text{(Equation 2.7)}$$

2.3.3. Piezoelectric Voltage Coefficient Properties

Another crucial parameter in the field of dielectrics and piezoelectricity is the piezoelectric voltage coefficient (g_{33}) which characterises the relationship between the piezoelectric charge coefficient and the dielectric permittivity and quantifies the ability of a piezoelectric material to generate voltage in response to an applied mechanical

stress or strain. This relationship can be depicted by the formula in Equation 2.8 [52] with a unit of (mVm/N) for the g_{33}.

$$g_{33} = \frac{d_{33}}{\varepsilon_0 \varepsilon_r} \qquad \text{(Equation 2.8)}$$

As observed the piezoelectric voltage coefficient is inversely proportional to the dielectric constant, and hence the majority of piezoelectric materials, which are typically inorganic ceramics with high dielectric constants, have low values for the piezoelectric voltage coefficient [53]. On the contrary, a viable alternative is the utilisation of ceramic-polymer composites, which offer the opportunity to attain a significant and measurable piezoelectric voltage constant. This can be accomplished by combining piezoelectric ceramic particles with a polymer matrix [54]. By incorporating the ceramic particles into the polymer matrix, the composite material benefits from the enhanced piezoelectric properties derived from the ceramic component and thus the resulting composite exhibits improved piezoelectric voltage response, enabling efficient conversion between mechanical deformation and electrical voltage [55].

2.3.4. Ferroelectric and Energy Storage Performance Measures

2.3.4.1. Ferroelectric Properties

After clarifying the ferroelectric nature and crystalline structure inherent in ferroelectric materials, it is imperative to discern their performance based on their corresponding parameters. The manifestation of ferroelectric characteristics in these materials is typically obtained through the observation of hysteresis loops in the P-E domain, thus portraying the material's reversible polarisation and the switching behavior provoked by external electric field stimulation. Figure 2.6 displays a representative hysteresis loop characteristic of dielectric materials [31].

To comprehensively analyse the energy storage capabilities of ferroelectric materials along with the corresponding polarisation behaviour, it is crucial to examine and evaluate several common critical points on the P-E loop hysteresis graph (shown in Figure 2.6). The highest possible polarisation value under the effect of an applied electric field is represented by saturation polarisation, P_s. It denotes the maximum degree of polarisation that the material is capable of and is a measure of how well a material can respond to an external electric field. The maximum electric field after which the polarisation is saturated and no longer takes place, is commonly refered to

as E_{max} of breakdown electric field. Upon the removal of this electric field, the residual polarisation that remains in the material, is referred to as remnant polarisation, P_r. It describes how well a substance can maintain its polarisation state and a material with a higher P_r value has a stronger ability to retain polarisation over time. For applications like non-volatile memory that demand long-term polarisation stability, this attribute is essential. A threshold magnitude of electric field, known as the coercive field, E_c, is needed to further facilitate polarisation switching of the material. A higher value of E_c denotes a material with greater polarisation stability since a larger electric field is required to reverse the polarisation [42,56,57].

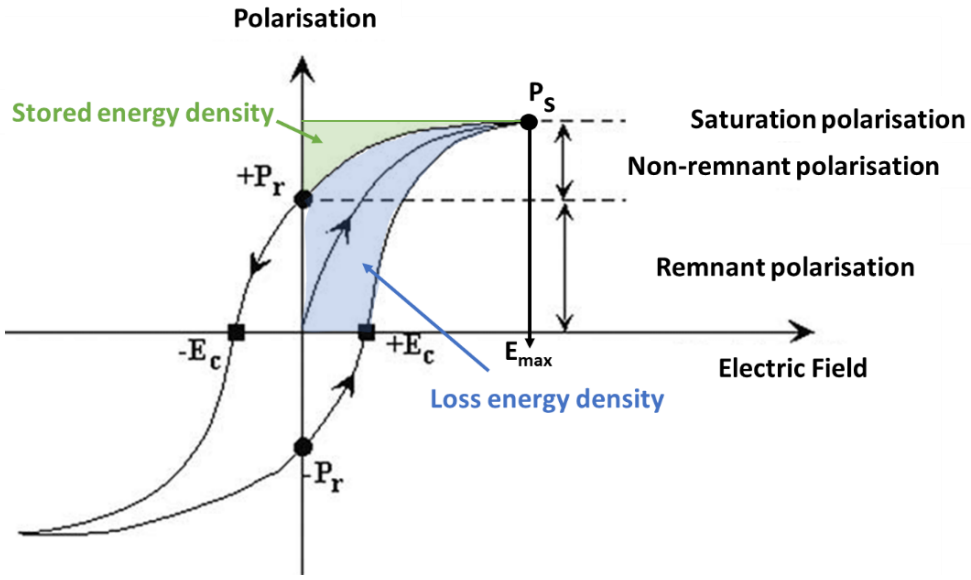

Figure 2.6: A schematic showing the P-E Ferroelectric Loop [31] with (adapted) stored/loss energy density

2.3.4.2. Energy Storage Properties

The P-E loop of ferroelectric materials may be further analysed by the area enclosed within and above the loop. The area within the loop indicates the energy loss density of the material which reflects the inefficiencies and losses encountered during the polarisation switching cycles of ferroelectric materials [58]. The area above the loop shown in green in the P-E loop in Figure 2.6 is the stored energy density, sometimes referred to as recoverable energy density or discharge energy density (U_e) represents the energy that can be retrieved or recovered from the material and thus signifies the amount of energy that can be stored within the material and subsequently released for use in various energy storage applications. The determination of this discharge energy density (U_e) usually depend on the applied electric field (E) and the electric

displacement (D) of dielectric materials and in the case of non-linear capacitators is can be evaluated using the formula shown in Equation 2.9 [59]. In the case of linear dielectrics, the U_e can be inferred using the formula shown in Equation 2.10 [59], whereas E_{max} is the maximum applied electric field to the material until breakdown, sometimes referred to as breakdown strength, and ε_r and ε_o hold the same definitions provided in earlier subsection. The formula presented in Equation 2.10 further reveals that the U_e is highly dependant on the E_{max} of the material and therefore generally those materials with increased breakdown strength depict superior discharge energy density [60].

$$U_e = \int_{Pr}^{Ps} EdD \qquad \text{(Equation 2.9)}$$

$$U_e = \frac{1}{2}\,\varepsilon_r \varepsilon_o {E_{max}}^2 \qquad \text{(Equation 2.10)}$$

2.4. Dielectric-based Ceramic Materials

This section provides an overview of various dielectric-based ceramic materials that have been extensively employed in a broad spectrum of electronic applications, including the manufacturing of capacitators, insulators, sensors, and other vital electronic devices across diverse industries, such as telecommunications and healthcare equipment manufacturing. These ceramic-based materials, particularly those dielectric ceramics displaying ferroelectric characteristics, have seen a remarkable increase in research in recent years. Amongst the various categories of ferroelectric materials such as layered bismuth oxides [61] and tungsten bronzes [61], the ferroelectric ceramic perovskites have garnered significant recognition due to their exceptional properties, including low acoustic impedance and the ability to exercise precise control over their structure and composition [62,63].

Perovskites are a category of ceramics primarily based on the mineral calcium titanate $CaTiO_3$ [64]. Their discovery can be attributed to their initial identification in the Ural Mountains of Russia and subsequent naming after the renowned chemist Lev Perovski (1792-1856) [65]. The general stoichiometry for a simple perovskite crystal structure within a cubic unit cell is denoted as ABO_3, where A and B represent cations, and O represents anions [66]. The typical unit cell of a perovskite structure is depicted in Figure 2.7 [67]. By incorporating additional metal ions into both the A and B sites

through doping, the properties of perovskite materials can be tailored to meet specific requirements [67].

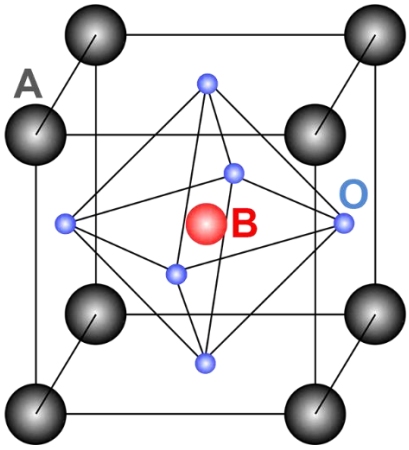

Figure 2.7: A schematic showing the crystal structure of a unit cell perovskite crystal [67], where A (in black) and B (in red) depict the cations and O (in blue) depict the anions

Ferroelectric ceramics with a perovskite structure encompass a range of compositions, including both lead-based and lead-free variants [53,68–72]. Examples of lead-based ferroelectric ceramics include lead zirconate titanate (PZT) and lead titanate [53], while lead-free options consist of materials such as barium titanate (BT) [51], sodium bismuth titanate (BNT) [51], and potassium sodium niobate (KNN) [51]. However, due to the toxicity of lead-based ceramics [73], significant research efforts have been directed towards the development of lead-free based alternatives. The following subsections provide an overview of the commonly known lead-free perovskite ceramics as well as an overview of the lead-based PZT.

2.4.1. Lead Zirconate Titanate (PZT)

Lead zirconate titanate, often known as PZT, is a well-known lead-based perovskite ceramic that has attracted significant interest since 1954 as a result of the greatly enhanced piezoelectric properties as well as the relatively increased operating temperature range compared to other perovskite ceramics [74–77]. It is mainly composed of lead (Pb), zirconium (Zr) and titanium (Ti) with $Pb[Zr_xTi_{1-x}]O_3$ as the chemical formula and x as the molar fraction composition between 0 and 1 [78]. The so-called morphotropic phase boundary (MPB), which is characterised as the region where rhombohedral and tetragonal phases simultaneously exist, separates the crystal structure of PZT into tetragonal structure for compositions rich in Ti (such as $PbTiO_3$)

and rhombohedral structure for compositions rich in Zr (such as $PbZrO_3$) [79]. The phase diagram of PZT is shown in Figure 2.8 (a) [53]. Around this MPB region, at room temperature and at a composition of $PbZr_{0.52}Ti_{0.48}O_3$, the crystal structure exhibits a sudden change, leading to its highest dielectric properties such as corresponding dielectric constant and electromechanical coupling factor, compared to non-MPB compositions. In context of piezoelectric materials, the electromechanical coupling factor, referred to as (k), indicates the rate of conversion between the mechanical and electrical energy [80]. The enhanced dielectric properties are attributed to the facilitated reorientation of dipoles across the domains [81,82]. The enhanced dielectric constant and increased electromechanical coupling factor around the MPB can observed in Figure 2.8 (b) [53].

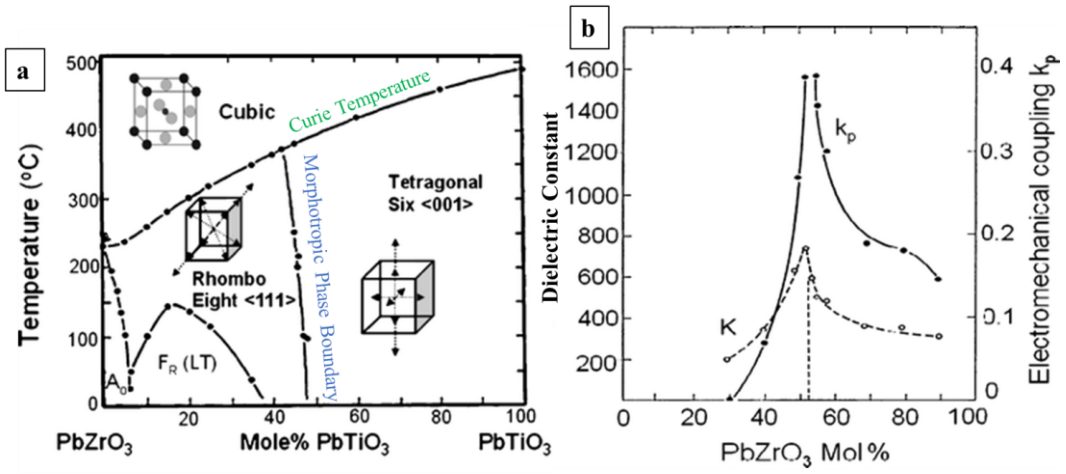

Figure 2.8: A schematic showing (a) phase diagram of PZT and (b) varying dielectric constant and electromechanical coupling factor around MPB as a function of molar fraction composition of the $Pb(Zr,Ti)O_3$ system [53]

2.4.2. Barium Titanate (BT)

Barium titanate (BT), also known as BTO ($BaTiO_3$) is recognised as one of the earliest known perovskite compounds [64]. Its ferroelectric behaviour was first identified in 1946, which greatly contributed to the advancement of ferroelectric and piezoelectric technology. Generally, BT can exist in different crystallographic states depending on the temperature it is exposed to. Figure 2.9 illustrates four common states of the BT unit cell at varying temperatures [83]. Figure 2.9 (d) shows that at relatively higher temperatures, BT adopts a cubic perovskite structure where Ba^{2+} ions occupy the corners, Ti^{4+} ions are located at the center, and oxygen ions are positioned at the face centers. This structure is centrosymmetric and exhibits octahedral coordination around

the titanium ion and dodecahedral coordination around Ba^{2+} and thus shows no ferroelectric characteristics. At the Curie temperature (T_C approximately 120-130°C), BT undergoes a phase transition from the paraelectric cubic phase to a ferroelectric tetragonal phase with a crystallographic orientation of 001 [83]. As the temperature further decreases, BT transitions to an orthorhombic ferroelectric phase at approximately 5-15°C, and then to a ferroelectric rhombohedral phase below around -80 to -90°C with crystallographic orientations of 011 and 111, respectively. These crystallographic and shape transitions correspond to distinct orientations of electrical charges within the crystal, which result in an increase of the macroscopic spontaneous polarisation (P_S) as the temperature decreases. It is also worth noting that, the ratio of the lattice parameters at room temperature in the tetragonal cell (a = b, c ≈ 4a) is roughly 1.011, indicating a deformation and spontaneous strain of about 1%. Even with such a slight distortion, the P_s can still be rather high, up to 20–25 mC/cm^2. It is further observed that, that the dielectric constant decreases with decreasing temperatures. At the transition temperatures, the dielectric constant exhibits distinct discontinuities which manifest as abrupt changes in the dielectric constant rather than a smooth and gradual transition between the observed values [83].

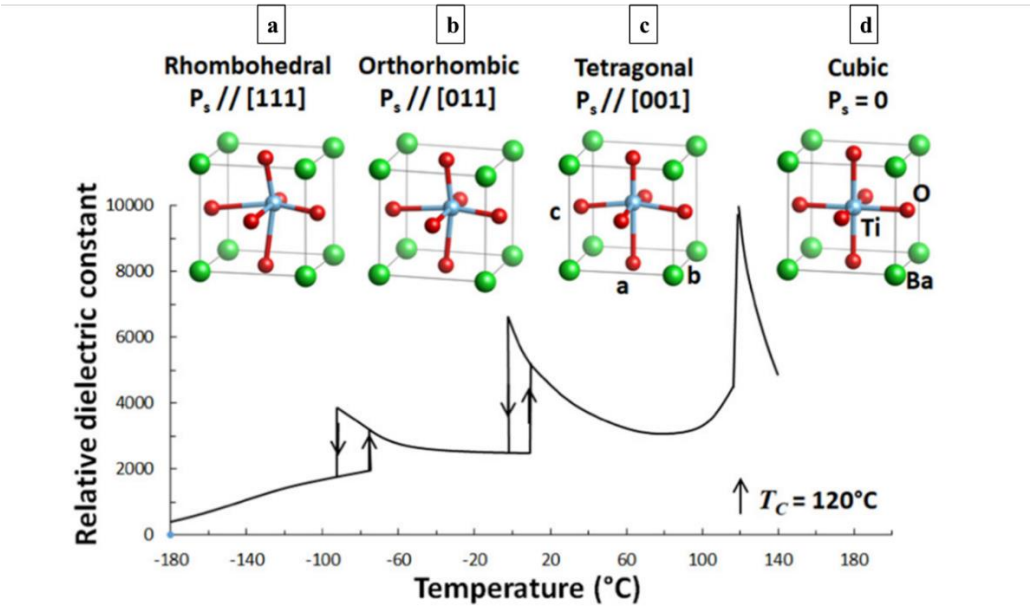

Figure 2.9: Phase transition of BT crystal structure with varying temperature along with the respective relative dielectric constant [83]

2.4.3. Bismuth Sodium Titanate (BNT)

Bismuth sodium titanate ($Bi_{0.5}Na_{0.5}TiO_3$), commonly known as BNT, is an electroactive-ceramic material belonging to the ABO_3 perovskite type. Its initial

discovery can be traced back to the early 1960s, credited to Smolenskii and colleagues [84]. Since then, BNT has found extensive utilisation in a wide range of electronic and electric applications, including but not limited to sensors and actuators, until the present day [85–87]. Its relatively higher T_c of around 300^{o}C compared to the BT, allows for its use in high-temperature based applications, such as piezoelectric sensors [88] and actuators [89], which require materials that can operate at high temperatures without losing their ferroelectric properties [90–92]. Additionally, it possesses unique dielectric properties, including a high remnant polarisation (P_r) of 38 $\mu C/cm^2$ and a high coercive field (E_c) of 73 kV/cm [93–97]. Research on BNT-based ceramics has revealed several key properties that make them useful for various applications. For instance, the high P_r and E_c values of BNT-based ceramics make them ideal for use in ferroelectric capacitors, where high charge density and high energy storage are necessary.

Interestingly the BNT possesses a structural complexity which has sparked continuous debates and investigations aiming to understand its precise arrangement until present day. Therefore, the crystallographic structure of BNT can be conceptualised and modeled from two distinct perspectives. The first perspective, proposed by [98], suggests that BNT adopts a rhombohedral structure with the R3c space group. This arrangement involves specific antiphase rotations of oxygen octahedra along the a−a−a directions. Within this rhombohedral structure, a three-dimensional cubic grid is formed by bonding TiO_6 octahedra to bismuth and sodium ions located at the center of the cube. However, with the advancement of higher-resolution single crystal XRD analysis, as undertaken by Gorfman and Thomas [99], the structure of BNT has undergone further scrutiny and refinement. This has led to the emergence of the second perspective, which suggests that the structure of BNT may be better represented by the monoclinic space group Cc. This alternative viewpoint is supported by the research conducted by Aksel et al. [100], thereby contributing to the ongoing discussions surrounding the precise structural nature of BNT. Notably, the displacement of Na, Bi, and Ti ions along the [111]p direction gives rise to the development of a polarised ferroelectric phase when subjected to an electric field. The two model perspective of the BNT structure are illustrated in Figure 2.10 [101].

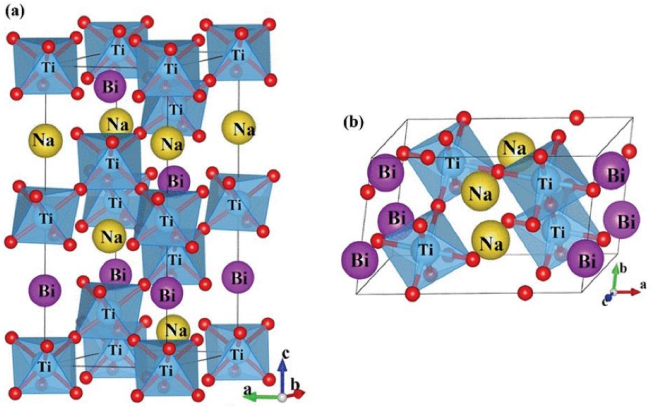

Figure 2.10: BNT crystal structure showing (a) rhombohedral R3c model (hexagonal setting) and (b) monoclinic Cc phase model [101]

Similar to BT, BNT can also manifest in diverse crystallographic phases contingent upon temperature variations. As such, it is observed that within the temperature interval of -260°C to 255°C, BNT assumes the rhombohedral phase denoted as R3c. Subsequently, spanning from 255°C to 400°C, BNT undergoes a coexisting phase in which both rhombohedral and tetragonal structures coexist [102]. As the temperature escalates from 400°C to 500°C, BNT transits into the tetragonal phase classified as P4bm. The temperature range of 500°C to 540°C witnesses an intermediate phase characterised by attributes belonging to both tetragonal and cubic structures. Ultimately, beyond 540°C, BNT adopts the cubic prototype phase designated as Pm3m. The variation in the corresponding crystallographic structure upon temperature change is depicted in Figure 2.11 (modified from [102]).

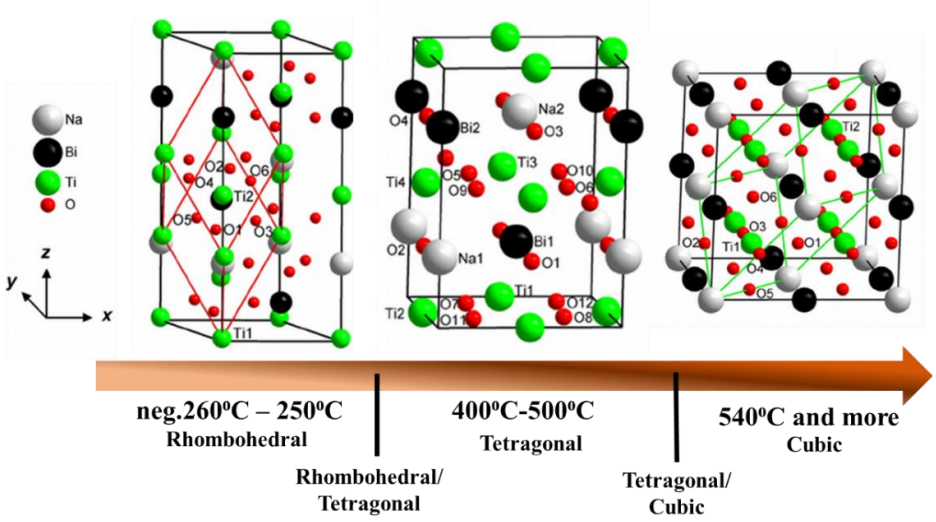

Figure 2.11: Variation of BNT crystal structure in response to increasing temperature; from rhombohedral to tetragonal to cubic (modified from [102] to reflect corresponding temperature)

2.4.4. Potassium Sodium Niobate (KNN)

Potassium sodium niobate, also referred to as KNN and denoted as $K_{0.5}Na_{0.5}NbO_3$, is another commonly known lead-free ceramic material that falls within the perovskite structure of ABO_3 [8,103,104]. It has garnered significant attention as a potential substitute for traditional piezoelectric materials, such as PZT, in a wide range of applications. Since its discovery in 1950 [105], KNN has attracted increased research interests due to its unique properties such as the relatively high T_C (>400°C), the enhanced piezoelectric response and the inherited ferroelectric properties.

The perovskite structure of KNN, characterised by its arrangement of A and B cations and oxygen ions, contributes to its remarkable ferroelectric and piezoelectric properties. With potassium (K) and sodium (Na) ions occupying the A-site and niobium (Nb) ions occupying the B-site, KNN represents a solid solution between two different constituents: $KNbO_3$ (a ferroelectric material) and $NaNbO_3$ (an antiferroelectric material). A schematic showing the typical KNN crystal structure is shown in Figure 2.12 (a) [103], whilst Figure 2.12 (b) shows the phase diagram of the KNN solid solution [106].

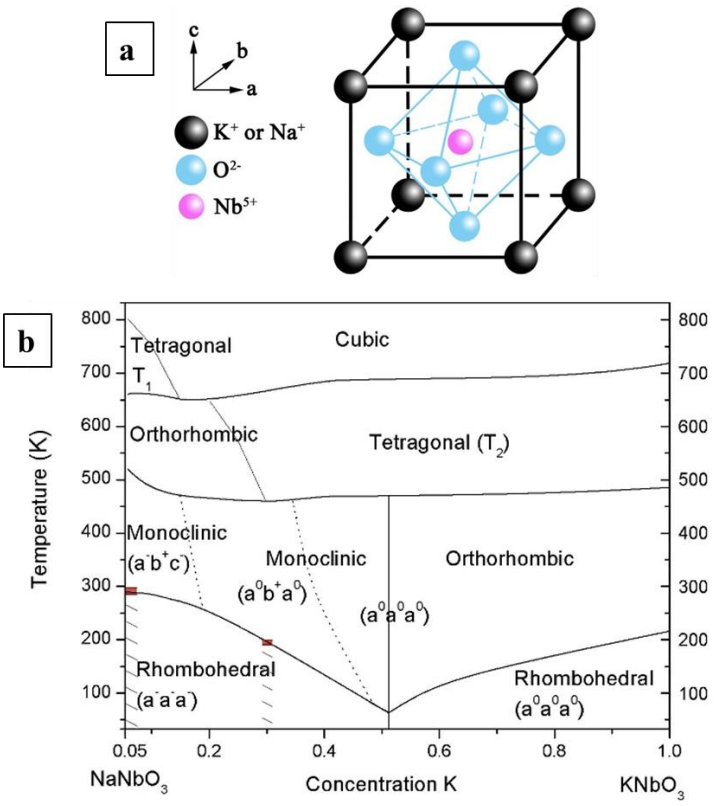

Figure 2.12: A schematic showing (a) the typical KNN crystal structure [103], and (b) the phase diagram of the solid solution KNN system [106]

At room temperature, the perovskite structure of KNN demonstrates an orthorhombic structure that has a space group of Amm2. It is worth noting that KNN is distinguished from its end members, $KNbO_3$ and $NaNbO_3$, by this crystal structure, which both display various symmetries under ambient circumstances. It is noteworthy that KNN displays several phase boundaries that vary based on the composition of its constituents (as observed in Figure 2.12 b). The molar fraction composition with a 0.5 ratio as the case of $K_{0.5}Na_{0.5}NbO_3$, has gained the most attention in research [107–110]. This is because this particular composition lays around the MPB of KNN, which separates two orthorhombic phases and shows a good balance between a modest dielectric constant and an ideal piezoelectric response, making it an attractive option for real-world applications. The $K_{0.5}Na_{0.5}NbO_3$ composition undergoes three phase transitions: from rhombohedral to orthorhombic at approximately −110°C, from orthorhombic to tetragonal around 220 °C, and from tetragonal to cubic at approximately 420 °C. These phase transitions represent structural changes in the material's crystal lattice, leading to varying dielectric properties, i.e. dielectric constant and dielectric loss as depicted in Figure 2.13 [111].

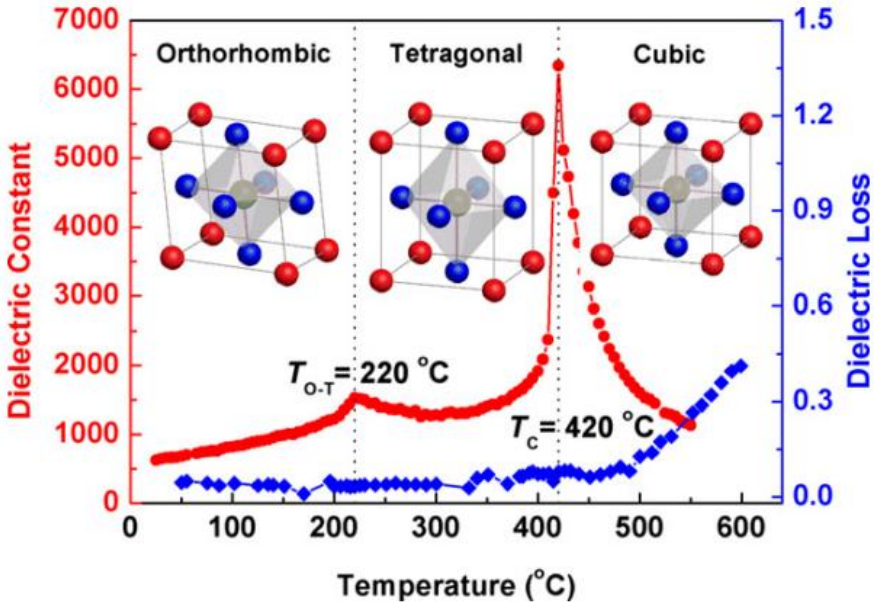

Figure 2.13: Variation of KNN crystal structure in response to varying temperature, along with the corresponding (temperature-dependent) dielectric constant and dielectric loss; whereas the blue, red and black points represent alkali elements in A and B sites, correspondingly [111]

A comparison between the dielectric constant of various lead-free perovskite ceramics can be depicted in Figure 2.14 [53]. The relationship between the piezoelectric charge

coefficient (d_{33}), room temperature dielectric constant values (ε_r) of lead-free perovskites, and the T_c, can be further depicted in Figure 2.14 (a) and (b), respectively [53]. Lead-based PZT is also included for reference. It can be observed that as the T_c decreases, the dielectric and piezoelectric properties are intrinsically enhanced for PZT-based materials. Conversely, the lead-free perovskite materials belonging to the three families of BT, BNT (or NBT) and KNN demonstrate minimal, if any, enhancement in these characteristics as the T_c decreases [53].

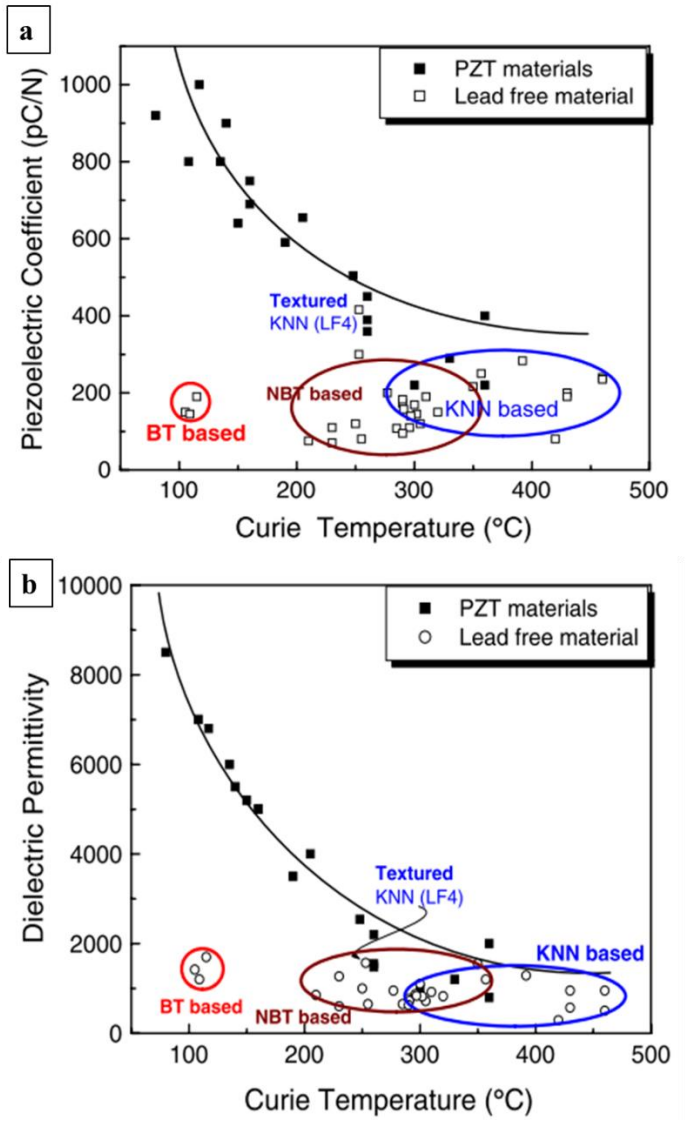

Figure 2.14: Variation of (a) piezoelectric charge coefficient and (b) room temperature dielectric constant values in repsonse to varying Curie temperature for various perovksite ceramics [53]

2.4.5. Ceramic Powder Synthesis Methods

In order to obtain and acquire the aforementioned ceramic powders exhibiting dielectric/ferroelectric/piezoelectric properties and even effectively control their morphology, it is essential to explore the synthesis methods employed in their fabrication. This section aims to provide a comprehensive analysis of the most widely employed synthesis techniques utilised for various ceramic powders' synthesis. Generally, the synthesis of ceramic powders involves various methods, each offering distinct advantages and enabling precise control over particle morphology. Among the various methods available for ceramic powder particle synthesis, the conventional solid-state reaction [112], hydrothermal method [113], molten salt synthesis method [13], and sol-gel method [114] are recognised as the most widely employed. By understanding these synthesis processes and their corresponding crucial synthesis parameters, the properties of ceramic powders can be tailored to meet specific dielectric-based application requirements.

2.4.5.1. Solid-State Reaction Synthesis Method

Amongst the above-mentioned various synthesis methods, the solid-state reaction (SSR) stands as one of the oldest and most widely employed [112]. It has been widely employed in the synthesis of various lead-free ceramics [115,116]. In this method (solid-state), the precursor powders are meticulously weighed, thoroughly blended, and subsequently subjected to a milling or grinding process to achieve a homogeneous distribution of the constituents. Following the milling step, the mixture is subjected to calcination at elevated temperatures [112], which vary depending on the specific material being synthesised, such as ~1200°C for BT [117]. However, the solid-state synthesis technique is often constrained by the requirement for higher synthesis temperatures compared to other synthesis methods. This elevated temperature can limit the control over the reaction and lead to non-uniform microstructures in the resulting ceramics [118]. Furthermore, achieving precise compositions can be challenging, and the scalability of the solid-state method is relatively limited [119].

2.4.5.2. Hydrothermal Synthesis Method

Another prominent method is the hydrothermal method which is utilised to crystallise chemical substances with the assistance of aqueous solvents [120,121]. It involves operating at elevated pressure and relatively low temperatures compared to other synthesis procedures such as molten salt and solid-state methods [120,121]. The

synthesis takes place in a closed system using a steel-made pressure vessel called an autoclave (seen in Figure 2.15 (a)) [122], enabling crystal growth or reactions to occur at high pressure and specific temperatures. This method is considered environmentally friendly as the closed system allows for recycling of the materials [122]. The typical procedural steps involved in the hydrothermal method is depicted in Figure 2.15 (b) [122]. One advantage of the hydrothermal process is the relatively low reaction temperature required, which offers benefits such as improved energy efficiency and reduced thermal stress on the materials [123]. Additionally, there is a variation of the hydrothermal synthesis called microwave-assisted hydrothermal [124], where thermal treatment is conducted using a microwave oven with controlled pressure. This variation offers advantages such as shorter reaction times, uniform nucleation of powders in suspension, and reduced costs compared to the conventional solid-state processes [124]. On the other hand, the hydrothermal synthesis process may be limited by the use of expensive autoclaves, which can increase the overall cost of the synthesis process, as well as the requirement for high pressure and controlled temperature conditions, which can restrict the scalability and practicality of the synthesis process.

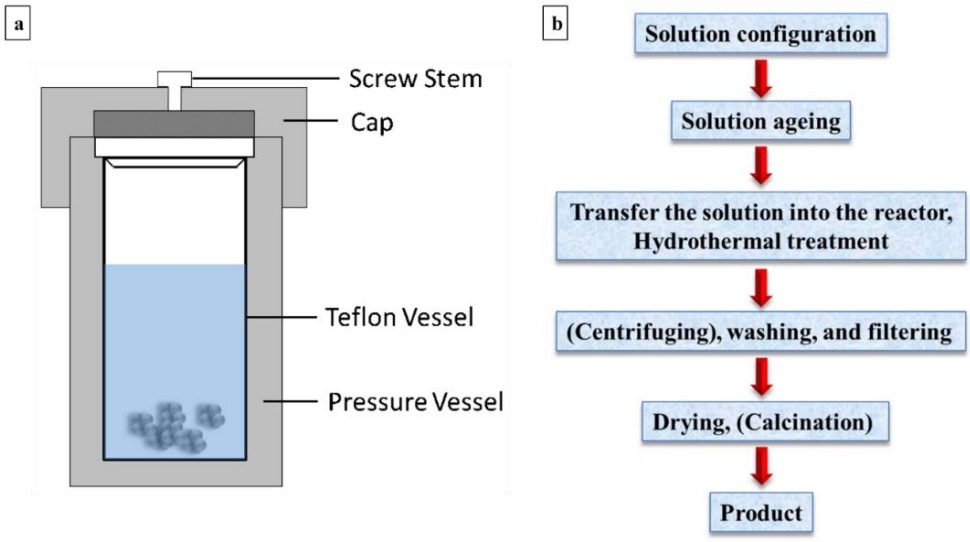

Figure 2.15: (a) A schematic showing the autoclave employed in hydrothermal synthesis; and (b) the steps of the hydrothermal synthesis technique [122]

2.4.5.3. Molten Salt Synthesis Method

Among various synthesis techniques employed for the fabrication of ceramic powders with desirable dielectric properties, the molten salt synthesis technique (MSS) has emerged as a promising method to synthesise these ceramic powders [125–128]. In this synthesis method, a substantial quantity of salt or a mixture of salts is used as a

solvent to expedite the reaction process [13]. The most extensively utilised salt flux is typically either NaCl or KCl or a combination of them due to their affordability, ease of washing with water, and availability [129]. Initially, the reactants are weighed according to stoichiometric ratios, after which the selected salt is added with a desired ratio to the reactants and then mixed together, usually using ball milling to obtain uniformly distributed mixture [130,131]. A surfactant may be also added during this step to obtain powder particles having nano-sized scale [13]. The next step involves heating the obtained mixture at a synthesis temperature, that is typically set higher than the melting temperature of the introduced salt/salt mixture, to allow the reactants to react within the molten salt. Generally, a synthesis temperature in the range of 800^{o}C – 1100^{o}C is selected with a holding time range of 30 – 60 minutes [13]. In certain systems, it was observed that the heating rate during this stage can impact the size of the particles. [132–134]. After the heat treatment, the obtained powder particles are washed with warm deionised water and dried to obtain the final ceramic powder. In general, any adjustments made to the synthesis temperature, heating rate, or duration can significantly influence the morphology of the final particles [13]. Generally, higher temperatures lead to increased material transport rate as well as increased salt evaporation rates which ultimately affect the shape of the product particles [13]. However, which exact temperature, holding time and heating rate would yield which exact dimensions of the product particles remains unclear. A schematic diagram illustrating the sequential steps involved in the molten salt synthesis (MSS) technique, along with the factors influencing the characteristics of the resulting ceramic powder at each stage, is presented in Figure 2.16 adopted from [135].

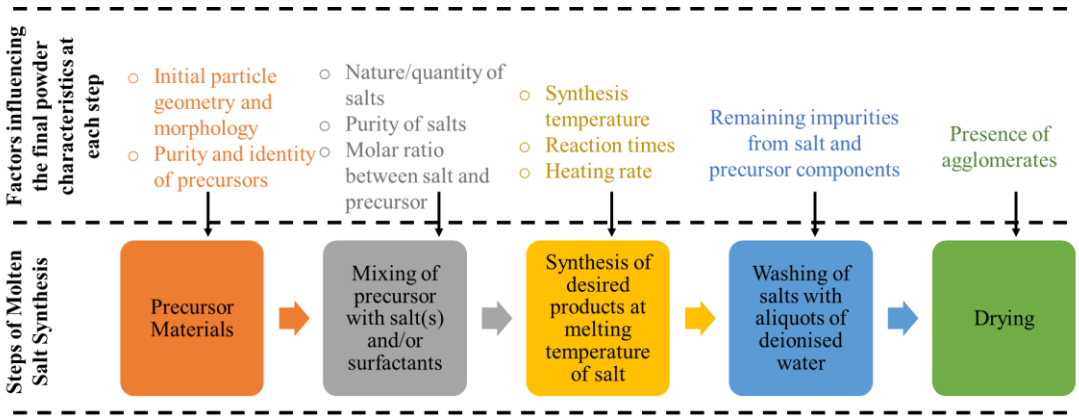

Figure 2.16: A schematic diagram illustrating the sequential steps involved in the molten salt synthesis (MSS) and the factors influencing the characteristics of the resulting ceramic powder at each stage (reproduced from [135])

MSS generally occurs during two stages. During the first stage, referred to as the reaction stage, reactant particles dissolve in the molten salt while product particles begin to form. This stage may be driven by the solution-precipitation or the solution-diffusion mechanisms, illustrated in Figure 2.17. The solution-precipitation mechanism occurs when the dissolution rate of the reactants is generally similar [136]. In such instances, the product particles are formed and precipitated as the introduced reactants dissolve within the molten salt (seen in Figure 2.17 (a)). Herein, the obtained shape of the product particles is inherent and typically prevents the achievement of anisotropic particles. On the other hand, the solution-diffusion mechanism, sometimes knows as template growth, occurs when the reactants have dissimilar dissolution rates [123]. As such, reactant particles with higher dissolution rate, dissolve faster in the molten salt and diffuse through it and consequently react with those reactants with a lower dissolution rate (seen in Figure 2.17 (b)). Herein, the shape of the product particles is generally similar to that reactant with the lower dissolution rate.

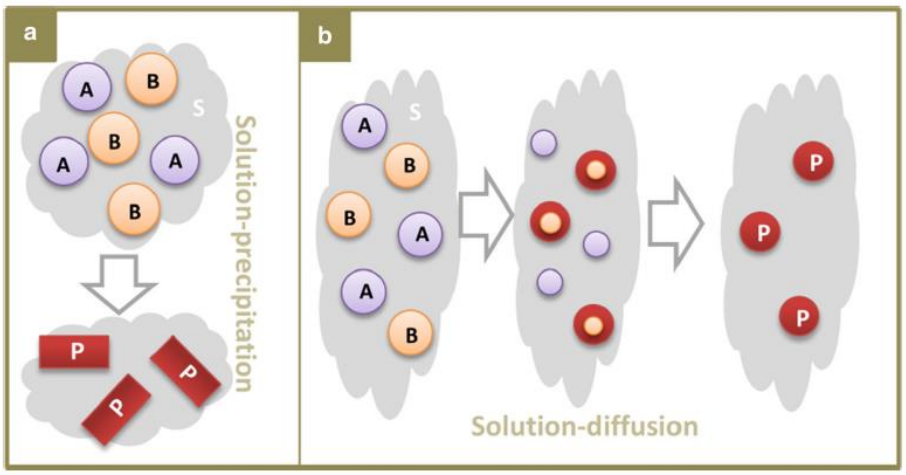

Figure 2.17: A schematic showing the product particles formation during the initial stage of MSS in which (a) depicts the solution-precipitation and (b) the solution-diffusion mechanism; whereas A, B and P represent reactant and product particles, respectively [129]

Upon completion of the first stage, the growth stage ensues, marked by complete dissolution of all reactant particles. At this stage, the only solid phase in the molten salt is the product particles and there is almost no longer any supersaturation. Herein, the particles grow larger and hence have larger surface area due to prolonged heating at elevated temperatures due to the Ostwald ripening phenomenon [13].

In some cases, to attain specific shapes of product particles such as plate-like or needle-shaped particles, the so-called topochemical microstructure conversion (TMC) is subsequently employed [137–139]. This involves diffusing supplementary material with the precursor particles within the molten salt reaction to preserve the shape of the precursor and obtain product particles with similar shape to that of precursor [13,129]. This is mainly driven by the solution-diffusion mechanism. Several perovskite ceramics with various crystal structures have been synthesised using this conversion approach, such as the obtained platelike particles of $NaNbO_3$ [140], $BaTiO_3$ [141], $CaTiO_3$ [138], $Bi_{0.5}Na_{0.5}TiO_3$ [142,143] and needle-like particles of $KNbO_3$ [144] prepared from relevant corresponding precursors.

The MSS approach is known for its superior reaction kinetics compared to solid-state reactions, primarily attributed to the reduced diffusion distances within the molten system and the enhanced mobility of oxides. One notable advantage is the enhanced reaction time compared to solid-state reactions, facilitated by the presence of molten salt that aids in the dissolution of the reactants. This promotes efficient mixing and increased surface contact between the reactants within the molten medium, resulting in a homogeneous product mixture [145]. Moreover, this technique enables the synthesis and control of powders with different sizes and shapes by manipulating the influencing synthesis parameter factors illustrated earlier. The manipulation and control of the resulting morphology may be advantageous in tailoring desired particle's geometry for specific dielectric-based applications as will be further elaborated in subsequent sections. Additionally, MSS is considered cost-effective, as it does not require specialised equipment such as the autoclave in hydrothermal synthesis for instance. Despite its general ease of implementation, the synthesised product particles may be limited by the contact area between the dissimilar reactants involved in the reaction [146]. This limitation arises from the requirement for effective interfacial interactions between the reactants, which can be influenced by factors such as particle size, shape, and surface characteristics.

2.4.5.4. Sol-gel Synthesis Method

Another versatile and widely employed ceramic synthesis technique, particularly for the production of lead-free ferroelectric ceramic powders, is the sol-gel synthesis method [147–149]. This method is based on a wet chemical approach, wherein a molecular precursor is dissolved in water or alcohol to form a sol [150]. The sol then

undergoes gelation through hydrolysis or alcoholysis, facilitated by heating and stirring. The resulting gel is typically wet or damp and requires appropriate drying methods to achieve the desired properties and application. The drying process depends on the solvent used in the gel, with alcohol burning being a common method for alcoholic solutions [151]. Once dried, the gels are transformed into powdered form and subjected to calcination. The employed drying method significantly influences the properties of the resulting dried gel, which are tailored to suit the intended applications. A schematic showing the various steps involved in the sol-gel synthesis process along with the various drying methods is depicted in Figure 2.18 [151].

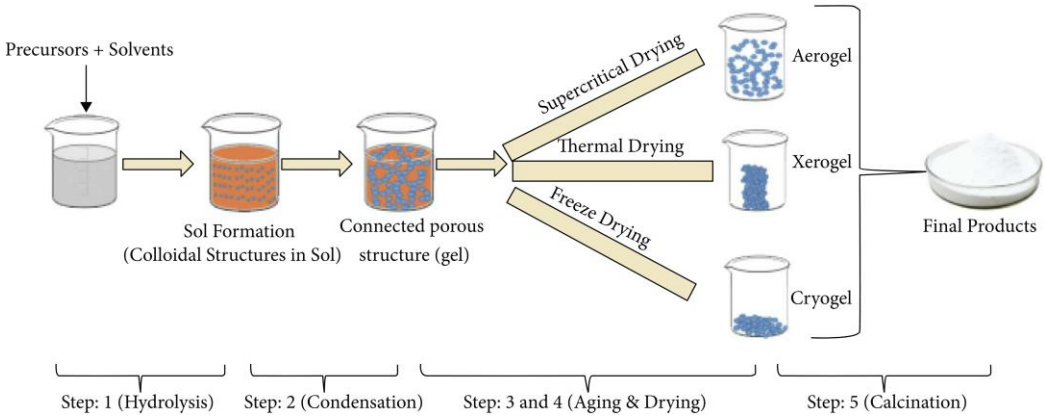

Figure 2.18: A schematic showing the sequential steps involved in the hydrothermal synthesis process [151]

The sol-gel method may offer several advantages such as the ability to operate at relatively low temperatures, produce fine powders, and achieve compositions that are not attainable through solid-state synthesis methods [152]. However, drawbacks of the sol-gel method include the requirement for careful drying processes and potential challenges in achieving uniform particle size distribution. Additionally, the cost of raw materials, particularly the chemicals used, can be high, making it an expensive process.

2.5. Dielectric-based Polymeric Materials

Generally, ceramics/inorganic materials demonstrate significantly higher dielectric constants compared to polymeric materials [153]. This is attributed to the presence of intrinsic ions and polar groups, which contribute to their elevated dielectric response. Nonetheless, polymer dielectric materials offer several advantages over ceramic counterparts, including their relatively lower density which makes them particularly appealing in lightweight applications, such as wearable sensors, where weight

reduction is crucial [154]. Additionally, they offer higher flexibility which allows for greater design freedom and enables them to be used in various forms and applications [154]. Although the dielectric constant of polymers is generally lower than that of piezoelectric ceramics, this characteristic results in a higher voltage coefficient, which may be advantageous in specific applications.

Polymers exhibit different dielectric properties depending on their polarity. They may be divided into polar and non-polar polymer based on the geometry of their relevant chains [154]. Polymethyl methacrylate (PMMA), polyvinyl chloride (PVC), polyamide/Nylon (PA), polycarbonate (PC) are among the commonly known polar polymers [154]. Generally, they possess a permanent dipole moment due to the presence of polar functional groups or asymmetric molecular structures and thus exhibit distinct dielectric properties. When those polar polymers are subjected to an alternating electric field, the dipole moments within the polymer chains (which were initially not aligned) need some time to align themselves. At very low frequencies, the dipoles generally have sufficient time to align with the field direction and before it changes its (electric field) direction. In contrast, at very high frequencies, the dipoles do not have enough time to align before the field changes its direction. The dielectric constant of polar polymers varies with the frequency of the alternating current. At low frequencies (e.g., 60 Hz), polar polymers generally demonstrate dielectric constants ranging from 3 to 9, while at higher frequencies (e.g., 100 Hz), the dielectric constant decreases and generally ranges from 3 to 5 [154]. This frequency dependence arises from the behavior of the dipoles in response to the changing electric field.

On other hand, non-polar polymers such as polyethylene (PE), polypropylene (PP), polystyrene (PS), and polytetrafluoroethylene (PTFE), are those polymers that lack a permanent dipole moment. In contrast to polar polymers, non-polar polymers have an even distribution of charge within their molecular structure, resulting in a balanced electron density. Therefore, they exhibit different dielectric properties when compared to polar polymers. In an alternating electric field, the absence of a dipole moment means that non-polar polymers do not require time to align their molecular charges with the changing field direction. The electron polarisation in this case is essentially instantaneous, regardless of the frequency of the applied alternating current. Due to their inherited non-polar nature, non-polar polymers generally have lower dielectric constant values (less than 3) compared to those of polar polymers which makes them

suitable for specific applications where low dielectric constant is desired. Figure 2.19 shows an example of the dipole moment of the non-polar PTFE and the polar PVC [154]. It can be observed that in the case of PTFE, the vectors are oriented in opposite directions, effectively cancelling each other out and hence non-polar, whereas that of the polar PVC are oriented parallel to each other and thus enhancing the overall strength of the dipole moment within the material.

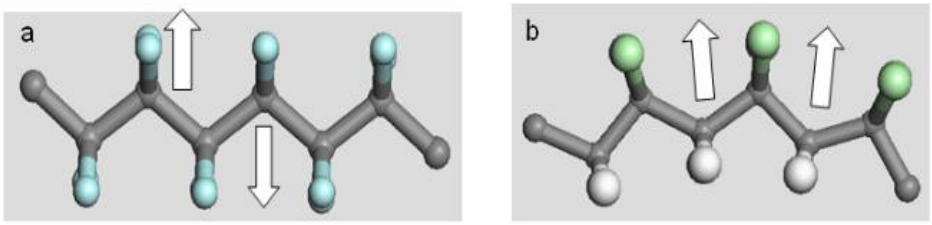

Figure 2.19: Net dipole moment exhibited by (a) non-polar PTFE and (b) polar PVC [154]

Another interesting polymeric dielectric material is the poly (vinylidene fluoride) (PVDF) which exhibits both polar and non-polar phases based on the fabrication method [155]. It has been widely investigated to its relatively higher dielectric constant (around 10) compared to other polymeric matrices, as well as the increased breakdown strength around 1500-5000kV/cm [156]. Generally, PVDF manifests five distinct crystalline polymorphs, namely α, β, γ, δ, and ε phases [157,158]. Among these phases, the α and ε phases of PVDF display non-polar characteristics due to the antiparallel alignment of dipoles within their crystal structures. In contrast, the remaining three phases possess inherent polarity, offering distinctive ferroelectric and piezoelectric attributes. The α, β, and γ phases of PVDF have been extensively investigated due to their notable properties and wide-ranging applications [155]. Among these, the α phase is particularly accessible, attracting considerable research attention towards exploring melt crystallisation of PVDF and the α to β phase transformation. Efforts to enhance the prevalence of the electrically active β and γ phases in PVDF continue to be pursued, given their significant potential for deployment in diverse domains such as spin valve devices, sensors, energy storage systems, and beyond. Figure 2.20 shows a schematic of the α, β, and γ phases of PVDF [155].

Generally, the α phase may be obtained through direct crystallisation from the melt. In the case of the β phase, the all-trans planar zigzag conformation (shown in Figure 2.20 [155]) of the hydrogen and fluorine atoms induces a substantial dipole moment.

Herein, the arrangement of hydrogen and fluorine in opposite configuration (located on both sides of the chain) leads to experiencing an electron-withdrawing force from the fluoride atoms. This electron-withdrawing nature of fluorine renders the β-phase polar, leading to the manifestation of ferroelectric properties. Conversely, the γ phase exhibits a weaker piezoelectric effect compared to β phase PVDF, primarily attributed to the presence of gauche bonds occurring every fourth repeat unit. Thus, the β phase of PVDF generally exhibits superior piezoelectric, ferroelectric, and pyroelectric properties when compared to the other polymorphs.

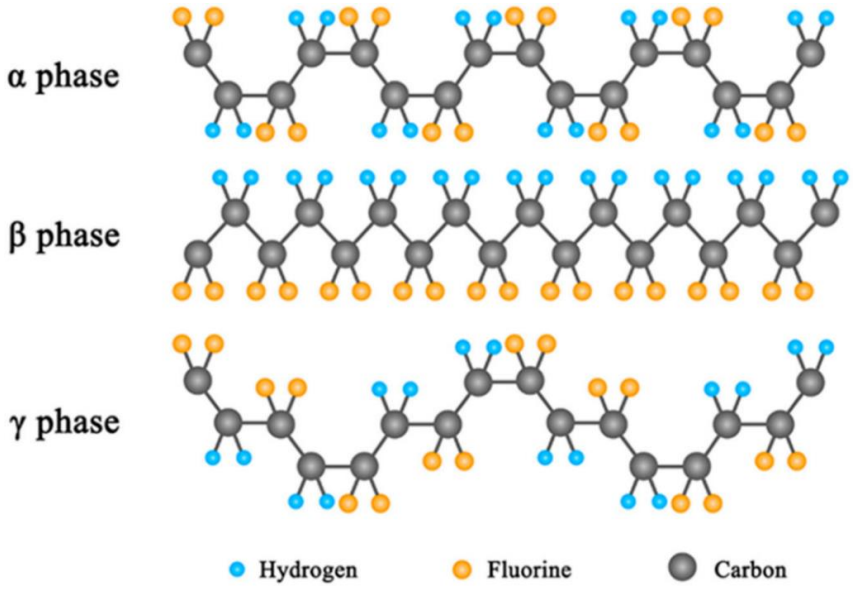

Figure 2.20: α, β and γ phase of PVDF [155]

2.6. Ceramic-Polymer Dielectric Composites

The previous subsections of this chapter have reviewed the distinct advantages offered by dielectric ceramics and polymers. Polymers have proven to offer flexibility, while ceramics are proven to provide unique ferroelectric properties and relatively higher dielectric constants. However, certain limitations still inhibit their widespread incorporation in numerous applications at an affordable cost. For instance, ceramics are limited by their high density and brittleness, whereas polymers are limited by their significantly lower dielectric values and their relatively higher production costs. In this context, ceramic-polymer dielectric composites emerge as a viable solution to circumvent these challenges by combining the advantages of both single-component based materials, effectively. These composites are anticipated to provide the required mechanical integrity and flexibility of polymers while incorporating the desirable dielectric properties of ceramics [159–164]. By integrating ceramic filler particles

within a polymer matrix, the composite structure leverages the enhanced dielectric properties of ceramics while maintaining the deformability and compliance provided by polymers. This synergistic combination allows for improved performance and expanded applications in the field of dielectric materials. Generally, a rule of thumb suggests that in order to fabricate dielectric composites to demonstrate electrical properties that resemble those of ceramics, it is necessary to incorporate a higher volume fraction of the filler material [165]. However, it should be noted that by carefully controlling the distribution of fillers during the composite fabrication process, it becomes possible to further tailor the properties of the composites to align with the specific requirements of different applications. This implies that the electrical characteristics and other relevant properties of the composite can be intentionally modified by precisely controlling the arrangement and concentration of the filler materials, allowing for customised composites that cater to the specific needs of various applications [166].

In this context, the concept of “connectivity” plays a significant role in defining the structural characteristics of ceramic-polymer composites. “Connectivity” refers to the degree of physical interconnection exhibited by the ceramic particles and the polymer matrix, considering the three-dimensional coordinates (x, y, and z). As an example, the numerical value "3" assigned to a phase signifies absolute connectivity in all three dimensions. When a composite is constituted of two different phases such as ceramic and polymer phases, as in the case of biphasic composites a numbering scheme comprising two digits is employed to characterise their level of connectivity. The initial digit represents the extent of connectedness among filler particles whereas the succeeding digit reflects that of matrix connectivity [167]. To illustrate these connectivity patterns, Figure 2.21 presents ten distinctive connectivity arrangements depicting the interconnection between the ceramic and polymer phases [167]. These patterns span from an unconnected 0-0 pattern, where neither the ceramic filler particles nor the polymer matrix are interconnected, to a fully self-connected 3-3 pattern, wherein both the ceramic and polymer phases demonstrate three-dimensional interconnections [168].

Among these connectivity patterns, the 1-3 connection pattern has been widely employed in several applications, such as in energy harvesting and biomedical fields, including ultrasound imaging, sensors, and hydroacoustic devices. The remarkable

benefits of this pattern, such as its high electromechanical coupling factor, enhanced hydrostatic voltage coefficient, and improved piezoelectric coefficient, have contributed to its rise in popularity [169–172]. Additionally, the desirable properties of the "bio-inspired" structure of this specific pattern is very well suited for applications that call for effective energy conversion, precise sensing capabilities, and improved performance in dielectric systems [173]. They have also found extensive applications in the field of nano-technology engineering with promising performance in wearable sensors and energy harvester applications [174,175]. With the fast-moving pace of technology, it becomes increasingly crucial to focus on the fabrication and design of these ceramic-polymer composites to enhance their performance and enable their widespread application across extended various domains. Achieving superior performance necessitates careful consideration of multiple factors, including material selection, fabrication techniques, and composite architecture. The next section discusses these factors and provides an overview of the various factors affecting the performance of dielectric ceramic-polymer composites.

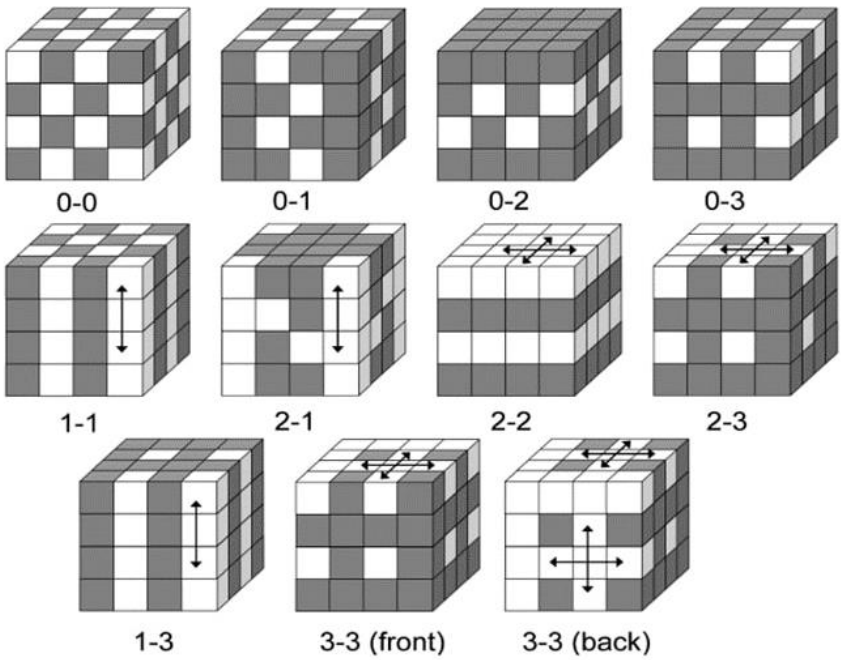

Figure 2.21: Various connectivity configurations of bi-phasic composite systems [167]

2.6.1. Factors Affecting the Performance of Ceramic-Polymer Composites

As stated in the previous subsection, the enhanced functioning of devices utilising dielectric composites significantly depends on various factors such as the chemical and physical properties of the parent phases as well as the fabrication process. This involves the necessity to consider the structural and functional attributes of the constituent phases that contribute to the composite, encompassing the imperative of maintaining geometric integrity. Consequently, it is of paramount importance to consistently ascertain the factors that exert influence on the performance of dielectric composites, with the aim of streamlining and establishing efficacious criteria for material selection that optimally align with the principal parameter indices throughout the fabrication process.

Based on the comprehensive review of relevant literature, the performance of ceramic-polymer composites, including their piezoelectric, dielectric, and ferroelectric properties, can be influenced by several key factors [176]. These factors can be broadly classified into seven distinct categories, as illustrated in the Fish-bone diagram depicted in Figure 2.22. Amongst these factors, the conductivity of either/both the matrix and the filler have proven to influence the overall dielectric properties [177]. Generally, the electrical conductivity of the matrix material is crucial as it affects the ability of the composite to withstand and distribute electrical charges [178]. A certain level of electrical conductivity is necessary to facilitate efficient poling of dielectric ceramics and to enable the alignment of electric dipoles. However, if the matrix material becomes highly conductive, it may lead to undesired short circuits or leakage currents, compromising the dielectric properties of the composite.

Furthermore, the addition of a third phase to the conventional bi-phasic ceramic-polymer composites have deemed to be amongst the various factors affecting the composite performance, in some instances [179,180]. The three-phase system allows for the incorporation of additional functionalities and tailoring of the material's properties to meet specific application requirements.

In general, by understanding and analysing the different factors affecting the performance of dielectric-based ceramic-polymer composites, it becomes possible to gain valuable insights into the intricate interplay that governs the overall performance

of such composites. The following subsections delve into a detailed exploration of some of these factors.

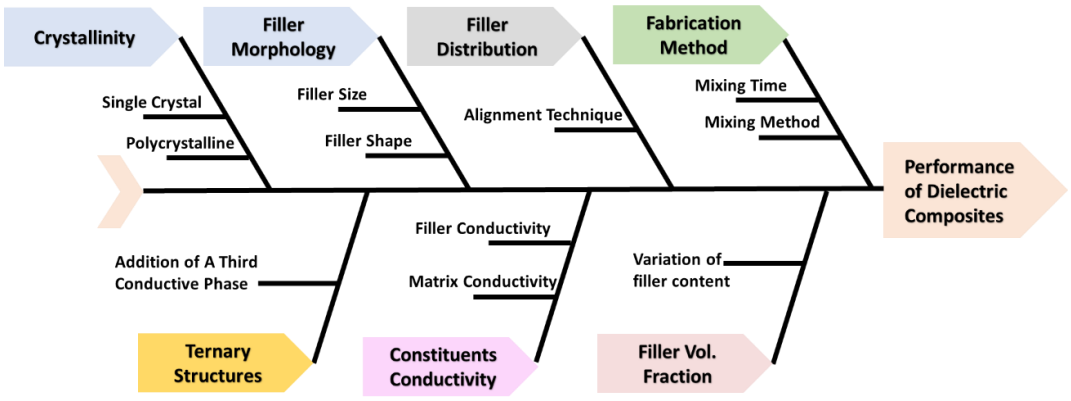

Figure 2.22: Fishbone diagram showing various influential factors that impact the overall performance of ceramic-polymer composites

2.6.1.1. Effect of Composite Fabrication Method

Fabrication methods play a crucial role in optimising the performance of dielectric composites and expanding their applications in modern technologies. The way these composites are fabricated, including the mixing time and method, ultimately determines their properties.

Specifically, for the above demonstrated 1-3 composites, there exist various approaches such as dice-and-fill [181], arrange-and-fill [181], injection molding [182], and lost mold [182] methods (shown in Figure 2.23). The dice-and-fill method involves cutting, backfilling, and polishing a sintered piezoelectric block to establish connectivity [183]. In contrast, the arrange-and-fill method entails filling sintered ceramics into the polymer matrix prior to the cutting process. However, it should be noted that improper alignment of ceramic fillers during the arrange-and-fill fabrication process can give rise to unfavourable electromechanical responses [181]. Injection molding, a conventional widely employed technique, enables the direct production of ceramic green bodies exhibiting the characteristic rod-like structure of 1-3 piezoceramic-polymer composites. Following sintering, these parts undergo a similar procedure as the diced ceramic block. Nonetheless, it is crucial to recognise that injection moulding is an expensive, time-consuming, and rigid process [184]. Another method, known as the lost mold method, offers enhanced accuracy compared to injection molding. This method involves utilising the LIGA (Lithography Galvano-forming and plastic molding) process to create a plastic mold that is subsequently filled

with a slurry. After drying, the mold is burned out, and the resulting structure is sintered to achieve an X-ray density exceeding 98% [183]. However, it is worth noting that the LIGA process is also characterised by its time-consuming nature and associated high costs [183].

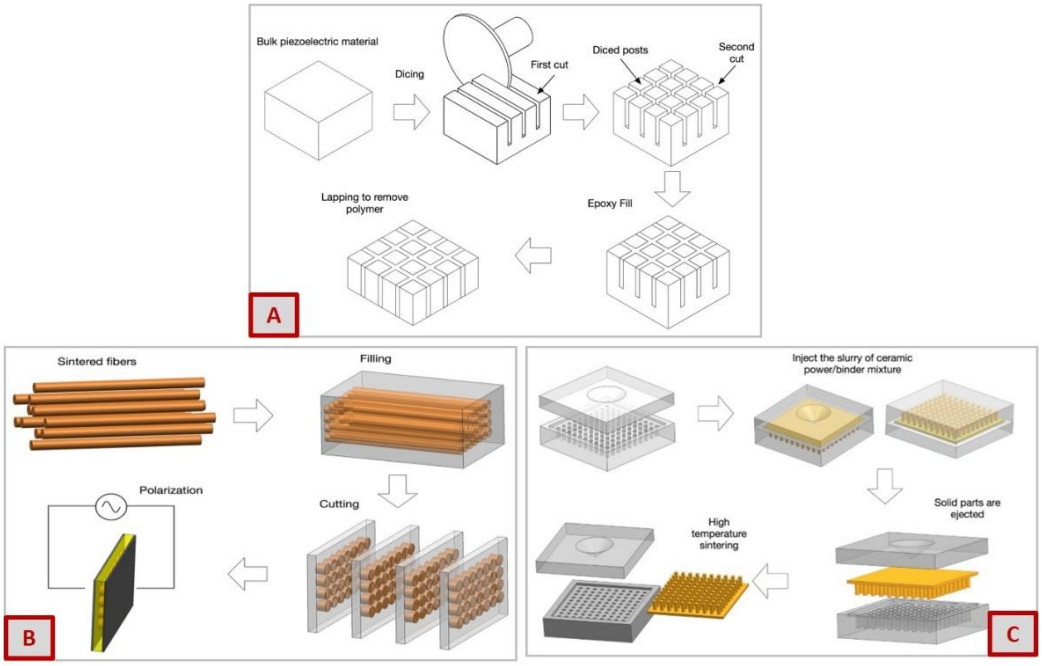

Figure 2.23: A schematic showing various 1-3 ceramic-polymer fabrication techniques, namely (a) dice-and-fill, (b) arrange-and-fill and (c) injection moulding techniques [182]

Ongoing advancements in technology have made it possible to fabricate those composites through innovative alternative methods, such as 3D printing. One notable technique, known as fused deposition modeling (FDM) or fused filament fabrication is commonly employed in 3D printing. It involves the layer-by-layer deposition of polymers to create complex structures [185]. Generally, FDM has gained widespread popularity due to its affordability and ease of operation. While this technique is primarily used for printing conventional polymers, it has been also be utilised to print polymer-based composites that contain ceramic filler particles. This capability was recognised by Crump, the inventor of fused deposition modeling, leading to the development of commercially available composite feedstock materials specifically designed for use in fused deposition 3D printers. For instance, Moulart et al. [186] conducted a study focusing on the fabrication and dielectric characterisation of a ceramic-polymer composite filament composed of $BaTiO_3$ microparticles in acrylonitrile butadiene styrene (ABS). Their research aimed to explore the potential of

fused deposition for producing electronic and microwave devices using the $BaTiO_3$/ABS filament. However, it should be noted that their study did not demonstrate the actual printing of this filament. However, subsequent research conducted by F. Castles et al. [176] has successfully demonstrated the fabrication of BT/ABS composites using commercial desktop 3D printing. The fused deposition method offers several notable advantages, including the relatively low cost of the machines and the ability to print composites using a wide range of commonly available thermoplastics such as ABS, polyethylene terephthalate, nylon, and polypropylene. In their study, the researchers achieved permittivity values ranging from 2.6 to 8.7, with loss tangents ranging from 0.005 to 0.027. Importantly, the permittivity values obtained were reproducible throughout the printing process and closely matched those of bulk unprinted materials, with a deviation of only approximately 1%. These findings suggest that the fused deposition method holds promise as a viable manufacturing process for producing high-quality dielectric composites.

Additionally, the impact of FDM on three-phase dielectric nanocomposites has been explored. In their study, Kim et al. have developed ternary-structure based composite material consisting of PVDF, BT and multiwall carbon nanotubes (CNTs) [187]. Herein, the incorporation of CNTs served a dual purpose, acting as a surfactant for BT and as an electrically conductive filler. The researchers observed an improvement in permittivity and dielectric constant, which was attributed to the enhanced dispersion of BT particles as well as the reduced loss tangent. The presence of a porous inorganic additive in a composite such as the one consisting of BT and Acrylonitrile butadiene styrene (ABS) can lead to a decrease in permittivity due to inadequate bonding between the particles and the polymer at the particle/polymer interface. However, the addition of organic esters as additives shows promise in improving permittivity by promoting better compatibility between the polymer and the filler ceramic particles in the composite [188]. Consequently, the use of dispersants, surfactants [189] and plasticisers [190] can enhance the composites' FDM printability by improving the dispersion of filler particles and reducing the viscosity of the composite, respectively

In summary, the careful selection of an appropriate composite fabrication technique is vital in enhancing the performance of dielectric composites and expanding their applications in advanced technologies. It involves finding the optimal balance between cost, time and ease-of-use while ensuring the desired quality and functionality of the

composites. In the present era, the utilisation of the 3D printing process has revolutionised the fabrication of ceramic-polymer composites, offering a diverse range of advantages and prospects for progress in terms of cost and time and the ability to produce complex geometry and intricate structures that would be challenging or even impossible to achieve using traditional fabrication methods. This opens up new possibilities for designing and manufacturing dielectric composites with tailored properties and functionalities to meet specific application requirements.

2.6.1.2. Effect of Distribution of the Fillers

The distribution and alignment of filler particles within the polymer matrix have proven to have a significant impact on the dielectric performance of ceramic-polymer composites. Numerous studies have demonstrated that aligning the ceramic particles within the polymer matrix can effectively influence the dielectric properties. In recent years, researchers have made several efforts to improve the alignment of particles during the fabrication process, aiming to achieve enhanced dielectric properties in the resulting composites [52,54,191].

The most commonly widely adopted technique for aligning ceramic particles during the fabrication process of ceramic-polymer composites is the so-called dielectrophoresis (DEP) [192–196]. Through the application of a non-uniform or alternating electric field, dielectrophoresis induces polarisation in ceramic particles, leading to their alignment in a quasi (structured) 1-3 chain-like structure that mimics the 1-3 structure [194]. Figure 2.24 visually presents different composite structure types, including random 0-3, quasi 1-3, and conventional ceramic pillar 1-3 structures, accompanied by corresponding scanning electron microscopy (SEM) images. Generally, quasi 1-3 structure is preferred over the random 0-3 and pillar 1-3 structure, as the obtained chain-like structure allows for a more flexible and less dense composite material compared to the rigid and dense arrangement of pillars in 1-3 composites. Additionally, the obtained chain-like structure can be achieved through relatively straightforward techniques and low-cost, which are similar to those used for 0-3 composites, but with enhanced dielectric properties [197]. DEP has been effectively employed to align various particle types, ranging from micron-sized cubes [54] and fibers [198] to random spherical particles [199], in several quasi 1-3 ceramic-polymer based composites. This alignment process generally leads to a reduction in the interparticle distance, resulting in a closer packing of the ceramic particles within

certain regions of the composite. The enhanced connectivity and reduced interparticle spacing contribute to an increase in the dielectric permittivity or dielectric constant of the material. As a result, the aligned composite exhibits a higher dielectric constant compared to composites with randomly distributed particles 0-3 configuration. The closer proximity and improved alignment of the ceramic particles facilitate a more efficient response to the applied electric field, leading to an enhanced dielectric performance in the aligned composite material.

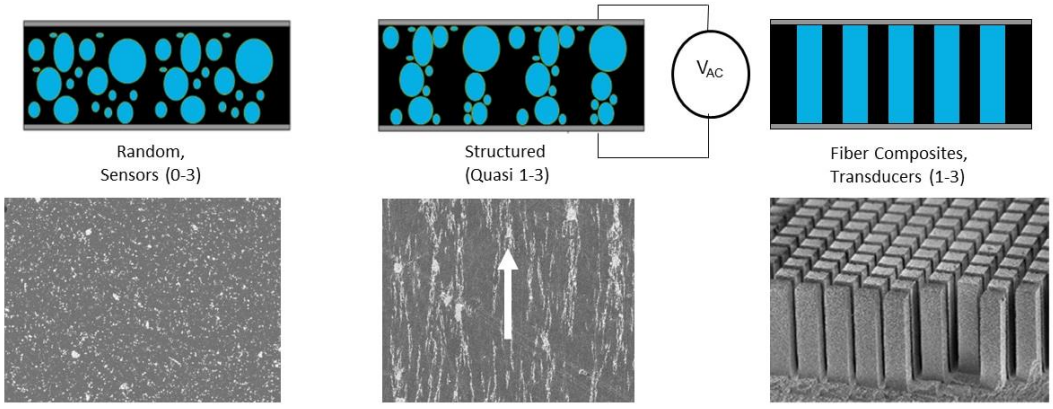

Figure 2.24. A schematic showing random 0-3, quasi 1-3 and conventional ceramic pillars 1-3 composite types along with their respective SEM micrographs; whereas, the polymer matrix is black and ceramic filler is blue coloured [200]

To predict the effective dielectric constant in ceramic-polymer composites, several theoretical models have been suggested, which account for the morphology of the constituents and their respective volume fractions. In [201] Yamada et. al. suggested that the ceramic-particle polymer-matrix composites can be regarded as a heterogeneous system composed of two distinct constituents within the domain of composite materials. Herein, they proposed a model aimed at elucidating the behavior of the dielectric constant of random 0-3 piezoelectric composites. This model considers the dielectric constant of both constituents (ceramic and polymer) involved in the composite as well as the incorporated volume percentage of ceramic particles [201]. The equation governing the Yamada model is presented in Equation 2.11, whereas ε_c and ε_p are the dielectric constants of BNT ceramic powder and polymer matrix respectively, φ is the ceramic volume fraction, and n is the reciprocal of the depolarisation factor for an ellipsoidal particle in the electric field direction. As for the structured 1-3 composites, Bowen et al. [18] put forth an analytical model for

predicting the effective dielectric constant of fully structured composites (using dielectrophoresis). The model considers the composite as a system of one-dimensional chains of particles separated by polymer gaps and is presented in Equation 2.12 where R represents the ratio of the average particle size to the interparticle distance (ip), while the remaining parameters hold the meanings previously defined.

$$\varepsilon_{random} = \varepsilon_p(1 + \frac{n\varphi(\varepsilon_c - \varepsilon_p)}{n\varepsilon_p + (\varepsilon_c - \varepsilon_p)(1-\varphi)} \quad \text{(Equation 2.11)}$$

$$\varepsilon_{structured} = \varphi\left(\frac{R\varepsilon_c\varepsilon_p}{\varepsilon_c + R\varepsilon_p)}\right) + (1-\varphi)\varepsilon_p \quad \text{(Equation 2.12)}$$

Furthermore, it is noteworthy to mention that Yamada et al. [201] made predictions regarding the d_{33} value of random 0-3 composites aligned in the poling direction. This prediction is represented by Equation 2.13, where $d_{33random}$ denotes the piezoelectric charge coefficient and α represents the poling ratio of the dispersed ceramic particles. The remaining parameters have been previously introduced in the dielectric constant equation above. On the other hand, Van den Ende et al. have developed an analytical model to determine the piezoelectric charge coefficient in structured 1-3 composites [73]. This model extends Bowen's model and calculates the d_{33} values of composites by considering the particle-matrix arrangements within chains as two in-series-connected capacitors that are in the electrical domain, and two in-series connected springs that are in the mechanical domain and is depicted by the formula in Equation 2.14. In this equation, Y_p represents the elastic modulus of the polymer matrix, while Y_c represents the elastic modulus of the ceramic particles along the chains. The variable R corresponds to the ratio between the average particle size and the effective distance between particles in the direction of the electric field.

$$d_{33random} = \frac{\varphi\alpha n\varepsilon_{random}d_{33c}}{n\varepsilon_{random} + \varepsilon_c - \varepsilon_{random}} \quad \text{(Equation 2.13)}$$

$$d_{33structured} = \frac{(1+R)^2\varepsilon_p\varphi d_{33c}Y_c}{\varepsilon_c + R\varepsilon_p[(1+R\varphi)Y_c + (1-\varphi)RY_p} \quad \text{(Equation 2.14)}$$

Figure 2.25 (a)-(c) demonstrates the impact of dielectrophoretically aligned ceramic lead titanate (PT) particles on the relevant d_{33}, g_{33} and ε_{33} of PT-Epoxy composites compared with that of unstructured composites at various PT volume fractions, respectively [202]. It is observed that not only the respective dielectric constant

exhibits an enhancement when the particles are aligned (structured), but also in terms assessing the piezoelectric performance, the corresponding d_{33} and g_{33} values were also enhanced. This enhancement can be attributed to the interplay between the d_{33} value, interparticle distance, and particle connectivity, as elucidated by the Van den Ende model (which is basically an extension of the Bowen's model) [203]. It is further observed that the increase in d_{33} is more pronounced at lower volume fractions compared to the observed increase at higher volume fractions. This observation aligns well with the theoretical predictions of the Van den Ende model, which presumes a rapid increase in d_{33} within the range of 0% to 10% ceramic volume fraction. This observed increase is consistent with the underlying theory that involves the presence of anisotropic electroactive particles uniformly distributed in a 1-3 configuration throughout the composites. Additionally, since g_{33} is dependent on d_{33}, it follows that a more pronounced increase in g_{33} is witnessed at lower volume fractions.

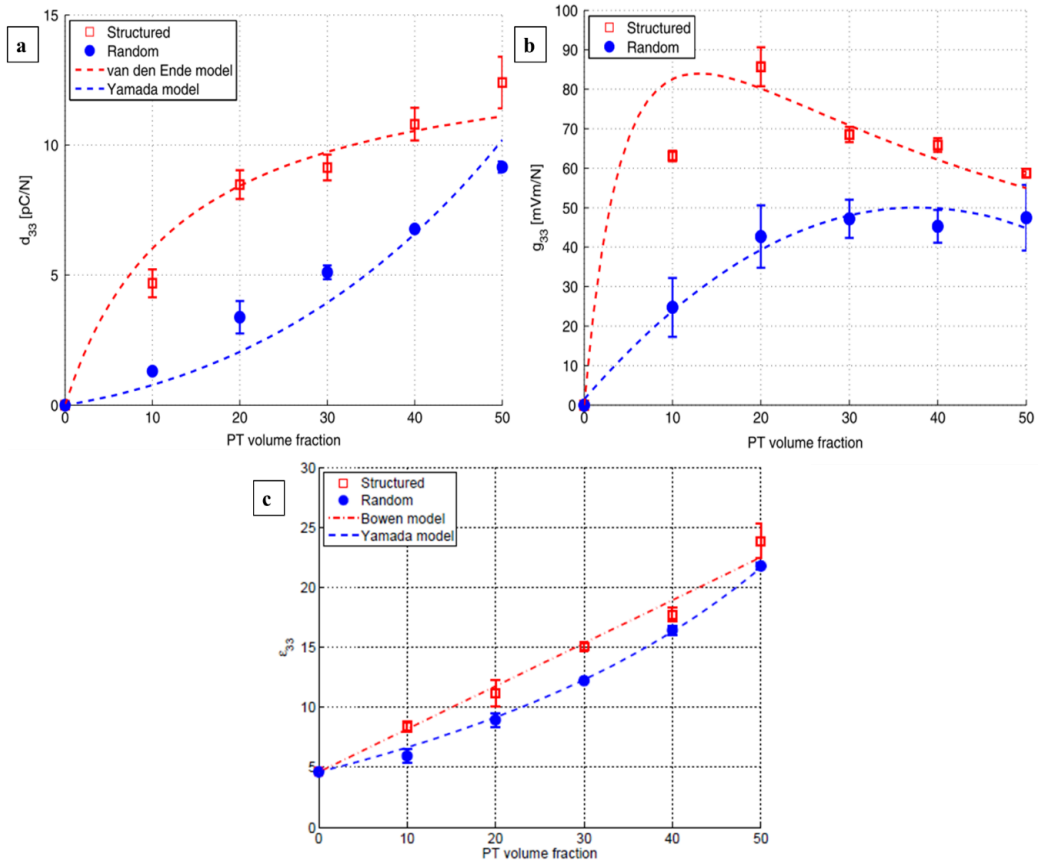

Figure 2.25: Variation of (a) d_{33}, (b) g_{33} and (c) ε_{33} of random and structured PT/Epoxy as a function of the PT volume fraction [202]

It is important to highlight in this context that the degree of poling of the ceramic phase plays a significant role in determining the overall piezoelectric properties of ceramic-

polymer composites at a macroscopic level [204]. High poling fields are required to achieve sufficient poling efficiency in fine-grained electroactive particles embedded in a polymeric matrix. Equation 2.15 [205] provides a means to calculate the electric field E_1 acting on an isolated spherical grain in a polymer matrix, where E_0 is the applied electric field and ε_p and ε_c hold the same meanings defined previously.

$$E_1 = \frac{3\varepsilon_p}{\varepsilon_c + 3\varepsilon_p} E_0 \qquad \text{(Equation 2.15)}$$

The piezoelectric properties of poled samples are known to be influenced not only by the strength of the poling field but also by the poling orientation and the direction of the applied electric field. A study by Raj Kiran et al. [206] investigated the impact of poling direction on the performance of piezoelectric materials operating in longitudinal (d_{33}) mode. The authors mathematically and experimentally demonstrated that the piezoelectric strain coefficients are affected by the direction of poling. During the poling process, the distribution of the electric field is affected by the ratio of the electrical conductivity of the polymer to that of the ceramics, which is denoted as σ_m/σ_c. Additionally, the mobility of charges in the polymer matrix is crucial to achieving the desired polarisation. For stable polarisation of a piezoelectric/ferroelectric material, it is essential to allow sufficient time for the electric charges to align themselves in response to the applied electric field [204]. This period should be longer than the sample's relaxation time, as it has been theoretically established that the poling time should exceed this time period (represented as τ in Equation 2.16) to achieve stable polarisation [204]. This ensures that the charges have enough time to align themselves in response to the applied electric field and that the resulting polarization in the material is stable.

$$\tau = \frac{\varphi 3\varepsilon_m + (1-\varphi)(\varepsilon_c + 2\varepsilon_m)}{\varphi 3\varepsilon_m + (1-\varphi)(\sigma_c + 2\sigma_m)} \qquad \text{(Equation 2.16)}$$

In the ongoing pursuit of achieving high-performance operating composites for dielectric applications, there have been research endeavors that explore modifications to the manufacturing process. As such, Khanbareh et al. have [207] investigated the integration of the alignment through dielectrophoresis with the poling procedure for quasi 1-3 composites at normal ambient temperature, where the polymer matrix remains in a liquid state, after which it is subjected to curing. This technique aims to

optimise the potential for poling by taking advantage of the electrical conductivity exhibited by polymeric matrices. In their study, Khanbareh et al. [207] has extensively explored the impact of electric conductivity on the dielectric properties of ceramic-polymer composites. The study underscores that a higher electrical conductivity within polymeric matrices results in shortened buildup time for ceramic particles' exposure to an electric field, leading to enhanced poling capability. Thus, it has emphasised the critical role played by the electrical conductivity levels of polymers in shaping the composite's dielectric traits.

To further investigate the influence of the particles' alignment on the dielectric properties of ceramic-polymer composites, a study conducted by Kim et al. in 2016 [208] has used an ice-templating technique for the fabrication of a BT/epoxy composite. This technique involves the formation of ceramic particle walls with pore channels using ice crystals as structural supports. Subsequently, an epoxy matrix is infiltrated into the structure, followed by perpendicular dicing and electrode coating. The ice-templating method facilitated the alignment of BT particles in a lamellar configuration architecture, with BT volume fractions ranging from 10 to 30 vol%. The results demonstrated a linear increase in the ε_r with increasing BT fraction, indicating the dependence of the ε_r on the volume fraction of the electro-active filler particles. Notably, the unique lamellar architecture achieved through the ice-templating method led to higher ε_r compared to conventionally produced composites. However, the ice-templating method yielded enhanced dielectric properties at a higher BT volume fraction (30%), which incurs greater costs, in contrast to a lower BT volume fraction (10%) utilised in conventional dielectrophoretic alignment [208]. Although the use of ice-templating method displays potential in augmenting composites' dielectric properties and sensitivity, their analysis failed to consider the role of electro-active particle-matrix interface. This particular parameter has been acknowledged as a decisive factor that affects composite materials' dielectric performance, with studies utilising DEP methods to explore its impact [54,196]. Employing DEP alignment when incorporating active ceramic particles into polymeric matrices appears advantageous in producing cost-effective yet highly sensitive composites.

In addition to the widely employed DEP, magnetic field alignment has emerged as an alternative method for achieving particle alignment. A study conducted by Kiho Kim et al. [209] aimed to align anisotropic boron nitride (BN) particles in a vertical

direction with the direction of heat transport by employing a magnetic field. To facilitate this process, iron oxide nanoparticles were introduced onto BN's surface and acted as magnetically responsive agents within the composite material. The incorporation of iron oxide nanoparticles was modifiable through changes in precursors that regulated its magnetic response capability allowing control over particle orientation during magnetic manipulation. The paramagnetic iron oxide particles were polarised by the applied magnetic field, and thus produced particles that were vertically aligned. The vertically aligned boron nitride (BN) composite exhibited improved thermal conductivity when compared to the randomly dispersed composite [209]. These findings hold promise for enhancing the performance of advanced electronic devices that demand high thermal conductivity and for dielectric applications involving materials with directional properties. In another study conducted by Yingqing Zhana et al. [210], hexagonal boron nitride (h-BN)/poly(arylene ether nitrile) nanocomposites were developed using a similar magnetic field alignment technique as described previously. This alignment approach resulted in improved alignment of the h-BN nanofillers within the polymer matrix, leading to enhanced interfacial adhesion between the two components. The addition of 30 wt% modified h-BN into the nanocomposites led to a significant increase in dielectric permittivity, from 3.2 to 16.4, representing a remarkable improvement of 413%. Notably, this increase in dielectric permittivity was accompanied by low dielectric loss. Furthermore, the thermal conductivity of the nanocomposites was enhanced by 140% at the same loading content. Importantly, the developed nanocomposites maintained high mechanical strength and thermal stability, even at high nanofiller loading contents [210]. These advantageous characteristics are anticipated to make them highly suitable for applications in energy storage devices.

Furtherly in 2019, a study by L A Lara et al. [211] has investigated the effect of magnetic alignment on the dielectric properties and performance of the magnetically aligned magnetite-polyester composites. During the curing process, magnetic fields were employed to align the particles in both vertical and horizontal orientations. The results indicated that a magnetite concentration of 20% with an average particle size of 21.48 μm in horizontal alignment to the applied magnetic field and transmission line yielded an ε_r of 3.88, accompanied by a low dielectric loss (0.054) within the frequency range of 150 KHz to 4 GHz, which was significantly higher than those

obtained at un-aligned structures, hence signifying the impact of particle's alignment on the overall performance of dielectric composites.

A recent study conducted in 2023 has delved deeper into the combination of magnetic and electric fields in order to investigate their synergistic effects on particulate-filled polymer matrix composites [210]. Specifically, the researchers focused on barium hexaferrite (BHF) dispersed in a polydimethylsiloxane (PDMS) matrix and explored various configurations of magnetic and electric fields to achieve diverse microstructures with a wide range of material characteristics. One of the key aspects introduced in this study is the concept of "orthogonal control," enabling precise manipulation of particle orientation along orthogonal axes, leading to tailored microstructures and varying dielectric and magnetic properties. Their experimental findings indicate that the permittivity of the composite material can be improved by up to two-fold at 1 kHz when the microstructures exhibit long continuous aligned macro-chains compared to microstructures without any macro-chains. By employing a multifield processing technique, a diverse range of dielectric constants could be achieved. For instance, in the case of a 1 vol% composite consisting of barium hexaferrite-polydimethylsiloxane (BHF-PDMS), the dielectric constant reached a value as high as 5.12 at a frequency of 100 kHz. This result demonstrates the potential of multifield processing in manipulating and optimising the dielectric properties of composite materials [210].

2.6.1.3. Effect of Morphological Characteristics of the Fillers

Indeed, the overall final dielectric properties of composites are not solely determined by the fabrication process and filler distribution within the composite. The morphology of the incorporated ceramic filler has also been shown to have a significant influence on the overall dielectric performance. In this context, the profound significance of the size and shape of the incorporated fillers in determining the overall performance of dielectric ceramic-polymer composites has been extensively explored through rigorous research efforts [212,213]. Through systematic investigations, researchers have gained valuable insights into the relationship between the size and shape of the fillers and the resulting composite's dielectric performance, paving the way for informed design and morphology tailoring approaches. Nevertheless, it is important to acknowledge that the shape and size of ceramics intended for incorporation in ceramic-polymer composites can be customised and tailored through the selection of

appropriate ceramic synthesis processes and the meticulous control of their associated synthesis parameters, as discussed in Section 2.4.4.

Generally, smaller filler particles have a larger surface area, because as the particle gets smaller, the proportion of its surface area to its volume increases. This relatively larger surface area of smaller particles leads to an increase in the strength of the composite by providing more contact points between the ceramic and polymer phases [214]. Furthermore, smaller particles may provide more effective stress transfer from the polymer matrix to the ceramic particles, resulting in a stronger composite [214]. However, the addition of smaller particles may also lead to an increase in interparticle distance, which can decrease the overall packing density of the composite. This may lead to a reduction in mechanical and electrical properties [215]. Additionally, smaller particles may have a greater tendency to agglomerate, which can result in a less homogenous composite. Moreover, larger particles tend to distribute more uniformly within the polymeric matrix [216]. As such, filler particles with two-dimensional shapes such as plate-like shapes or fibres have shown to result in higher dielectric constant values and improved energy storage performance compared to spherical-shaped filler particles [217].

The origins of the relationship between the shape and morphology of particle size and the corresponding dielectric properties of composites can be traced back to the seminal work of Yamada et al [201]. This influential model (shown in Equation 2.11) takes into account the dielectric constants of both, the ceramic filler (ε_c) and the polymer matrix (ε_p), while also incorporating a shape parameter (n) specifically attributed to the shape of ellipsoidal particles ($n = 4\pi/m$). The parameter n, which is contingent upon the shape of particles, demonstrates variability with varying particles shapes such that elongated particles exhibit higher values of n. Consequently, the diverse values of n ultimately manifest in the respective dielectric constant and thus the overall performance of the dielectric based composites.

As has been elaborated earlier, the size of the incorporated ceramic filler highly depends on the employed synthesis method along with the corresponding synthesis parameter. In this context a study by Jing Fu et al. [189] investigated the impact of calcination temperature on particle size and its consequent influence on the dielectric properties of composite materials. In their study, modified barium titanate (PVP/BT)-

PVDF composites were fabricated by utilising molten salt synthesised single-crystalline BT nanostructures. The BT particles were calcined at different temperatures ranging from 600°C to 1000°C for a duration of 5 hours. The experimental results demonstrated that higher calcination temperatures led to an increase in particle size, which may be attributed to the accelerated growth of crystals in high-temperature molten salt environments. To determine the optimal particle size for composite preparation, the researchers evaluated the polarisation characteristics of particles with varying sizes. Herein, they have explored the correlation between the spontaneous polarisation (P_s) exhibited in BT particles and the tetragonality of the crystal structure (c/a) (Equation 2.17) [218], which was established by several earlier research investigations. It is noteworthy that a rise in temperature induces an escalation in the tetragonality of the crystals and since (c) is directly proportional to the Ps, thus the polarisation effect is enhanced due to the volumetric changes resulting from atom displacement within the perovskite structure exhibited at higher temperatures.

$$P_s \approx (\frac{c}{a})^{0.5} \qquad \text{(Equation 2.17)}$$

As a result, the composites were fabricated at various volume fractions, utilising the largest particle sizes obtained, which demonstrated the highest polarisation levels. Furthermore, the study investigated the variation of the dielectric constant at different temperatures. Generally, the dielectric constant of the composites exhibited an increasing trend with higher volume fractions of the filler, which was further amplified at elevated temperatures. Across the investigated volume fractions, the dielectric constant consistently increased with increasing temperature and volume fraction, reaching a peak at a volume fraction of 60%. Moreover, at an 80% volume fraction, the dielectric constant reached its maximum value at the highest investigated temperature of 130°C. The enhanced dielectric constant was primarily attributed to the P_s induced by larger BT filler particle sizes, particularly at the peak volume fraction of 40%. These findings were influenced by both the particle size of the filler material and the melt temperature (T_m) requirements of the polymer matrix, as these factors significantly affected the polarisation of the filler particles.

Although ceramic filler particles have the potential to increase the average dielectric constant of the composites, yet their presence can create non-uniform electric fields that weaken their corresponding. This weakening effect occurs because of inadequate

breakdown strength and insufficient dispersion of the electric field away from the electrco-active particles [41], [86]. Nevertheless, the use of surfactants and dispersants can effectively enhance the characteristics of the incorporated filler particles resulting in improved interface compatibility and addressing the issues related to inhomogeneous electric fields.

In light of the aforementioned background, a research conducted by Daniella Deutz et al. in 2017 [198] has provided evidence for the enhanced dielectric properties achieved through the inclusion of sodium lithium niobate (KNLN) fibers compared to spherical counter particle fillers. The researchers employed dielectrophoresis to fabricate a quasi 1-3 KNLN/PDMS composite with the aim of exploring its potential for energy harvesting applications. The results demonstrated that the improved dielectric properties observed in the composite with fiber-based filler were associated with the reduced inter-particle distance achieved through the specific shape of the filler and the alignment process using dielectrophoresis [198].

Moreover, in 2022, a recent research by Yijia Fu et al.[219] has investigated the influence of particle size on the dielectric performance of 3D printed composites. The study specifically examined the incorporation of large and small BT particles in a UV-curable resin for SLA-based fabricated composites. Notably, the research findings indicated that smaller BT particles exhibited slightly higher dielectric constant values compared to larger particles. This was attributed to the larger specific surface areas of the small-sized particles, which result in increased surface energies and heightened surface activities. As a consequence, the surface atoms of these small-sized fillers become highly unstable, leading to stronger interface polarisations within the composites [211]. Consequently, composites incorporating small-sized filler particles demonstrated a modestly greater increase in their relative dielectric constant [219]. Figure 2.26 demonstrates the large and small size of the incorporated BT particles along with the corresponding dielectric constant of the BT/UV composites [219].

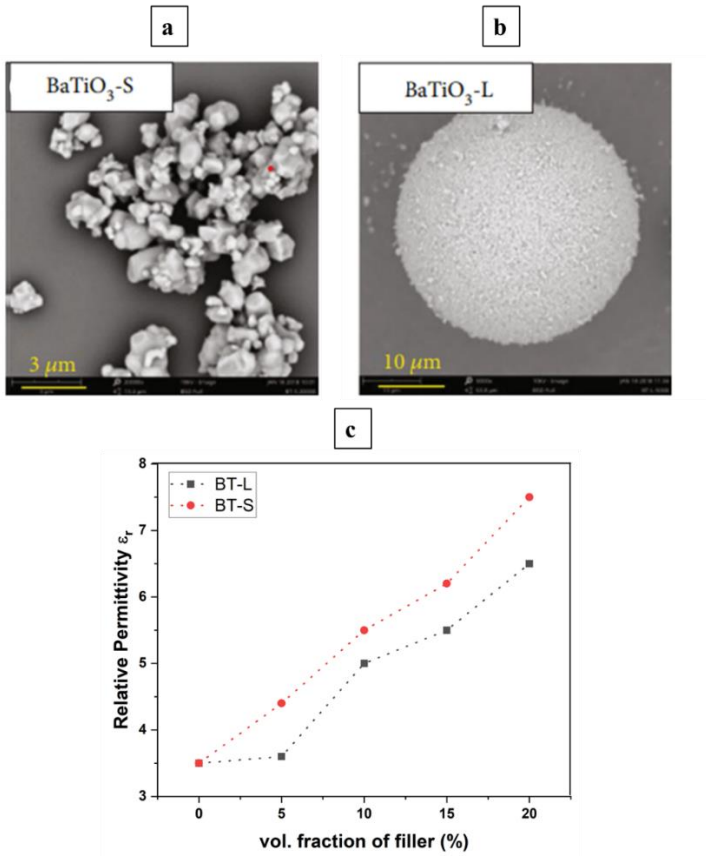

Figure 2.26: SEM micrographs of (a) large and (b) smaller sized incorporated BT particles and (c) their corresponding dielectric constant of the BT/UV composites [219]

Interestingly, within the context of this study, it was observed that composite systems containing large particle size fillers exhibited a reduction in the scattering of UV radiation. This reduction in scattering allowed UV radiation to penetrate deeper into the composite material during the curing process. As a result, the curing depths of composite systems with large particle size fillers were improved. In practical terms, this implies that the UV radiation can effectively reach and cure a greater depth of the composite material, leading to enhanced curing performance during SLA printing.

Further in 2021, a study by Xu Lu et al. [220] highlighted the importance of the filler size on the dielectric properties of the resulting composites. In their study, they have investigated the effects of ceramic spherical-shaped nanofiller sized particles on the related dielectric properties of BT/ P(VDF-CTFE) nanocomposites filled with BT nanoparticles of varying sizes (50, 100, 150, and 200 nm). Experimental results revealed that the dielectric constant of the BT/P(VDF-CTFE) nanocomposites increased significantly as the size of the nanofiller increased. By applying

Lichtenecker's mixing law, the ε_r of the BTO nanoparticles was calculated based on the ε_r of the nanocomposites. The findings [220] indicated that the ε_r of the BTO nanoparticles also increased with larger sizes ranging from 50 to 200 nm. The observed increase in the dielectric constant of the nanocomposite was attributed to the progressive splitting of the XRD peak at an angle of 45 degrees as the particle size increases. This splitting indicates a structural transformation of the nanoparticles from a cubic to a tetragonal phase. Consequently, it was anticipated that the dielectric constant ε_r of the BT nanoparticles will experience substantial variations as a function of particle size. These variations, in turn, exert a direct influence on the dielectric constant ε_r of the resulting nanocomposite material [220]. Furthermore, experimental observations revealed that the polarisation under the same electric field exhibited minimal changes as the size of the BT nanofiller increased. However, the maximum breakdown strength (E_{max}) of the nanocomposite decreased significantly with larger BT nanofiller sizes which suggested that smaller ceramic nanofillers are more desirable for achieving higher dielectric strength in the nanocomposite material. This may be due to the increased dielectric mismatch-induced stress at the filler-polymer interfaces that is exhibited with larger sized particles. In contrast, using smaller particle sizes can help reduce the interface area and minimize the dielectric mismatch, thus preserving a higher breakdown strength in the composite material [221].

Besides the morphological structure, the crystallinity of the embedded filler is also a crucial aspect affecting the composite performance. In the realm of energy storage-based applications and the ongoing progress in their fabrication, generally embedding single crystal ceramic particles is preferred over polycrystalline ceramic particles. This may be due to the superior performance in terms of coupling coefficient and energy density exhibited by single crystal ceramics. Therefore, their incorporation into polymer-based composites has been widely investigated. In this context, Christopher Bowen et al. [176] have investigated the various properties of a three-component composite consisting of a single-crystal/polymer/polymer system with a 1-2-2 connectivity. The composite structure comprised parallel piped-shaped single-crystal (KNNTL:MN) rods embedded within a layered polymer matrix. The polymer matrix consisted of two distinct polymers, referred to as Polymer I (polyurethane) and Polymer II (polyethylene), whereas polymer I was characterised by a higher stiffness

compared to polymer II within the laminar matrix. They have demonstrated that the composite material, with a lower proportion of the single crystal (SC), exhibited a higher piezoelectric voltage coefficient (g_{33}). This increase was primarily attributed to the lower dielectric permittivity of the embedded single crystal. Comparing the values, the g_{33} of the composite material was approximately nine times greater than that of the KNNTL:Mn single crystal [176]. This composite is anticipated to be potentially used in piezoelectric transducers and sensors.

The dielectric performance of dielectric-based composites is influenced not only by the crystallinity of the ceramic filler but also by the crystallinity of the polymeric matrix. In applications requiring high heat resistance for instance, achieving high rates of polymeric crystallisation is crucial. This is due to the amorphous state of polymers being prone to rapid aging and degradation under ambient conditions. Thus, obtaining a high degree of crystallinity is essential to enhance the durability and stability of these materials in such demanding environments. However, based on the required application, the crystallinity of the polymer may behave differently. As such, a study conducted by Eung Soo Kim et al. [222] has analysed the effect of three thermoplastic polymers, namely polytetrafluoroethylene (PTFE), polypropylene (PP), and polystyrene (PS), on the dielectric constant of a polymer-based composite filled with $ZnNb_2O_6$ particles. The results revealed that the degree of crystallinity significantly influenced the dielectric behavior of the composites. In their research however, the composites with amorphous polystyrene (PS) exhibited lower energy dissipation compared to those with semi-crystalline polypropylene (PP) and polytetrafluoroethylene (PTFE). This distinction can be attributed to the molecular structure and mobility of the polymer chains as well as the various behaviour of the $ZnNb_2O_6$ particles when incorporated within different crystalline polymeric matrices [222]. These findings underscore the importance of considering the crystalline nature of the polymer matrix during the design of composites to optimise their dielectric properties.

There is nothing as such as an optimal particle size, shape or crystallinity that can be incorporated to all dielectric composites to enhance their performance. The geometry and the shape of the filler particles as well as the corresponding crystallinity vary significantly depending on the specific application and the desired performance. Additionally, the desired performance characteristics, such as high dielectric constant,

low losses, and improved mechanical strength, does not solely depend on the particles' morphology but rather relies on a combination of multi-factors as explained within these subsections.

2.6.1.4. Effect of Volume Fraction of the Fillers

The quantity of ceramic volume fraction dispersed within the polymer matrix is another crucial factor that significantly influences the overall performance of dielectric properties in ceramic-polymer composites [223]. Consequently, in order to thoroughly assess the dielectric capabilities of a composite material, the determination of the incorporated filler volume fraction assumes a critical role in the morphological analysis of the composite material. Generally, the determination of volume fraction (V_f) involves analysing microscopic images acquired from the specimen's cross-sectional perspectives. This assessment entails measuring the overall area of the studied cross-section (A), in addition to the area occupied by filler particles (A_f). By the formula shown in Equation 2.18 [224], the filler volume fraction can be calculated with precision.

$$V_f = \frac{A_f}{A} \times 100 \qquad \text{(Equation 2.18)}$$

Understanding the impact of the filler volume fraction on the dielectric constant of composite materials is essential for comprehending their overall performance. As stated earlier, the dielectric constant is a key parameter that plays a pivotal role in evaluating the dielectric behavior of these composite materials. Thus, investigating how filler volume fraction influences the dielectric constant is crucial in gaining insights into the overall performance of composites in terms of their electrical storage properties. To gain insights into this relationship, researchers have explored the equation proposed by Yamada et al. in [201]. The Yamada model, as discussed earlier in Equation 2.11, establishes the theoretical dielectric constant, which is influenced by various factors, including the filler volume fraction ($\varphi = V_f$). Equation 2.11 demonstrated that an increase in the volume fraction of the filler results in a heightened impact of the ceramic component on the overall dielectric properties. However, it is crucial to recognise that higher volume fractions may not always yield optimal outcomes. This consideration is particularly significant within the realm of flexible dielectric devices, where a harmonious combination of flexibility and dielectric

performance is sought after. In order to optimise the performance of flexible devices, careful deliberation must be given to the selection of an appropriate filler volume fraction that strikes a delicate balance between dielectric performance and the flexibility of the composite material.

In response to this challenge, a recent study conducted by Meng Cao et al. offered a pioneering solution [86] where the researchers explored a novel approach to fabricate $BaTiO_3$ ceramics with remarkable characteristics, utilising a combination of a high sintering temperature (T_s) and the incorporation of a porogen (to induce pores or voids within the material during the processing stages) during the processing stages. By employing a high sintering temperature (T_s) and incorporating a porogen, the researchers were able to achieve the production of $BaTiO_3$ ceramics characterised by exceptional connectivity and significant porosity. The experimental results have demonstrated that these composites exhibit significantly higher ε_r values compared to conventional 0-3 composites with higher V_f. Moreover, the composites demonstrate low dielectric loss and exhibit good frequency and temperature stability of ε_r, suggesting their suitability for practical applications. Finite element simulation reveals that the enhanced connectivity of $BaTiO_3$ within the composite plays a critical role in influencing its dielectric response. Notably, a composite with a T_s of 1300°C and a ceramic volume fraction of 38.1% exhibited an impressive dielectric constant ε_r of 466.8 at a frequency of 1 kHz. This value represented a remarkable nine-fold improvement compared to the counterpart composite with a higher V_f of 60.8%.

Furtherly, Jayendiran and Arockiarajan in [225], conducted an experimental study to validate the theoretical model that describes the relationship between filler volume fraction and various dielectric properties, including remnant polarisation, saturation polarization, and coercive electric field. The investigation focused on a 1-3 piezoelectric composite composed of PZT fibres embedded within an epoxy matrix. The findings of the study revealed that a decrease in the volume fraction of the PZT fibres corresponded to a decrease in the ferroelectric properties, specifically remnant polarisation and saturation polarisation (as shown in Table 2.1). These results indicate a direct correlation between the filler volume fraction and both remnant polarisation and saturation polarisation. Notably, the mean values obtained from the experiments closely matched the theoretical values for both P_r and P_s. Moreover, it was noted that the average polarisation saturation of the composite remarkably increased when 65%

PZT fibers were utilised in terms of volume fraction. This effect became more notable as higher V_f (80% or 100%) were employed subsequently. With a decrease in filler volume, there have been fewer dipoles which resulted to decreased resistance for domain orientation caused by those dipoles [226]. Such occurrence has vital consequences on the dielectric permittivity of the substance and can be credited to both processing methods used [227,228] and the materials' microstructure [227,229].

Table 2.1. Remnant and saturation polarisation of 1-3 ceramic-polymer composites in response of varying ceramic filler volume fraction [225].

Fibre (PZT) vol. fraction (%)	Remnant polarisation (c/m^2)		Mean Remnant polarisation (c/m^2)	Saturation polarisation (c/m^2)		Mean Saturation polarisation (c/m^2)
	Exp.	Theo.		Expt.	Theo.	
35	0.1	0.1	0.1	0.11	0.1	0.1
65	0.23	0.2	0.22	0.27	0.25	0.26
80	0.28	0.28	0.28	0.35	0.34	0.35
100	0.35	0.36	0.36	0.39	0.37	0.38

Other crucial characteristics to consider when compromising the dielectric performance and the filler volume fraction are the frequency and temperature dependencies of the dielectric composite materials. In a study conducted by Khan et al. in 2017 [44], the frequency and temperature dependencies of the ε_r and loss tangent (tanδ) were investigated for a piezoelectric (dielectric) composite composed of randomly distributed barium titanate (BT) ceramic filler particles in a thermoplastic polyurethane (TPU) matrix. In this context, the dielectric loss (tanδ) represents the amount of electric energy dissipated as heat when a material is subjected to an external electric field. The research noted that by increasing the content of BT in the composite, both ε_r and tanδ showed proportionate increases for every volume fraction of BT as listed in Table 2.2. Herein, the experimental results exhibited a reasonable agreement with the theoretical values of the ε_r . The continuous increase in the dielectric constant with an increasing volume fraction of the incorporated electro-ceramic material contributed to the enhancement of the loss tangent and the electro-mechanical response of the material [44]. However, it should be noted that increasing the volume fraction

of BT may introduce temperature and frequency dependence in the ε_r and the tanδ [44]. While there were no considerable variations in the values of loss tangent reported for different volume fractions, it is vital to recognise that factors like polarisation hysteresis defects [182,230], dielectric leakages [182,189], environmental conditions, and technical methods [51] can also impact a material's dielectric loss. Therefore, it is crucial to consider these aspects as well to comprehensively evaluate the dielectric performance and optimise the filler volume fraction in composite materials.

Table 2.2. Mean dielectric constant and dielectric loss tangent as a function of varying BT volume fraction in a BT/PU composite model[a] [44].

BT Volume fraction (%)	Dielectric Constant (ε_r)		Mean[b]	Dielectric loss tangent (tanδ)
	Expt.	Theoretical		
0	7.5	6.25	6.88	0.05
10	14.37	13.75	14.06	0.05
20	20.0	20.5	20.25	0.038
30	31.25	28.75	30	0.04

[a] Source of results: Khan et al. [44]; [b] Mean represents averages between experimental and theoretical ε_r values for each volume fraction.

To further elaborate on the influence of ceramic volume fraction on the overall dielectric performance of the composite material, Kun Yu et al. conducted a study in 2019 [231], to explore the influence of $(K_{0.475}Na_{0.495}Li_{0.03})\ NbO_3$-$0.003ZrO_2$ (KNNL-Z) on the performance of a hot-pressed (KNNL-Z)/PVDF composite. The researchers herein confirmed that incorporating KNNLZ-ceramic powder into the composite resulted in an increase in the dielectric permittivity. This improvement may be attributed to the higher dielectric permittivity of KNN compared to that of PVDF [232]. These findings indicate that while the filler volume fraction plays a significant role in determining the dielectric properties of the composite, the specific electro-mechanical capabilities of the incorporated ceramic material also directly contribute to enhancing its dielectric performance. In line with the objective of consistently striving to enhance the dielectric performance of composite materials, Zhang et al. [233] focused on studying the impact of porosity on the dielectric performance of lead-free porous $0.5Ba(Ca_{0.8}Zr_{0.2})O_3$-$0.5(Ba_{0.7}Ca_{0.3})TiO_3$ (BCZT) ceramic- based material. In their research, they have observed that notably, the increase in porosity resulted in

a significant decrease in the piezoelectric performance as such a decrease in the d_{33} value, primarily due to a decline in the remnant polarisation. This decrease in remnant polarisation can be attributed to the concentration of the electric field in regions with lower permittivity, particularly during the poling process [234,235]. It is important to highlight that previous research by Siponkoski et al. has also demonstrated that the porous structure of a dielectric composite reduces the contact area between the matrix and the electrodes, leading to a decrease in permittivity [236].

2.7. Summary

This chapter has provided an overview of the fundamental principles related to dielectric, piezoelectric and ferroelectric concepts. The classification of dielectric materials into distinct groups based on their distinctive properties such as ferroelectric, pyroelectric and piezoelectric materials has also been exemplified. Furthermore, the commonly utilised performance measures to evaluate the characteristics of these materials, including the dielectric constant, piezoelectric voltage and charge coefficient, P-E loop hysteresis, and energy storage potentials were reviewed. Additionally, various ceramic and polymeric dielectric materials along with their corresponding crystallographic structure and their respective dielectric properties have been demonstrated. In this context, various ceramic synthesis techniques together with their corresponding advantages and disadvantages were reviewed, with an emphasis on molten salt synthesis technique. The combination of ceramics and polymers together to develop dielectric-based ceramic-polymer composites have emerged as a promising approach that addressed the challenges exhibited by each individual constituent, effectively. To enhance their performance and expand their applicability in a wider range of applications, this chapter has provided a comprehensive exploration of the various factors that are known to significantly influence the overall performance and the dielectric properties of such composites. It is worth noting that there's nothing as such a ceramic-polymer composite with optimum piezoelectric, dielectric, or ferroelectric properties. Instead, the enhancement of these properties is contingent upon the specific application in which the composite is intended to be used. Hence, the presented factors herein have covered a wide range of properties that are relevant to diverse applications.

Chapter 3

3. Experimental Work

The chapter is divided into two main parts: Part I presents the experimentation related to the ceramic synthesis process along with the materials and characterisation equipment related to this part. Part II presents the experimentation related to the composite fabrication, along with the involved materials and the characterisation equipment.

Part I (Powder Synthesis)

3.1. Molten Salt Synthesis (MSS)

In this work, molten salt synthesis has been selected to synthesise ceramic powder for incorporation in dielectric ceramic-polymer composites. As explained in chapter 2, molten salt synthesis (MSS) emerges as a promising synthesis technique for synthesising ceramic fillers with controlled size and shape for enhanced dielectric applications using low-cost and simple instrumentations [13,14].

This section is concerned with the synthesis of $Na_{0.5}Bi_{0.5}TiO_3$ (BNT) ceramic powder particles along with the equipment used during the synthesis procedure. The synthesis of BNT powder can be accomplished through either a two-step or a three-step reaction. The two-step method involves synthesising $Na_{0.5}Bi_{4.5}Ti_4O_{15}$ (NBiT) precursor as the first step, which is then utilised for the growth of BNT. In contrast, the three-step method involves the initial synthesis of $Bi_4Ti_3O_{12}$ (BiT), followed by the production of NBiT precursor through a reaction of BiT and oxides, and finally the growth of BNT using NBiT precursor. The three-step synthesis offers precise control over intermediate phases and properties but often yields similar final characteristics to the two-step method, such as morphology and grain size [142,237]. The three-step method being more time- consuming than the two-step method, it was decided to focus on the two-step method in this thesis. The schematic diagram in Figure 3.1 demonstrates the reactions of a two-step and a three-step MSS.

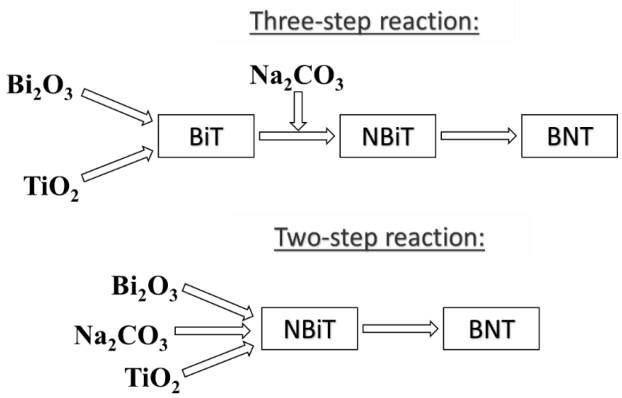

Figure 3.1: Schematic diagram showing the steps of a three-step and a two-step reaction of the MSS

3.1.1. Materials Preparation for the NBiT precursor

To synthesise the precursor $Na_{0.5}Bi_{4.5}Ti_4O_{15}$ (NBiT) powder, commercially available bismuth oxide, Bi_2O_3 (99.99%), titanium oxide, TiO_2 (99.7%) and sodium carbonate, Na_2CO_3 (BioXtra, ≥ 99.0%) were used. All the raw materials were purchased from Sigma Aldrich UK and have been used without any further treatment. Specific characterisation of the starting materials is presented in Table 3.1.

Table 3.1: Characteristic properties of the starting materials

Material	Physical State	Molecular Weight	Density	Melting Point/Range
Bi_2O_3	Powder	465.96 g/mol	8.93 g/cm3 at 20 °C	825 °C
TiO_2(anatase)	Powder	79.87 g/mol	3.78 g/cm³	1,825 °C
Na_2CO_3	Powder	105.99 g/mol	2.53 g/cm³	851 °C

The raw materials were mixed according to stoichiometric ratios (Equation 3.1). Sodium chloride, NaCl, from Fisher Scientific, UK, was added to the mixture in a 1:1 ratio with the total weight of the starting materials to act as a salt flux. The mixture was then ball milled using ethanol (C_2H_5OH) as a milling medium and zirconia balls as grinding medium to attain a homogenous blend [238,239]. A relatively low rotation speed was chosen to facilitate the mixing without causing excessive mechanical degradation [240].

$$2.25Bi_2O_3 + 0.25\ Na_2CO_3 + 4\ TiO_2 \rightarrow Na_{0.5}Bi_{4.5}Ti_4O_{15} + 0.25CO_2 \quad \text{(Equation 3.1)}$$

After mixing, the resultant powder was dried on a hot plate to evaporate the residual ethanol, and then transferred into alumina crucibles for subsequent heat treatment under varying heating conditions, using a carbolite GWF1100 furnace. A

comprehensive description of the designed experiments along with details of the selection of the varying heating conditions is explained in Chapter 4.

To guarantee the purity of the resulting product powder, it was essential to remove any remaining salt from the mixture after the heat treatment. This was achieved by washing the powder multiple times using warm deionised water at a temperature of 40-50°C. The warm deionised water aids in the dissolution of residual salt, which can then be removed through the washing process. Using warm water accelerates the rate of dissolution of residual salt, resulting in a more effective removal of salt from the powder. Deionised water was used to prevent the addition of any new ions that could react with the powder and alter its properties. The NBiT precursor was then subjected to drying on a hotplate to eliminate any residual moisture. The characterisation methods for the obtained NBiT precursor powder are described in section 3.2.

3.1.2. Materials Preparation for the BNT powder

The second step of the synthesis reaction is to synthesise final BNT powder particles. This was synthesised using optimally synthesised NBiT precursor powder as the starting material. In this context, optimally synthesised NBiT precursor refers to the precursor powder that has been synthesised using optimised molten salt synthesis parameters. Details for the optimally synthesised NBiT precursor are illustrated in Chapter 6. To synthesise BNT powder ($Na_{0.5}Bi_{0.5}TiO_3$), the optimally synthesised NBiT powder was mixed with Na_2CO_3 and TiO_2 according to Equation 3.2 with stoichiometric ratios. NaCl was additionally added as a flux with a weight ratio of 1:1.

$$Na_{0.5}Bi_{4.5}Ti_4O_{15} + 2Na_2CO_3 + TiO_2 \rightarrow 9Na_{0.5}Bi_{0.5}TiO_3 + 2CO_2 \qquad \text{(Equation 3.2)}$$

Herein, the raw materials were subjected to two different mixing techniques, namely roller mixing and magnetic stirring. Typically, magnetic stirring is conventionally employed to facilitate the mixing of the NBiT precursor with Na_2CO_3 and TiO_2, ultimately yielding BNT powder [143,241]. However, in this research the ball milling was also investigated as an alternative mixing method to examine its impact on the characteristics of the final powder and contrasting its efficacy with the commonly employed magnetic stirring.

Once more, ethanol (≥ 99%) served as the mixing solvent, which was subsequently dried and removed using a hotplate at a temperature of 80℃. The dried powders were

put in alumina crucibles and calcined at 1100℃ for 270 minutes at a heating rate of 7 ℃/min (the optimum process setting parameters obtained from DoE and explained in details in chapter 5) to transform into BNT. To eliminate the NaCl salt and other impurities, the final product powder was thoroughly washed multiple times using hot deionised water.

3.1.3. Equipment

3.1.3.1. Roller Mixer

A Stuart SRT6D roller mixer (shown in Figure 3.2) has been used to help ensure that the starting powder was thoroughly mixed and homogenised, which is critical to the success of the synthesis process. The primary principle of a roller mixer is to provide a controlled rocking and rolling action to facilitate complete mixing of samples. The gentle yet efficient motion of the rollers ensures thorough dispersion and homogenisation of the contents within vials or bottles. By rotating the sample tubes or vials at a controlled speed and using zirconia balls to provide gentle agitation, the roller mixer helps to break up any clumps or agglomerates of the powder, resulting in a more uniform distribution of the starting material. The mixer has a speed range of 5 to 60 rpm and a built-in timer for up to 90 minutes. The inclusion of a programmable timer further enhances the control and reproducibility of the mixing process.

Figure 3.2: Overview of the Stuart SRT6D roller mixer equipment

In this work, the raw materials were loaded into sample tubes along with Yttria Stabilised Zirconia ceramic balls (3 mm), in both the precursor and final powder synthesis steps. Ethanol was added to aid the mixing process of the raw materials in

the sample tubes. The tubes were then placed on the platform of the roller mixer, and the rollers were set to rotate at a speed of 60 rpm for 4 hours.

3.1.3.2. Hotplate

A Glassco 900.DNDG.01 magnetic stirrer (Figure 3.3) with digital hotplate has been used in this study. The hotplate can heat up to a maximum temperature of 350°C, with a heating rate of up to 5°C per minute and a heating accuracy of +/- 1°C. The device has a built-in magnetic stirrer that can provide stirring speeds of up to 1500 RPM. It is equipped with a digital display for precise temperature control and a timer function for convenient monitoring of the reaction time.

The hotplate was used in this study to facilitate the drying process of the powders, both after mixing with ethanol and after washing with deionised water. After the raw materials were mixed with zirconia balls and ethanol, the hotplate was set to a temperature of 80°C and the mixture was dried for approximately three hours to evaporate the ethanol. For drying the washing hot deionised water, the hotplate was set to 110°C for almost three hours.

The magnetic stirrer was utilised in the second step of the synthesis reaction during the mixing of the raw materials for the final BNT powder.

Figure 3.3: Overview of the Glassco 900.DNDG.01 magnetic stirrer with digital hotplate.

3.1.3.3. Furnace

A carbolite CWF 1100 furnace (Figure 3.4 (a)) was used to perform high-temperature heat treatment (calcination) on the synthesised powder particles, with a maximum operating temperature of 1100°C and a programmable temperature controller that allowed for precise temperature control. Additionally, the programmable controller allowed for choosing specific heating rate at which the powder was heated and specific holding times at specific temperatures. It features a robust construction with a ceramic fibre lining for improved thermal insulation, and a stainless-steel casing for durability and resistance to corrosion, with an internal chamber volume of approximately 8 litres. To ensure uniform heating, the sample powders were loaded into alumina crucibles (with lids on to prevent evaporation and contamination) and placed individually at the centre of the furnace chamber. A thermocouple was inserted into the furnace chamber alongside the sample to monitor the temperature throughout the heating process to ensure accurate temperature control (Figure 3.4 (b)). The powder samples were then allowed to cool naturally in the furnace chamber to room temperature, with the furnace turned off and the door closed to prevent any external cooling influences.

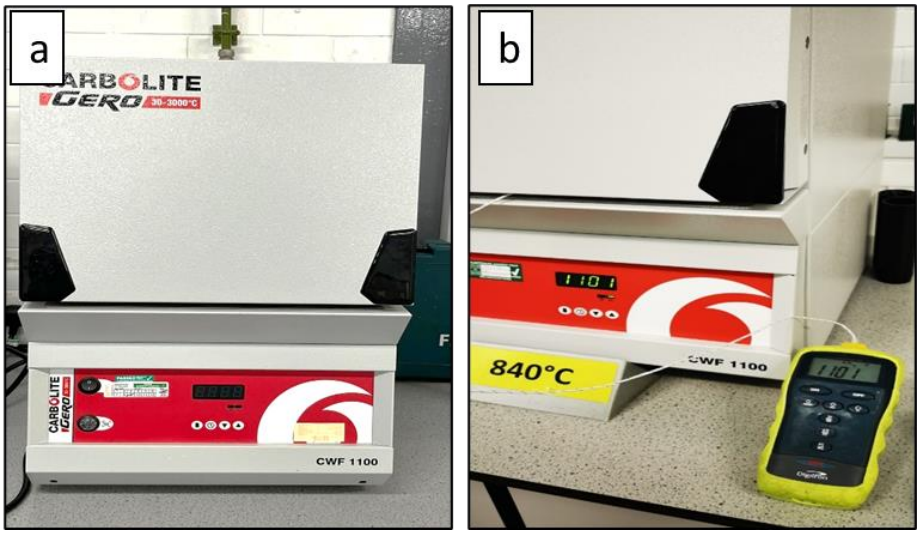

Figure 3.4: Overview of (a) a carbolite CWF furnace and (b) installed thermocouple confirming the internal temperature of the furnace

3.2. Characterisation Methods

This section provides an overview of the characterisation methods utilised to assess both the properties of the ceramic powder particles synthesised using the molten salt method, as well as the microstructure of the composites fabricated using these powder particles. A range of techniques, including scanning electron microscopy (SEM),

energy-dispersive X-ray spectroscopy (EDS), X-ray diffraction (XRD), and mastersizer diffraction instrument. Image processing software, Image J, was used to examine the crystal structure, particle size, elemental composition, and morphology of the materials.

3.2.1. Scanning Electron Microscope and Energy Dispersive X-ray Spectroscopy

SEM is a powerful imaging technique that utilised a high-energy electron beam to generate high-resolution images of a sample's surface and internal structure and allows for the visualisation of fine surface details at the micro and nanoscale. Generally, the SEM works by projecting a focused stream of electrons onto a sample's surface and scanning it in a raster pattern [242]. The interaction between the electrons in the beam and the sample generates different types of signals that provide valuable information about the sample's topography and composition. These signals include secondary electrons, backscattered electrons, and characteristic X-rays, each carrying unique information about the sample's properties. Secondary electrons (SE) are released from the sample's surface when the primary electron beam strikes it. The sample's surface morphology is revealed by these low-energy electrons, enabling the visualisation of microscopic surface details and characteristics. These released electrons are caught and measured by secondary electron detectors, which creates an image that depicts the topographical features of the material. Backscattered electrons (BSE), in addition to SE, are produced as a result of the primary beam's interaction with the sample's atoms. Depending on elements like the sample's atomic number and density, these higher-energy electrons are deflected or scattered back from the surface of the material, hence indicating valuable information about the sample's composition and atomic arrangement [243,244]. Additionally, the sample's atoms may be excited by the primary electron beam, which will result in the emission of distinctive X-rays. The energy of these X-rays is distinctive and depends on the components in the sample. It is thus possible to ascertain the elemental content and distribution inside the sample by spotting and examining the distinctive X-rays[243,244].

In this work, SEM TESCAN MIRA3 (Figure 3.5 (a)) was utilised to investigate the morphology, shape, size, and particles properties of both the synthesised NBiT precursor and BNT powder. The samples were initially coated with platinum (5nm thickness) using a Quorum Q150R rotary pumped coater to produce high-quality

pictures (Figure 3.5 (b)). The high-degree magnification helped in examining and understanding the microstructure and surface characteristics of the synthesised powder particles that were heat-treated using various heating conditions. It was thus powerful in giving insights about the impact of the heat-treatment conditions on the particle's properties.

Additionally, the SEM along with the BSE was used to capture high-resolution images of the BNT-Epoxy composites developed in this research and explained in detail in section 3.3 of this chapter. The obtained images helped to show the distribution and orientation of the ceramic particles within the epoxy matrix, providing information on the composite's properties and behaviour under different conditions. Moreover, the SEM images can reveal any defects or damage within the composite, which can impact its mechanical and electrical properties. Herein, the cross-sections of the composites were cut and coated with silver paint (G3691, Agar Scientific).

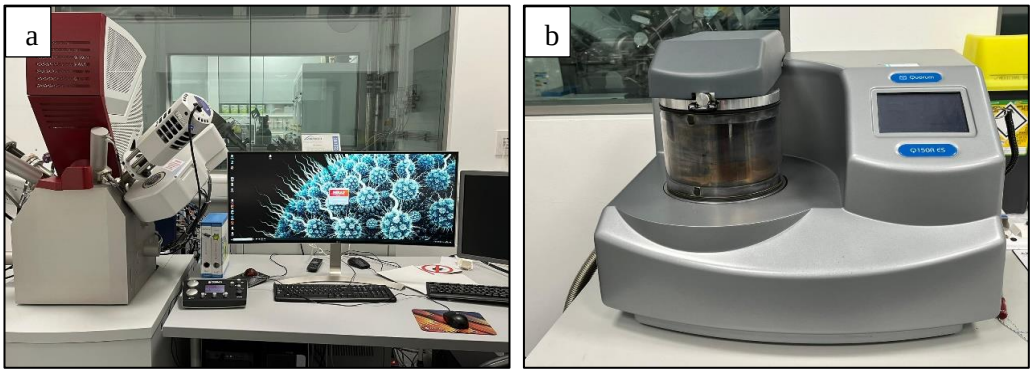

Figure 3.5: (a) Overview of the TESCAN MIRA3 SEM machine and (b) Quorum Q150R rotary pumped coater

Moreover, to confirm the elemental composition of the developed BNT-Epoxy composites and help tracing any impurities, the Energy-dispersive X-ray spectroscopy (EDS) was utilised. EDS is a powerful analytical tool that works by detecting the X-rays emitted by the sample when it is bombarded with a electrons' beam, which excites the sample's atoms and causes them to emit characteristic X-rays. The energy and intensity of these X-rays are then used to determine the elemental composition of the sample.

3.2.1.1. Image J

To analyse and study the microstructure properties of the synthesised powder particles, the captured SEM images were transferred to image J (ImageJ v1.54b). It is a powerful

image analysis software that provides a wide range of tools and functions for analysing and processing digital images, including measuring distances, areas, and angles, performing image segmentation and thresholding, and generating three-dimensional (3D) reconstructions. In this research, ImageJ has been used to measure several particles properties such as the area, the thickness, the Feret's diameter, the circularity, and the aspect ratio of the synthesised powder.

3.2.2. Mastersizer

To assess the particle size and particle size distribution of the synthesised NBiT powder particles and gather valuable data for the design of experiments and analysis of the material's physical properties, a mastersizer (Malvern Mastersizer 3000) has been used. A schematic of the optical layout of the diffraction instrument is shown in Figure 3.6 (a).

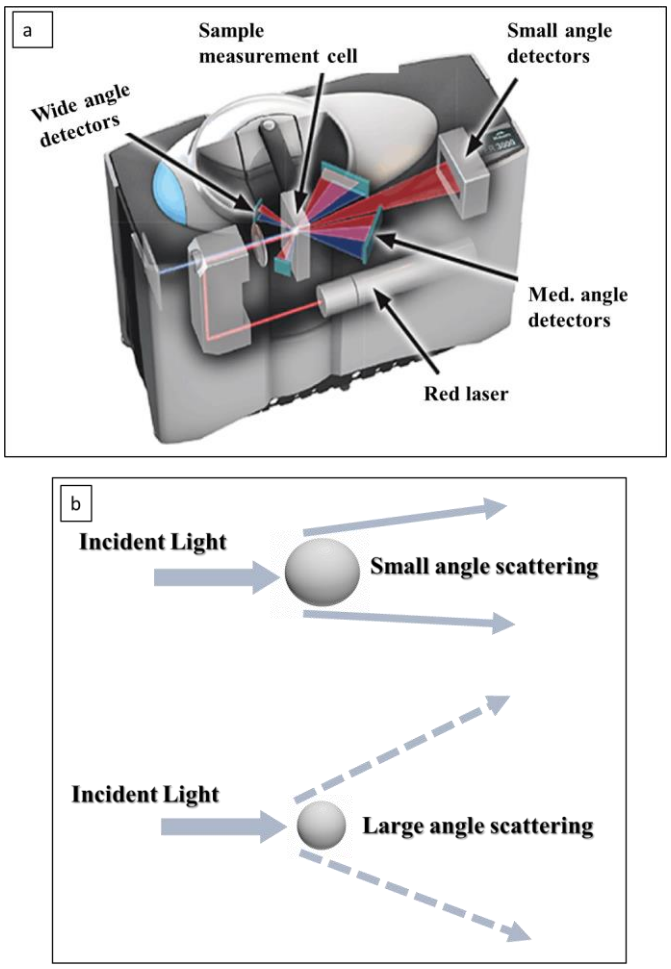

Figure 3.6: Schematic showing (a) the optical layout of a mastersizer diffraction instrument and (b) light scattering for small and large sized particles.

Mastersizer is capable of measuring particles in the size range of a few nanometres up to several millimetres. It works by measuring the intensity and angle of light scattered by particles as they pass through a sample cell (Figure 3.6 (b)). The data obtained from this measurement is then used to calculate the size distribution and average particle size of the sample (SOP-editor). Water has been used as a dispersant with the synthesised powder particles to achieve a homogenous suspension of particles in the dispersant liquid. Dispersing agents or surfactants help to reduce the surface tension of the liquid, allowing the particles to separate and remain suspended in the liquid medium. This ensures that the particles are uniformly distributed and can be accurately measured by the instrument.

3.2.3. X-ray Diffraction

X-ray diffraction (XRD) is a non-destructive analytical technique that provides information about the crystallographic structure, phase composition, lattice parameters, phase purity, and crystalline size of a material. It works by exposing a sample to X-rays and observing the resulting diffraction pattern, which is produced when the X-rays interact with the arrangement of the atoms in a crystal lattice, causing them to scatter in a specific pattern. It is based on the concept of Bragg's law, which relates the angle of incidence of X-rays to the spacing of atomic planes within the crystal lattice [237]. Bragg's law is depicted by the formula in Equation 3.3 [245], whereas n is an integer that represents the order of the diffraction peak, λ is the wavelength of the X-rays, the spacing between the crystal lattice planes is depicted by d and the diffraction angle is represented by θ. Bragg's law states that when an X-ray beam interacts with parallel atomic planes within a crystal lattice at a particular angle of incidence, constructive interference results. As a result, a diffraction pattern is created with peaks that are particular to the crystal's interplanar spacing. The spacing between the atoms in the crystal lattice can be calculated by measuring the angles at which the diffraction peaks appear, which provides important information about the crystal's structure and organisation [245]. Geometric requirements for diffraction expressing the Bragg's law are presented in Figure 3.7.

$$n\lambda = 2d_{hkl}sin\theta \qquad \text{(Equation 3.3)}$$

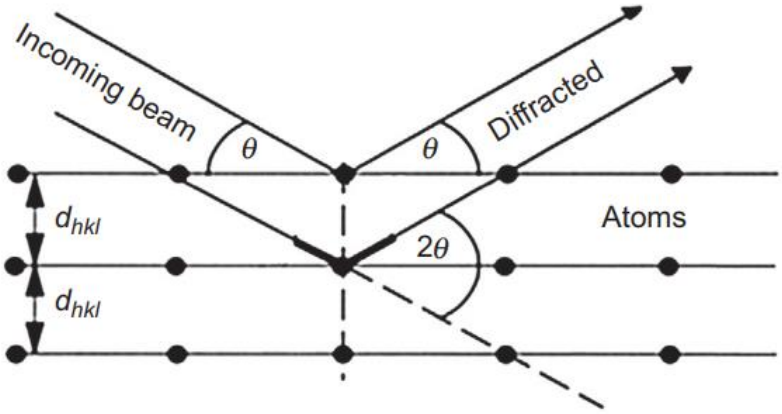

Figure 3.7: A schematic showing the geometric criteria for diffraction occurring from lattice planes according to Bragg's law [245]

In this work, XRD was performed using a Rigaku Smartlab II instrument with Cu-radiation source, which emits X-rays with a wavelength of 1.54 Å, at room temperature. Figure 3.8 (a) and (b) provide an overview image of the Rigaku Smartlab instrument showing the external and internal of the machine, respectively. Figure 3.8 (c) illustrates a schematic of the five-circle goniometer Rigaku system [246], where the sample is manipulated with 3- circles (ω, χ, φ) and the detector is moved with 2-circles (2θ and 2θχ).

The sample powder was placed onto a square glass plate sample holder (20mmx20mm), spread out evenly and pressed lightly using another glass plate, onto the holder to ensure good contact between the holder and the powder and to achieve accurate results. Data for the XRD peaks of the NBiT precursor were collected in the 2-theta range of 10º-80º, whilst XRD peaks of the BNT powder were in a 2-theta range of 20º-80º with the help of Smartlab studio II v4.3.115.0 software. The difference in the 2-theta range is based on the anticipation that the BNT powder will not exhibit significant XRD peaks at lower angles (before 20 theta) [247,248]. The step size for the peak collection was set to 0.01 degrees, and the scanning speed was 10 degree/min, to achieve higher resolution and more accurate data. The obtained XRD peaks were then identified and analysed using PANalytical's X'Pert HighScore version 2.1 software.

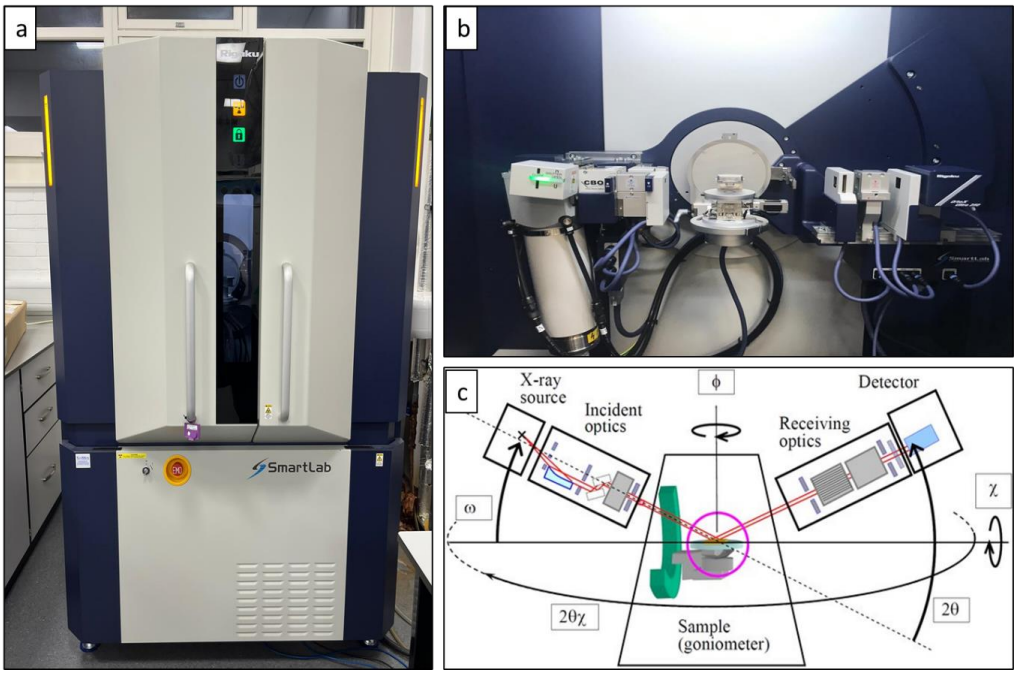

Figure 3.8: An overview of the (a) Rigaku Smartlab XRD machine and (b) the internal components of the instrument and (c) a schematic of the five-circle goniometer Rigaku system [246].

Part II (Composite Fabrication)

3.3. Ceramic-Polymer Composite Fabrication

This section pertains to the fabrication of ceramic-polymer composites, beginning with an overview of the fabrication approach and subsequently detailing the fabrication procedure. Moreover, the equipment utilised in the fabrication process, such as the speed mixer, the doctor blade, and the muffle oven, are also discussed in detail.

3.3.1. Composite Fabrication through a Novel Mechanical Alignment Approach

In the quest of developing dielectric composites with enhanced performance for energy storage purposes, the second aim of this work was to manufacture quasi 1-3 ceramic-polymer composites with a particle configuration that exhibits the favorable chain-like structure [194] utilising a straightforward and economically viable fabrication approach. Quasi 1-3 composites, characterised by the alignment of ceramic particles within a polymer matrix in a chain-like manner, have been widely acknowledged as highly desirable for various dielectric applications. This is due to their superior properties compared to 0-3 and 1-3 composites as explained in Chapter 2. The attainment of this specific structure can be achieved through various methods,

including injection molding [249], freeze-casting [250], and the application of external stimuli such as an electric field in the case of dielectrophoresis [193,195] or a magnetic field in the case of electromagnetic alignment [251]. However, these techniques may be challenging and time-consuming due to the need for meticulous control over the alignment process. Additionally, they may be further limited by the requirement for specialised experimental setup and equipment such as in the case of dielectrophoresis for example. Moreover, the process can be expensive, particularly for large-scale production.

Therefore, in this research, an alternative alignment technique has been employed to mechanically align ceramic particles with optimised two-dimensional plate-like shapes within a polymeric matrix using a doctor blade and eventually achieve fabrication of quasi 1-3 ceramic-polymer composites for dielectric applications.

The use of a doctor blade in the fabrication of ceramic-polymer composites offers several advantages over conventional techniques. Firstly, it is a relatively simple and cost-effective method that does not require any specialised experimental setup or equipment, making it accessible to a wider range of researchers. Secondly, it allows for a high degree of control over the thickness and uniformity of the composite layer, which can be crucial for achieving consistent results in large-scale production. Figure 3.9 (a) illustrates a schematic representation of the mechanical alignment technique, which was used to align two-dimensional plate-like shaped ceramic particles within a polymeric matrix in the x-direction (Figure 3.9 (b)).

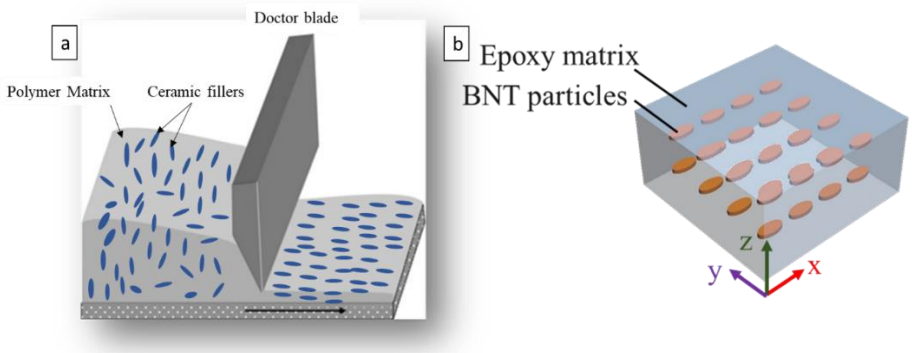

Figure 3.9: (a) Schematic of the doctor blade aligning ceramic particles and (b) anticipated chain-like alignment of plate-like ceramic particles within the polymeric matrix in the in x-direction

Generally, the process commences with the mixing of a ceramic-polymer composite material wherein two-dimensional, plate-like ceramic particles are uniformly dispersed within a polymeric matrix. Initially, these ceramic particles exhibit a random orientation within the matrix. Subsequently, a doctor blade, characterised by its slender, rigid structure, is brought into contact with the surface of the composite material leading to the exertion of mechanical force. As the doctor blade moves across the substrate at a constant speed, facilitating the creation of a smooth and uniform film, the particles undergo alignment in one direction. Details of the herein utilised doctor blade and how it works is further explained in section 3.3.3.1 of this thesis.

3.3.2. Composite Preparation

In this work, ceramic-polymer composites were developed using the optimally synthesised BNT ceramic powder and a two-component epoxy system, namely Epo-Tek 302-3M Epoxy. The Epo-Tek 302-3M Epoxy system is based on diglycidyl ether bisphenol-A (DGEBA) resin (Part A) and poly(oxypropyl)-diamine (POPD) multifunctional aliphatic amine hardener Part B). The selection of epoxy as the polymer matrix in this study was based on its excellent mechanical properties, strong adhesion to ceramic fillers, and low dielectric loss [252]. The high mechanical strength of epoxy is attributed to its high crosslinking density, which enables it to resist deformation and maintain its shape under external stress [253]. Additionally, the high adhesion strength of epoxy to ceramic fillers ensures that the ceramic particles are well dispersed and uniformly distributed throughout the polymer matrix [254], resulting in a homogeneous composite with improved mechanical and electrical properties. The low dielectric loss of epoxy [255] is advantageous for dielectric applications as it ensures minimal energy dissipation and high energy storage efficiency. This is in addition to the simplicity of processing, which includes curing at room temperature. Therefore, epoxy was a suitable choice as the polymer matrix for the quasi 1-3 ceramic-polymer composites, and it is expected to enhance the overall performance of the composites. Characteristic properties of Epo-Tek 302-3M are summarised in Table 3.2.

Table 3.2: Characteristic properties of Epo-Tek 302-3M epoxy system

Property	**Value**
Color	Part A & B (colourless)
Mix ratio by weight	100:45
Glass transition temperature	≥ 55 °C
Density	1.13-1.15 g/cm^3
Viscosity (at room temp)	800 - 1,600 cPs
Curing schedule	3 hours at 65ºC or 1 hour at 100ºC

Initially, the ceramic powder was first mixed with the epoxy resin (Part A) using a high-speed mixer (Pulsar Alginate Mixer). After this initial mixing, the curing agent (Part B) is added, and the preparation is mixed again for another 5 minutes. This ensures that the ceramic particles are well dispersed throughout the epoxy matrix and that the curing agent is evenly distributed.

The next step involved casting the mixture onto a strong foil paper using a doctor blade, while choosing the thickness of the samples. Several composites with various ceramic volume fractions ranging from 5% to 35% were fabricated using this method. The composites were mixed using a mix by weight ratio using a speed mixer. When attempting to fabricate composites with higher ceramic volume fractions, i.e. above 35%, the mixture became too viscous and laborious to deal with and spread unevenly onto the foil paper. Therefore, the ceramic volume fraction was limited to 35% or below to ensure the quality and uniformity of the composites. Generally, the composite layers of BNT varied ranging from around 3 to approximately 13 layers, with corresponding composition percentages falling between 5% and 35%.

Afterwards, the composites with the foil were then cured at 100ºC for 1 hours in a Memmert oven to ensure proper curing of the epoxy matrix. After curing, the composites were cut into circular and square shaped small samples and coated on one side with the conductive G3691 Agar Scientific silver paint for the dielectric measurements. Furtherly, some of the samples were left uncoated and have undergone further treatment, namely poling. This is explained in detail under the poling subsection. A schematic showing the composite fabrication procedure is shown in Figure 3.10.

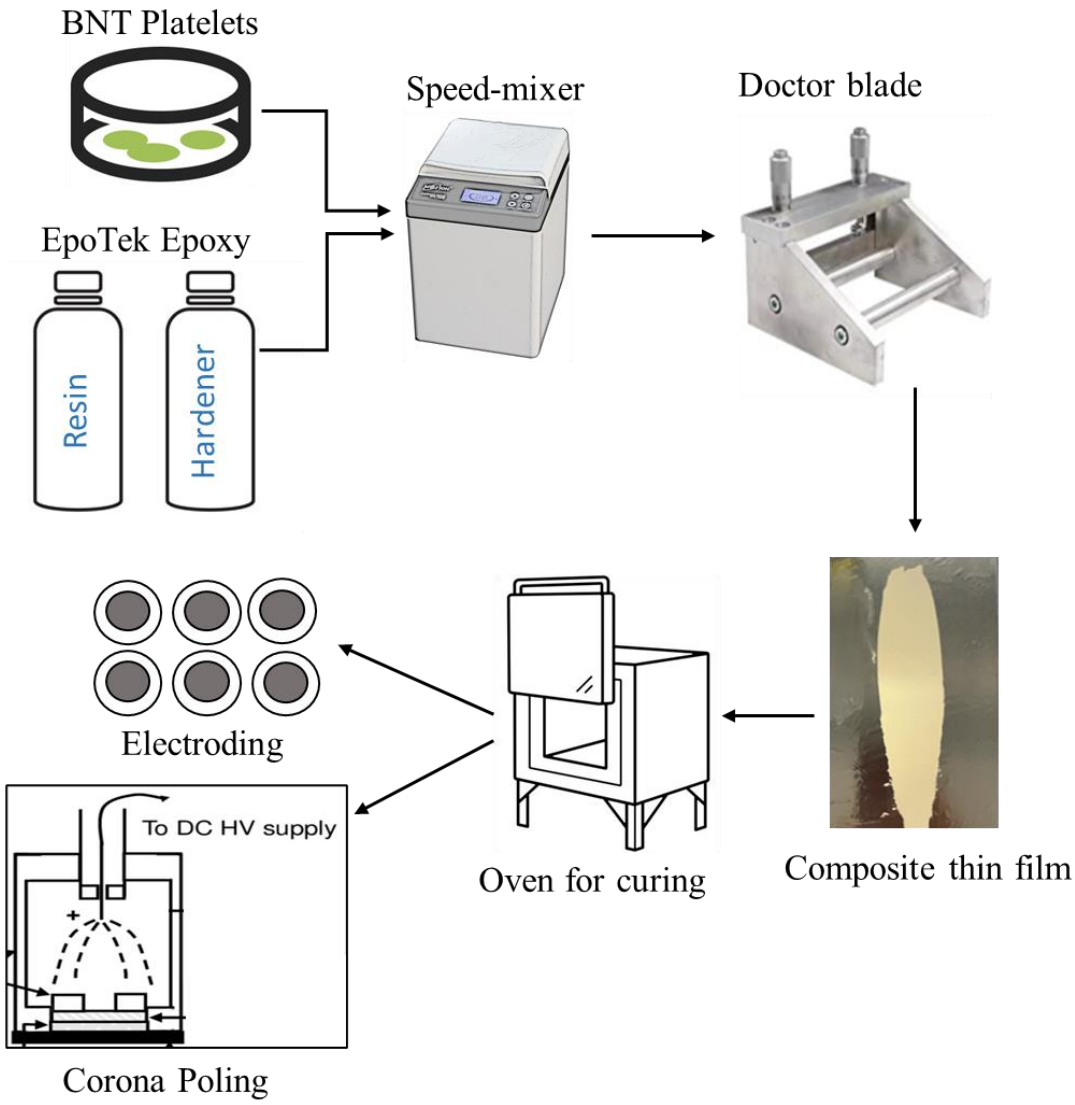

Figure 3.10: Schematic representing the fabrication of BNT-Epoxy composites using the doctor blade

3.3.3. Equipment

3.3.3.1. Doctor Blade

The doctor blade utilised in this study was a CGOLDENWALL KTQ-II film applicator (Figure 3.11). It is a high-precision instrument used in various industries to achieve uniform and controlled film thickness. The instrument is specifically designed for the application of coating solutions onto flat substrates, such as glass or metal plates (in this case foil), with a maximum size of 200 x 300 mm. The film applicator operates by spreading a coating solution uniformly onto the substrate using a blade with a precise gap height that determines the thickness of the resulting film. The blade height can be adjusted to the desired thickness, typically ranging from 10 to 500 µm, depending on the application. The blade is then moved across the substrate at a constant speed,

resulting in a smooth and uniform film formation. In this thesis, the thickness of the fabricated composites has been set to 150 µm. However, due to the particle distribution in some of the composites as well as retraction of the mixture on the foil during the removal of the doctor blade, the thickness was not always the same. To ensure an accurate value of the fabricated thickness layer, a micrometre was used to measure the thickness of the cured composites.

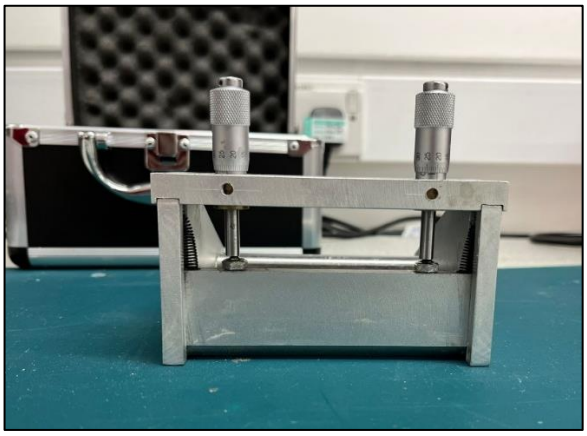

Figure 3.11: Overview image of the CGOLDENWALL KTQ-II doctor blade

3.3.3.2. Speed Mixer

A Pulsar Alginate Mixer MX300 (Figure 3.12) has been used in this research to mix ceramic particles with the epoxy resin and hardener. The mixer has a unique vortexing mechanism that allows for efficient mixing and dispersion of particles in liquids. The high-speed mixing capabilities, with the mixer being capable of reaching speed of up to 3000rpm, ensured a thorough mixing of the ceramics and the epoxy.

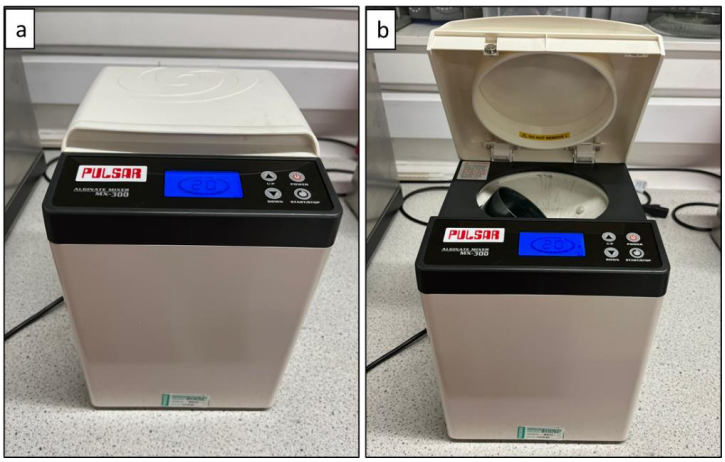

Figure 3.12: Overview image of (a) exterior and (b) interior of the Pulsar alginate MX300 mixer

3.3.3.3. Oven

In this study, a Memmert UNB 400 (by Fisher Scientific) muffle oven (shown in Figure 3.13) was used to cure the BNT-epoxy composite samples. This oven has a temperature range of up to 400°C with a maximum heating rate of 20°C/minutes. It is equipped with a digital temperature controller and a timer, which allows for accurate and repeatable curing of the composite samples. It has an internal chamber size of 400 x 400 x 320 mm, a maximum power consumption of 2500 W and requires a 230 V AC power supply.

During the curing process, the BNT-epoxy composite samples were placed on a heat-resistant surface and then inserted into the muffle oven. The oven was then heated to a temperature of 100°C and held at that temperature for one hour.

Figure 3.13: Overview image of the Memmert UNB 400 muffle oven

3.4. Electrical Characterisation

This section aims to provide a comprehensive overview of the electrical characterisation process carried out on the BNT-epoxy composite samples using various techniques. Initially, the first subsection puts emphasis on the poling process of the samples, which is a vital step in the piezoelectric characterisation procedure. Following this, the section covers several techniques used for capacitance measurements, P-E loop measurements, piezoelectric coefficients measurements.

3.4.1. Poling Procedure

To investigate the impact of poling on the mechanically aligned-optimally synthesised BNT-Epoxy composites and study the extent to which the poling process enhances the piezoelectric properties of these composites, a poling procedure has been carried out. Poling is the process of aligning the electric dipoles within a ferroelectric material with

the direction of a strong DC electric field. This alignment results in a net polarisation within the material, which persists even after the electric field is removed (residual polarisation).

Amongst various contact and contactless poling techniques [256,257], this study employed a contactless poling technique, namely corona poling. It entails creating a strong electric field between a plate with a grounded surface and an electrode with a sharp tip, whereas the sample is placed in between. As the corona electrode generates ions, a secondary field develops across the sample, causing the ions to migrate towards the surface. The alignment of ferroelectric domains is facilitated by this movement, which causes charge redistribution [256]. In this work, corona poling was selected as it provides several advantages over other techniques. Generally, corona poling poses lower risks of damage to the sample compared to contact poling in an oil bath for example, which requires careful control of temperature and pressure. Additionally, the ability to pole samples without the need for deposited electrodes or with only one electrode [258]. In corona poling higher electric fields can be achieved when compared to sandwich contact poling [259].

To pole the BNT-Epoxy composites samples, an experimental setup shown in Figure 3.14 was built up, and an overview schematic of the corona poling setup is depicted in

Figure 3.15. Herein, a high voltage power supply (Gamma high Voltage Research ES440P-5W), a corona electrode (stainless steel knitting needle), and a grounded counter electrode were used. High voltage poling involves simultaneously heating a sample and subjecting it to a high voltage, and hence a hotplate was used. This imparts an electrostatic charge in the sample and the charge remains even when the high voltage and heat are removed.

Figure 3.14: Overview of the poling experimental setup

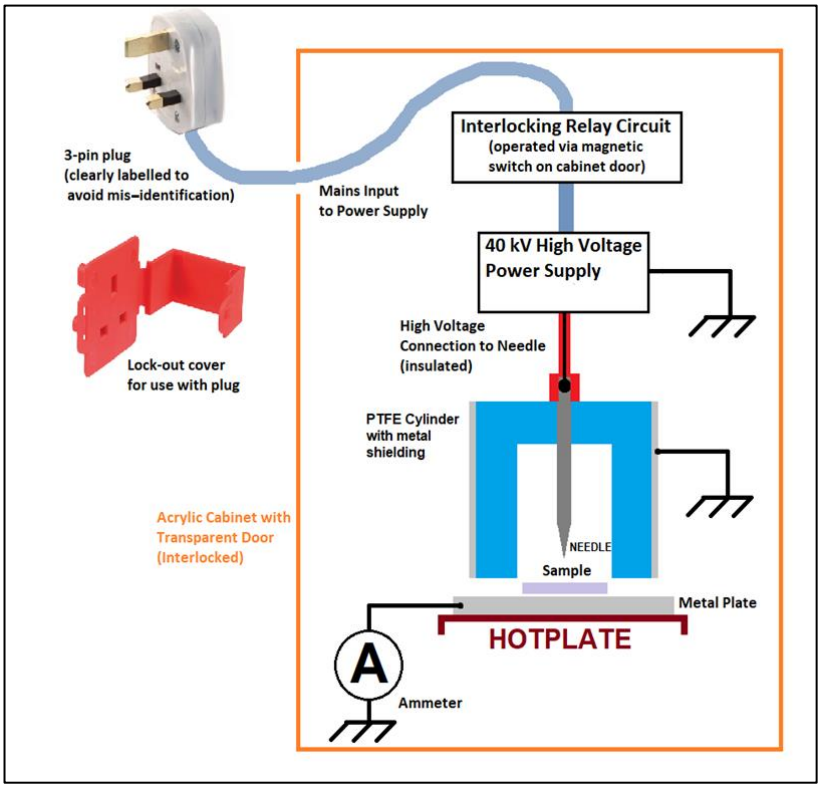

Figure 3.15: Overview schematic of the corona poling setup

A voltage of around 17kV DC was applied to the 300-series needle protruding into a shielded Teflon - PTFE tube. Two corona polarities, positive and negative, were tested during the experimental procedure. Below the tube the BNT-Epoxy composites samples were positioned on metal tube and heated on a hotplate to a maximum of

80°C. To investigate how the orientation of the applied electric field affects the piezoelectric properties of the samples, the samples were placed in two different positions. In the first position, the samples were left uncoated (with only foil as the bottom electrode) and were placed horizontally (Figure 3.16 (a)): parallel to the metal plate and BNT plate-like particles perpendicular to the electric field. In the second position, the samples were placed in a vertical position (Figure 3.16 (b)), parallel to the electric field. To avoid the flow of the ions towards the foil in this vertical position and avoid potential short-circuit, it was attempted to remove/ peel off the foil from the samples.

The metal plate underneath the samples was earthed via an ammeter. During poling the current reading will gradually fall until a steady state value is reached, indicating that the process is complete. Poling was conducted for two hours. For safety, the entire setup has been contained within an interlocked acrylic enclosure, equipped with a transparent sliding access door.

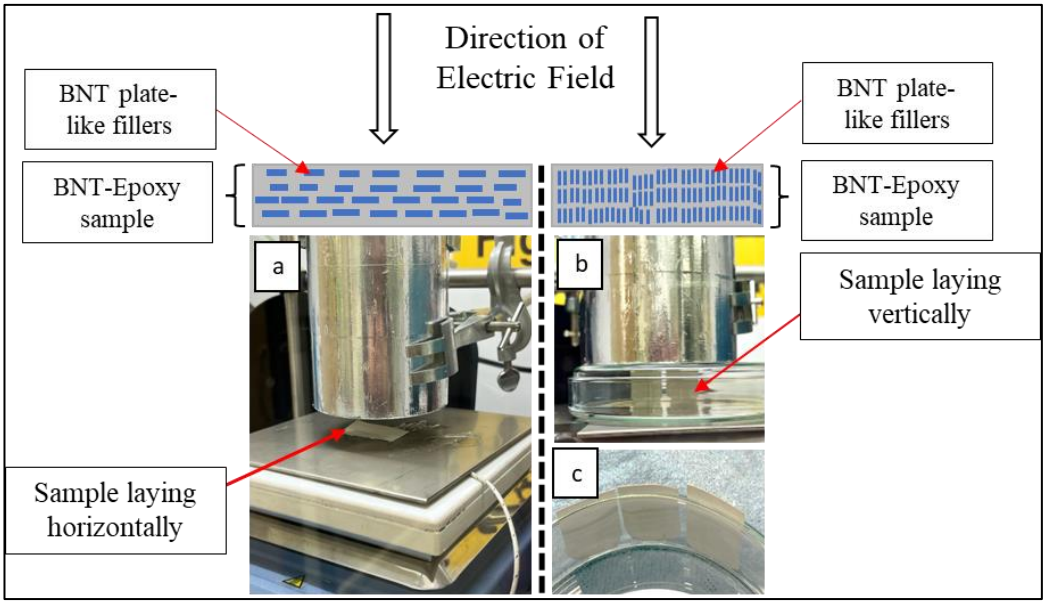

Figure 3.16: Overview image of positioning samples (a) horizontally, with a schematic displaying electric field direction is perpendicular to the incorporated particles in the sample and (b) vertically, with a schematic showing direction of electric field parallel to the incorporated particles (c) close-up view of samples in parallel position to the electric field

3.4.2. LCR Meter for Capacitance Measurement

To ultimately calculate the dielectric constant of the BNT-epoxy composites, the measurement of their capacitance was necessary. This was performed using the

Waynne Kerr automatic LCR meter shown in Figure 3.17 (a), which offers a frequency range of 20 Hz to 1 MHz with a basic accuracy of 0.05% and a resolution of 0.001(smallest increment that can be detected by the instrument), allowing for precise measurements. By using the measured capacitance, the dielectric constant of the BNT-Epoxy composites was calculated and are discussed in detail in Chapter 7.

To measure the capacitance, the electrodes connected to the LCR meter were positioned on opposite sides of the coated (conductive) BNT-Epoxy composite samples as shown in Figure 3.17 (b), and measurements were taken at a frequency of 1 KHz. Multiple measurements were taken to obtain an average value for the capacitance.

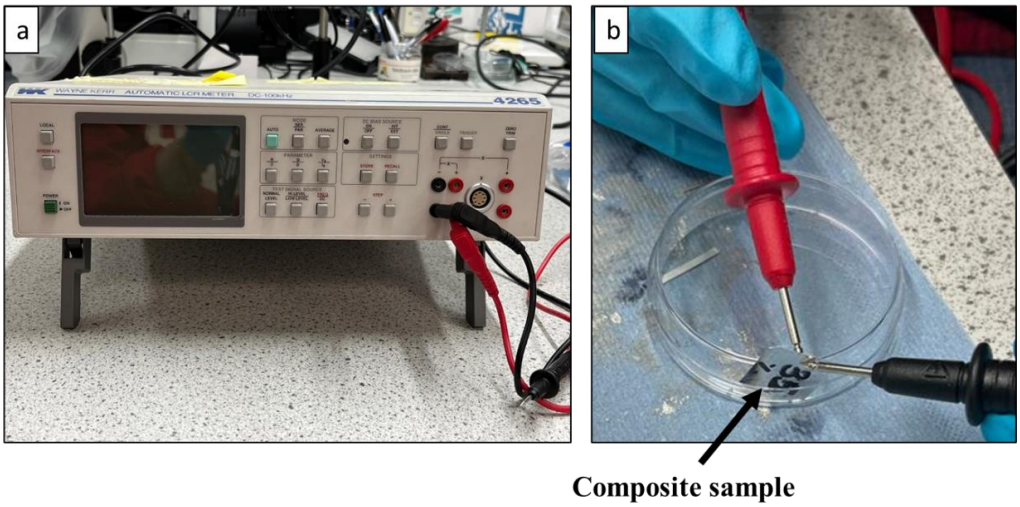

Figure 3.17: Overview of (a) Waynne Kerr LCR meter and (b) samples holding during measurements

3.4.3. Ferroelectric Tester for P-E loop hysteresis

To further investigate and analyse the dielectric properties of the developed BNT-Epoxy composites, P-E loop hysteresis testing was performed. This testing allows for the analysis of crucial ferroelectric properties such as remnant polarisation, coercive field, and saturation polarisation of the fabricated composite samples. The coercive field value indicates the strength of the electric field required to switch the polarisation direction of the material, while the saturation polarisation value indicates the maximum polarisation that can be induced in the material [42,56,57].

In this work, the P-E loop was measured using the Radiant RT66C-HVi ferroelectric test system, illustrated in Figure 3.18 (a). The circular shaped coated samples (shown in Figure 3.18 (b)) were mounted onto the sample holder of the RT66C ferroelectric

tester, ensuring that they were securely held in place and in electrical contact with the electrodes. Next, they were connected to the RT66C ferroelectric tester, which is equipped with a built-in high voltage amplifier. This amplifier is designed to generate a programmable AC or DC voltage signal with an output voltage range of up to 10 kV. Features of the Radiant RT66C-HVi ferroelectric test system is tabulated in Table 3.3. To then initiate the measurement, the voltage has been swept from negative to positive and then back to negative values. During this voltage sweep, the RT66C ferroelectric tester automatically records both the voltage, current signals generated by the BNT-Epoxy composites and the corresponding polarisation. Measurements were taken at a frequency of 0.1kHz and a period of 10 msec. The P-E loops were then constructed using the obtained data for the driven voltages and their corresponding polarisation.

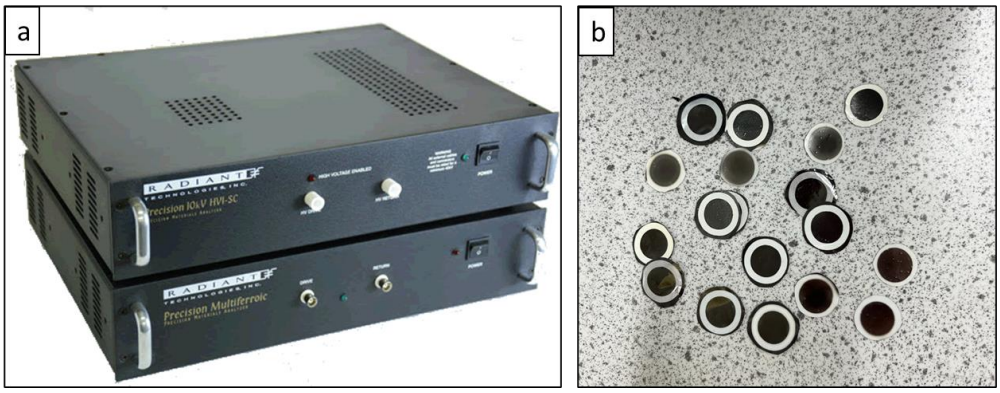

Figure 3.18: Overview image of (a) the radiant RT66C-HVi ferroelectric test system and (b) the BNT-Epoxy coated and masked samples

Table 3.3: Features of the Radiant RT66C-HVi ferroelectric test system

Feature	**Value**
Voltage test (built-in amplifier)	+/- 200 V
High voltage limit	+/- 10kV
Maximum hysteresis loop frequency	1 kHz
Minimum hysteresis loop frequency	1/8th Hz
Minimum hysteresis period	8 seconds
Peak output current	50 mA

3.4.4. Piezometer for piezoelectric measurements

In this study, the PM300 Piezometer developed by Piezotest (shown in Figure 3.19) was used to measure the d_{33} piezoelectric coefficient of the BNT-Epoxy composites. The instrument measures the d_{33} by clamping the sample and applying a relatively low

frequency force between 10Hz to 1kHz. The electrical signals produced by the sample are then processed and compared to a built-in reference, which provides a direct reading of d_{33}. This represents the material property that quantifies the charge generated per unit force applied in the direction of polarisation.

The PM300 PiezoMeter employs the so called "quasi-static" or "Berlincourt" method, which involves the application of a quasi-static force to the sample which means that the force is applied slowly and without oscillation. In this study, a static force of 10N and a dynamic force of 0.25N was applied to the composite samples as commonly employed in a similar epoxy-based biphasic ceramic-polymer composite system [195].

The PM300 PiezoMeter has a wide frequency range of up to 50 kHz and can measure piezoelectric signals with amplitudes of up to 10 V. The device also has a high sensitivity, with a resolution of 0.1 pC and an accuracy of 1% or better. The d_{33} measurements have been take at a frequency of 110 Hz. Measurements were taken for both horizontally poled samples, ranging from 5% to 35%, and vertically poled samples, ranging from 25% to 35%.

Figure 3.19: Overview image of the PM300 Piezometer by Piezotest

Chapter 4

4. Implementation of a DOE Approach for Optimised Molten Salt Synthesised Two-Dimensional Particles

4.1. Introduction

This chapter aims to offer significant insights into the utilisation of the DOE in the molten salt synthesis process and its effective application to optimise the synthesis process of two-dimensional particles based on BNT as a case study. The chapter starts by highlighting the significance of implementing DOE in the context of MSS and emphasises the existing research gap. To the best of our knowledge, no study has been conducted to comprehensively investigate the significance of each MSS parameter, assess the combined effect of multiple parameters, identify the most influential parameter affecting particle morphology, and propose predictive models for accurately depicting the shape and size of the synthesised particles. This research gap limits the ability to achieve precise control over the synthesis process and hinders the development of optimum conditions for synthesising two-dimensional plate-like particles with enhanced electrical performance. Therefore, the chapter addresses this research gap by presenting a methodological framework for implementing DOE in MSS. Additionally, the literature background related to the assessment of ANOVA and regression models are also presented within the chapter. The chapter then proceeds by explaining the adopted experimental design approach along with the identification of the input and output variables.

4.2. The Need for DOE in MSS

As discussed in chapter 2, the dielectric properties of ceramic-polymer composites is influenced by various factors, amongst which the morphology of the incorporated ceramics is has proven to show a significant impact [212,213]. Thus, tailoring particle shape and size of the incorporated ceramic filler presents an avenue for potentially achieving enhanced dielectric properties in the resulting composites [91,260]. As such, the incorporation of two-dimensional (2D) ceramic particles, such as plate-like particles, in dielectric-based composites has been a subject of extensive research and development [261]. These particles have proven to exhibit enhanced dielectric properties and energy storage capabilities compared to 0D and 1D particles [262,263]. As mentioned earlier in chapter 2, one key advantage of such shape compared to

spherical-shaped particles for example, is the increased interfacial area between the 2D particles and the matrix, which allows for more efficient charge transfer.

It is noteworthy, that one way to control the shape and size of the incorporated powder is to manipulate the synthesis parameters within the ceramic synthesis process [11,12]. To achieve precise control over the synthesis parameters and understand their impact on the ceramic morphology, researchers often employ Design of Experiments (DOE) techniques [264–267]. DOE allows for systematic variation of multiple synthesis parameters while minimising the number of experiments required. By carefully designing a series of experiments based on statistical principles, the intricate parameter space can be efficiently explored and the optimal conditions for obtaining desired ceramic morphologies can be identified.

DOE has found extensive application in diverse synthesis techniques, such as its utilisation in the hydrothermal synthesis of bismuth titanate ($Bi_4Ti_3O_{12}$) [268] nanoparticles, where the authors aimed to examine the impact of certain key process parameters, namely temperature, reaction time, and pH, on the yield of $Bi_4Ti_3O_{12}$ nanoparticles. Furthermore, the utilisation of DOE has been observed in the optimisation of Ni-decorated ZnO nanoparticles through the sol-gel method [269]. In this particular investigation, the authors examined the influence of several parameters such as dye concentration, catalyst dosage, pH value, and Ni percentage in the Ni-decorated ZnO structure on the dye degradation process.

In this context and with the goal of synthesising two-dimensional ferroelectric ceramic particles with enhanced electrical performance for a diverse range of dielectric applications, this study aims to explore the implementation of the DOE in MSS. The first aim of this work to comprehensively investigate and identify the significance level of molten salt synthesis parameters and their combined interaction effect on the resulting shape and size of synthesised two-dimensional particles, with the ultimate objective of establishing predictive models for future MSS synthesis based on BNT as a case study.

In the quest of synthesising two-dimensional ferroelectric particles in a manner that maximises their performance in electrical applications, enhancing their applicability across a wide range of dielectric applications, this work will investigate the effect of the complex synthesis parameters on the powder characteristics. In this work, the DOE

was employed to allow for a more comprehensive understanding of the molten salt synthesis process and to help identify the optimal synthesis conditions that yield desired BNT powder characteristics, which can be used as ceramic filler in dielectric ceramic-based composites. This will effectively reduce the number of experiments needed in future MSS of two-dimensional particles, resulting in significant time and resource savings as well as providing an avenue for controlling the shape of two-dimensional plate-like particles using MSS. By employing RSM in MSS, researchers can navigate the complex parameter space of MSS, providing valuable insights into the optimal conditions required to achieve the desired particle size and shape. Once these desired characteristics are achieved, the synthesised particles can be incorporated into ceramic-polymer composites, thereby enhancing their overall performance as elaborated in chapter 2.

4.3. Methodological Framework for DOE in MSS

This section outlines the methodological framework employed for the implementation of DOE in the context of MSS of two-dimensional plate-like particles based on the BNT as a case study, as follows:

1. Selection of experimental design and identification of input and output variables:

Initially, the experimental design approach is selected, followed by the selection of input and output variables. An experimental plan is prepared based on the chosen design approach, and experiments are conducted to collect relevant data. This is presented in section 4.4. of this chapter

2. Data Analysis using ANOVA and Regression Models:

The next step entails the utilisation of the analysis of variance technique to evaluate the significance of the input parameters and their combined interaction effect. ANOVA helps determine if the observed differences in the data are due to random variation or if there are systematic effects caused by the factors being studied [270]. This analysis involves the examination of several indicators to assess the models and determine their suitability for the data. These indicators encompass the calculated P-value, obtained R^2 value, the disparity between the adjusted and predicted R^2 values, and the significance of the lack of fit. The calculation of these values was performed using the

Design Expert software built-in equations. These equations are reported in Appendix A. ANOVA results are presented throughout chapter 5.

Herein, it is worth noting that the P-value is based on an F-distribution and is a relative measure of the strength of evidence against the null hypothesis, ranging from 0 to 1 [271]. The null hypothesis, which presumes that the process parameters have no effect, is rejected when the p-value is less than 0.05 (95% confidence level) [272,273]. Rejecting the null hypothesis means that the statistical analysis has found evidence of a relationship or effect between the variables being studied. Hence, parameters with P-values ≤ 0.05 are considered significant and imply that the process parameters being tested have a significant effect on the outcome. However, the strength of evidence against the null hypothesis can be categorised as following: highly statistically significant ($P < 0.001$), strong evidence ($P < 0.01$), moderate evidence ($P \leq 0.05$), weak or poor evidence ($P< 0.1$) or insignificant ($P>0.1$) [274].

Additionally, the calculation of the coefficient of determination (R^2) would quantify the extent to which the independent variable of a regression model can account for the variability observed in the dependent variable [275]. In essence, the R^2 value is indicative of the extent to which a statistical model can effectively predict the outcome represented by its dependent variable, and generally higher R^2 values indicate a better fit between the model and the data, whereas lower R^2 values suggest that the model may not be a good fit. Therefore, assessing the R^2 value for each model helps to determine the degree of correlation between the model and the data and to evaluate the quality of the model's fit. The adjusted R^2 value considers the number of variables in the model and is a more reliable measure of the model's fit than the R^2 value alone. It penalises overfitting of the model by adjusting the R^2 value for the number of parameters in the model, thereby providing a more accurate indication of the model's goodness of fit. The difference between the adjusted and predicted R-squared values can also provide insight into the model's performance. A large difference between these values (>0.2) indicates that the model may not be reliable in predicting future observations [276], while a small difference suggests that the model is more accurate and can be used to predict future outcomes with more confidence.

By comparing the variance of the residuals within groups to the variance of the residuals between groups, the lack of fit test evaluates the model's fit. The disparities

between a dependent variable's observed values and the matching expected values from the model are referred to as residuals [277]. A substantial lack of fit test indicates that the model does not effectively fit the data and may need to be improved or modified, for as by transforming the data [278]. Analysing the results of the lack of fit test can therefore help to spot any potential model flaws and provide guidance for adjusting the model to increase its accuracy. In general, it is preferable to have a lack of fit that is insignificant.

Furthermore, by normalising the response variable's distribution, evaluating whether the data need to be transformed can help to enhance the model's fit [279]. This can be done by subjecting the data to mathematical modifications, including logarithmic or square root transformations. Common data transformations include logarithmic, square root, and reciprocal transformations, which are applied to the data based on the results of the initial ANOVA analysis [280,281]. Any problems with the distribution of the data can be identified and the necessity for data transformation can be decided by looking at the significance of the lack of fit.

Following a rigorous statistical analysis of the experimental data using ANOVA, a mathematical equation is derived to represent the underlying model. This can be depicted using a second-order polynomial equation (Equation 4.1) which is commonly referred to as a second-order response surface model, whereas the Y presents the predicted response variable [282]. Herein, the constant coefficient is expressed by b_0, the linear coefficient is b_i, the pure second order/quadratic effect is b_{ii}, the interaction coefficient is b_{ij}, the design factors are $x_{i/j}$ and the random error term is $\in$. The developed models representing the morphological characteristics of the two-dimensional molten salt synthesised particles are presented in chapter 5. These equations may be depicted by their coded values as illustrated in Equation 4.2, whereas the coded value of the ith independent variable is x_i, the uncoded value of the ith independent variable is x_i, the center point of the independent variable, ith, is represented by the uncoded value x_i^*, while the step change value, Δx_i, denotes the amount by which it is altered [283].

$$Y = b_0 + \sum b_i x_i + \sum b_{ii} x_i^2 + \sum b_{ij} x_i \, x_j + \in \qquad \text{(Equation 4.1)}$$

$$x_i = \frac{x_i - x_i^*}{\Delta x_i} \qquad \text{(Equation 4.2)}$$

3. Analysis of the Effects

The next step involved providing detailed explanation of why certain factors are considered significant while others are not. The effect of the studied synthesis parameters on the morphological characteristics as well as on the phase purity and crystallinity of the output variables were analysed and presented in chapter 6.

4. Optimisation and Validation

Subsequently, an optimisation process was conducted using a multi-objective approach, aiming to achieve the larger size and desirable shape of two-dimensional BNT particles. The optimisation process has been carried out with the aid of the Design Expert software by employing the genetic algorithm, GA. The GA is a bio-inspired computing algorithm that used to generate a set of candidate solutions and evaluate their fitness based on the objective function [284]. This meta-heuristic computational method was initially introduced by John Holland in the 1970s [285] to rapidly find nearly optimal solutions. By mimicking the natural selection process, the genetic algorithm involves the survival of the fittest individuals in successive generations, eventually resulting in a new generation of better individuals and fitter offspring.

The final step involves model validation, which is crucial to assess the reliability and accuracy of the models and their predictions. Validation includes testing the model's predictive performance on new, unseen data that was not used during model development. The objective is to ensure the model exhibits high predictive accuracy and generalises well to novel data. Optimisation and validation results are presented within chapter 6.

A schematic depicting the statistical framework employed during this work to synthesise optimum two-dimensional plate-like powder using MSS based on the case of BNT is shown in Figure 4.1.

Design Expert v 7.0.0, a powerful statistical software, was used in this research for implementing the experimental design, conducting statistical analyses, and optimising the process. The software provided a range of tools and features for designing and analysing experiments with multiple factors and levels and helped to visualise and optimise their results.

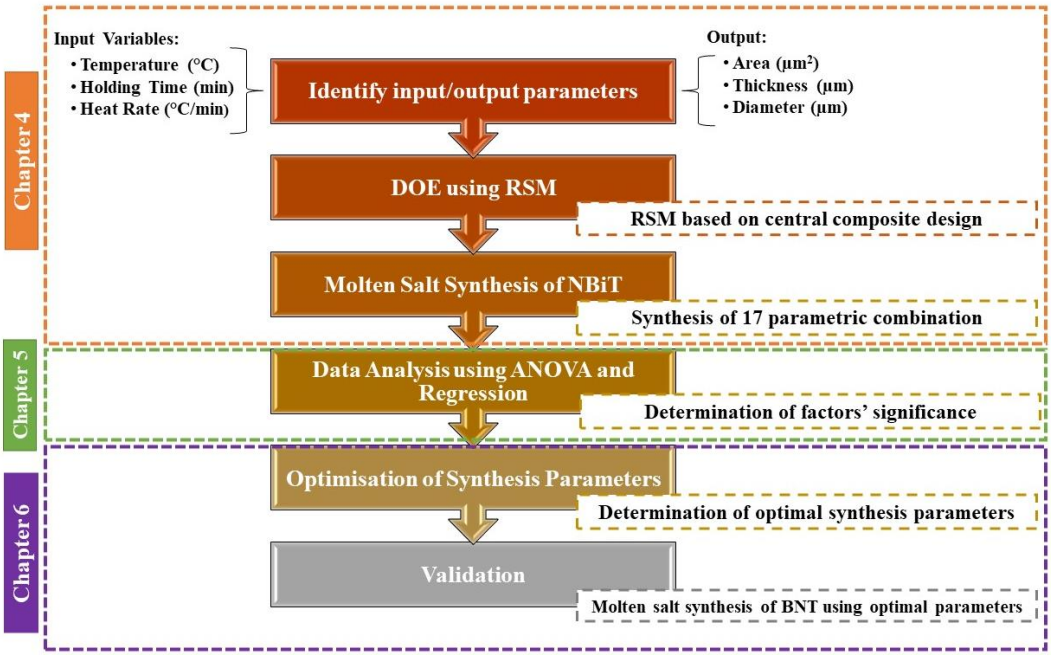

Figure 4.1: A schematic showing the methodological framework of the DOE in MSS and a detailed outline of chapter 4,5 and 6

4.4. Experimental Design

4.4.1. Experimental Design Approach

In this work, the Response Surface Methodology (RSM) was utilised to investigate the influence of the molten salt synthesis parameters on the output characteristics of the synthesised powder particles. RSM was preferred over conventional design of experiments techniques, such as the factorial design method, due to its numerous advantages [286]. Firstly, it enables the estimation of the response surface, which is a mathematical model that describes the relationship between the input variables and the response variables. This model facilitates the prediction of the response of the system for any given combination of input variables, even if the combination has not been tested experimentally. Secondly, RSM enables the identification of optimal synthesis parameters for achieving the desired response. The regions where the response is optimal can be identified, and the optimal input variables for achieving the desired response can be determined. This feature of RSM can significantly reduce the number of experiments needed to identify the optimal process parameters, thereby saving time and resources. Thirdly, RSM is capable of investigating complex nonlinear relationships between the input variables and the response variables [287]. In contrast, the factorial design method is limited to linear relationships between the input

variables and the response variables [288]. As a result, RSM is better suited for investigating complex processes with nonlinear relationships between input variables and response variables [289].

Among various experimental design approaches used in the RSM, such as Box-Behnken design [290], Plackett-Burman design [291] and D-optimal design [292], the central composite design CCD [293,294]is the one that is most commonly used [295]. This design allows for the estimation of the coefficients of a quadratic model, making it more accurate and reliable. Another advantage of CCD is that it doesn't require a three-level factorial experiment for building a second-order quadratic model, unlike other designs such as Box-Behnken. Additionally, CCD is more efficient than D-optimal design when considering the number of experiments required for a given model accuracy [295].

4.4.2. Selection of Input Parameters of MSS

As mentioned in section 4.3 of this chapter, the initial stage of the optimisation process involves the selection of key process parameters and the determination of their upper and lower levels (see Figure 4.1). As previously elaborated in chapter 2, a multitude of variables exert influence on every stage of the MSS steps as depicted in the accompanying schematic in Figure 2.16. Notably, the synthesis temperature, reaction times, and heating rates are the variables with the most significant influence on the attainment of the desired synthesised products, specifically pertaining to their morphology [135]. Therefore, in this study, three synthesis parameters were chosen as the independent input variables namely heating temperature at which the synthesis was carried out (referred to as factor A), holding time at the synthesis temperature (referred to as factor B) and heating rate to reach the synthesis temperature (referred to as factor C). These factors are known to have significant effects on the characteristics of the resulting synthesised powder. Each of these factors have been varied over three levels representing the upper, medium, and lower bound of each parameter, which are placed at one of three equally spaced levels, such as −1, 0, +1. The data representing the upper and lower limits of each factor have been selected based on literature [296–298] and are presented in Table 4.1.

Table 4.1: The range of matrix building parameters.

Parameter	Unit	Levels		
		-1	0	1
Temperature (Factor A)	ºC	850	975	1100
Holding time (Factor B)	min	90	180	270
Heat rate (Factor C)	ºC /min	3	5	7

4.4.3. Selection of Response Variables for Optimisation

The selection of response variables is a critical aspect of any experimental design, as it determines the information that can be extracted from the study. In this work, five response variables were chosen to provide a comprehensive understanding of the properties of the molten salt synthesised NBiT precursor and BNT powder and the impact of input variables on these properties. The chosen response variables were carefully selected to represent different aspects of particle size and shape, including the area of particles (denoted as R1), the thickness of the particles (denoted as R2), the Feret's diameter of the particles (denoted as R3), the aspect ratio of the particles (AR) (denoted as R4), and the overall particle size (denoted as R5). These parameters are known to be among the most widely employed descriptors to represent and characterise the morphology of two-dimensional ceramic particles [299,300]. Table 4.2 summarises the selected response variables and their denotations. By selecting these response variables, this research aims to gain a better understanding of how the molten salt synthesis parameters influence the properties of the synthesised powder and to optimise the process to achieve desirable particle characteristics.

Table 4.2: Summary of selected response variables and their denotaions

Response	Description
R1	Average area of the particles
R2	Average thickness of the particles
R3	Average Feret’s diameter of the particles
R4	Average aspect ratio of the particles
R5	Average particles’ size

The Feret's diameter (R3) is a versatile and widely used measurement parameter that provides a simple and efficient way to estimate the size of particles or objects with irregular shapes and is calculated by measuring the distance between the two points on the particle boundary that are farthest apart [301]. One of the key advantages of the Feret's diameter is that it considers the entire object's dimensions, including any

protrusions or indentations [302]. This is especially important when characterising complex shapes since other measures of size, such as diameter or radius, may not provide sufficient information. The aspect ratio, AR (R4) generally denotes the ratio between the dimension of the major axis to that of the minor axis and in plate-like shaped particles it denotes the ratio between the Feret's diameter and the thickness of the particles [303] and is an important factor in determining the anisotropy of the powder particles [304]. The first 4 responses (R1-R4) have been measured using a combination of SEM and Image J. To ensure the accuracy and reliability of the measurements, 100 particle measurements were taken for each response variable at every parametric combination. This high level of replication helps to minimise the impact of measurement errors and provides a more robust dataset for analysis. By taking multiple measurements, any random variability in the measurements can be averaged out, and a more precise estimate of the response variable can be obtained. The schematic in Figure 4.2 depicts the dimensions measurements of the first four responses. Appendix B includes bar charts depicting the spectrum of particle measurements for the first four responses obtained at each of the 17 experimental runs, along with their corresponding frequencies.

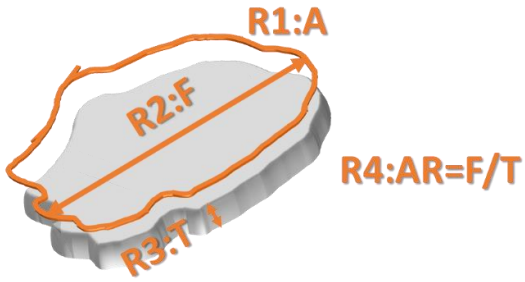

Figure 4.2: A schematic depicting the carried-out dimensions' measurements of the first responses R1-R4

With respect to the measurement of the fifth response, particles' size, this has been attained through the utilisation of the Malvern Mastersizer 3000. However, it is worth noting that the Mastersizer determines the particle size using the equivalent sphere theory. It involves defining the particle size based on the diameter of an equivalent sphere that would exhibit the same properties as the actual particle [305]. Additionally, it does not provide information about each individual particle in a sample, but rather the particle size distribution of the sample as a whole. The particle size distribution

represents the range of sizes present in the sample and is reported as a graph showing the percentage of particles at each size range.

4.4.4. Description of the Experimental Design Matrix

After selecting the input and variables for the optimisation of molten salt synthesis, a face-centred central composite design (CCD) was employed. This is commonly used when working with a three-factor design each having three different levels [306]. This design approach involves the use of both factorial points and star points. Star points are additional experimental runs that are strategically added to the design to estimate the curvature of the response surface. These points are located at fixed distance away from the centre point along each axis, with the distance determined by the value of alpha, which was set to 1 in this research. Additionally, the repetition of the centre points was selected to be 3 times. This means that the experiment will include 3 additional runs at the centre of the design, where all three factors are set to their midpoints (coded level of 0), which helps in estimating the pure error. This experimental design generated a total of 17 parametric combinations of experimental runs. Table 4.3 illustrates the breakdown of experimental runs in a face-cantered central composite design with an alpha value of 1, three centre point repetitions, and a three-level-three factors design.

Table 4.3: Breakdown of the experimental runs

Design Component	**Number of Points/Runs**
Factorial Points	8
Star Points	6
Centre Points	3
Total Experimental Runs	17

4.4.5. Data Collection

To assess the significance of the three molten salt synthesis parameters affecting the characteristics of the resulting powder and determine which parameter(s) have the greatest influence, 17 different combinations of heating conditions were employed to synthesise NBiT precursor, and their corresponding resulting responses (R1-R5) were recorded, providing a comprehensive dataset for ANOVA and regression statistical analysis. These conditions were based on the implemented CCD-RSM design matrix as illustrated in Table 4.4. As can be seen, the centre points with a heating temperature of 975^0C, holding time of 180 minutes and a heating rate of 5ºC/min, have been

repeated three times in S3, S8 and S15. This is to ensure reliability and reproducibility of the results. Moreover, the experiments have been performed in a randomised order to minimise the impact of any potential biases or confounding factors. This approach of using randomised experimental designs with central replicates is commonly employed in RSM and is considered a robust method for assessing the significance of various factors on the response of interest.

Table 4.4: The CCD design matrix for the three variable factors and their corresponding average area, average thickness, average Feret's diameter, average aspect ratio of the synthesised particles and the weighted average of particles size

Sample Number	Temperature (◦ C)	Holding Time (Min)	Heat Rate (◦ C/Min)	R1: Avg. Area (um^2)	R2: Avg. Thickness (um)	R3: Avg. Feret's Diameter (um)	R4: Avg. Aspect Ratio	R5: Weighted Avg. of Particles Size (um)
S1	850	90	7.000	2.163	0.205	1.968	9.60	69.54777
S2	850	90	3.000	1.058	0.209	1.367	6.54	8.235012
S3	975	180	5.000	3.793	0.267	2.455	9.19	8.632701
S4	1100	180	5.000	120.548	0.770	14.079	18.28	19.33197
S5	1100	270	3.000	143.853	0.833	15.764	18.92	29.01242
S6	850	270	7.000	1.500	0.139	0.827	5.95	7.153265
S7	850	270	3.000	1.688	0.149	1.460	9.80	5.902423
S8	975	180	5.000	5.105	0.290	2.927	10.09	6.410173
S9	1100	90	7.000	42.742	0.728	8.647	11.88	17.16043
S10	975	270	5.000	8.137	0.306	3.953	12.92	6.760201
S11	1100	270	7.000	168.204	1.442	17.980	12.47	19.36505
S12	850	180	5.000	1.994	0.184	1.800	9.78	11.56409
S13	975	180	7.000	7.285	0.265	3.679	13.88	6.72384
S14	1100	90	3.000	61.626	0.911	10.343	11.35	17.2548
S15	975	180	5.000	6.549	0.381	3.955	10.38	6.138999
S16	975	180	3.000	4.244	0.290	2.752	9.49	8.942408
S17	975	90	5.000	9.595	0.246	3.978	16.17	39.30668

4.5. Summary

This chapter has discussed the need for DOE in MSS and presented a methodological framework for its implementation. It highlighted how the employed RSM can be utilised to predict and optimise the size and shape of future molten salt synthesised particles. The development of these predictive models is anticipated to offer a way to tailor the morphology of the particles intended for specific applications. Moreover, the chapter has presented the fundamental basics of the RSM, statistical analysis using ANOVA, as well as the optimisation process. The chapter then delved into the detailed explanation of the selected experimental design approach, along with a demonstration of the selected input and output variables. The parametric combination of the carried-out experiments along with their corresponding responses were also presented within this chapter.

Chapter 4

5. Statistical Analysis Using ANOVA and Regression Models Results

5.1. Introduction

The primary objective of this chapter is to thoroughly analyse and investigate the collected data pertaining to the various responses, using ANOVA and regression analysis. The chapter is mainly divided into two main sections that delve deeper into the preliminary and enhanced statistical analysis. The first part presents the preliminary statistical analysis which constitutes an initial exploration of the data using ANOVA and regression modelling techniques prior to data transformation. The ANOVA analysis is initially employed to investigate the relevance of the proposed responses in characterising the shape and size of the synthesised molten salt powder. The statistical significance of the developed response models is evaluated to determine which responses (if any) should be excluded from the study. Furthermore, this preliminary analysis is essential to determine whether the models should undergo data transformation. The data transformation process involves modifying the data distribution to meet the assumptions of the statistical tests and modelling techniques used in subsequent analyses.

The second part describes the enhanced statistical analysis, providing a thorough ANOVA analysis for each of the selected significant response models after data transformation. Additionally, mathematical models were developed utilising regression analysis techniques to accurately predict characteristics of the synthesised powder. The adequacy of developed models and their performance analysis are confirmed by conducting residual analysis as well as comparing actual values with predicted ones in both preliminary and enhanced statistical analyses.

5.2. Preliminary Statistical Analysis (Before Data Transformation)

This section presents the results of the preliminary initial statistical analysis.

5.2.1. Preliminary ANOVA and Regression Analysis

Following the data collection for each of the five responses at each parametric combination (presented in

Table 4.4 in chapter 4), the data for each of these five responses were analysed using ANOVA and regression analysis, leading to the development of five distinct models. Each model depicts the impact of the individual factors (MSS parameters) and their combined interaction effect on the corresponding response and identifies the most significant one (s). As a part of the analysis procedure, the Design Expert software recommends the most suitable model for fitting the data by suggesting the order of the polynomial before moving to ANOVA step. Herein, at this first step, the results of the data analysis indicated that a quadratic fit was appropriate for each of the five responses. The appropriateness of the quadratic fit suggests that the variables being studied have a nonlinear relationship with the corresponding responses and that the quadratic model is better suited for describing this relationship.

The resulting P-values, R^2 values, the adjusted and predicted R^2, and the significance of the lack of fit for each model (response) are tabulated in Table 5.1. Detailed ANOVA tables for the initial model's analysis are reported in Appendix C.

Table 5.1:Summary of the five response models' results

Response Variable	Model		R^2	Adj. R^2	Pred. R^2	Lack of fit		Recommended Trans
	P-Value	Significance				P-value	Significance	
R1	0.0002	significant	0.97	0.93	0.7	0.0061	significant	Natural log
R2	0.0016	significant	0.95	0.91	0.53	0.1407	not significant	Sqrt
R3	< 0.0001	significant	0.98	0.95	0.74	0.2575	not significant	Sqrt
R4	0.21	not significant	0.7	0.33	-0.7	0.0302	significant	None
R5	0.065	not significant	0.85	0.65	-1.3	0.0143	significant	None

The results in Table 5.1 showed that among the five models depicting five responses, only R1, R2, and R3 were statistically significant with P-values of less than 0.001 [307]. R1 shows a high R^2 value of 0.97 (close to 1), indicating a good agreement between the experimental data and the model predicted results. However, the difference between the predicted and adjusted R^2 is more than 0.2, which suggests that

there might be overfitting of the model to the training data [308]. This can lead to the model performing well on the training data (actual current collected data) but poorly on new data. Generally, a difference of less than 0.2, indicate a good agreement between the two and further signify the strength of the model [309]. It is also worth noting that although R1 has a high R^2 value, the lack of fit for this response is yet significant. This suggests that while the model can explain a large portion of the variability in the response variable R1, it does not fit the data well overall, meaning that that the model does not accurately capture the behaviour of the response variable. Therefore, while the model may provide a good prediction for certain portions of the data, it may not be reliable for predicting the behaviour of the response variable as a whole. Thus, a transformation to a natural log based-equation model was suggested by the software based on the calculated skewness and lack of normality of the data, to address the lack of fit and improve the model's performance [281,310,311]. This observation aligns with the findings of S. Foorginezhad et al. [312] during the employment of the RSM technique to optimise the operational parameters affecting the color removal of cationic dyes, where a data transformation was performed upon a significant lack of fit. In a recent study by Raziyeh Ghelich et al. [313], the researchers utilised the CCD-based RSM to even examine the influence of various process variables such as PVP concentration, applied voltage, flow rate, and boron-to-hafnium ratio, among others, on crucial output parameters such as the average diameter, quality, and uniformity of the nanofibrous PVP-B-Hf composites. Herein, the lack of fit was found to be statistically significant, indicating the need for further refinement in representing the relationship between the response and test variables. To address this, the authors employed an inverse square root transformation to better capture the complex interplay between the response variables and the experimental factors.

Furthermore, R2 has a P-value of 0.0016 indicating that the model itself is significant. The high R^2 value of 0.95, suggests that the model's predicted results align well with the experimental data. However, the difference between the predicted and the adjusted R^2 is more than 0.2, which suggests that the model may not generalise well to new data or may be overfitting the current data. Therefore, it is important to consider both the R^2 and the lack of fit in evaluating the performance of a model. In this case, a transformation to a square root based model is still needed even if the lack of fit is insignificant [314,315], to improve the model's ability to generalise to new data or to

avoid overfitting. Similarly, R3 has a significant P-value and also the variation between adjusted an predicted R2 was marginally higher than 0.2. Although the lack of fit tested for insignificance, a transformation of the data to a square root-based model was still suggested to enhance the model's performance. This recommendation is supported by the large difference between the predicted and adjusted R^2 values, which suggests that the current model may not generalise well to new data.

In opposite to the first three responses, R4 and R5 were not significant, with P-values of 0.21 and 0.065, respectively. This suggests that the predicted models for R4 and R5 does not provide strong evidence that the predictor variables (MSS synthesis parameters) have a statistically significant effect on the response variable. R4 had an R^2 value of 0.7, indicating a moderate correlation between the response variable and the model. However, the adjusted and predicted R^2 values were lower at 0.33 and -0.7, respectively. Additionally, the lack of fit test for R4 shows as significant, which indicates that the model does not fit the data well for that particular response variable. This could be due to several reasons such as inadequate model specification, incorrect assumption of error distribution, or insufficient variation in the data. Since the model itself was found to be insignificant, no specific data transformation was suggested for R4.

Similarly, the R5 had an R^2 value of 0.85, indicating a moderate correlation between the average particles' size as a response variable and the model-predicted results. As observed, the predicted R^2 value for R5 is an unusual negative value of -1.3 which suggests that the model is performing worse than a constant function that always predicts the mean of the data. This indicates that the model is not providing any improvement over simply taking the average value of the response variable. A negative R^2 value is a clear indication that the model is not a good fit for the data and needs to be revised or replaced with a different approach. Furthermore, there is a significant lack of fit, indicating the inadequacy of fitting to the model and hence no data transformation was proposed.

5.2.2. Preliminary Residuals Analysis

To gain a more comprehensive understanding of the results and the developed models, this section employs various plots, such as predicted versus actual plots and residuals versus predicted plots, to assess the performance of the developed models and to

identify potential issues with the data. The predicted versus actual plots depict the relationship between the actual values and the predicted values for each response variable, enabling an assessment of how well the regression model fits the data. Additionally, the residuals versus predicted plots complement the predicted versus actual plots by identifying whether the model has any consistent bias or deviation in the measurements or observations from their true value. Herein, the horizontal axis of the plot represents these predicted values, and the vertical axis represents the residuals. By analysing these plots, it is possible to identify discrepancies between the predicted and actual values, as well as detect any patterns or trends that may be present in the data, such as overestimating or underestimating the actual values.

In this work, the actual vs predicted along with predicted vs residuals plots have been constructed for the five responses. The plots for each response are as follows:

Response 1

Figure 5.1 (a) shows the actual vs predicted plot for the average area of the particles in the 17 experiments. Each point on the plot represents a data point from the 17 designed experiments. Figure 5.1 (b) offers a closer view of the plot, providing a more detailed understanding of the graph, as such the data on the straight line represent the model's predicted values whilst the square point near the line represent the actual (experimental) values and the difference between them is the residual. It is evident from Figure 5.1 (a), that the actual points are scattered near to the straight line. This could suggest that the developed model (in Appendix A) can reasonably describe the relationship between the molten salt synthesis parameters and the area of the particles [316,317]. However, the negative values of the predicted responses (seen on the plot) complement the significant lack of fit that was exhibited during the ANOVA testing. Figure 5.1 (c) illustrates a plot of the ascending predicted response values versus their corresponding residuals. The data points are roughly equally distributed on both sides of the zero residual, indicating that the model is not biased and is not systematically over- or under-predicting the response variable. The negative values of the residuals indicate that the predicted values are larger than the actual values. Additionally, the data points are randomly scattered around the zero residual which suggests a consistent variance across all experiments. The residual vs. predicted response plot presents a scenario where the residuals exhibit a random dispersion, suggesting a consistent

variance across all experiments [318,319]. However, it was suggested previously that the data transformation would develop a better performing model.

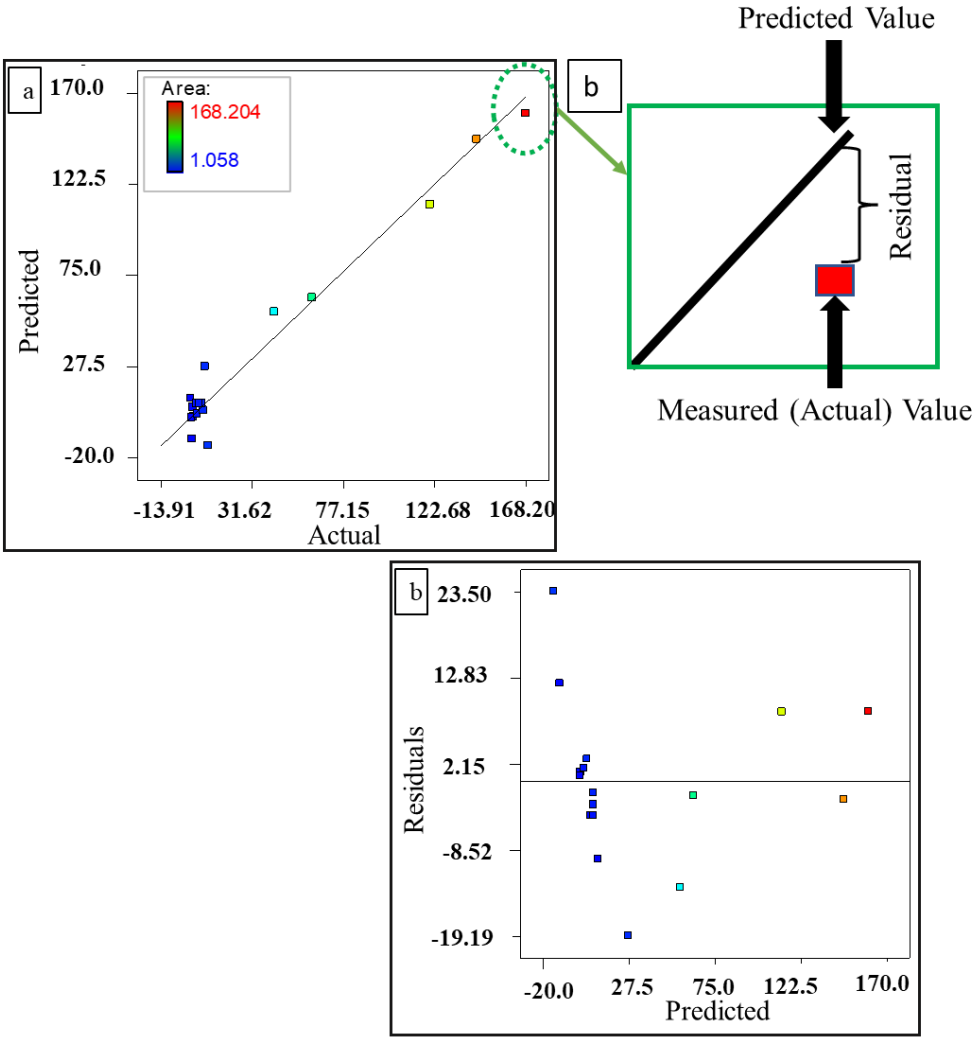

Figure 5.1: (a) The predicted vs actual plot for R1, (b) close-up view of the predicted vs actual plot providing a detailed explanation of the data presented and (c) the residuals vs predicted plot for R1; before data transformation

Response 2

The predicted versus actual plot of the second response model (in Figure 5.2 (a)), which portrays the average thickness of the particles, exhibits a pattern akin to that of the first response model. Specifically, the data points in both models are dispersed near the straight line, suggesting a high degree of concordance between the predicted and actual values [320]. Figure 5.2 (b) displays the predicted versus residual plot of the second response model, which further illuminates the model's performance. The plot reveals that the data points are distributed across both sides of the zero residual line, but the residual values tend to be greater for higher data points (e.g., above 0.75). This

phenomenon suggests that the model's predictions may have a greater degree of error or deviation for higher particle thicknesses. This observation may warrant further investigation into the bias in the model's design, such as data transformation.

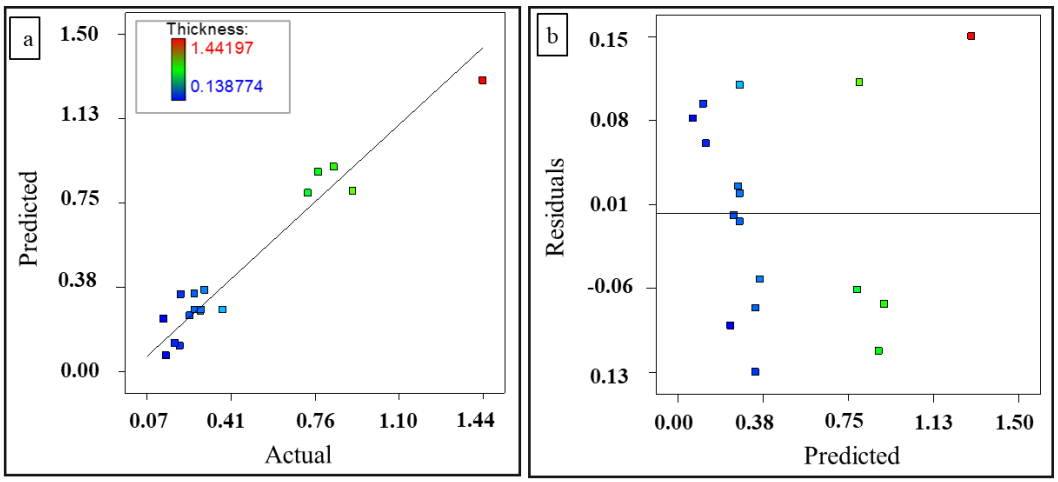

Figure 5.2: Plot of the (a) actual vs predicted and (b) residuals vs predicted for R2 before data transformation.

Response 3

Similarly, the actual vs predicted plot depicting the third response (Figure 5.3) displays a favourable distribution of data points near the line of best fit. Figure 5.3 demonstrates the predicted vs residuals plot. As can be observed, there's a random scattering of data points on both sides of the zero residual line which indicates again that the model is making unbiased predictions. It is evident that the highest residuals are depicted at lower values. This suggests that the model is overestimating the values in this range. Hence, data transformation is needed.

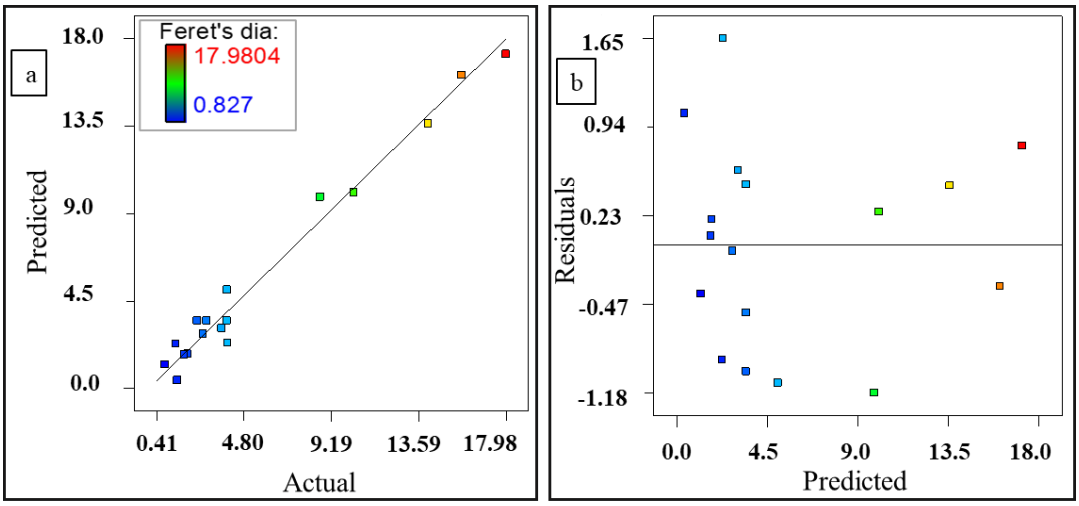

Figure 5.3: Plot of the (a) actual vs predicted and (b) residuals vs predicted for R3 before data transformation.

Response 4

In contrast to the favourable performance of the developed models in predicting the first three responses, the data points on the predicted vs actual plot of the fourth response (Figure 5.4) display a noticeable deviation from the line of best fit. Specifically, the data points are not distributed near the line, indicating that the model's predictions for the fourth response are less accurate than those for the earlier responses. This complements the fact that the model was tested as insignificant during the ANOVA analysis. Figure 5.4 (b) illustrates the scatter of the data points of the residuals against their corresponding predicted values.

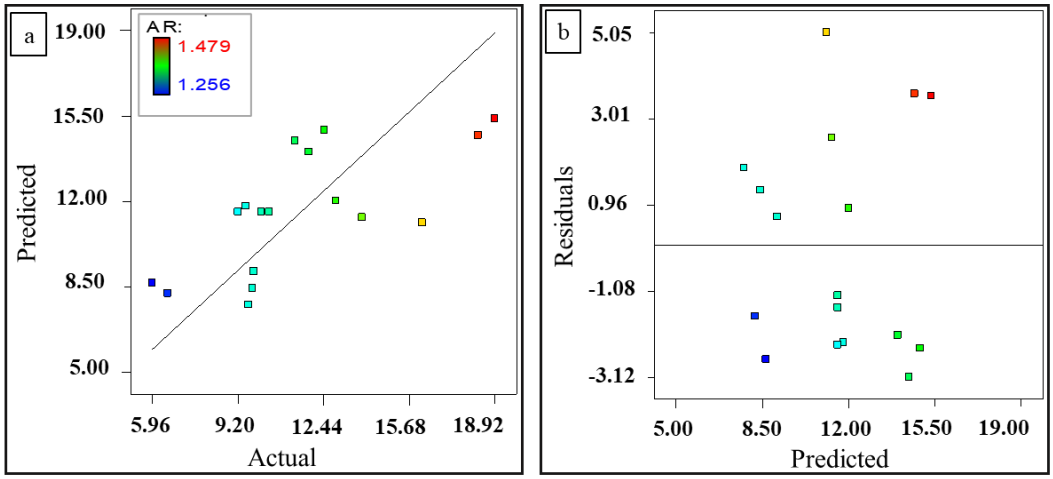

Figure 5.4:Plot of the (a) actual vs predicted and (b) residuals vs predicted for R4 before data transformation.

Response 5

Moreover, the actual versus predicted plot for the fifth response (Figure 5.5) exhibits a greater degree of randomness in the distribution of the data points, in contrast to the first three responses, suggesting inadequacy of the model [321]. Additionally, the residuals vs predicted plot (in Figure 5.5 (b)) shows higher degree of residuals for more data points, compared to the degree of residuals of the first three responses.

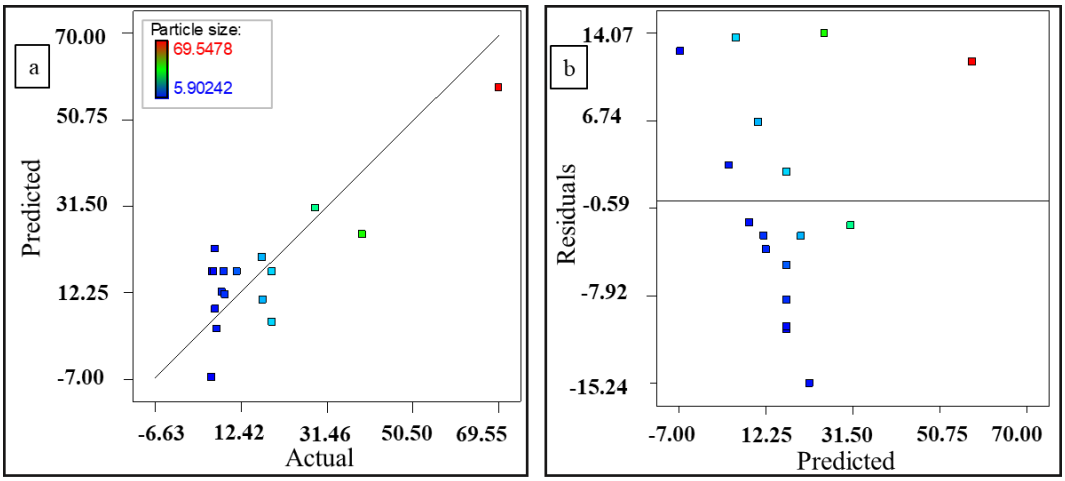

Figure 5.5: Plot of the (a) actual vs predicted and (b) residuals vs predicted for R5 before data transformation.

5.2.3. Preliminary Statistical Analysis Conclusions (Refining Responses)

The ANOVA results obtained in the previous subsection have confirmed the significance of responses R1, R2, and R3 within the study. These responses have been found to be influential in determining the characteristics of the synthesised NBiT powder particles, and the developed models have adequately captured the underlying relationships between the molten salt synthesis parameters and the corresponding responses. Consequently, the models' significant p-values indicate a statistically significant relationship between the dependent variable and at least one independent variable in the model. Moreover, as highlighted in the previous subsection, the current developed models are suggested to undergo data transformation to enhance the performance of the models. Hence, the next section will illustrate the ANOVA and regression analysis results of the models after transformation.

On the other hand, the lack of significance of R4 and R5 suggests that the null hypothesis cannot be rejected. This implies that there is insufficient evidence to support the hypothesis, which presumes that the molten salt synthesis parameters have a significant effect on the studied output response. In simpler terms, the response

models representing the AR and particle size of the synthesised particles do not provide a complete description of the relationship between the synthesis parameters and the studied output. Therefore, it can be inferred that these response models are not suitable for comprehensively characterising the properties of the synthesised powder or the impact of the synthesis parameters on the output.

Indeed, the shape of the synthesised particles may be quantitively measured using the AR of the particles and has been extensively used to describe particle morphology. However, a definite connection between the synthesis parameters and the AR remains unclear. By referring to Table 4.4 in chapter 4, it can be observed that at a temperature of 1100°C, for instance, the AR ranges from a high of 18.92 (S2) to a low of 11.35 (S14). Additionally, higher AR values were also observed at relatively lower temperatures, such as 16.17 at 975°C (S17).

The lack of significance of R4 in the response model could be attributed to the limited ability of the AR of a particle to fully characterise its size and shape as a function of synthesis temperature, holding time and heating rate. It may also be attributed to the findings that the models of the second and third responses, namely thickness and diameter were significant and could effectively capture the relationship between the synthesis parameters and the corresponding variables. Hence, any modifications in the synthesis parameters would alternate the responding thickness and diameter. Since the AR is the ratio of edge length to thickness, thus the AR may remain unchanged if thickness and diameter changed as a result of changing synthesis parameters. In other words, while modifications in the synthesis parameters have a clear impact on thickness and diameter (significant models), the AR is determined by the relationship between these two variables. Therefore, if changes in thickness and diameter occur simultaneously and in a manner that maintains a consistent ratio between them, the AR will remain relatively constant despite variations in the synthesis parameters. Even in cases where changes in thickness and diameter do not occur in a consistent manner, it is possible that their individual effects on the AR may still not be significant and thus the AR may not be sensitive enough to directly reflect changes of the herein studied synthesis parameters.

In the case of R5, insignificance of the model depicting the particle size based on the impact of various synthesis parameters could be attributed to the limitations of the

measurement technique used to collect the data. Specifically, the use of a mastersizer to measure particle size may not provide an accurate representation of the actual size of the synthesised particles. As the mastersizer employs the concept of the nearest sphere to estimate the particle size, an actual numerical value for the size of the particles may not be provided. As a result, the data collected from the mastersizer may not be an adequate representation of the true size of the particles, and therefore, may not be insufficient to fully depict the impact of the synthesis parameters on the particle size. Additionally, the use of mastersizer may be further limited by the potential formation of particle agglomerates during synthesis. In such cases, the mastersizer may misinterpret these agglomerates as single, larger particles, leading to inaccurate measurements of particle size.

As a result, the scope of this research will solely focus on optimising the first three response variables, while excluding R4 and R5 from further analysis.

5.3. Enhanced Statistical Analysis (After Data Transformation)

5.3.1. ANOVA for Area of the Particles (R1)

The dataset pertaining to the first response model was subjected to additional data processing through natural logarithmic data transformation (using the Design Expert software), as recommended during the preliminary ANOVA analysis. Subsequently, the transformed model was subjected once more to ANOVA to assess its significance and determine the variables that exert the most significant influence on the area of NBiT particles. The ANOVA results for R1 are presented in Table 5.2. The F-values in the table indicate the significance of the effect of the respective variables and their interactions on the considered response. (The more the F-value exceeds 1, the larger are the effects on the response). F-value is calculated using the sum of squares (SS) and mean square values [322]. The (df) is the degree of freedom and represents how many values are free to vary or be chosen without violating any constraints or restrictions imposed by the data or the statistical model and is taken into account when calculating the P-value [323]. It is worth noting that the table presents only the results for the significant model terms, those factors with insignificant impact, i.e., P-values > 0.05, have been eliminated from the model as commonly done in RSM [324–326].

Table 5.2: ANOVA for particles average area

Source	SS	df	MS	F-Value	P-value	
Model	44.41	4	11.1	96.13	< 0.0001	significant
Factor A	41.27	1	41.27	357.37	< 0.0001	
Factor B	0.46	1	0.46	4.02	0.0681	
AB	0.56	1	0.56	4.85	0.048	
A^2	2.11	1	2.11	18.3	0.0011	
Residual	1.39	12	0.12			
Lack of Fit	1.24	10	0.12	1.65	0.435	not significant
Pure Error	0.15	2	0.075			
Cor Total	45.79	16				

R^2	0.9697
Adj R^2	0.9597
Pred R^2	0.9396
Adeq. Precision	24.917

The results indicate that the model is significant overall, as indicated by a very small p-value of less than 0.0001 and an F-value of 96.13. This means that at least one of the molten salt synthesis parameters predictors in the model is significant in explaining the variability in the R1. Additionally, the lack of fit with a p-value of more than 0.05 also confirms the fitting of the data into the proposed model. The insignificant lack of fit indicates that the regression model does adequately describe the functional relationship between the affecting (experimental synthesis parameters) factors and the area of the synthesised particles.

Based on the obtained values in Table 5.2 it is evident that the synthesis temperature (factor A) is the most significant factor affecting the average area of the particles with a p-value of less than 0.001 and the highest F-value. Holding time (factor B) with a p-value >0.05 and yet less than 0.1, shows weak evidence against the null hypothesis, however it has not been eliminated from the model as its corresponding interaction with term A is less than 0.05. The interaction between the temperature and the holding time (factor AB) shows a significant effect on the area of the particles with p-value less than 0.05. Consequently, it has been concluded that although the holding time factor individually (separately) does not have a significant effect on the average area of the particles, but the simultaneous effect of the time and temperature shows significant effect on the process output. The main effect of the heat rate (factor C) and the effect of its combined interaction with the two other factor, i.e., AC and BC showed

insignificant effects with p-value >0.1 and have been hence eliminated from the model. Finally, the A^2 term has a significant effect on the response variable, with an F-value of 18.3 (p = 0.0011), that the quadratic effect of A-Temperature is significant and that the relationship between the A-Temperature and the area of the NBiT is not linear.

The obtained R^2 value is 0.97 which is close to 1, indicates an excellent agreement between the experimental data and the model predicted results. Further, the difference between the predicted and the adjusted R^2 is less than 0.2 which shows that there is a fair agreement between the two and hence signifying the strength of the model.

The model has then been formulated as a function of the affecting factors, in this case the synthesis temperature, the holding time at that synthesis temperature and their interaction. Equation 5.1 presents the (predicted) average area of the particles as a function of the heating temperature (A) and the holding time (B). The coefficients of the varying factors in the equation are denoted by their coded values according to Equation 4.2 of chapter 4. Once more, it is evident from the developed equation that factor A imposes the largest impact on the area of the particles, whilst factor B has the least impact. The positive sign in this equation indicates the interdependency of the factors on the output response, so it can be concluded that more heating temperature and more holding time would result in larger particles area. Details of how the factors and their interaction affect the resulting response, along with corresponding contour and 3D plots are further explained in Chapter 6.

$$\text{Ln Area} = +1.80 + 2.03xA + 0.22xB + 0.26xAxB + 0.72xA^2 \qquad \text{(Equation 5.1)}$$

5.3.2. ANOVA for Thickness of the Particles (R2)

The model of the second response, representing the average thickness of the particles and its relationship with the various process parameters, was subjected to ANOVA. Table 5.3 below presents the ANOVA results for the second response. In this model, factors (model terms) such as B, C, B^2, C^2, BC and AC have been excluded due to their insignificance with P-value of >0.1. As can be seen, the model F-value of 52.5 implies that model is significant. The insignificant lack of fit implies that the proposed model fit the experimental data and that the independent process parameters have considerable effects on the output response. Results reveal that the second response is also most significantly impacted by the synthesis temperature. Similar to R1, herein

the (main effect) of each the holding time and the heating rate have no impact on the average thickness of the particles. Yet, the combined interaction effect between the holding time and the heating temperature tends to have significant effect on the average thickness of the particles with a P-value of 0.027. The resulting R^2 corresponding to this model is 0.946, indicating a fair agreement between the experimental data and the predicted results. As opposed to the observation made for R2 prior to data transformation (see Table 5.1), it is evident that after data transformation (see Table 5.3), the difference between predicted and adjusted R^2 for R2 is less than 0.2, highlighting the model's strength.

Table 5.3:ANOVA for average thickness of the particles

Source	SS	df	MS	F-Value	P-value	
Model	0.87	4	0.22	52.50	< 0.0001	significant
Factor A	0.73	1	0.73	176.72	< 0.0001	
AB	0.026	1	0.026	6.34	0.0270	
A^2	0.093	1	0.093	22.57	0.0005	
Residual	0.050	12	4.1 E-003			
Lack of Fit	0.044	10	4.4E-003	1.56	0.4526	not significant
Pure Error	5.6E-003	2	2.8E-003			
Cor Total	0.92	16				

R^2	0.9459
Adj R^2	0.9279
Pred R^2	0.8541
Adeq. Precision	21.510

The relationship between the model factors and the resulting average thickness of the particles is formulated in Equation 5.2. The developed model equation indicates that the synthesis temperature and holding time at that temperature work synergistically to affect the average thickness of particles, with a positive correlation. Additionally, it is evident from the equation that the synthesis temperature has a more significant influence on average particle thickness than the holding time and the heating rate individually.

$$\text{Sqrt (Thickness)} = +0.54 + 0.27xA + 0.057\ xAxB + 0.15xA^2 \qquad \text{(Equation 5.2)}$$

5.3.3. ANOVA for Feret's Diameter of the Particles (R3)

The ANOVA results for the average Feret's diameter of the particles are presented in Table 5.4. The model is statistically significant with a p-value of less than 0.0001. Based on the obtained results presented in the table, it can be inferred that both factor A and factor B along with their simultaneous interaction effect have an impact on the Feret's diameter of particles; however, they demonstrate different levels of significance. Notably, the synthesis temperature appears to exert the most significant effect on the Feret's diameter of the synthesised particles, compared to the main effect of the holding time and heating rate. It can be inferred that while the holding time exhibits moderate evidence of statistical significance with a p-value of less than 0.05, the simultaneous interaction effect of the synthesis temperature and the holding time, demonstrates a higher level of statistical significance in influencing the average Feret's diameter output and hence concludes that the combined interaction effect (AB) is the second most significant factor affecting the resulting Feret's diameter. Insignificant model terms, i.e., the main effect of factor C, the combined effect of AC and BC have been eliminated from this model due to their insignificant impact, which were obtained using the Design expert software. The lack of fit for R3 was found to be insignificant, which indicates that the model is a good fit for the data, and that the model adequately describes the relationship between the response variable and the independent variables.

Table 5.4: ANOVA for average Feret's diameter of the particles

Source	SS	df	MS	F-Value	P-value	
Model	17.05	4	4.26	112.79	< 0.0001	significant
Factor A	14.61	1	14.61	386.63	< 0.0001	
Factor B	0.25	1	0.25	6.72	0.0236	
AB	0.79	1	0.79	20.81	0.0007	
A^2	1.40	1	1.40	37.00	< 0.0001	
Residual	0.45	12	0.038			
Lack of Fit	0.36	10	0.036	0.79	0.6780	not significant
Pure Error	0.092	2	0.046			

R^2	0.9741
Adj R^2	0.9655
Pred R^2	0.9461
Adeq. Precision	28.879

Additionally, the model's corresponding R^2 is 0.974, hence implying an excellent agreement between the experimental data and the predicted resulting output. The

adjusted and predicted R^2 differences are less than 0.2, indicating the robustness of this model.

Based on the regression analysis, the equation that describes the model is illustrated in Equation 5.3. The Feret's diameter is expressed in terms of the heating temperature, the holding time and their combined simultaneous effect. Factor A with the largest coded coefficient imposes the most significant influence on the Feret's diameter, whilst the simultaneous effect of both factors A and B together show the second largest significance level on this model.

$$\text{Sqrt (Feret's diameter)} = +1.83 + 1.21xA + 0.16xB + 0.31xAxB + 0.58xA^2 \quad \text{(Equation 5.3)}$$

5.3.4. Enhanced Residuals Analysis

The plots in Figure 5.6 illustrate the actual vs predicted plots for the three response models following (after) data transformation. It is apparent that the observed points on all three plots are distributed close to the diagonal regressed line representing predicted data, signifying that each of the developed models can adequately depict how synthesis parameters influence various responses examined in this study, thereby indicating successful model development. Furthermore, in contrast to the actual versus predicted plot for R1 prior to data transformation (Figure 5.1), where negative values were observed for the predicted values, the current analysis of R1model after data transformation reveals that all the predicted values are presented as positive values, indicating logical outcomes. The actual vs predicted plots are commonly utilised in conjunction with optimisation using RSM. The herein developed plots exhibit strong concordance with actual versus predicted plots for optimisation of other synthesis processes such as in sol-gel synthesis [327,328] and in hydrothermal synthesis [329,330], thereby substantiating the agreement between the actual and predicted outcomes.

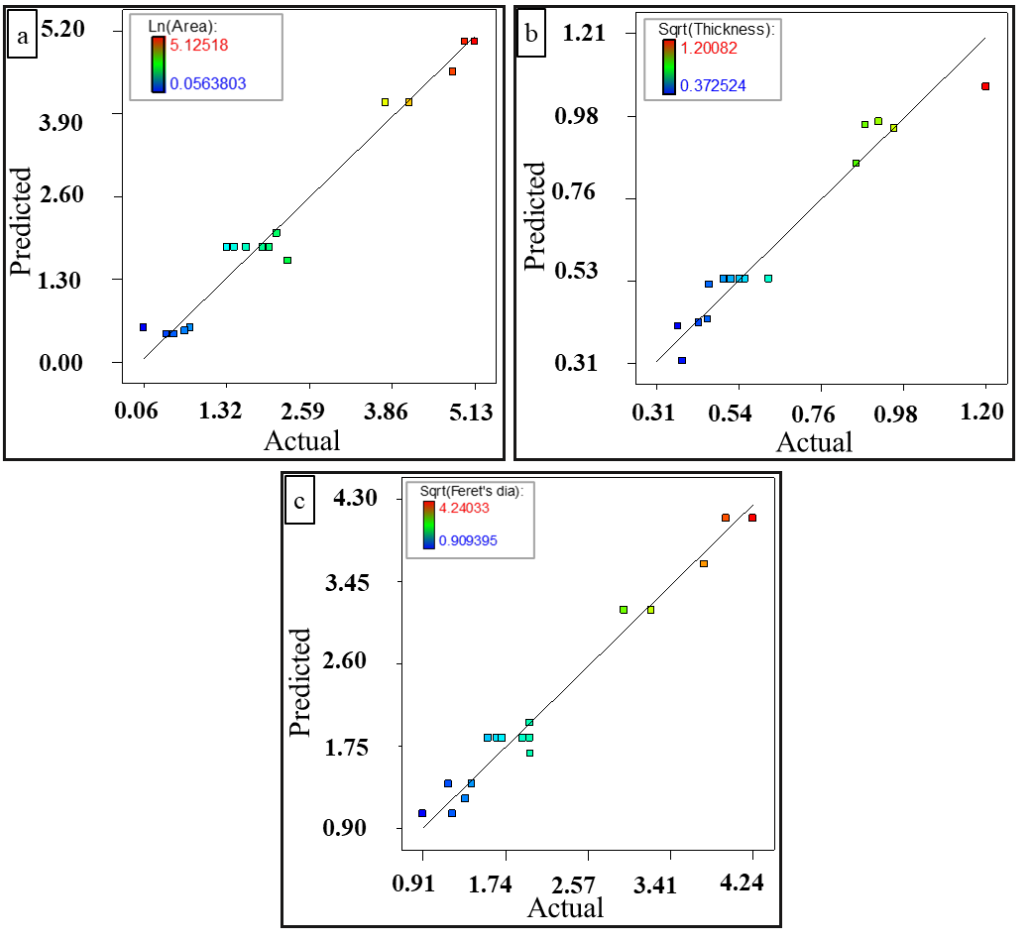

Figure 5.6: The predicted vs actual plot for (a) R1, (b) R2 and (c) R3.

5.4. Summary

This chapter provided a thorough analysis of the influence of individual parameters involved in molten salt synthesis (factor A, B and C) and their combined interaction effect on the properties of the synthesised NBiT particles (R1-R5). The ANOVA technique has been employed to establish statistical significance for both the main effects and the simultaneous interaction effect of the synthesis parameters, while also identifying the most crucial one(s) for optimum particle's synthesis. A preliminary ANOVA analysis revealed that the AR (R4) and particle size (R5) models were insignificant, indicating that they were not sufficient in elucidating the effect of the synthesis parameters on the output response and have been excluded from this research. Furthermore, during the analysis, a data transformation was suggested for the first three responses. After the data transformation of the first three responses, the transformed models were subjected to the ANOVA again resulting in enhanced ANOVA analysis. The obtained R^2 values for the area (R1), the thickness (R2), and the Feret's diameter (R3) were 0.97, 0.95, and 0.97, respectively. The R^2 values being

close to 1 indicated a strong agreement between the experimental data and the model's predicted output. The differences between the adjusted and predicted R^2 values were less than 0.2 for all three responses, further signifying the robustness of the developed models. The ANOVA analysis revealed that the synthesis temperature was the most significant factor affecting the three responses depicting the size and shape of molten salt synthesised powder. The main effect of the holding time was found to be moderate to poor on particle area, significant on Feret's diameter, and entirely insignificant on particle thickness. The heating rate has proven to be insignificant on all three models. Interestingly the combined effect of the synthesis temperature and the holding time emerged as the second most influential factor impacting all three responses. The insights gained from this chapter shed light on how DOE can be effectively employed to optimise molten salt synthesis processes, anticipate output characteristics of synthesised powder, and enhance its applicability. Chapter 6 provides a detailed account of the underlying reasons why certain factors have been deemed significant, while others have not.

Chapter 6

6. Investigation of the Effects of MSS Parameters: Analysis, Optimisation and Validation

6.1. Introduction

This chapter focuses on ANOVA findings and associated models for determining the shape and size of particles synthesised via the molten salt method. To establish a thorough comprehension of the ANOVA results pertaining to the influence of synthesis parameters on the morphology of synthesised powder, this chapter explains detailed analysis of the underlying reasons and mechanisms governing the impact of these parameters on particle morphology. The chapter initially analyses the significance of these parameters on the phase purity of the synthesised powder by investigating the obtained XRD patterns. Further, the chapter elaborates on the effect of each parameter on the area, thickness, and Feret's diameter of the NBiT powder, thereby emphasising the importance of considering these parameters to control the size, shape, and purity of future two-dimensional plate-like particles' synthesis based on BNT as an example. The chapter concludes with an optimisation analysis that presents the obtained optimum synthesis parameters to achieve optimally synthesised BNT powder. Furthermore, the validation of the models used for the optimisation is presented, demonstrating that all three models were successfully validated, and the actual results matched reasonably well with the predicted ones.

6.2. Synthesis Parameters Effects on Crystal Phase Composition

The validation of phase purity within the molten salt synthesised samples represents an integral component of the analysis process, alongside the presentation of ANOVA results. By assessing the X-ray diffraction patterns of the 17 samples, any possible multi-phase compositions can be identified. This is essential, as the presence of multiple phases could be indicative of suboptimal synthesis conditions or insignificant synthesis parameters. Figure 6.1 illustrates the XRD pattern of 17 different synthesised NBiT precursor samples arranged in ascending order of synthesis temperature, with a closer view of the 109 diffraction peaks. The XRD analysis reveals that the peaks in the diffraction pattern of the 17 samples synthesised using various synthesis conditions are consistent with the tetragonal phase of $Na_{0.5}Bi_{4.5}Ti_4O_{15}$, as documented in the PDF card no. 01-074-1319. The absence of any additional peaks in the pattern indicates the presence of a single-phase material. This observation can be attributed to the structural homogeneity of the samples and is a clear indication of successful phase pure NBiT

precursor synthesis. The crystal structure of the matching tetragonal $Na_{0.5}Bi_{4.5}Ti_4O_{15}$ belongs to space group 14/mmm, with lattice parameters a (Å): 3.84, b (Å): 3.84, and c (Å): 40.75.

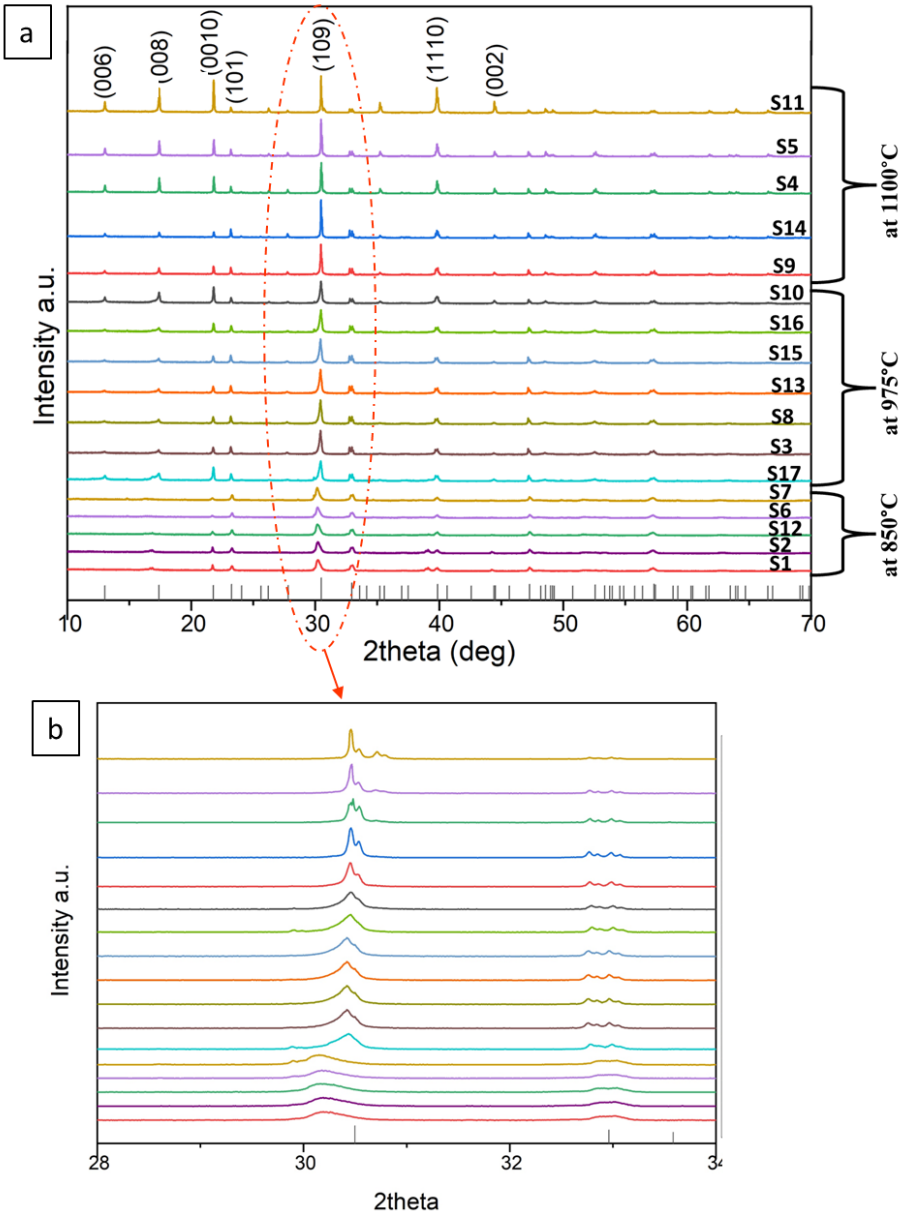

Figure 6.1: (a) X-ray diffraction (XRD) pattern of 17 NBiT precursor samples arranged in ascending order of synthesis temperature, and (b) a closer view of the 109 diffraction peaks

A clear trend between the synthesis temperature and the broadening and intensity of the peaks is observed in Figure 6.1 (a), whereas an increase in the synthesis temperature from 850°C to 1100°C generally resulted in higher intensity and narrow diffraction peaks. Since peak intensity in an XRD pattern corresponds to the number of atoms in the crystal that contribute to that diffraction angle, a higher peak intensity

indicates a larger volume of the material in that specific crystallographic orientation [331]. As the temperature increases, there is an increase in the mobility of atoms within the crystal structure leading to a higher rate of nucleation and crystal growth. This results in larger, well-defined crystals with fewer defects and disorder. When these crystals are subjected to XRD, the atoms within the crystal lattice scatter the X-rays, producing a distinct pattern of diffraction peaks. Hence, when the temperature is increased, more atoms contribute to the diffraction peaks, resulting in higher peak intensities and indicating a higher degree of crystallinity. Additionally, the narrower peaks observed in the XRD pattern synthesised at relatively higher temperatures, i.e., 975^{o}C and 1100^{o}C suggest that the crystal size is larger. This is because the broadening of the peaks has been proven to be inversely proportional to the size of the crystallites, according to the Scherrer's equation [331,332]. On the other hand, the XRD pattern for the samples synthesised at 850^{o}C did not exhibit any discernible diffraction peaks. This observation can be interpreted in two ways: the material may consist of ultrafine particles, or it may be in an amorphous phase. In other words, the lack of diffraction peaks suggests that the material has no long-range order, which could be due to the small size of the particles or their amorphous nature. This finding highlights the importance of carefully controlling the synthesis temperature to obtain materials with the desired crystalline structure and properties.

It is also noteworthy that those sample synthesised at the same temperature of 1100^{o}C, yet with varying holding time and heating rate such as S9 [1100^{o}C; 90 min; 7^{o}C/min], S14 [1100^{o}C;90min; 3^{o}C/min], S4 [1100^{o}C; 180min; 5^{o}C/min], S5 [1100^{o}C;270 min, 3^{o}C/min] and S11 [1100^{o}C; 270 min; 7^{o}C/min] , did not exhibit any significant difference in peak intensity and broadening as can be observed in the relevant XRD pattern in Figure 6.1. This comparable peak broadening behavior further implies that the crystallite size distribution was similar even though the holding time and heating were altered while maintaining a constant synthesis temperature as the peak broadening is generally dictated by the crystallite size [333]. The insignificant influence of the holding time on the XRD pattern of the material highlights the dominant role played by the synthesis temperature in determining the particle size and crystallinity of the synthesised material.

The XRD pattern analysis of 17 samples revealed the dominance of the (109) peak, observed in all synthesised samples as presented in Figure 6.1 (b), suggesting that the

crystallographic plane parallel to 101 has been prominent in all samples. The bulk intensities observed at 006,008, 0010 and 002 suggest that the particles have a higher degree of orientation (preferred orientation) parallel to the 001 plane. Interestingly, a noticeable shift to the lower 2 theta was observed in the peaks of samples synthesised at a temperature of 850°C, namely S1, S2, S6, S7, and S12. Conversely, samples synthesised at higher temperatures of 975°C and 1100°C exhibited the (109) peak at a 2θ of 30.5 degrees, whereas the same peak occurred at a 2θ of 30.19 degrees for samples synthesized at 850°C. This shift in peak position towards the left can be attributed to the change in the lattice parameter and crystal size of the material. The lattice parameter decreases as the synthesis temperature decreases, resulting in a contraction of the crystal structure, causing the shift towards the left as observed in similar $BaTiO_3$ [334] and other perovskites [335]. Furthermore, the shift in the peak position can also indicate the presence of a strain in the crystal structure due to defects or impurities, affecting the atomic spacing and consequently shifting the peak position towards the left. This again emphasises the impact of the synthesis temperature in comparison to holding times and heating rates in molten salt synthesis.

6.3. Synthesis Parameters Effects on Particles Morphology

Following the ANOVA and determination of the most significant factors, this section endeavors to provide an in-depth explanation and further analysis of the impact of the synthesis parameters on each response. In this regard, comprehensive 3D and contour plots have been generated to visually represent the findings of the ANOVA and regression models. These would facilitate identifying the significance of the combined interaction effect of the synthesis parameters at different points.

6.3.1. MSS Parameters Effects on Particles' Area (R1)

Based on the ANOVA results (chapter 5) for the model of the average particles' area (R1), the synthesis temperature, factor A, is the most significant factor affecting the area of the synthesised powder. Holding time and heating rate have proven to be poorly significant and insignificant, respectively. This is in contrast to other findings that have suggested through trial-and-error experimentation that the heating rate significantly affected the morphology of anisotropic plate-like perovskite $Sr_3Ti_2O_7$ particles, which were synthesised using the MSS [132]. Further, a study by Yongke Yan has suggested that a higher heating rate of 10^oC/min destroyed the plate-like structure of the molten

salt synthesised $Bi_{2.5}Na_{3.5}Nb_5O_{18}$ and thus reduced the heating rate to 1°C/min, which indeed indicate a longer time to the synthesis reaction [133].

Interestingly, the simultaneous effect of both factors, heating temperature and holding time has proven to have the second most significant impact on the area. The developed model equation for R1 (Equation 5.1 of chapter 5) has indicated that the effect of the synthesis temperature and the interaction effect of both factors (AB) is synergistic. Specifically, higher synthesis temperatures lead to larger area of the synthesised particles, further amplified by prolonged heating. The underlying mechanism responsible for this phenomenon is the Ostwald ripening exhibited during MSS, which is affected by changes in temperature [13]. This phenomenon also explains the simultaneous effect of the synthesis temperature and the holding time on the area of the synthesised particles. Due to the effect of higher temperature on the interfacial energy, the growth rate is promoted [134]. Additionally, the growth rate is further enhanced by larger diffusion coefficients and solubility, which facilitate the transportation of material within the molten salt [13]. The main effect of the individual factors of the synthesis temperature and the holding time is demonstrated in Figure 6.2. As can be seen, the increase in temperature has resulted in an exponential increase of the corresponding area, whilst the poorly significant impact of the holding time has slightly affected the area by demonstrating a gentle upward curve as time increases. To aid in the interpretation of the results, the figure includes dotted lines that represent the 95% confidence band on the mean prediction of particle thickness at any given synthesis temperature. This provides a measure of the precision and accuracy of the predicted values and serves as a useful tool for evaluating the reliability of the observed trend.

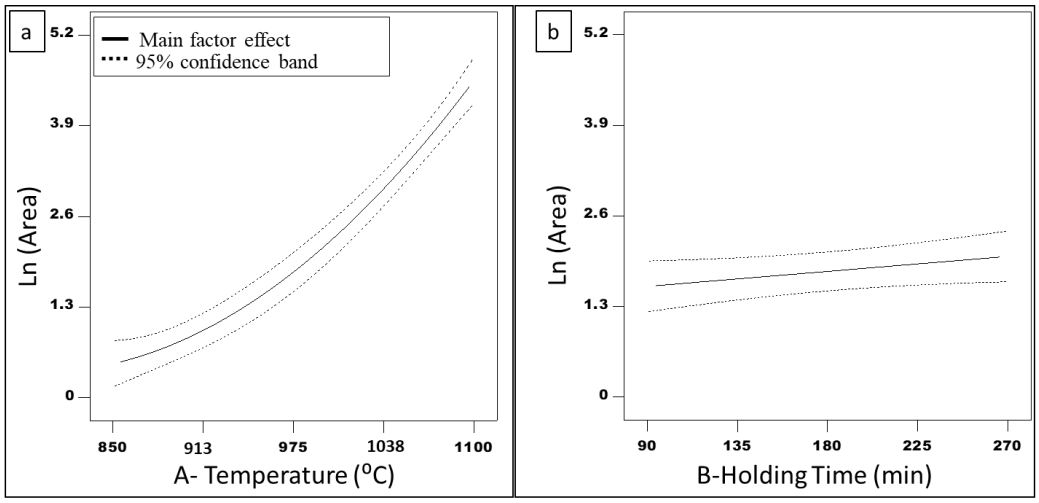

Figure 6.2: Main effect of (a) factor A- Temperature and (b) factor B-Holding time on the area of the synthesised particles along with the 95% confidence band

The combined interaction effect showing the simultaneous impact of the synthesis temperature and the holding time on the resulting area is depicted via the contour plot and the 3D plot in Figure 6.3 (a) and Figure 6.3 (b), respectively. The plot displays a color scale ranging from blue, indicating small area, to yellow/orange, indicating larger areas. A notable increase in the area is observed in Figure 6.3 (a) as the duration of the holding time exceeds approximately 200 minutes, surpassing an area of 100 μm^2. At a temperature of approximately 1050°C and a holding time of around 265 minutes, the area of the particles is predicted to be approximately 118 μm^2. However, at lower holding times of app. 90 minutes, the area growth observed with increasing synthesis temperature is relatively moderate in comparison to that at higher holding times. This implies that a longer duration of heating facilitates a more substantial effect on particle size increase due to varying temperatures. This trend is also observed in 3D plot. Since the heat rate has proven to be insignificant, it was kept constant during the generation of these plots.

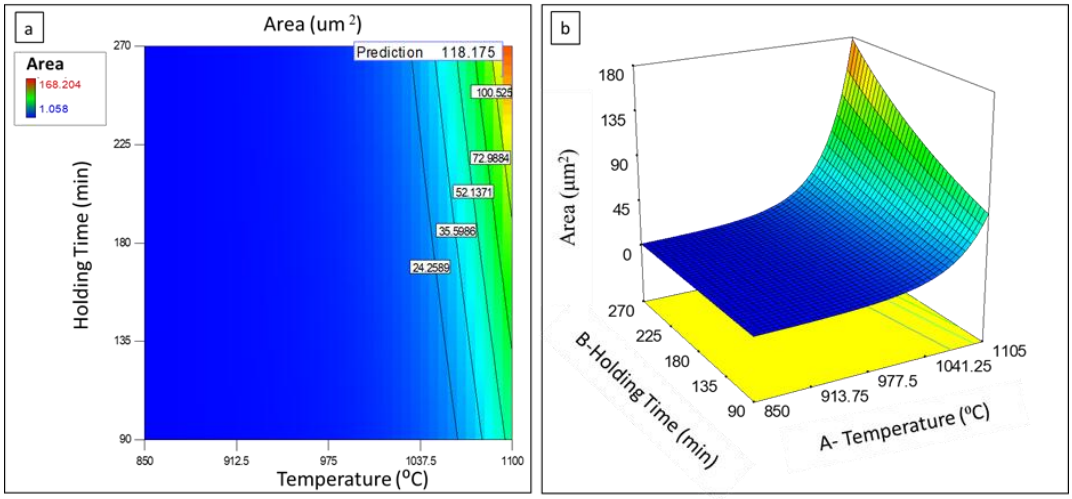

Figure 6.3: Schematic showing (a) contour and (b) 3D plot for the combined effect of the synthesis temperature and holding time on the area of the particles

The above observations are further complemented by the SEM micrographs in Figure 6.4 which illustrate the effect of three varying temperatures at constant holding time, 850ºC, 975ºC and 1100ºC on the average area of the synthesised particles, ranging from 1.9 um^2 to 3.8 um^2 to 120.5 um^2, respectively. At relatively lower temperatures, i.e., 850ºC, smaller spherical-shaped particles are apparent (as illustrated in Figure 6.4 (a). Typically, particle aggregation takes place during the reaction stage of molten salt synthesis where supersaturation levels are high and nuclei production is rapid, which leads to an increased tendency for particles aggregation [123]. As temperature rises beyond 975ºC with a constant holding time, there is significant expansion observed in the area covered by these particles as shown in both Figure 6.4 (b) and (c). An example of how the area of lower temperature synthesised agglomerated particles was measured is provided in Figure 6.5. Furthermore, Figure 6.6 provides evidence of the insignificance of the holding time on the area, as demonstrated by SEM micrographs synthesised at constant temperature but with varying durations of holding time. Notably, the SEM images depict comparable particles' area despite differences in duration.

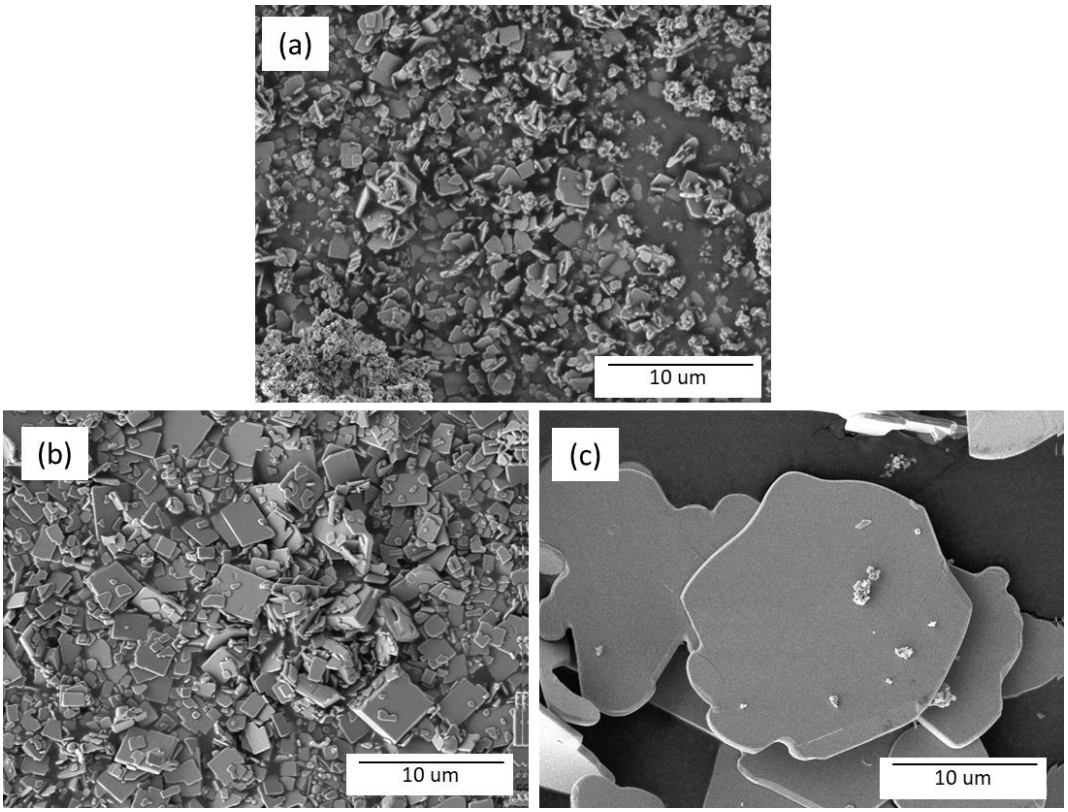

Figure 6.4: SEM micrograph showing the area and Feret's diameter of the NBiT particles synthesised at varying temperature and constant holding time (a) S12 [temp:850^{0}C/holding time:180 mins], (b) S3[temp: 975^{0}C/holding time:180 mins] and (c) S4 [temp: 1100^{0}C/ holding time: 180 mins]

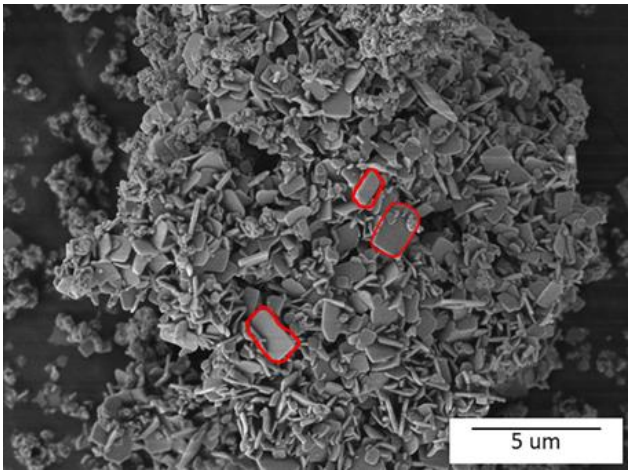

Figure 6.5: Close-up SEM micrograph of S12 showing an example of how the area was measured for agglomerated samples synthesised at 850ºC

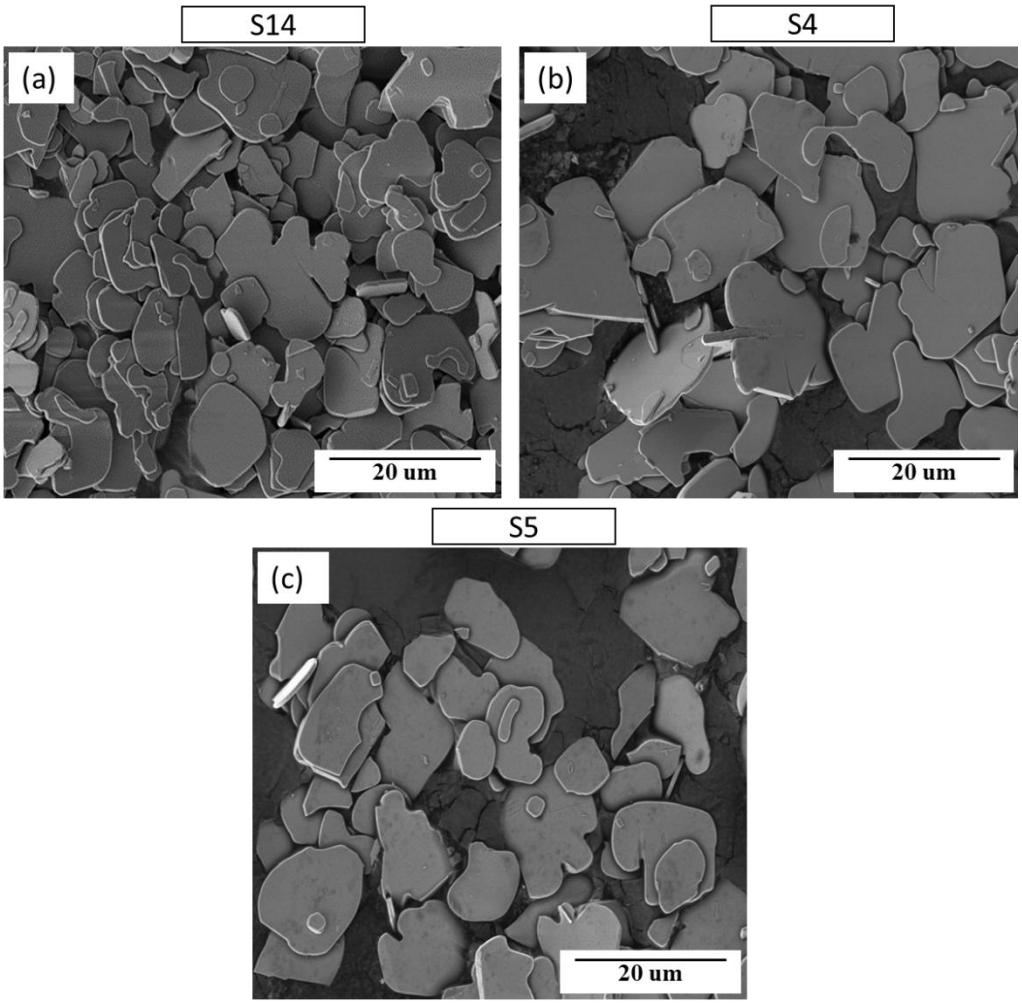

Figure 6.6: SEM micrograph of (a) S14 [90 min], (b) S4 [180 min] and (c) S5 [270 min] showing the impact of varying holding times and constant temperature (1100ºC) on the area and Feret's diameter of the particles

6.3.2. MSS Parameters Effects on Particles' Thickness (R2)

The ANOVA results for R2, the average thickness of the synthesised particles revealed that the most dominant factor affecting particle thickness is the synthesis temperature. Specifically, the developed model equation depicted that an increase in synthesis temperature leads to an exponential increase in the average thickness of the synthesised particles. This trend is presented is Figure 6.7, elucidating the main effect of the synthesis temperature on the thickness of the synthesised particles.

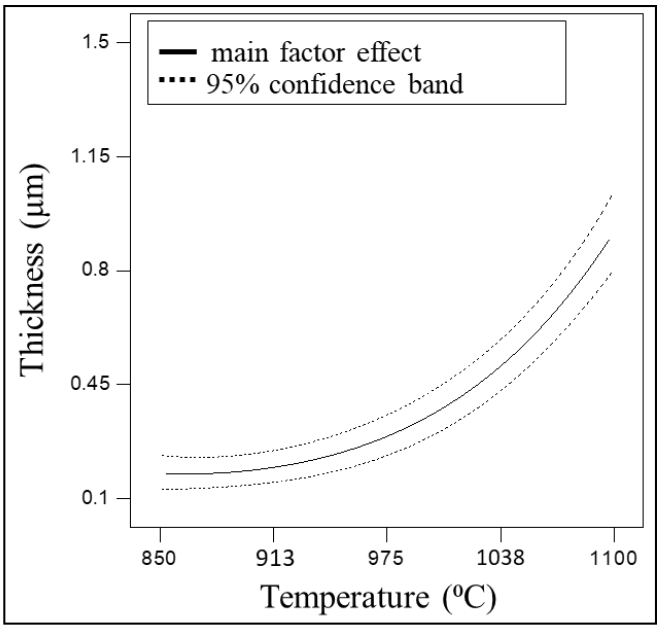

Figure 6.7: Main Effect of synthesis temperature on the thickness of the particles along with the 95% confidence interval (dotted lines)

During the molten salt synthesis, the synthesis temperature does not only affect the surface area of the synthesised particles as elaborated earlier, but it also has a significant impact on the thickness of the product particles. The thickness of the particles is mainly determined during the initial stage of particle formation, the reaction stage. During this stage, the dissolution rate of the reactants mainly dictated the shape and formation of the particles. Therefore, the higher solubility of Na_2CO_3 (with a solubility of approximately 212.5 g/l as per the SDS by Sigma Aldrich) leads to faster dissolution and diffusion in the molten salt compared to Bi_2O_3 and TiO_2. The increase in the product layer thickness is thus due to higher solubility particles which diffuse from the molten salt/product interface to the product/lower solubility reactant interface [13]. Since dissolution and diffusion rates depend on temperature, higher temperature increases reactant solubility, concentration, collision likelihood, and diffusion rate, resulting in thicker product particles [118].

In addition to the role of the synthesis temperature on the solubility and dissolution of the particles, the interplay between the synthesis temperature the duration of the holding time also plays a significant role in the formation of the particle's thickness. Due to the aforementioned Ostwald ripening effect, the precipitation of smaller solid particles' grains onto larger ones also results in an increase of the particles' thickness. The simultaneous impact of the combined interaction effect of temperature and

holding time can be depicted using the contour and 3D plot in Figure 6.8. It is observed that the thickness of the particles underwent a significant increase, rising from approximately 0.35 um to over 1 um, representing an increase of almost 200%, when the synthesis temperature was increased from 980ºC to approximately 1070ºC at a holding time of greater than 220 minutes. However, it is noteworthy that the effect of temperature on particle thickness is not as significant at lower holding times, specifically those below 180 minutes. This suggests that the rate of thickness growth may be limited by the available reaction time at lower holding times, thereby diminishing the impact of temperature on particle size and morphology.

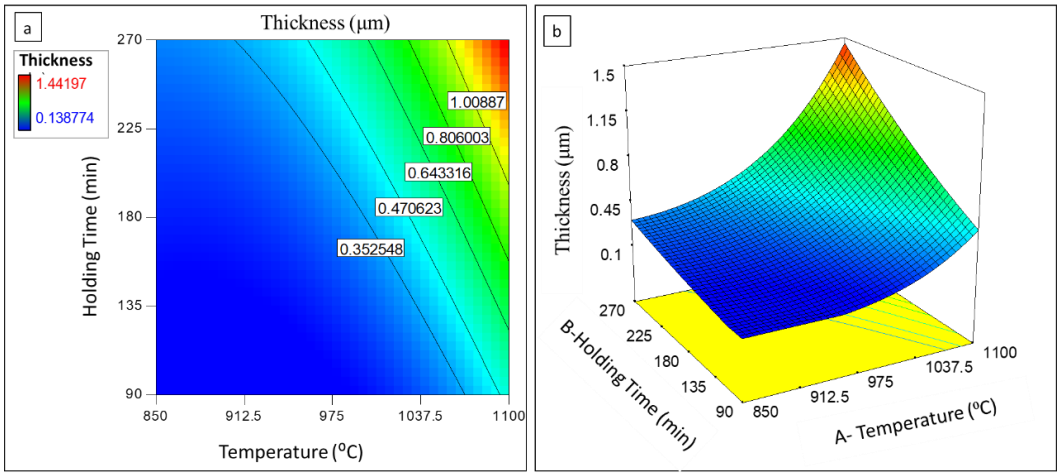

Figure 6.8: Schematic showing (a) contour and (b) 3D plot for the combined effect of the synthesis temperature and holding time on the thickness of the particles

SEM micrographs in Figure 6.9 further illustrate the impact of the synthesis temperature on the thickness of the particles at constant holding times. The thickness of the NBiT aggregated particles synthesised at 850ºC, as well as larger NBiT particles obtained at synthesis temperatures of 975ºC and 1100ºC, are depicted in Figure 6.9 (a), Figure 6.9 (b), and Figure 6.9 (c), respectively. The arrows in the SEM images in Figure 6.9 , illustrate an example of how the thickness was measured during this study.

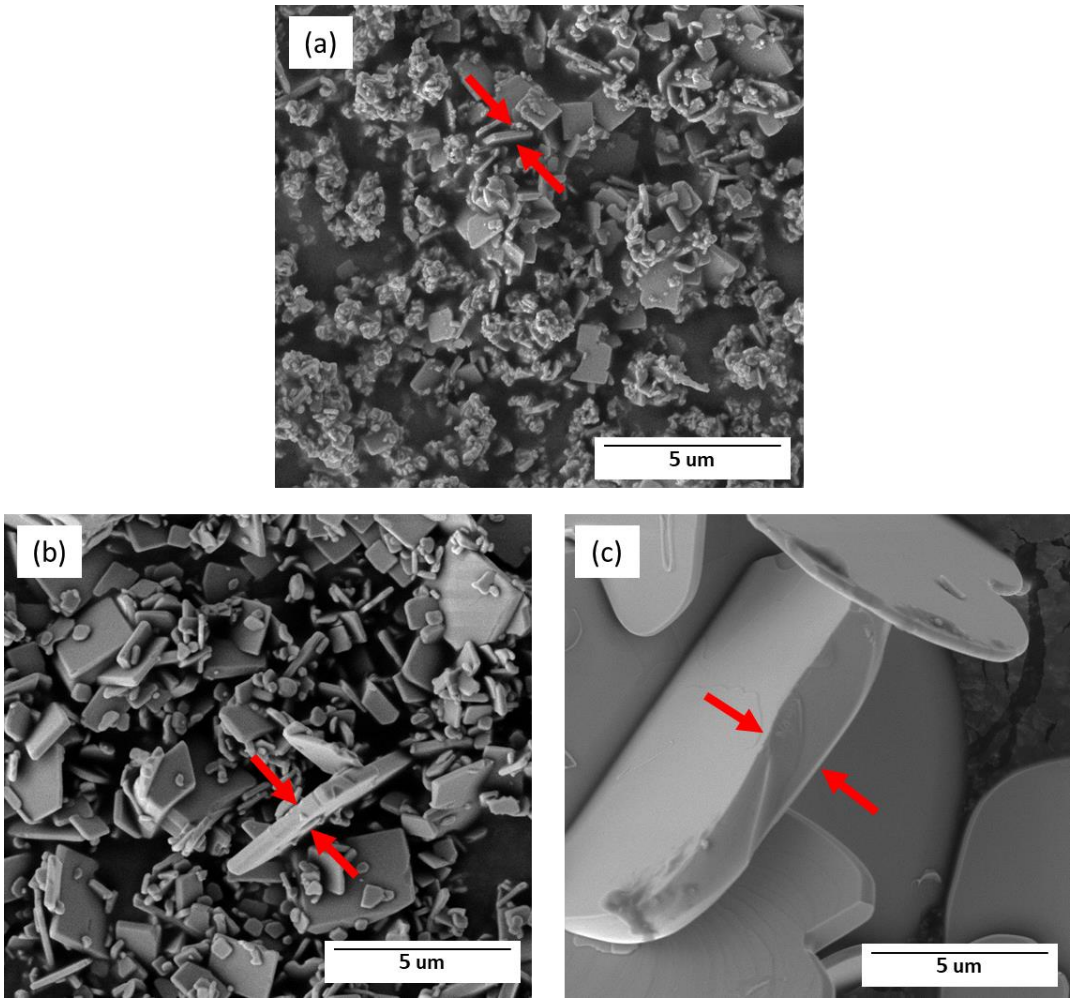

Figure 6.9: SEM micrograph showing sample thickness of NBiT particles synthesised at varying temperatures and constant holding time for (a) S12, (b) S3 and (c) S4

6.3.3. MSS Parameters Effects on Particles' Feret's Diameter (R3)

While the area of particles in R1 has been observed to be mostly affected by synthesis temperature, this does not necessarily imply a corresponding impact on the Feret's diameter. As the Feret's diameter depicts the maximum distance between two tangents; it is not directly related to changes in particle area. Therefore, this section aims to investigate and analyse the effects observed in the ANOVA presented in Chapter 4. The ANOVA results revealed that once more the synthesis temperature proves to be the most significant factor affecting the size and shape of the particles, specifically the resulting Feret's diameter. It is noteworthy that in the present model, holding time was also found to be significant, albeit with less significance than the main effect of synthesis temperature and the combined effect of temperature and holding time. The main effect of synthesis temperature and that of the holding time are depicted in Figure

6.10 (a) and (b), respectively. As observed, there is an exponential growth in the Feret's diameter with increasing synthesis, at a constant time of 270 minutes. Further, there's an increasing non-linear upward trend seen with increasing holding times at a constant temperature of 1100ºC.

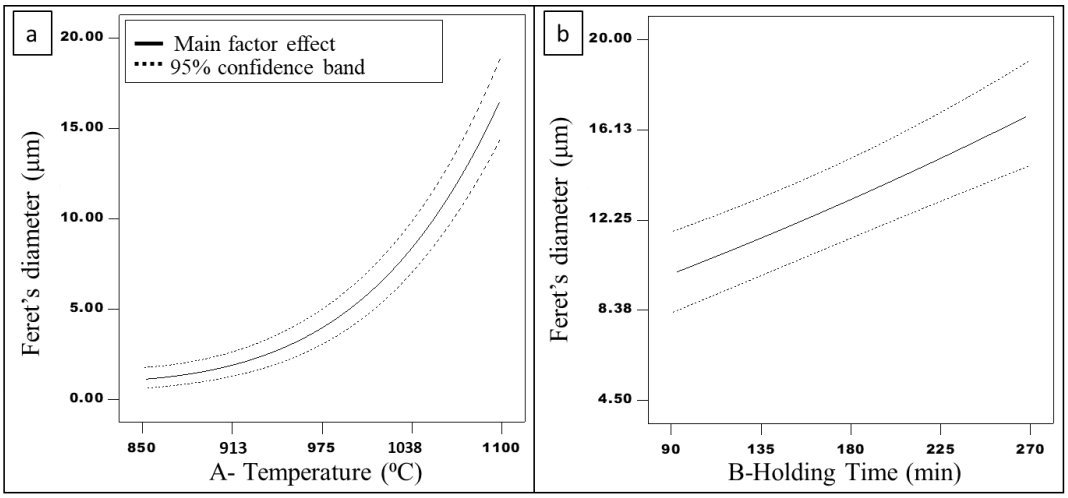

Figure 6.10: Main Effect of (a) Synthesis Temperature and (b) Holding Time on the Feret's diameter of the particles

In molten salt synthesis, higher temperature not only affects the area of the particles but also their shape, as indicated by the Feret's diameter. This is because at higher temperatures, the nucleation and growth of particles are enhanced due to the increased mobility and reactivity of the reactants. This can result in anisotropic growth, where growth is faster in certain directions than others. This can be observed in the formation of plate-like particles, where growth occurs faster in the plane of the plate than perpendicular [336] to it and thus increasing the Feret's diameter. This is complemented by further change in the reaction kinetics exhibited at higher temperatures. At elevated temperatures, the reaction can become more kinetically favorable for the formation of specific crystal phases or morphologies, leading to changes in particle shape and size which thus can enhance the anisotropic growth. This behavior is similar to the observed anisotropic growth behaviour of plate-like $Bi_4Ti_3O_{12}$ structure which was synthesised in molten salt flux [337]. However, the findings of this study suggest that edge nucleation requires a high degree of supersaturation, resulting in minimal changes in particle thickness and the dominance of epitaxial growth as the primary process [337]. The impact of the varying synthesis temperature on the Feret's diameter can be observed in Figure 6.4 as well. The Figure 6.4 reveals that at the same holding time, and a higher synthesis temperature of 1100ºC

the particles tend to have a flattened, elongated plate-like shapes with a larger aspect ratio compared to cubic-shaped particles observed at a temperature of 975ºC. The clear shape transition from aggregated small spherical-shaped particles to cubic-like shaped particles to plate-like shaped particles that is exhibited with increasing temperature is driven by the thermal expansion of the particles.

It is also worth noting that the interaction between temperature and holding time can further complicate the relationship between temperature and Feret's diameter. For example, a higher synthesis temperature combined with a longer holding time results in more pronounced changes in the reaction kinetics and thermodynamics, leading to even larger changes in particles shape and thus Feret's diameter. The combined interaction effect of synthesis temperature and holding time is depicted in Figure 6.11. The contour plot reveals that the Feret's diameter of the particles significantly increases with higher holding times, i.e., more than 180 minutes and higher temperatures, i.e., more than1050ºC compared to those obtained at lower holding times and temperatures.

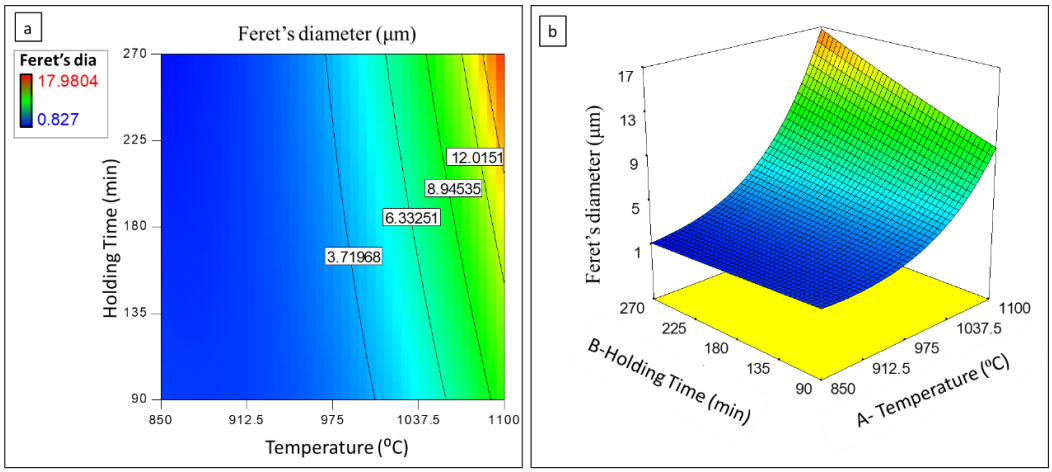

Figure 6.11: Schematic showing (a) contour and (b) 3D plot for the combined effect of the synthesis temperature and holding time on the Feret's diameter of the particles

The simultaneous effect of the synthesis temperature and the holding time can be also observed in Figure 6.12, which depicts SEM micrographs of two samples synthesised at lower synthesis temperature and lower holding time, and the other sample at higher temperature and higher holding time. Herein, the tendency of plate-like growth at higher temperatures is again clearly observed. This aligns well with the observation that the XRD peak intensities parallel to the {00l} family such as 006, 008,0010 and 002, were clearly enhanced with temperature increase (see Figure 6.1), suggesting a preferred orientation along the 001 direction. These findings suggest that the synthesis

conditions, particularly temperature and holding time, can be optimised to tailor the size and shape of particles for specific applications.

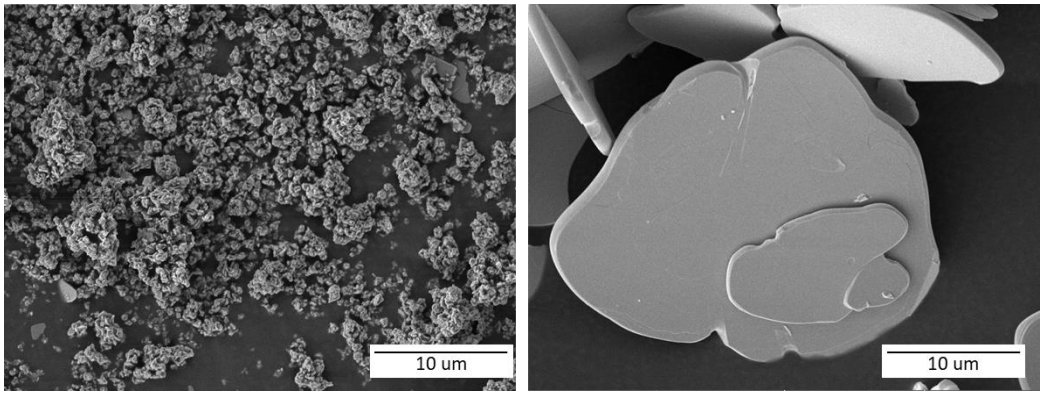

Figure 6.12: SEM micrograph of (a) S2 - temp:850ºC/holding time:90 mins and (b) S11- temp 1100ºC/holding time:270 mins

6.4. Optimisation

In this study, a multi-objective optimisation was performed to maximise the three responses: the average particle area, average Feret's diameter, and the thickness of the particles. The optimal conditions constraints have been listed in the Table 6.1. The three response model equations presented in Equation 5.1, Equation 5.2 and Equation 5.3 of chapter 5 have been solved simultaneously.

Table 6.1: Constraints for optimal conditions

Name	Goal	Lower Limit	Upper Limit
Temperature (°C)	is in range	850	1100
Holding Time	is in range	90	270
Heat Rate	is in range	3	7
Area	maximise	1.058	168.204
Thickness	maximise	0.138774	1.44197
Feret's dia	maximise	0.827	17.9804

Based on utilising the GA, the software offers multiple solutions for optimal conditions. The contour plot in Figure 6.13 displays the desired regions for optimum synthesis settings. As can be seen, regions with higher desirability (above 82%) correspond to higher temperatures (i.e., 1100 ºC) and higher holding time (above 180 minutes). For obtaining the optimum synthesis conditions the solution with the highest desirability, in this case 97.5%, has been chosen. This solution suggests that the optimum values of the synthesis temperature and the holding time at that specific

temperature would be 1100 ºC and 270 min, respectively. The selection of the heating rate does not significantly alter the size or the shape of the synthesised particles, as it is negligible (insignificant factor).

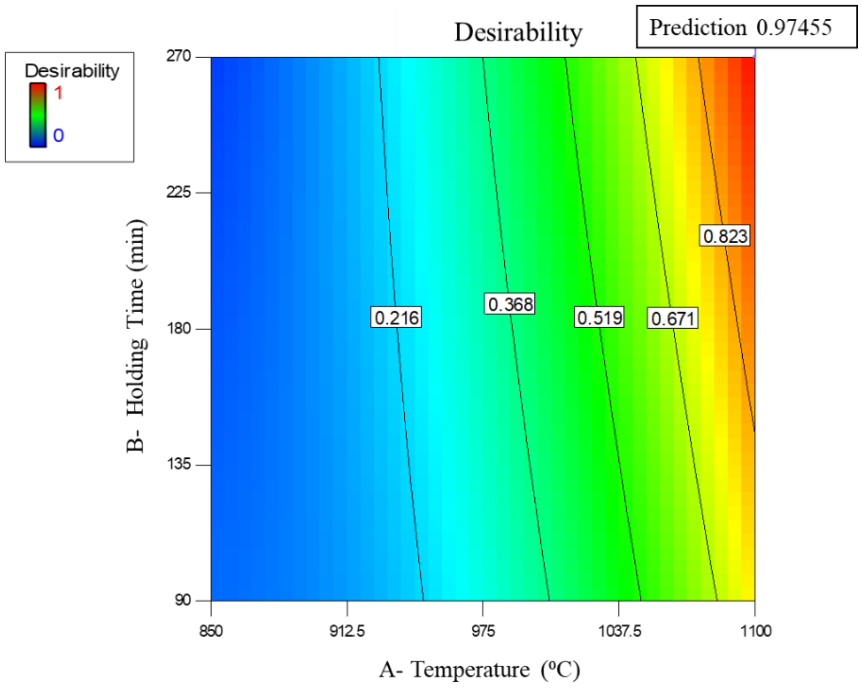

Figure 6.13: Contour plot of desirability for optimum synthesis conditions.

At the optimum synthesis conditions, the predicted average particle area is 153.29 µm^2, the average thickness is 1.27 µm and the average Feret's diameter is 16.78 µm. These optimum setting conditions and their corresponding optimum responses are tabulated in Table 6.2.

Table 6.2: Optimum process setting parameters along with their corresponding actual(experimental) and predicted results.

Factor A: Temp. (ºC)	Factor B: Time (min)	Factor C: Heat Rate (ºC/min)	Area (µm^2)		Thickness (µm)		Feret's diameter (µm)	
			Actual	Pred.	Actual	Pred.	Actual	Pred.
1099.76	269.80	6.99	156.56	153.29	1.46	1.27	17.18	16.78

6.5. Validation

To validate the developed models, BNT powder was synthesised using the obtained optimum settings of parameters utilising the optimally synthesised two-dimensional NBiT precursor.

6.5.1. Phase Purity Validation

To ensure the phase purity of the optimally synthesised BNT particles, XRD analysis was conducted on both samples mixed with magnetic stirring and roller mixer. The XRD pattern of the synthesised BNT particles was compared to the rhombohedral BNT phase in JCPDS card number 00-046-0001, with lattice parameters of a (Å): 5.5530, b (Å): 6.6750, and c (Å): 5.5200. The XRD patterns of both magnetic stirring mixed BNT (referred to as MS) and roller mixer mixed BNT (referred to as RM) are shown in Figure 6.14. The analysis confirmed the achievement of single-phase BNT as all diffraction peaks of the synthesised BNT were consistent with the rhombohedral BNT phase for both MS and RM samples. The well-defined and sharp peaks observed in the XRD pattern of both MS and RM mixed BNT confirm the high crystallinity of the synthesised BNT powder particles. This high degree of crystallinity is desirable for BNT powder particles as it leads to an enhancement of their mechanical and electrical properties. Specifically, the high crystallinity of BNT particles improves their piezoelectric, ferroelectric, and pyroelectric properties, which are essential for their use in various applications, including energy harvesting, actuation, sensing, and biomedical imaging. Considering the XRD pattern analysis, which revealed no noticeable difference between the BNT powder particles mixed via magnetic stirring (MS) and roller mixer (RM), it is evident that the choice of mixing method is not a critical factor in achieving the desired phase purity and high crystallinity of the synthesised BNT powder particles. Overall, the successful synthesis of high-quality BNT particles with good phase purity and high crystallinity using the optimised parameters obtained from the GA-based optimisation approach was confirmed by the XRD analysis.

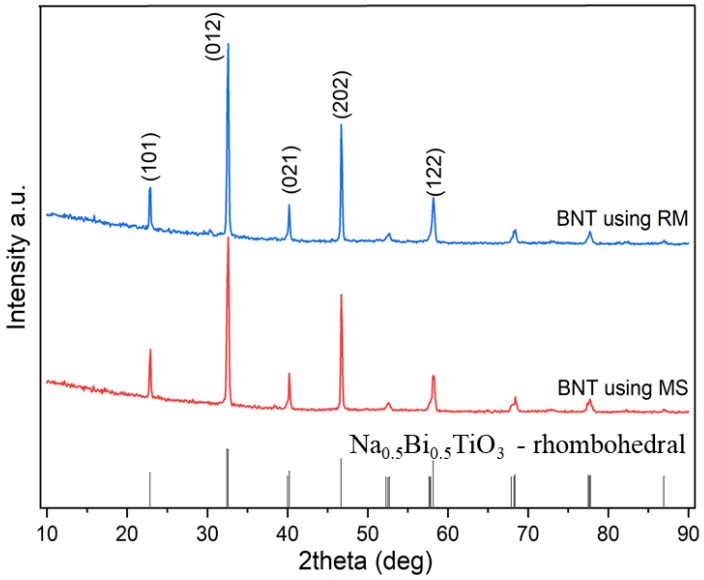

Figure 6.14: XRD pattern of final BNT powder prepared at optimum condition using molten salt synthesis technique.

6.5.2. Morphology Validation

After confirming the phase purity of the optimally synthesised BNT powder particles and validating the synthesis of single-phase BNT using the GA-based optimisation approach, the subsequent step was to validate the developed models that predicted the morphology of the molten salt synthesised powder (presented in chapter 5). To achieve this goal, a comprehensive analysis of the morphology of the optimally synthesised BNT powder was performed using a combination of SEM and ImageJ. This analysis involved a comparison of the actual average area, thickness, and Feret's diameter of the optimum BNT powder with the models' predicted results. The influence of the mixing techniques, namely MS and RM on the morphology of the final (BNT) powder was also investigated. Furthermore, the analysis aimed to examine whether MS could effectively preserve the particles' morphology as was intended.

Figure 6.15 shows SEM micrograph of (a) MS mixed BNT and (b) RM mixed BNT. While no significant difference was observed in the XRD pattern of the two employed mixing methods, intriguingly, the synthesised BNT exhibited distinct morphologies when different mixing techniques were utilised. MS mixed BNT showed spherical-shaped particles with relatively smaller area compared to RM mixed BNT particles which showed plate-like morphology with larger particles area. Conventionally, plate-like particles are preferred over spherical particles for dielectric applications, owing to

their larger surface area and high aspect ratio, which offer better charge storage and improved electrical insulation properties. The variation in morphology of the synthesised BNT particles can be attributed to the difference in mixing mechanisms employed by the two techniques. Magnetic Stirring (MS) involves the application of a magnetic field to rotate the stir bar and mix the reactants, while Roller Mixing (RM) relies on the rolling action of the vessel to induce mixing. During MS, the stirring action creates turbulence in the reaction mixture, leading to the formation of droplets, which subsequently solidify to form spherical particles. On the other hand, RM induces shear forces in the mixture, causing the formation of plate-like particles due to the preferential growth along the crystallographic plane. Although, the main purpose of utilising magnetic stirring in this step was to attempt preserve the original shape of the NBiT precursor and prevent any damage to its morphology, it was concluded that the preservation of the plate-like morphology of the NBiT precursor in the final BNT powder requires the use of a roller mixer during synthesis.

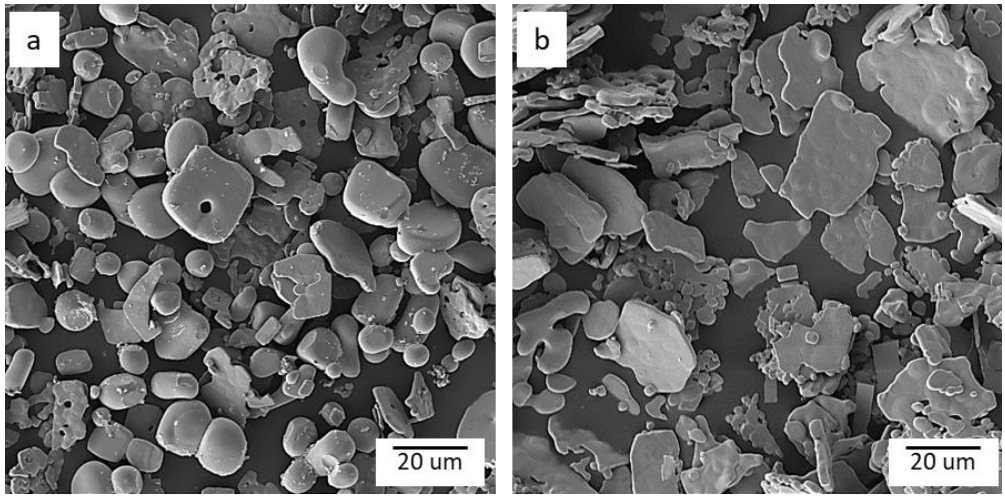

Figure 6.15: SEM micrograph of final BNT powder mixed using (a) magnetic stirring and (b) roller mixer

In Table 6.2, the experimental BNT responses are compared with their predicted values under optimum synthesis conditions. The experimental values were obtained using the RM mixed BNT. The results show a close agreement between the predicted and actual values for the three different responses. The high degree of correspondence between the predicted and actual values is indicative of the robustness of the predictive models developed in this research.

At the optimum synthesis conditions, the predicted average particle area is 153.29 μm^2, the average thickness is 1.27 μm and the average Feret's diameter is 16.78 μm. These optimum setting conditions and their corresponding optimum responses are tabulated in Table 6.2.

Table 6.2The SEM micrographs of the optimally synthesised BNT powder particles, presented in Figure 6.16, illustrate that the final product particles retain the morphology of the precursor, which is one of the essential requirements for achieving platelike particles. The majority of the BNT particles, like the NBiT precursor particles, had plate-like shapes with an average area of 156.56 μm^2, an average thickness of 1.467 μm, and an average measured Feret's diameter of 17.18 μm.

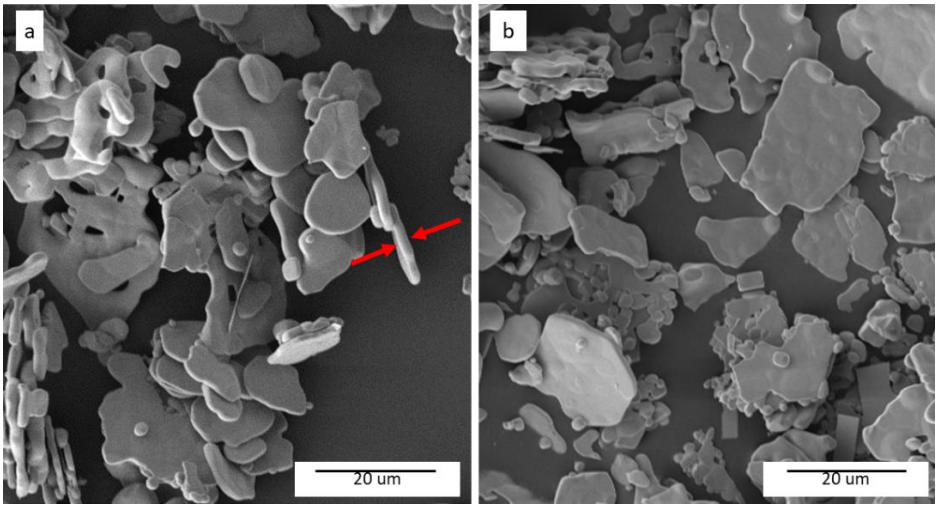

Figure 6.16: SEM micrograph of optimally synthesised BNT powder particles showing (a) average thickness and (b) average particles area.

The results obtained from the implementation of the statistical DOE approach, as validated in Table 6.2 and Figure 6.16 demonstrate the viability of using RSM in conjunction with the statistical design of experiments to optimise molten salt synthesis parameters and investigate the significance of both the main and combined interactive effects of the process parameters. This approach offers an effective means of predicting the physical properties of materials based on their individual characteristics, which has significant implications for the field of ceramic-based dielectric composites.

Table 6.3 presents a comparison of the thickness and Feret's diameter of the herein synthesised two-dimensional BNT plate-like particles with those of other molten-salt synthesised plate-like particles reported in literature. It was observed that the molten salt-synthesised two-dimensional BNT plate-like particles of obtained in this study

exhibit comparatively larger thickness and Feret's diameter when compared to the corresponding dimensions reported in previous studies for similar plate-like two-dimensional particles. The table further includes the reported particle size dimensions. Traditionally, the morphology of synthesised particles is commonly characterised and reported using the parameter 'size'. Yet, since the particle size is commonly measured using the equivalent sphere approach [338], the exact dimensions, or specific characteristics that the term 'size' refers to are not explicitly specified, leading to ambiguity and a lack of precise dimension definition. Moreover, this method may not always be suitable when dealing with non-uniformly shaped particles, such as those that have a plate-like morphology. In contrast, the present study addresses this ambiguity by developing a predictive model that establishes a relationship between the synthesis parameters and the area of the particles. By focusing on the area measurement, this work offers a more precise and quantifiable characterisation of the particle morphology.

The findings of this study may serve as a useful guide for future research into the synthesis of two-dimensional plate-like particles and may contribute to the development of novel materials with tailored properties.

Table 6.3: Comparison of various molten salt synthesised plate-like particles

Material	Area (μm^2)	Size (µm)	Avg. Thickness (µm)	Avg. F. diameter (µm)	Ref.
$Bi_{4.5}Na_{0.5}Ti_4O_{15}$			0.95*	9*	[339]
$BaTiO_3$		3–8	0.35*		[340]
$BaTiO_3$			0.75*	10.5*	[341]
$Bi_{2.5}Na_{3.5}Nb_5O_{18}$ (BNN5)		15	0.5		[133]
$Bi_4Ti_3O_{12}$			0.4		[337]
$Bi_4Ti_3O_{12}$			0.2	3	[342]
BNT			0.88*	15*	[297]
$BaBi_4Ti_4O_{15}$			0.3	10	[343]
$BaTiO_3$		5–10	0.5		[141]
$Na_{0.5}K_{0.5}NbO_3$			1.25*	15*	[344]
BNT	156.56		1.5	17.18	This Work

* Calculated average based on reported maximum and minimum values

6.6. Summary

This chapter discussed the effects of molten synthesis parameters obtained from ANOVA results on the morphology and phase purity of the synthesised particles. The phase purity of the 17 NBiT samples synthesised under different conditions was confirmed by the XRD analysis. The peak intensities were more pronounced at higher synthesis temperature with a higher degree of orientation parallel to the 00l plane. The holding time did not significantly influence the XRD pattern, with synthesis temperature being the main determinant of particle size and crystallinity. The ANOVA outcomes for R1, which identified the synthesis temperature as the most significant factor affecting the area of the synthesised particles, followed by the combined effect of synthesis temperature, and holding time, was attributed to the Ostwald ripening phenomenon, which is influenced by factors such as temperature, diffusion coefficient, and solubility. The ANOVA outcomes for R2 and R3 were further explained by the solution-diffusion mechanism, as well as the observed behaviour of the XRD peaks. Based on the extensive ANOVA analysis, the heating rate showed no significant impact on the three responses under investigation, contradicting the findings of some other reported studies. The NBiT precursor was mixed using two different techniques, namely roller mixer and magnetic stirring to obtain BNT. XRD analysis of the final product revealed the attainment of single-phase BNT with high crystallinity for both mixing techniques, although the morphology of the synthesised BNT was found to be influenced by the method of mixing, with the use of a roller mixer preserving the plate-like morphology of the NBiT precursor in the final BNT powder. Furthermore, the chapter presented the results of the conducted multi-objective optimisation. The predictive models were validated and large plate-like BNT particles with an average area of 156.56 μm^2, an average thickness of 1.46 µm, and an average Feret's diameter of 17.18 µm, were obtained at optimum conditions of 1100 ºC and 270 minutes. Notably, thickness and Feret’s diameter of the herein synthesised particles surpassed those of others reported in literature for similar two-dimensional plate-like particles.

Chapter 7

7. Optimised Synthesis and Mechanical Alignment: Key Factors in Tailoring the Properties of BNT-Epoxy Composites

7.1. Introduction

As previously illustrated in Chapter 2 of this dissertation, the effectiveness of ceramic-polymer composites depends upon several influencing factors, including filler shape, size, and particle alignment within the polymer matrix. Chapter 6 has highlighted the optimal synthesis of BNT ceramic particles through the implementation of the RSM-based DOE approach in molten salt synthesis, with the objective of enhancing the dielectric performance when incorporating these fillers in ceramic-polymer dielectric composites. This chapter aims to examine the influence of incorporating these optimally synthesised ceramic fillers and aligning them in a quasi 1-3 structure within the composites utilising an easy and cost-effective mechanical technique, on the subsequent dielectric and piezoelectric performance of the composites. This chapter starts by conducting a comprehensive examination of the microstructure of BNT-Epoxy composites fabricated using both optimally synthesised and non-optimally synthesised BNT particles to validate the significance of employing optimally synthesised BNT particles in influencing the microstructure of the developed composites. Within this context, composites having varying BNT volume % content were fabricated ranging from 5% to 35%. The chapter further demonstrates the results of the elemental analysis conducted utilising the EDX.

As the second aim of this thesis was to fabricate high-performance dielectric quasi 1-3 composites with properties comparable to state-of-the-art ceramic-polymer composites, the following sections of this chapter present an in-depth analysis of the obtained dielectric, piezoelectric, and ferroelectric performance of the composites. Moreover, the obtained ferroelectric hysteresis loops are presented and analysed, along with the results of the obtained discharge energy density of the developed composites. The last section of this chapter demonstrates a comprehensive comparative analysis between the dielectric properties and energy density values of the herein developed composites and those of state-of-the-art similar composites reported in literature.

7.2. Microstructure and Elemental Analysis

7.2.1. Effect of Non-Optimally synthesised BNT-Epoxy Composites

Prior to the fabrication of BNT-Epoxy composites using the optimally synthesised BNT powder, this section presents a comprehensive overview of the fabrication of BNT-Epoxy composites utilising non-optimally synthesised BNT powder.

In order to synthesise BNT particles according to experimental trial and error data from literature [142], the precursor NBiT was heated at a rate of 5^{o}C/min to 1100^{o}C and maintained at this temperature for 90 minutes. The transformation process into BNT involved heating the precursor to 950^{o}C for another 90 minutes while maintaining all mixing techniques previously mentioned in Chapter 3 constant, leading to the morphology obtained in Figure 7.1 for the product BNT powder. Figure 7.1 (a) and (b) demonstrate SEM images of the same non-optimally synthesised BNT powder at higher and lower magnification, respectively. In contrast to the optimally synthesised plate-like BNT particles illustrated in Figure 6.15 (b) in Chapter 6, the final BNT powder synthesised under these non-optimal conditions did not preserve the morphology of the precursor and exhibited particles with irregular sizes and shapes, including rectangular, plate-like, and spherical particles.

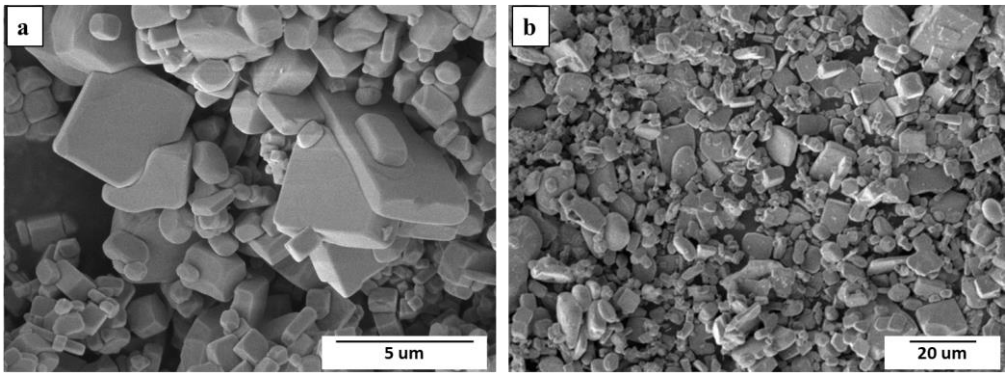

Figure 7.1: SEM image of BNT powder synthesised at non-optimal conditions at (a) higher magnification and (b) lower magnification.

Subsequently, the non-optimally synthesised BNT powder was incorporated into an epoxy matrix, and BNT-epoxy composites were fabricated with varying BNT volume fractions (ranging from 5% to 35%) using the mechanical alignment technique discussed in Chapter 3. The resulting composite microstructures were examined by SEM, as illustrated in Figure 7.2. It was observed that increasing the BNT volume fraction resulted in the formation of more densely packed composites. At 25% and above some of the incorporated BNT particles demonstrated a weak particle alignment

in a chain-like structure, as highlighted in the figure. However, a well-structured 1-3 composite cannot be determined in the x-direction. Furthermore, the BNT particles exhibit an uneven distribution within the epoxy matrix, with some areas lacking BNT particles. The irregular shape and inhomogeneous size of non-optimally synthesised BNT particles complicates reorientation during the mechanical alignment using the doctor blade. Moreover, as the particles has comparatively smaller thickness than that of the composite, the particles tend not to be distributed while moving the doctor blade. Due to the varying size of the non-optimally synthesised BNT powder, smaller-sized particles tend to agglomerate at higher BNT volume content as observed in the 35% BNT -Epoxy composite (Figure 7.2). This may be ascribed to the attractive Van-der-Waals forces that become more pronounced at higher filler volume fractions as a result of the reduced interparticle distance and the increased surface area to volume ratio of smaller sized particles [345,346]. The agglomeration of particles within a polymeric composite system has proven to adversely affect the mechanical properties of the composites, in which agglomerations are anticipated to weaken the overall mechanical properties due to stress concentrations and regions of localised stress [347]. Furthermore, these agglomerations may decrease the overall dielectric performance of the composites, as they can disrupt the required dispersion or alignment of the particles. Therefore, controlling, and minimising particle agglomeration is crucial for maintaining the mechanical integrity and dielectric performance of the composites and thus highlighting the importance of optimal synthesis conditions and particle morphology in the development of high-performance BNT-based dielectric composites.

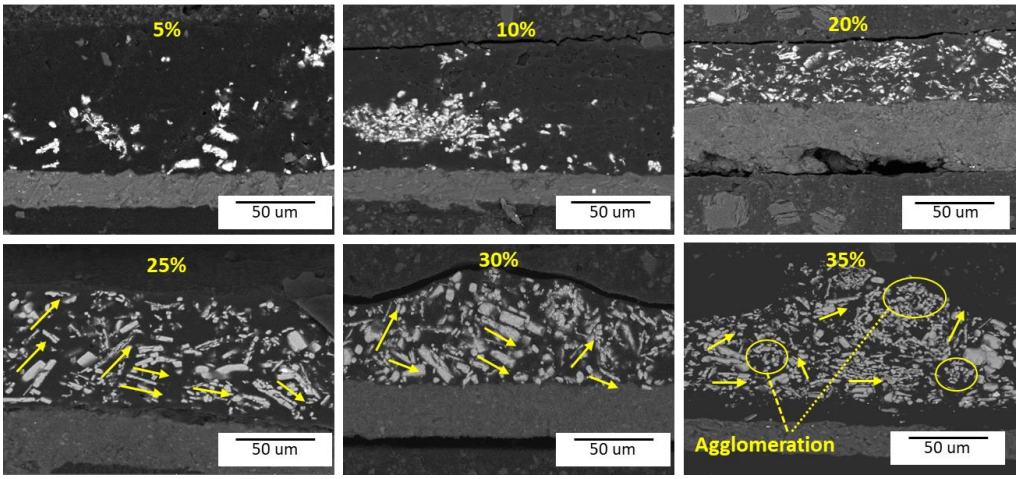

Figure 7.2: SEM overview of BNT-Epoxy composites at varying BNT volume content fabricated using non-optimally synthesised BNT powder

7.2.2. Effect of Optimally Synthesised BNT on The Alignment Of BNT-Epoxy Composites

This section investigates the use of optimally synthesised BNT ceramic powder in fabricating BNT-Epoxy composites with a doctor blade. A broad overview of the BNT-Epoxy composites fabricated using optimally synthesised BNT powder for different BNT volume fractions in the composite, ranging from 5% to 35%, is depicted in Figure 7.3.

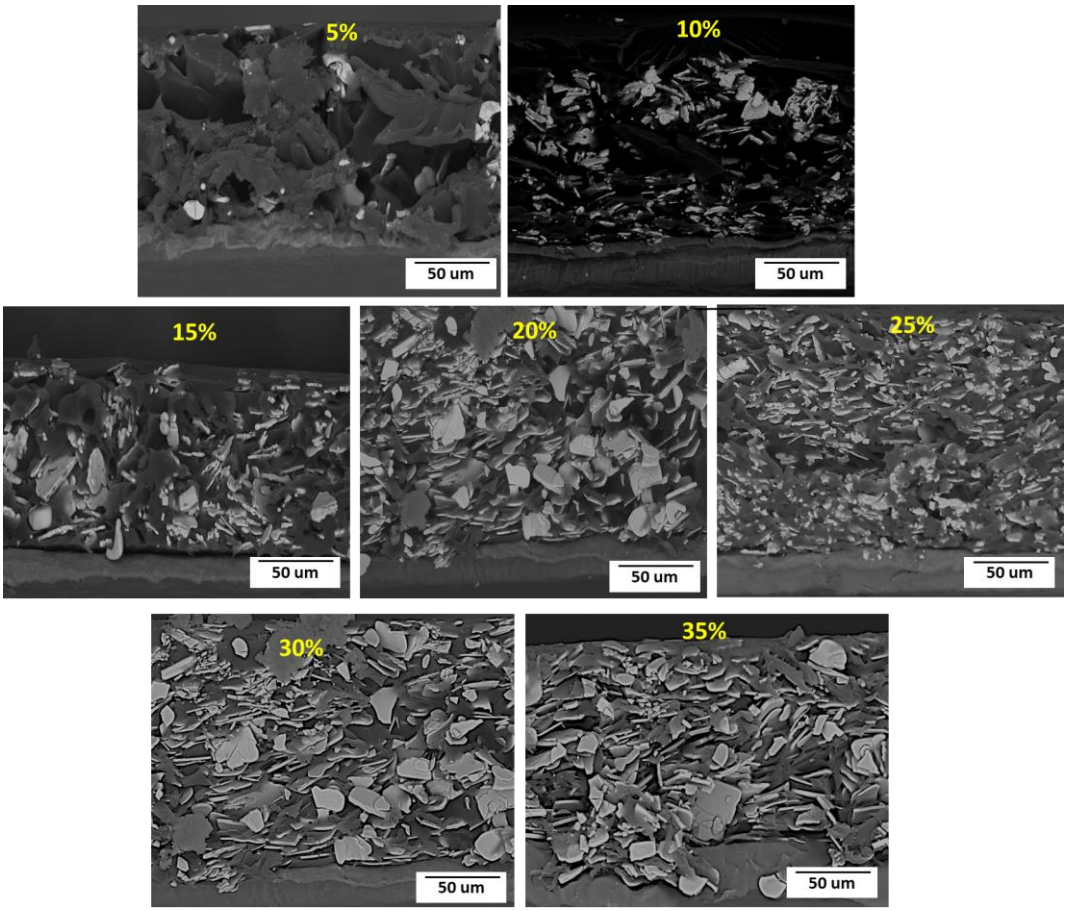

Figure 7.3: SEM overview of BNT-Epoxy composites at varying BNT volume content fabricated using optimally synthesised BNT powder.

A higher magnification SEM images of the 5% and 10% BNT volume fraction in the composite is presented in Figure 7.4. The BNT particles in both the 5% and 10% BNT-Epoxy composites had a poor alignment along the direction of blade, with noticeable BNT free regions, indicating that the alignment was dependent on the concentration of ceramic particles in the composite. The poor alignment may be attributed to the low concentration of particles within a unit volume, as such the presence of more free space surrounding the particles provides them with greater freedom to change their direction when subjected to the doctor blade during the fabrication process. This is anticipated

to have an adverse impact on the dielectric characterisation of the fabricated BNT-Epoxy composites, as presented in later sections.

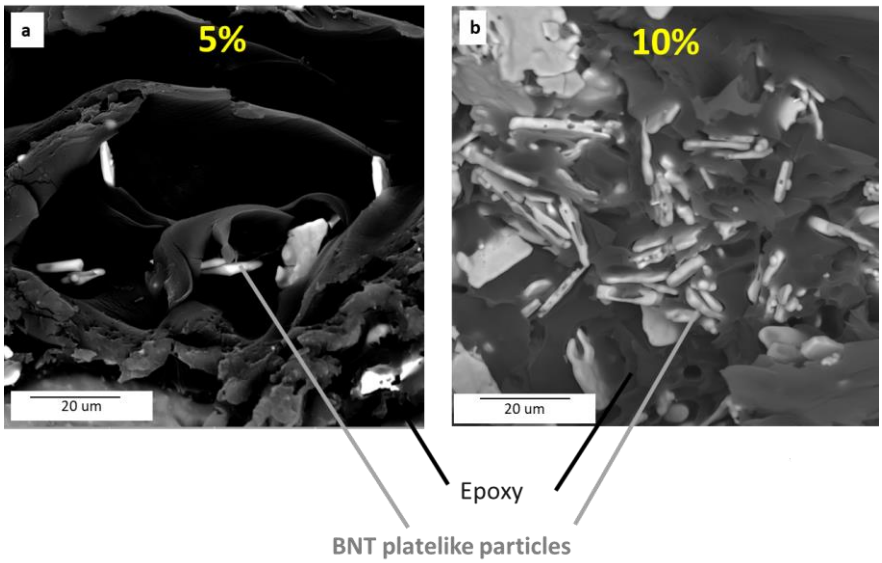

Figure 7.4: SEM image of (a) 5% BNT-Epoxy and (b) 10%BNT-Epoxy composites

Figure 7.5 shows SEM images of epoxy composite with (a): 15% and (b) 20% BNT particles. It was observed that increasing the BNT volume fraction in the composite matrix can lead to a higher degree of alignment of the ceramic particles within the matrix compared to 5% and 10% BNT-Epoxy composites. With BNT volume fractions of 15% (Figure 7.5 (a)) an improvement in the alignment is observed, with 20% (Figure 7.5 (b)) composite behaving slightly better. However, it is crucial to note that increasing the ceramic volume fraction within the composite matrix may also lead to increased stiffness and reduced flexibility, which could hinder its application in certain contexts. This is because higher ceramic filler content, requires higher stress for deformation [348]. As such, a balance between achieving optimal particle alignment and preserving the required mechanical properties of the composite must be carefully considered.

Figure 7.6 shows the 25% and 30% BNT-Epoxy composites. Again, it is observed that the level of particle homogeneity distribution in the fabricated composites increases with an increase in ceramic volume fraction. When the BNT ceramic volume fraction is at 25%, a higher degree of particle alignment is observed in comparison to those composites with volume fractions of 20% and lower. Further analysis through the zoomed-in SEM micrograph (Figure 7.6 (b) and (d)) reveals that the composite displays plate-like particles arranged in parallel orientation, with each layer stacked on

top of another. It may be thus inferred that the utilisation of mechanical alignment with a volume fraction equal to or greater than 25% has the potential to produce structured 1-3 BNT-Epoxy composites.

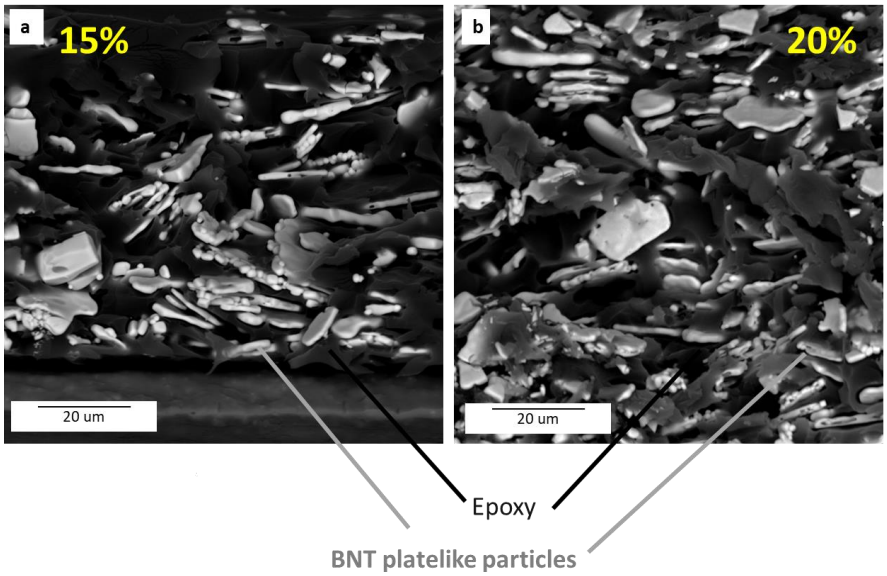

Figure 7.5: SEM image of (a) 15% BNT-Epoxy and (b) 20%BNT-Epoxy composites

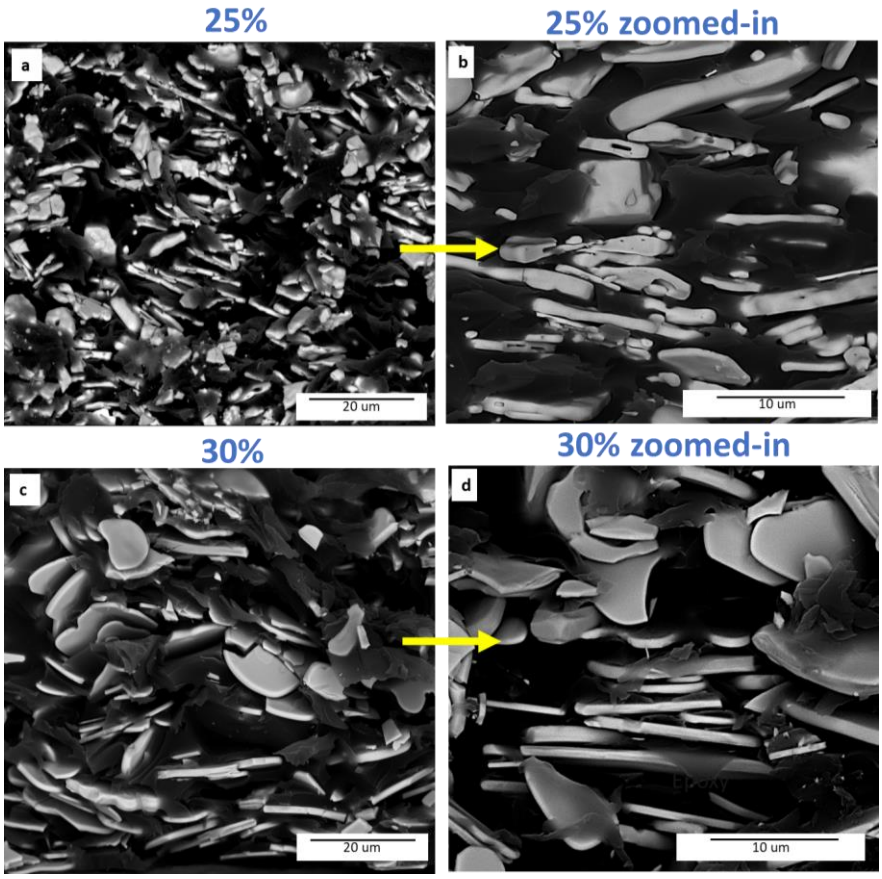

Figure 7.6: SEM image of (a) 25% BNT-Epoxy , (b) higher magnification of 25%BNT-Epoxy, (c) 30%BNT-Epoxy and (d) higher magnification of 30%BNT-Epoxy showing close-up view of particles alignment within the composite

BNT-Epoxy composites with 35% volume fractions are shown in the SEM micrographs of Figure 7.7 which reveals the highest alignment of the plate-like BNT particles within the polymer matrix investigated in this research. At a higher magnification Figure 7.7 (b), it is evident that the BNT particles are in a chain-like structure horizontal alignment in x-direction, stacked parallel on top of each other, within the epoxy matrix. The BNT particles' alignment using a doctor blade seems to be precise and consistent throughout the composite material with reduced inter-particle distance. In contrast, the composites with 40% BNT volume fraction were found to be more challenging to fabricate due to the high viscosity of the composite mixture, making it difficult to obtain uniform thickness using the doctor blade technique. Additionally, the high filler content led to a stiff and brittle composite, which lacked the flexibility needed for practical applications. Therefore, this study has focused on BNT-Epoxy composites encompassing various ceramic volume fractions up to 35% BNT in the composite, at which optimal BNT platelike particles' alignment was observed. BNT-Epoxy composites with 35% BNT, offer a balance between ease of fabrication and desired material properties.

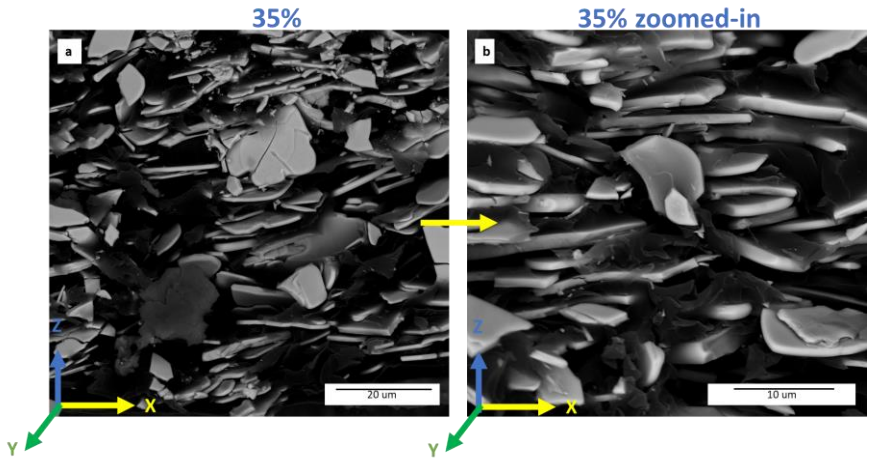

Figure 7.7: SEM image of (a) 35% BNT-Epoxy and (b) higher magnification of 35%BNT-Epoxy close-up view of particles alignment within the composite

7.2.3. EDX Analysis of BNT-Epoxy Composites

Figure 7.8 (a) shows the energy spectrum surface scan area of the fabricated 25% BNT-Epoxy thin film composite. The figure illustrates that the film cross-section surface is relatively homogenous with embedded plate-like BNT particles, which are aligned in chain-like structure parallel to each other. Additionally, the figure shows a high degree of coverage by the embedded plate-like particles, with fewer empty sections on the

surface of the film. Figure 7.8 (b) displays the total map of all elements, whereas Figure 7.8 (c)-(h) represent the distribution of individual elements, including Bi, Na, Ti, C, O, and Al, respectively. The Bi, Na, Ti and O elements are sourced from the $Bi_{0.5}Na_{0.5}TiO_3$, while C is derived from the Epoxy matrix and Al from the aluminum foil on which the composite was deposited. Locations, where plate-like particles are present in the composite film, are Bi, Na, and Ti. These elements are found to be aggregated at the particle locations and display a corresponding distribution with each other. In contrast, the locations where no particles exist show an absence of these elements, and instead, the carbon content indicative of the epoxy matrix is observed. Notably, the oxygen element is found to be present throughout the sample, including the areas where particles are absent, and its distribution is complementary to the distribution of Na, Bi, and Ti.

The X-ray energy spectrum content, as illustrated in Figure 7.8. (a) and displayed in Figure 7.9 exhibits primary peaks corresponding to Bi, Na, Ti, and O, indicating the synthesis of pure BNT using the optimum synthesis conditions. The weight % of the observed elements are also included in Figure 7.9. Notably, the presence of Aluminum in the sample substrate may contribute to the detection of Al peaks in the spectrum, as the X-ray excitation can penetrate the sample, exciting Al atoms in the substrate. Furthermore, the detection of C peaks in the spectrum may be attributed to Epoxy matrix, which contains C atoms, while small peaks for Pt, are from the platinum coating on the composite film. Notably, the acceleration voltage was set to 15 kV, which was sufficiently high to penetrate through the film material and allowed for the detection of the Pt peaks in the substrate. The analysis of the EDX figures further suggests the horizontally aligned plate-like particles in the composite material comprise the dielectric component, which is BNT, while the remaining portion consists of the Epoxy matrix.

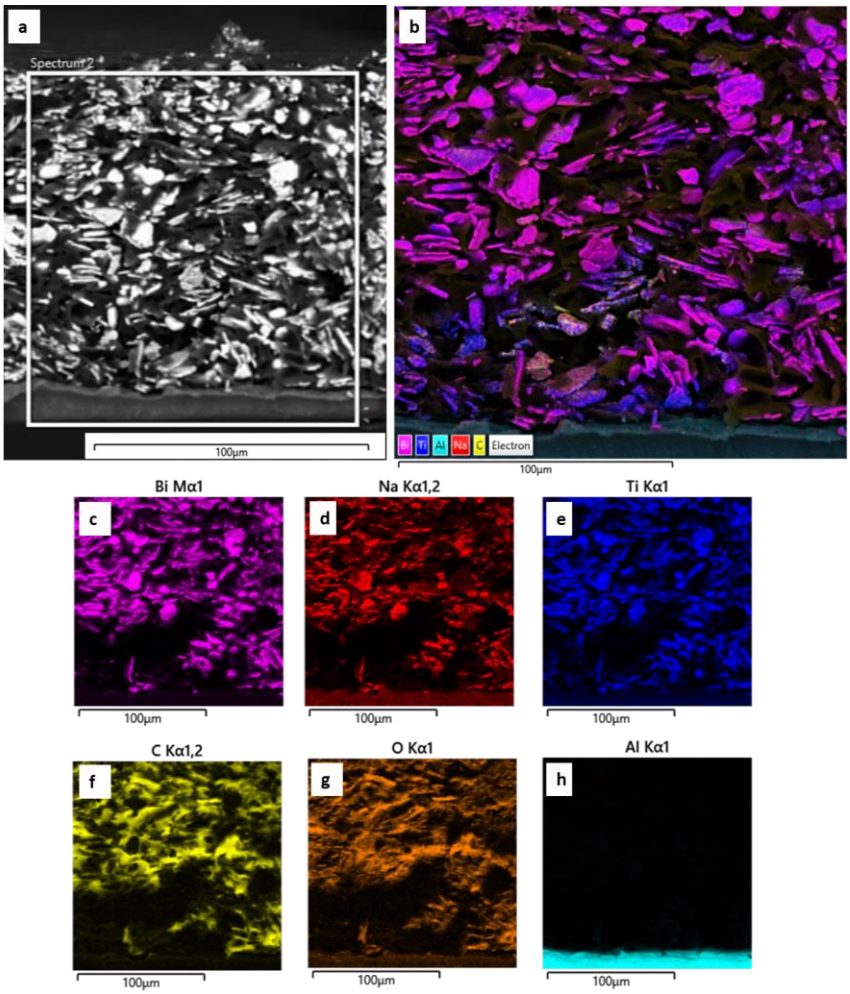

Figure 7.8: (a) Energy spectrum scan surface area of 25%BNT-Epoxy composites, (b) EDX map of total elements, (c) Bi element, (d) Na element, (e) Ti element, (f) C element, (g) O element and (h) Al element

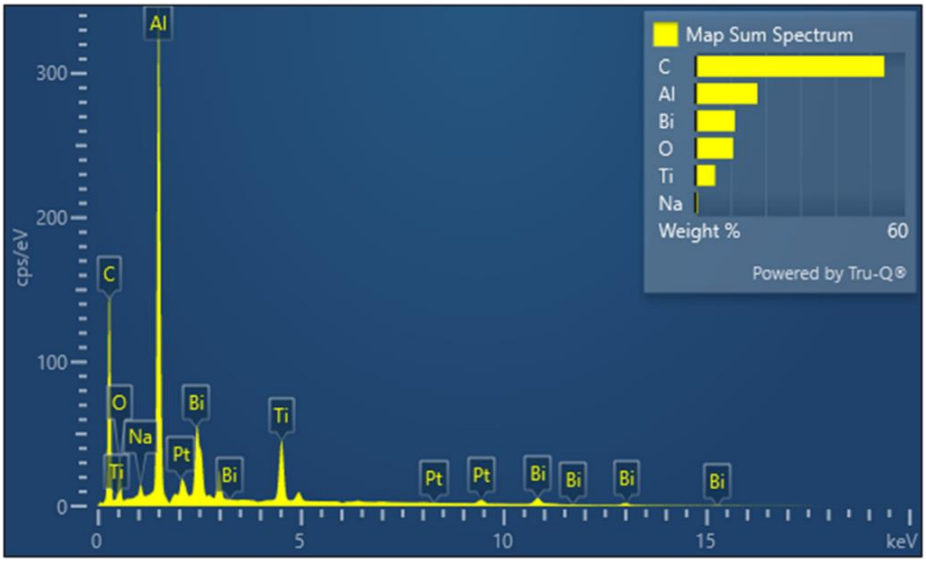

Figure 7.9: EDX energy spectrum content with weight% of the obtained elements

7.3. Dielectric Performance of BNT-Epoxy Composites

To assess the dielectric performance of the composites highlight the correlation between the optimisation of the synthesis process for the ceramic fillers, the employment of a mechanical alignment fabrication technique, and their impact on the electrical properties of the fabricated composite, the dielectric constant has been assessed as a function of the varying BNT volume fraction as shown in Figure 7.10, alongside the theoretical dependencies of Yamada and Bowen's models. It was observed that an increasing BNT content resulted in an increased value of the corresponding dielectric constant. At a BNT content of 35%, the dielectric constant reached a maximum value of 52, indicating a significant enhancement. At higher BNT ceramic loading fractions, the shielding provided by the polymer matrix may not be adequate for the complete coverage of individual ceramic particles [349]. Consequently, the contribution of the ceramic phase to the dielectric constant of the composite becomes more pronounced at higher volume fractions. This is consistent with literature in which dielectric constant had a direct relation with the volume fraction [350,351].

The best fit for Yamada's model (presented in Equation 2.11) was achieved at n=7 indicating elongated particles [352]. A low value of n implies that the filler particles are almost spherical, whereas a high value of n suggests that the filler particles are mostly non-spherically formed [353]. The dielectric constant of the BNT powder and the utilised Epotek Epoxy system are provided in Table 7.1.

Table 7.1: Dielectric and piezoelectric properties BNT and Epoxy

Material	**ε at 1 KHz**	**d_{33} (pC/N)**	**Y(GPa)**
BNT	302.6 [354]	80	16.7 [355]
(EpoTek) Epoxy	5.53	-	1.7

The fitted Yamada model was found to predict lower dielectric values than those observed experimentally for the developed 1-3 BNT-Epoxy composites. This finding is consistent with the expectation that 1-3 composites would exhibit enhanced dielectric behavior due to the alignment and enhanced connectivity of the ceramic particles in the composite structure. Additionally, the experimental data obtained for the structured BNT-Epoxy composites have been further analysed and compared with Bowen's model, where the interparticle distance was varied between 3μm to 5μm. The

findings reveal that the experimental values are in good agreement with Bowen's model, particularly for an interparticle distance of equivalent to 4μm for a volume % of BNT above 25%. This was consistent with the interparticle distance measured using ImageJ from the SEM images of the 25% composite. This suggests that the developed composites may possess a desirable interparticle distance that could potentially lead to improved dielectric properties. The utilisation of the mechanical alignment to homogeneously distribute and align the particles, along with the size of the herein optimally synthesised two-dimensional particles may have contributed to the obtained interparticle distance.

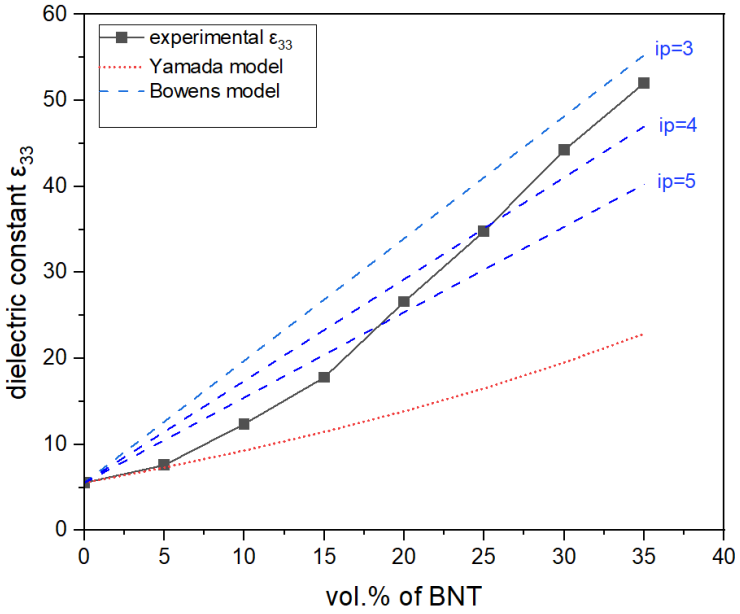

Figure 7.10: Variation of the dielectric constant with varying BNT volume content, along with Yamada and Bowens model comparison

7.4. Piezoelectric Performance of BNT-Epoxy Composites

To gain a comprehensive understanding of the characteristics of the fabricated BNT-Epoxy composites, this section presents an investigation of the relevant piezoelectric characteristics.

Since, the piezoelectric properties of poled samples are known to be influenced not only by the strength of the poling field but also by the poling orientation and the direction of the applied electric field [206],it is therefore crucial to determine the appropriate polarity and direction of the applied electric field to achieve effective poling of fabricated BNT-Epoxy composite samples. The samples were poled in two different positions, with the electric field applied perpendicular to the aligned particles

in one position (designated as horizontally poled), and parallel to the aligned particles in the other (designated as vertically poled), using a 17kV DC voltage as shown in Figure 3.16 in chapter 3. It was aimed to determine which of these orientations would lead to the most effective poling of the samples and thus improved values of the resulting d_{33} coefficients.

The poling process has been designated to last for a duration of 120 minutes for each sample during this study. Additionally, to investigate any variations in the d_{33} values, certain samples were subjected to both negative and positive polarity during the experimentation process.

7.4.1. Piezoelectric Charge Coefficient d_{33} Properties

The piezoelectric charge coefficient, d_{33}, has been measured for both, the parallel and perpendicular, and positive and negative poled BNT-Epoxy composites at a static force of 10N and a dynamic force of 0.25 N at a frequency of 110 DC. No significant difference in the d_{33} values of the positively and negatively poled samples was observed and hence the results presented herein are based on the measurements of the positively poled samples (positive polarity employed during corona poling).

Figure 7.11 demonstrates the relationship between the volume percentage of incorporated BNT and the corresponding d_{33} values for perpendicular (horizontally) and parallel (vertically) poled samples. Due to the difficulty in removing the foil from the samples at lower volume fractions, which often resulted in sample breakdown, vertical poling of samples was only possible for volume fractions equal to or greater than 25%. A clear trend of the increase in the d_{33} values is observed with an increase in the BNT volume fraction. This indicates that the piezoelectric properties of the composite material are directly influenced by the amount of BNT which is consistent with the findings of the Yamada model. The experimental data was fitted to Yamada's model for both horizontally and vertically poled composites assuming same depolarisation factor n=7 as in the fitting of the dielectric constant model. Moreover, the best fit of the experimental data to the model predictions (presented in Equation 2.13 of chapter 2) resulted in α values of 0.1 and 0.2 for horizontally and vertically poled samples, respectively (seen in Figure 7.11). These findings suggest a higher poling efficiency for parallel (vertically) poled composites compared to the perpendicular (horizontally) poled samples. The obtained results indicate a notable

difference in the piezoelectric response of the vertically and horizontally poled samples, particularly at higher volume fractions (i.e., above 30%). The vertically poled samples exhibited higher d_{33} values compared to the horizontally poled ones. A maximum value of 4.5 pC/N was obtained at 35% in the vertically poled composites. These findings are consistent with previous studies [206], which suggested that the direction of poling plays a critical role in determining the piezoelectric response of the material. Therefore, it can be inferred that poling of the mechanically aligned and optimally synthesised BNT-Epoxy composite samples in a parallel direction to the electric field is a more effective method for enhancing their piezoelectric properties, particularly at higher volume fractions.

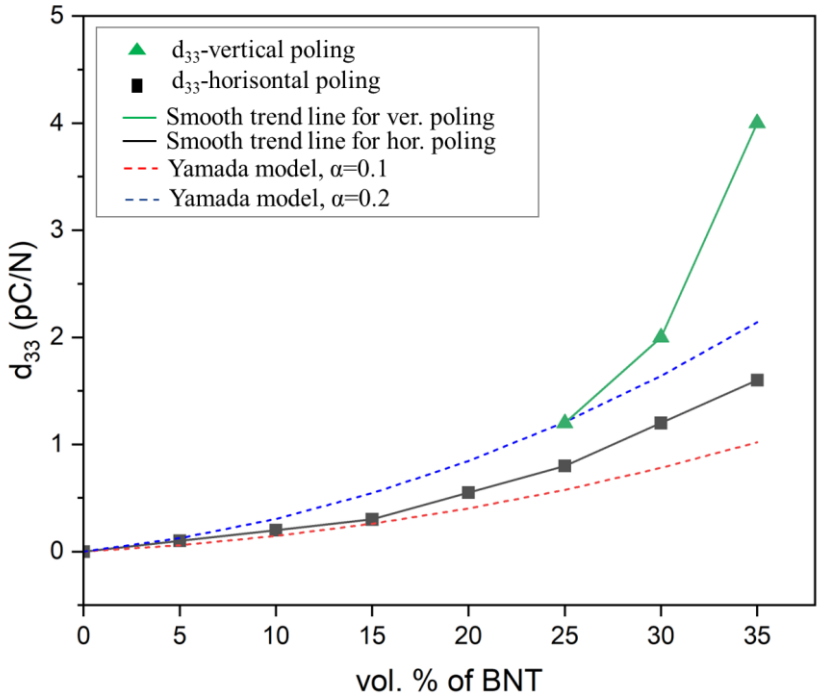

Figure 7.11: Variation of the piezoelectric charge coefficient (d_{33}) with varying BNT volume content

7.4.2. Piezoelectric Voltage Coefficient g_{33} Properties

Figure 7.12 shows the variation of the g_{33} values with the corresponding BNT volume fraction which was calculated using Equation 2.8 presented in Chapter 2 and given the data for the d_{33} of the horizontally poled sample. It is clearly observed that an increase in the BNT volume content in the polymer results in a gradual increase in the respective g_{33} coefficient. A maximum value of 3.5 mV.m/N was observed at 35%. It is suggested that the increase in the g_{33} coefficient may be attributed to the simultaneous increase in both the d_{33} coefficient and the dielectric constant. However, it may be primarily

driven by the significant increase in the corresponding dielectric constant as it exhibited a substantial rise with increased ceramic volume fraction compared to the d_{33} rise that was exhibited in the horizontally poled samples. This may further suggest that the influence of the dielectric constant on the g_{33} coefficient is more dominant in the herein developed composite system.

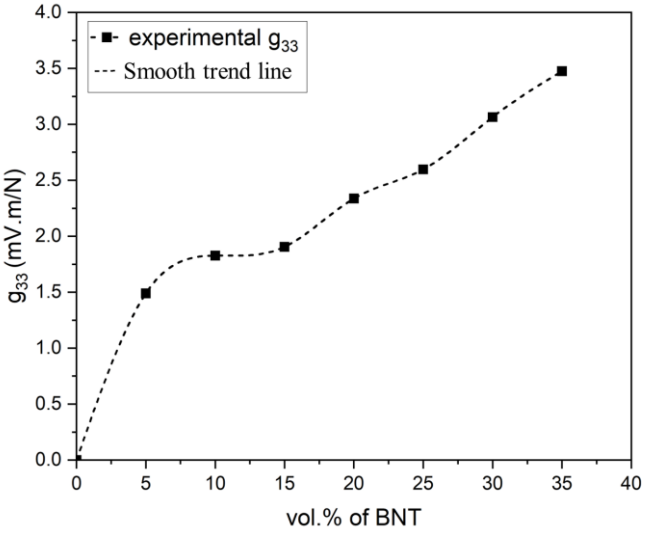

Figure 7.12: Variation of the piezoelectric voltage coefficient (g_{33}) with varying BNT volume content

7.5. Ferroelectric Performance of BNT-Epoxy Composites

This section delves deeper into assessing the ferroelectric and energy storage potential of the developed BNT-Epoxy composites.

7.5.1. P-E loop Hysteresis Analysis

The P-E loops for the varying BNT volume fractions-Epoxy composites have been investigated at various applied electric fields in the range of 65kV/cm – 200kV/cm at room temperature, and the obtained P-E loops for 5%-35% are shown in Figure 7.13 respectively. The ferroelectric nature of the developed quasi 1-3 BNT-Epoxy composites has been confirmed through the acquired hysteresis loops. As observed, the composites exhibit increased polarisation degrees as a function of increasing the applied electric field. This is due to the increased reorientation of dipoles within the BNT ceramic particles that are exhibited with increasing electric field strength. The experimentally obtained P-E loops of the composites show similar loop shapes comparable to the ideal loop shape form of the Rayleigh model [356], which presumes

that the polarisation response of a ferroelectric material is directly proportional to the power of the applied electric field [356].

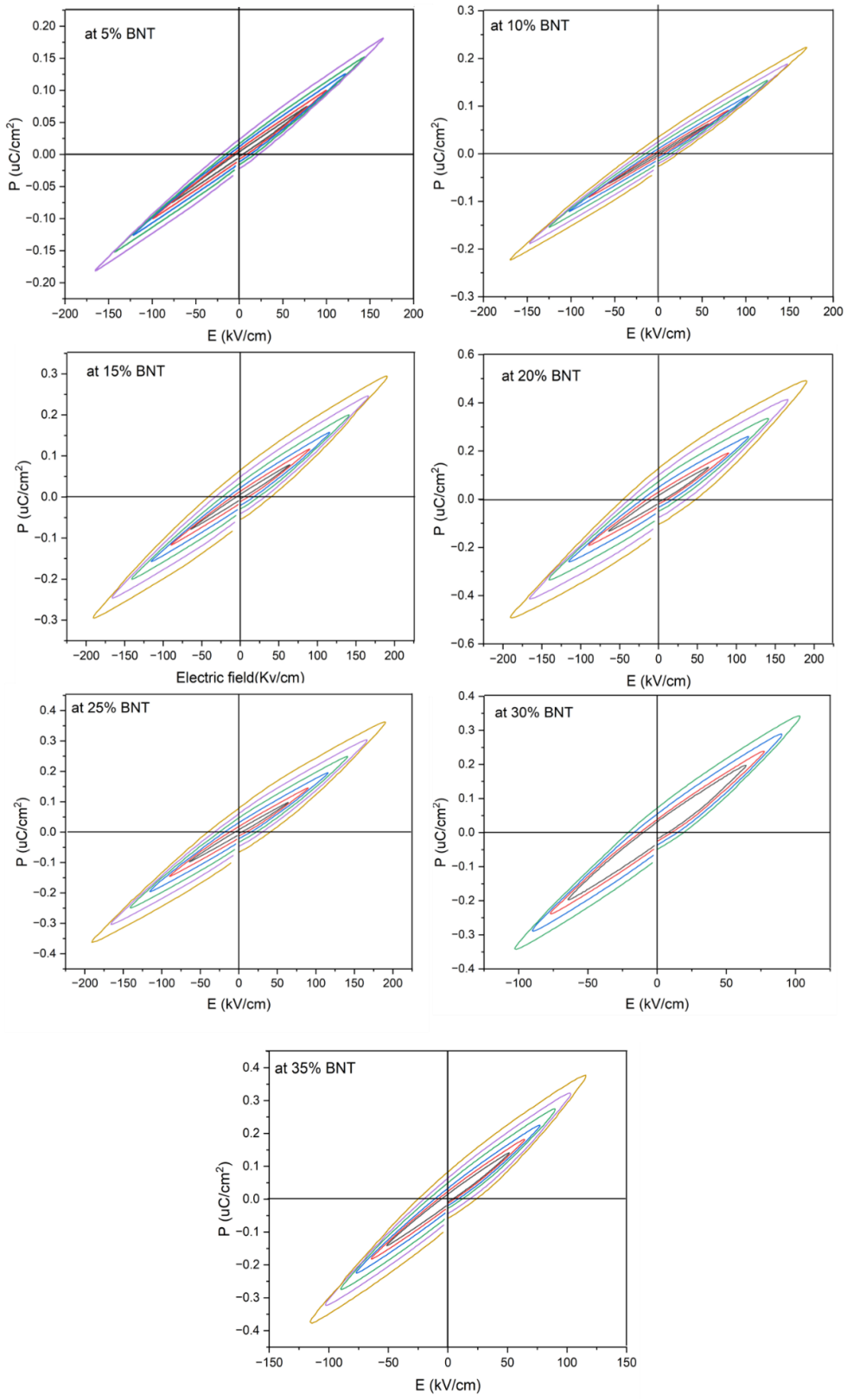

Figure 7.13: P-E hysteresis loops of BNT-Epoxy composites with varying BNT volume content

It is further observed that the fabricated composite samples did not exhibit fully saturated P-E loops at high electric fields (Figure 7.13). This may be attributed to the presence of oxygen vacancies and current leakage in the incorporated synthesised BNT ceramic particles [357]. The oxygen vacancies arise from the volatilisation of Bi and Na elements during the high-temperature molten salt synthesis, resulting in lowered breakdown strength and reduction of Ti^{4+} at the B site to Ti^{3+}, thereby increasing the level of leakage and limiting the ferroelectric properties [357].

Figure 7.14 depicts the P-E loop for various BNT ceramic volume fractions at an applied electric field of 120kV/cm. It is worth noting that the estimation of the maximum applied electric field was challenging due to the samples breaking down at various electric fields and hence a common, relatively high, applied electric field was selected for the comparison of the hysteresis behavior. All hysteresis loops exhibit a narrow shape, suggesting minimal energy dissipation characterised by the enclosed area within the loops. The observed trend (in Figure 7.14 (b)) reveals that an increase in the volume fraction of the BNT ceramic filler from 5% to 35% leads to a significant rise in the composite material's saturation polarisation (Ps), reaching a maximum saturation polarisation of P_s= 0.39 μC/cm^2 at 35% BNT. Upon closer examination of the polarisation (P_s) plot, it became apparent that there is a gradual rise in P_s until a notable and sudden increase is observed at the 25% BNT content. Subsequently, the curve continues to exhibit a linear increase. This behavior can be attributed to the alignment of a substantial portion of particles, which became evident at the 25% threshold. Undoubtedly, the alignment of the particles in one direction facilitates the reorientation of the dipoles. Meanwhile, the polarisation P_r plot continues to grow non-monotonously as the BNT volume content increases, reaching a maximum of approximately 0.55 μC/cm^2 at 35%. The coercive electric field, E_c, required to reduce the polarisation of the fabricated composites to zero after being polarised, also increases with increasing BNT content. This is indeed due to the increased ferroelectric domains within the BNT particles, which would require the increased electric field to overcome the material’s internal resistance to change polarisation.

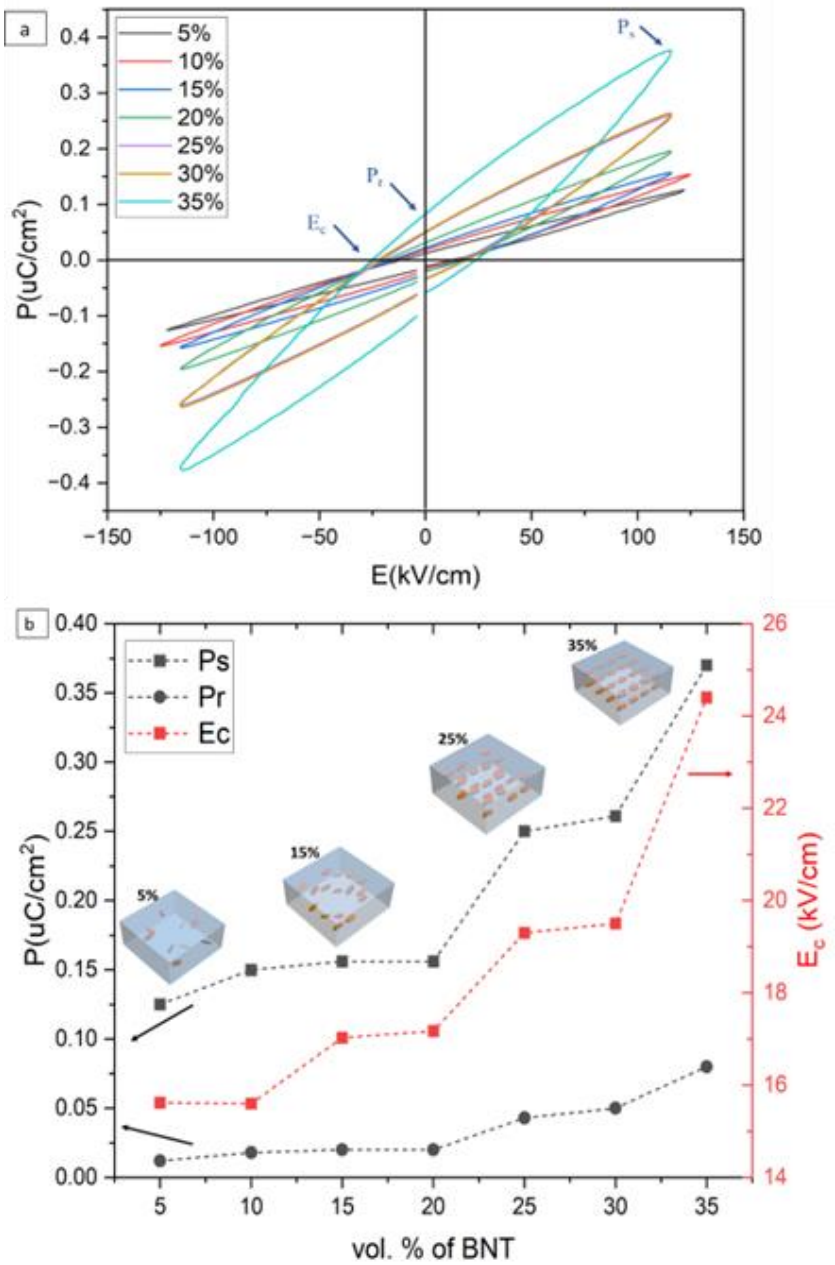

Figure 7.14: (a) Variation of BNT volume content impact on P-E hysteresis at 120kV/cm electric field, and (b) corresponding Ps, Pr, Ec values along with corresponding alignment schematic.

The attained E_c of the fabricated BNT-Epoxy composites containing 35% is 25.5 kV/cm. This value surpasses values obtained in lead-based ceramic-polymer counter composites as shown in Table 7.2. The higher E_c obtained in PVDF based composites is due to the inherent ferroelectric properties of the PVDF itself. Overall, the relatively high obtained E_c values indicate their relatively reduced leakage current and their enhanced energy storage density. The energy storage potential of the fabricated composites is further illustrated in the next section.

Table 7.2: Coercive electric field (E_c) of BNT and various composite systems

System	E_c(kV/cm)	Ref
BNT	73	[358]
0.6PZT/PVDF	7.82	[359]
PZT/PDMS	6.6	[360]
0.4 BCZT/PVDF	35.22	[361]
BFO/PVDF	42.52	[362]

7.5.2. Energy Storage Potential

The energy storage potential of the fabricated composites has been investigated by measuring the discharged energy density of the developed BNT-Epoxy composites utilising Equation 2.10 presented in Chapter 2, whereas E_{max} is the maximum applied electric field to the composite until breakdown. Due to the presence of extrinsic defects such as dust particles and air bubbles within the composite matrix which introduced heterogeneity in the observed breakdown electric fields, the true breakdown electric field could not be detected and hence was selected in this study as 1267 kV/cm based on a similar composite system [363]. Table 7.3 presents the obtained discharge energy density at varying BNT volume content.

Table 7.3: Discharge energy density (U_e) of the BNT-Epoxy composites at varying BNT volume content

Vol. % of BNT	U_e (J/cm^3)
5	0.54
10	0.88
15	1.26
20	1.89
25	2.47
30	3.14
35	3.7

The impact of the volume fraction of BNT particles on the discharged energy density in the BNT-Epoxy composites is clear, as illustrated by the increase in the obtained U_e with increasing volume content, presented in Table 7.3. At a BNT volume fraction of 35%, the mechanically aligned BNT-Epoxy composites exhibited a notable maximum energy density potential, reaching U_e=3.7 J/cm^3. This value was almost 6 times higher than the value obtained for the composites containing 5%. This enhancement may be attributed to the improved connectivity of the two-dimensional BNT particles at higher volume fractions, which indeed facilitated efficient charge transfer and thus enabled

more effective storage and release of energy. However, it is worth noting that increasing the ceramic filler volume fraction may lead to the formation of defective voids and other imperfections due to the increased local electric field because as a result of the mismatch between the dielectric constant of the ceramic filler and that of the polymer [364]. Therefore, in order to achieve higher energy storage density, it is always relevant to enhance the breakdown strength of the composites.

The energy density potential of the BNT-Epoxy composite has been compared with that of different ceramic-polymer composites, and the results are presented in the subsequent section for analysis.

7.6. Prospects of BNT-Epoxy Composites in Energy Storage Systems and Comparison with state-of-the-art composites

In this study, a remarkable dielectric constant (ε) of 52.1 was achieved by incorporating a 35% volume fraction of two-dimensional BNT ceramic particles in the Epoxy-based composites. This was compared to values reported in literature to establish a benchmark for evaluating the performance and potential applications of the herein developed composites as presented in Table 7.4. It is evident that the ε of the herein developed BNT-Epoxy composites surpassed the value of those reported in literature for other BNT-polymer based composites. Notably, in [365] and [366], lower percentages of BNT were incorporated into BNT-PVDF composites, i.e., 30%, resulting in a dielectric constant of 14.5 and 31.7, respectively. However, in this study, with a slightly higher BNT content of 35% (only 5% extra BNT), the dielectric constant value increased significantly by 258.62% and 63.08% compared to those of the BNT-PVDF composites, respectively. The herein achieved ε also demonstrated superior performance when compared to other epoxy-based systems, including a comparable value of ε = 51 achieved in a doped BTO-Epoxy composite system in [367], at relatively lower volume fraction (25%), yet through the utilisation of doping and solid-state reaction, which typically necessitates a longer processing time and involves multiple steps. In contrast, the ε of this study was achieved through a simpler and shorter ceramic synthesis process and without the need for doping. Consequently, while achieving the desired ε in this study required a higher ceramic filler percentage (35%) to achieve a comparable dielectric constant of 52, the preparation process, particularly that of the incorporated ceramic fillers, offered a more cost-effective and

straightforward approach. Obviously, the ε obtained in this study also surpassed those of other two-phase ceramic-polymer composites with comparatively lower incorporated BNT content, as demonstrated in the last section of the table. A comparison of the ε between composites aligned through DEP, such as the ZnO/PDMS composite prepared in [368] and the PZT/poled CBT composite prepared in [196], or via magnetic alignment, as demonstrated in BN/Fe_3O_4/PEN prepared in [369], reveals a notable enhancement of approximately 3.5 times greater for the proposed mechanical alignment technique. Remarkably, this superior dielectric performance was achieved in the ZnO/PDMS composite [368] with an even lower filler content. These findings suggest that the proposed mechanical alignment method to obtain quasi 1-3 composites allowed for the achievement of higher dielectric performance compared to that of other alignment techniques. This comparative analysis further highlighted the significant influence of particle size and shape, indicating that even with a lower volume percentage of particles, a higher dielectric constant can be achieved.

Table 7.4: Comparison of the obtained dielectric constant with various ceramic-polymer systems reported in literature

Ceramic-Polymer System		**Fabrication Process**	**φ of filler (%)**	**ε at 1 kHz**	**REF**
Filler	**Matrix**				
$Bi_{0.5}Na_{0.5}TiO_3$ (BNT)			-	302.6	[354]
	Epoxy		-	5.53	This work
BNT-based two-phase system					
BNT	PTFE*	Mould pressing	80%	15	[370]
BNT	PVDF	Solution casting + Hot pressing	30%	14.5	[365]
BNT	PVDF	Injection moulding (0-3)	30%	31.7	[366]
$Bi_{0.49}Na_{0.49}Ba_{0.02}TiO_3$ (BNBT)	PVDF	Solution casting	50%	22.5	[371]
Epoxy-based two-phase system					
BTO NP	Epoxy	Comma roll-coater	50%	40	[372]
BTO	Epoxy	Casting through film applicator	25%	13.27	[373]
BTO (doped with Ca and Zr)	Epoxy	Solution mixing	25%	51	[367]
Al_2O_3-AgNPs	Epoxy	Solution casting	70%	9.55	[374]

Table 7.4: Comparison of the obtained dielectric constant with various ceramic-polymer systems reported in literature (continued)

Ceramic-Polymer System		**Fabrication Process**	**φ of filler (%)**	**ε at 1 kHz**	**REF**
Filler	**Matrix**				
$Ba_{0.85}Ca_{0.15}Zr_{0.1}Ti_{0.9}O_3$	Epoxy	Solution casting	30%	24.16	[375]
Other two-phase based systems					
$BaNd_2Ti_4O_{12}$	LCP *	Hot pressing	60%	7.2	[214]
PZT (NW)	PVDF	Alignment through uniaxial stretching	40%	45	[376]
BTO	PEI*	Film casting + thermal imidisation	50%	37	[377]
BTO	TPU*	Conventional mixing	30%	31	[44]
BN	PI*	In-situ polymerisation	20%	3.75	[378]
$Ba_{0.6}Sr_{0.4}TiO_3$	PMMA*	Inkjet technology	50%	55	[379]
TiO_2-HfO_2	PVDF	Solution casting	10%	12.56	[380]
$CaCu_3Ti_4O_{12}$ (CCTO)	TPU*	Solvent casting	40%	56	[381]
$BaTiO_3$-Ag,	PVDF	Coaxial electrospinning	15%	19.4	[382]
$Ba_{0.6}Sr_{0.4}TiO_3$	PEEK*	Cold pressing	40%	23	[383]
Cu doped $PbTiO_3$	PMMA	Solution casting	5%	22.5	[384]
Pb $(Zr_{0.52}Ti_{0.48})$ O_3	PVDF	Solution casting	20%	25	[385]
BTO	PDMS	Mixing + moulding	15%	10.97	[386]
Co doped – TiO_3	Silicone Rubber	Mechanical mixing + hot pressing	50wt%	5.06	[387]
$Ba_{0.6}Sr_{0.4}TiO_3$	PVDF	Solution casting	40%	33.8	[388]
ZnO	PDMS	Dielectrophoresis	44%	15.5	[368]
PZT	Poled CBT*	high-temperature Dielectrophoresis	20%	15	[196]
BN/Fe_3O_4	PEN*	Magnetic Alignment	30%	12.5	[369]
PZT	LCT/PA	Hot pressing	50%	42	[389]
PZT	PDMS	Hot pressing	50%	37	[390]
$Ca_{0.55}Nd_{0.3}TiO_3$	PTFE*	Cold compression	70%	17.5	[391]
This Work					
BNT	Epoxy	Mechanical Alignment	35%	52	This Work

* LCP: liquid crystalline polymer; * PEI: polyetherimide;
* TPU: thermoplastic polyurethane; * PI: polyamide;
* PMMA: poly (methyl methacrylate); * PEEK: polyether ether ketone;
*CBT: cyclic butylene terephthalate; *PTFE: poly(tetrafluoroethylene)

Table 7.5 compares the discharged energy density attained in the current study to that of state-of-the-art composites reported in recent years, together with the accompanying breakdown electric field values. A maximum discharge energy density value of approximately 3.7 J/cm^3 was achieved at a breakdown electric field of E_{max} = 1267kV/cm, which is nearly eleven times higher than pure molten salt synthesised BNT and almost four times higher than pure epoxy. Although another BNT-based system, i.e. BNT/PA composite prepared in [363] exhibited the same breakdown electric field, however the herein achieved energy density is almost three times higher than that of the BNT/PA system. Significantly, in the context of a comparable breakdown field of 1243 kV/cm, the achieved discharged energy density of this study surpasses that of a BTO-Epoxy system [373] by a considerable margin. The BTO-Epoxy system exhibits a U_e value of 0.34 [373], whereas the energy density attained in this study reaches 3.7, representing an approximately tenfold increase. The enhanced energy density performance of the developed BNT-Epoxy composites is further evidenced by the comparison with other two-phase based systems such as in the case of a $K_{0.5}Na_{0.5}NbO_3$ –0.15 $SrTiO_3$/PVDF composite prepared in [392], where a higher breakdown electric field of 1500kV/cm resulted in an even three time lower energy density value, although higher breakdown electric field are anticipated to result in higher energy density values. This further proves that the attained dielectric constant of this study significantly affects the corresponding discharge energy density.

Table 7.5: Comparison of the obtained energy density with various ceramic-polymer systems reported in literature

Ceramic-Polymer System		**Fabrication Process**	**E_{max} (kV/cm)**	**U in (J/cm^3)**	**Ref.**
Filler	**Matrix**				
$Bi_{0.5}Na_{0.5}TiO_3$ (BNT)			150 from [393]	0.31 (calc.)	[393]
	Epoxy		2016 from [394]	0.99 (calc.)	[394]
BNT-based two-phase system					
BNT (MSS platelets)	PA *	In-situ polymerisation	1267	1.24	[363]
BNT	PVDF	Solution casting + hot pressing	2080	2.58	[365]
Epoxy-based two-phase system					
$BaTiO_3$(BTO)	Epoxy	Free casting	60	0.196	[395]

Table 7.5: Comparison of the obtained energy density with various ceramic-polymer systems reported in literature (continued)

Ceramic-Polymer System		**Fabrication Process**	**E_{max} (kV/cm)**	**U in (J/cm^3)**	**Ref.**
Filler	**Matrix**				
BTO	Epoxy	Capillary force + vacuum defoaming	100	0.11	[396]
BTO	Epoxy	Casting through film applicator	1243	0.34	[373]
Al_2O_3-AgNPs	Epoxy	Solution casting	200	0.01	[374]
3D-BTO	Epoxy	Freeze drying + Epoxy Injection	100	0.02	[397]
$Ba_{0.85}Ca_{0.15}Zr_{0.1}Ti_{0.9}O_3$	Epoxy	Solution casting	1460	2.28	[375]
Other two-phase based systems					
BTO @ SiO2	PVDF	Solution casting	1450	1.08	[398]
PZT (NW)	PVDF	Alignment through uniaxial stretching	150	1.28	[376]
BTO	PEI	film casting and thermal imidization	1.5	1.28	[377]
BTO	PVDF	Mixing + quenching in ice-water bath	2250	3.24	[399]
$Ba_{0.95}Ca_{0.05}Zr_{0.15}Ti_{0.85}O_3$ (BCZT)	PVDF	Solution casting method	679	2	[163]
$K_{0.5}Na_{0.5}NbO_3$ – 0.15 $SrTiO_3$	PVDF	Solution casting	1500	1.34	[392]
BTO	TPU *	Conventional mixing	1500	3.1	[44]
Graphene	PVDF	Drop casting + compression moulding	275	3.1	[400]
$CaCu_3Ti_4O_{12}$ (CCTO)	TPU *	Solvent casting method.	810	0.8	[381]
This Work					
BNT	Epoxy	Mechanical Alignment	1267	3.7	This Work

With a dielectric constant of 52 and a discharge energy density of 3.7 J/cm³, the developed BNT-Epoxy composites hold promise for various dielectric applications. Due to its high dielectric constant, it has the potential to enhance the performance of capacitors, enabling them to store more electrical energy. Additionally, the significant energy discharge density suggests that these BNT-Epoxy composites can effectively release stored energy when needed, making it suitable for applications in energy storage systems, power electronics, and pulsed power devices. The figures presented in Figure 7.15 below provide additional visual insights (based on the provided data in

Table 7.4 and Table 7.5) into the comparison between the dielectric constant and discharge energy density achieved in this study and those of the state-of-the-art two-phase ceramic-polymer composite system.

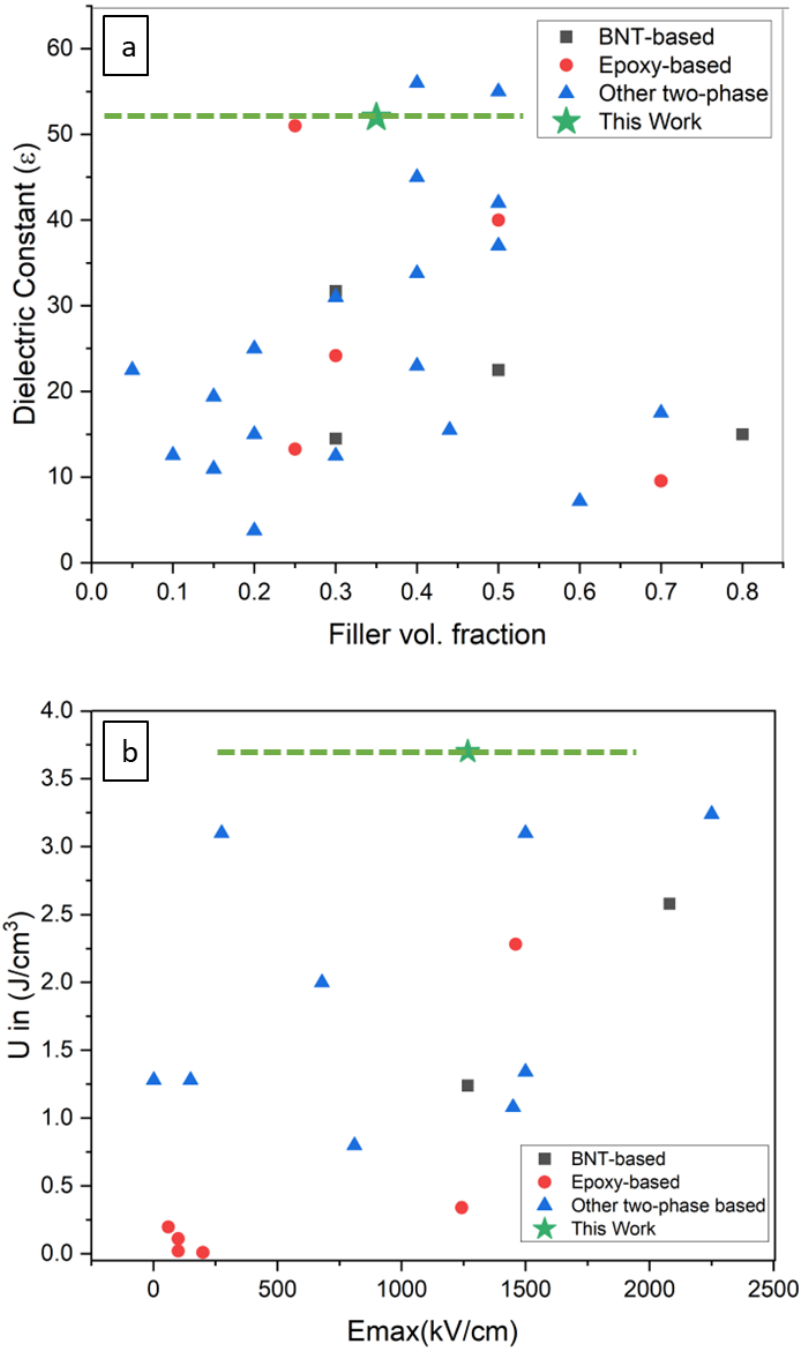

Figure 7.15: A schematic showing visual comparison of (a) dielectric constant and (b) discharge energy density achieved in this study and those of the state-of-the-art bi-phasic composite system.

7.7. Summary

In this chapter, the results of the fabricated BNT-Epoxy composites are presented. These composites were prepared by using optimally synthesised two-dimensional BNT particles as fillers and implementing a mechanical alignment approach to develop quasi 1-3 structures. A comprehensive microstructure analysis revealed that composites fabricated with non-optimally synthesised powder exhibited poor alignment, with areas of agglomerations at higher volume fractions compared to composites fabricated with optimally synthesised powder which demonstrated successful chain-like alignment at higher volume fractions (above 25%), with an optimum alignment observed at 35%. This further confirmed the impact of filler size on the alignment and validated the effectiveness of mechanical alignment in achieving a chain-like structure of two-dimensional plate-like particles. This chapter has also evaluated the dielectric, piezoelectric, and ferroelectric performance of the composites. A maximum ε of 52 was obtained at a 35% BNT volume content in the composite. The poling direction has proven to significantly affect the d_{33} of the composites, in which composites poled in a parallel direction to the applied electric field showed higher d_{33} values compared to those poled in a perpendicular direction, with a maximum of 4.5 pC/N obtained at 35%BNT volume content. At this volume content the corresponding g_{33} value achieved a maximum of 3.5 mV.m/N. Additionally, the ferroelectric nature of the quasi 1-3 BNT-Epoxy composites was confirmed through the obtained hysteresis loops, showing increased saturation polarisation with increasing applied electric field. Under a maximum breakdown electric field of 1267 kV/cm, a maximum discharge energy density of 3.7 J/cm^3 was achieved at 35% BNT volume content. The herein attained dielectric constant and discharge energy density surpassed values reported in literature for other BNT-based, Epoxy-based and other two-phase based ceramic-polymer composites. The dielectric constant achieved in this study, notably surpassed that of reported dielectrophoretically aligned composites, highlighting the superior effectiveness of the proposed mechanical alignment approach with an enhancement of nearly 3.5 times greater.

Chapter 8

8. Conclusions

This study has successfully developed and optimised predictive mathematical models that provide a comprehensive depiction of the intricate shape and precise size of two-dimensional plate-like ceramic particles synthesised using molten salt synthesis. Furthermore, this research has explored the use of an alternative mechanical alignment method, which effectively resulted in a higher dielectric constant and increased discharge energy density for quasi-1-3 ceramic-polymer composites when compared to the current state-of-the-art composites. A schematic showing a summary of the herein obtained contribution to knowledge is depicted in Figure 8.1.

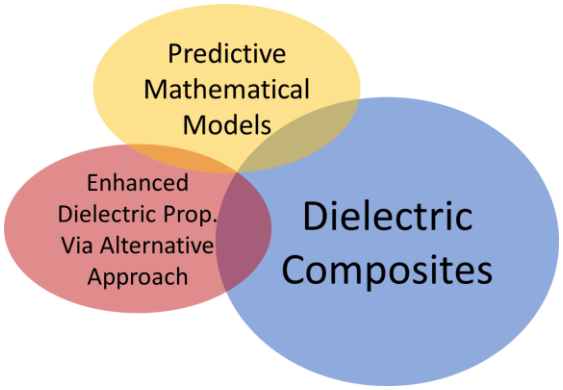

Figure 8.1: A schematic showing a summary of the contribution to knowledge.

The herein developed models consider the variable molten salt synthesis parameters and their simultaneous influence on the resulting particle characteristics, based on the synthesis of BNT as a case study. The main (individual) effect of three molten salt synthesis parameters, namely synthesis temperature, holding time, and heating rate, as well as the combined interaction (simultaneous) effects of these parameters on the morphology of the synthesised powder particles were systematically examined with the aid of the central composite design based RSM. In this context, the particle's morphology of the synthesised particles was initially depicted by five different responses, area, thickness, Feret's diameter, particle size and aspect ratio.

Based on the comprehensive statistical ANOVA analysis, the particle size and AR responses have deemed to be insignificant models with significant lack of fit and P-values of 0.21 and 0.052, respectively, suggesting that the response models for the particle size and AR of the synthesised particles do not fully capture the relationship between the synthesis parameters and the studied output. In fact, the parameter 'size'

lacks a clear and explicit definition of the exact dimensions or specific characteristics of the particles, especially when depicting irregular two-dimensional shaped particles. Data transformation for the first three responses was performed after analysing the ANOVA results. After which, three successful predictive mathematical models for the area (R1), thickness (R2) and Feret's diameter (R3) of the synthesised particles were developed as a function of the affecting interplay of the molten salt synthesis parameters. With an R^2 value of 0.97, 0.95, and 0.97 for R1, R2 and R3, respectively, these models suggested a strong correlation between the experimental data and the predicted outcomes of the models, thus signifying the reliability of the analysis.

Analysis of the ANOVA results further indicated that the main effect of the synthesis temperature was the factor with the most significant impact (P-value <0.0001) on the response variables in the MSS process, out of the three synthesis parameters under investigation. The main effect of both holding time and heating rate had no significant effect on the response variables. Interestingly, the combined effect of the interaction between synthesis temperature and holding time was identified as the second most significant factor affecting the morphology of the synthesised particles. These findings imply that holding time and heating rate may be neglected in regulating the response variables in future MSS experiments, with a focus instead on the synthesis temperature and its interaction with holding time. The predictive models were simultaneously solved, and the optimum synthesis parameters based on the GA-based multi-objective optimisation were obtained at a synthesis temperature of 1100ºC, and a holding time of 270 minutes at a heating rate of 7ºC/min, at which the particles are anticipated to have an average area of 152.671 µm^2, average thickness of 1.21 µm and an average Feret's diameter of 16.75 µm. Models have been validated based on the synthesis of the two-dimensional plate-like BNT powder and the actual results were BNT particles with an area of 156.56 µm^2, an average thickness of 1.467 µm and an average measured Feret's diameter of 17.18 µm. The good agreement between the predicted and actual results further confirmed the accuracy of the developed models. The herein synthesised BNT powder showed larger area, thickness and Feret's diameter compared to other molten salt synthesised two-dimensional ceramic particles.

By utilising a mechanical alignment approach, the optimally synthesised BNT powder was imbedded and aligned in a chain-like structure within a polymeric Epoxy matrix to achieve various quasi 1-3 ceramic-polymer composites with varying BNT volume

content. Optimally synthesised BNT particles exhibited a higher degree of alignment in the x-direction compared to non-optimal particles, indicating the importance of optimal shape and size in the alignment process. At 35% BNT content in the Epoxy matrix, perfectly chain-like aligned particles were successfully obtained. The evaluation of dielectric performance showed that the developed composites achieved a maximum dielectric constant of 52 at a BNT volume content of 35%, which was in good agreement with the Bowen's model for structured 1-3 composites. This value significantly surpassed the dielectric constants reported for other BNT-based, Epoxy-based, and two-phase based ceramic-polymer composite systems with almost 3.5 times higher and with even with a lower utilised ceramic volume content. This may be attributed to the larger particle size of the incorporated ceramic fillers as well as the efficacy of the proposed mechanical alignment technique. The piezoelectric performance was also assessed, and it was found that the d_{33} was primarily affected by the poling direction. Composites that were poled in parallel direction to the electric field, demonstrated higher d_{33} values compared to those poled in a perpendicular direction, particularly at higher volume fractions. A maximum d_{33} value of 4.5 pC/N was achieved at a 35% BNT volume content. In can be thus concluded, that parallel poling is more efficient in improving the piezoelectric characteristics of the mechanically aligned and optimally synthesised BNT-Epoxy composites. In the context of the piezoelectric voltage coefficient, g_{33}, an increasing trend with the increase of BNT volume content was observed, with a maximum of 3.5 mV.m/N at 35% BNT. The increasing trend of the g_{33} values was believed to be due to the substantial increase in the corresponding dielectric constant which was exhibited with increasing BNT volume content.

Ferroelectric properties of the developed composites were evaluated through performed P-E loops, confirming their ferroelectric nature. Composites with 25% BNT volume content and higher, exhibited a significant increase in their corresponding P_s and P_r with increasing BNT volume content, which was primarily attributed to the improved particle alignment observed at BNT volume fractions of 25% and above. At 35% the composites showed values of 0.39 $\mu C/cm^2$ and 0.55 $\mu C/cm^2$ for the P_s and P_r, respectively. The energy storage performance capabilities of the developed composites demonstrated promising results. Specifically, at a BNT volume content of 35%, the composites achieved a maximum discharge energy density of 3.7 J/cm^3 under a

maximum breakdown electric field of 1267 kV/cm. This value also outperformed other energy storage capabilities of various two-phase ceramic-polymer composite systems.

This study has provided valuable insights into the synthesis of two-dimensional ceramic particles with large plate-like shapes, with a means of providing predictive mathematical models that can facilitate easier control and prediction of the size and shape of future molten-salt synthesised particles. The highly obtained dielectric properties and energy storage capabilities observed in this study shed light on the effect of the mechanical alignment technique. The composites developed in this study show promising potential for capacitators, energy storage devices, microwave and RF devices.

Chapter 9

9. Recommendations for Future Work

Proposed recommendations for future work are as follows:

- The herein developed predicted models studied the influence of three molten salt synthesis parameters that were known to mainly affect the molten salt synthesis of desired products (refer to Figure 2.15). However, expanding the investigation to include additional synthesis parameters, such as the salt species, salt purity, and molar ratio between the salt and the precursor, alongside the parameters already studied in this work, may provide a more comprehensive understanding of the molten salt synthesis process. This broader exploration of parameters has the potential to lead to further optimisation and development of predictive models that capture the morphology of synthesised particles as a function of all affecting synthesis parameters.
- Further, the developed models were validated and tested by utilising the two-dimensionally plate-like shaped BNT powder. To further validate these models and signify their robustness, these models may be tested on other various two-dimensional perovskite materials.
- The efficacy of the proposed mechanical alignment method involving the use of a doctor blade has not been assessed on rods. It remains unclear whether the alignment of rods using a doctor blade will yield comparable results to the alignment achieved with BNT plate-like particles or not. Therefore, the mechanical alignment of rod-like shaped particles may be investigated in the future. The P-E loop of the herein synthesised pure BNT may be also measured.
- During this study, the effect of poling direction on the resulting piezoelectric performance of the developed composites, i.e., the d_{33}, has been investigated. The temperature was held constant during the poling procedure and was selected based on common poling temperatures for similar systems. In future studies it may be worthwhile to further investigate the effect of the poling temperature alongside the effect of the poling direction on the resulting piezoelectric performance. Moreover, to achieve enhanced piezoelectric performance of the developed composites, the utilisation of interdigitated electrodes may be an alternative. This may involve masking the composites with interdigitated electrodes during the poling procedure.

References

[1] R. Setiawan, M.M.V. Devadass, R. Rajan, D.K. Sharma, N.P. Singh, K. Amarendra, R.K.R. Ganga, R.R. Manoharan, V. Subramaniyaswamy, S. Sengan, IoT based virtual E-learning system for sustainable development of smart cities, J. Grid Comput. 20 (2022) 24.

[2] R.R. Shivwanshi, N. Nirala, Role of artificial intelligence in industries for advanced applications, in: Adv. Signal Process. Ind. 4.0, Vol. 1 Evol. Commun. Protoc. Appl. Manuf. Syst., IOP Publishing Bristol, UK, 2023: pp. 1–8.

[3] A.A. Basheer, Advances in the smart materials applications in the aerospace industries, Aircr. Eng. Aerosp. Technol. 92 (2020) 1027–1035.

[4] M. Ammar, A. Haleem, M. Javaid, S. Bahl, S.B. Garg, A. Shamoon, J. Garg, Significant applications of smart materials and Internet of Things (IoT) in the automotive industry, Mater. Today Proc. 68 (2022) 1542–1549.

[5] S. Sahoo, S. Ratha, C.S. Rout, S.K. Nayak, Self-charging supercapacitors for smart electronic devices: A concise review on the recent trends and future sustainability, J. Mater. Sci. 57 (2022) 4399–4440.

[6] J. Ponmozhi, C. Frias, T. Marques, O. Frazão, Smart sensors/actuators for biomedical applications, Measurement. 45 (2012) 1675–1688.

[7] C.-W. Kan, Y.-L. Lam, Future trend in wearable electronics in the textile industry, Appl. Sci. 11 (2021) 3914.

[8] N. Sezer, M. Koç, A comprehensive review on the state-of-the-art of piezoelectric energy harvesting, Nano Energy. 80 (2021) 105567. https://doi.org/10.1016/j.nanoen.2020.105567.

[9] W.A. Smith, The role of piezocomposites in ultrasonic transducers, in: Proceedings., IEEE Ultrason. Symp., IEEE, 1989: pp. 755–766.

[10] H. Wu, F. Zhuo, H. Qiao, L. Kodumudi Venkataraman, M. Zheng, S. Wang, H. Huang, B. Li, X. Mao, Q. Zhang, Polymer-/Ceramic-based Dielectric Composites for Energy Storage and Conversion, ENERGY Environ. Mater. 5 (2022) 486–514. https://doi.org/10.1002/eem2.12237.

[11] S. Bardakhanov, V. Lysenko, A. Nomoev, D. Trufanov, Ceramic Preparation of Nanopowders and Experimental Investigation of Its Properties, 2011. https://doi.org/10.5772/24939.

[12] I. Gonzalo-Juan, R. Riedel, Ceramic synthesis from condensed phases, ChemTexts. 2 (2016) 1–21. https://doi.org/10.1007/s40828-016-0024-6.

[13] T. Kimura, Molten Salt Synthesis of Ceramic Powders, in: Adv. Ceram. - Synth. Charact. Process. Specif. Appl., InTech, 2011. https://doi.org/10.5772/20472.

[14] N. Díez, A.B. Fuertes, M. Sevilla, Molten salt strategies towards carbon materials for energy storage and conversion, Energy Storage Mater. 38 (2021) 50–69. https://doi.org/10.1016/J.ENSM.2021.02.048.

[15] D. Karoblis, A. Zarkov, T. Murauskas, A. Kareiva, Molten Salt Synthesis of

Micro-Sized Hexagonally Shaped REMnO3 (RE = Y, Er, Tm, Yb), Inorganics. 11 (2023) 178. https://doi.org/10.3390/inorganics11050178.

[16] X. Zhu, J. Zhou, M. Jiang, J. Xie, S. Liang, S. Li, Z. Liu, Y. Zhu, J. Zhu, Z. Liu, Molten Salt Synthesis of Bismuth Ferrite Nano- and Microcrystals and their Structural Characterization, J. Am. Ceram. Soc. 97 (2014) 2223–2232. https://doi.org/10.1111/jace.12897.

[17] F. Madaro, R. Sæterli, J.R. Tolchard, M.-A. Einarsrud, R. Holmestad, T. Grande, Molten salt synthesis of K4Nb6O17 , K2Nb4 O11 and KNb3O8 crystals with needle- or plate-like morphology, CrystEngComm. 13 (2011) 1304–1313. https://doi.org/10.1039/C0CE00413H.

[18] C.P. Bowen, R.E. Newnham, C.A. Randall, Dielectric properties of dielectrophoretically assembled particulate-polymer composites, J. Mater. Res. 13 (1998) 205–210. https://doi.org/10.1557/JMR.1998.0027.

[19] Z. Zhang, F. Wen, Z. Sun, X. Guo, T. He, C. Lee, Artificial intelligence-enabled sensing technologies in the 5G/internet of things era: from virtual reality/augmented reality to the digital twin, Adv. Intell. Syst. 4 (2022) 2100228.

[20] R. Sudarmani, K. Venusamy, S. Sivaraman, P. Jayaraman, K. Suriyan, M. Alagarsamy, Machine to machine communication enabled internet of things: a review, Int J Reconfigurable Embed. Syst ISSN. 2089 (2022) 4864.

[21] F. Cheng, J. Liang, Z. Tao, J. Chen, Functional materials for rechargeable batteries, Adv. Mater. 23 (2011) 1695–1715.

[22] P. Lv, X. Lu, L. Wang, W. Feng, Nanocellulose-based functional materials: from chiral photonics to soft actuator and energy storage, Adv. Funct. Mater. 31 (2021) 2104991.

[23] G. Shao, D.A.H. Hanaor, X. Shen, A. Gurlo, Freeze casting: from low-dimensional building blocks to aligned porous structures—a review of novel materials, methods, and applications, Adv. Mater. 32 (2020) 1907176.

[24] M.E. Villafuerte-Castrejón, E. Morán, A. Reyes-Montero, R. Vivar-Ocampo, J.A. Peña-Jiménez, S.O. Rea-López, L. Pardo, Towards lead-free piezoceramics: Facing a Synthesis Challenge, Materials (Basel). 9 (2016). https://doi.org/10.3390/ma9010021.

[25] M. Prauzek, J. Konecny, M. Borova, K. Janosova, J. Hlavica, P. Musilek, Energy harvesting sources, storage devices and system topologies for environmental wireless sensor networks: A review, Sensors. 18 (2018) 2446.

[26] L. Hongbo, Dielectrics under Electric Field, in: Electr. F., InTech, 2018. https://doi.org/10.5772/intechopen.72231.

[27] L. Yang, X. Kong, F. Li, H. Hao, Z. Cheng, H. Liu, J.-F. Li, S. Zhang, Perovskite lead-free dielectrics for energy storage applications, Prog. Mater. Sci. 102 (2019) 72–108. https://doi.org/10.1016/j.pmatsci.2018.12.005.

[28] J.F. Keithley, The story of electrical and magnetic measurements: from 500 BC to the 1940s, John Wiley & Sons, 1999.

[29] P. Barber, S. Balasubramanian, Y. Anguchamy, S. Gong, A. Wibowo, H. Gao, H. Ploehn, H.-C. Zur Loye, Polymer Composite and Nanocomposite Dielectric Materials for Pulse Power Energy Storage, Materials (Basel). 2 (2009) 1697–1733. https://doi.org/10.3390/ma2041697.

[30] S. Thomas, P. Balakrishnan, M.S. Sreekala, Fundamental Biomaterials: Ceramics, Elsevier Science, 2018. https://books.google.ae/books?id=WR2KswEACAAJ.

[31] M. Iqbal Khan, T. Chandra Upadhyay, General Introduction to Ferroelectrics, in: Multifunct. Ferroelectr. Mater., IntechOpen, 2021. https://doi.org/10.5772/intechopen.97720.

[32] Alexander K. Tagantsev ; L. Eric Cross ; Jan Fousek, Domains in Ferroic Crystals and Thin Films, Springer Nature, 2010.

[33] C.E. LAND, P.D. TEACHER, G.H. HAERTLING, Electrooptic ceramics, in: 1974: pp. 137–233. https://doi.org/10.1016/B978-0-12-002904-4.50010-3.

[34] R.S. Dahiya, M. Valle, Robotic Tactile Sensing, Springer Netherlands, Dordrecht, 2013. https://doi.org/10.1007/978-94-007-0579-1.

[35] G.H. Olsen, Ferroelectric Tungsten Bronzes, 2016.

[36] M. A. Wahab, Solid State Physics: Structure and Properties of Materials, Narosa Publishing House, 2005.

[37] Anthony R. West, Basic Solid State Chemistry, 2nd ed., Wiley–Blackwell, 1999. https://doi.org/10.1002/(SICI)1099-0739(200004)14:43.0.CO;2-F.

[38] J. Holterman, P. Groen, An Introduction to Piezoelectric Materials and Applications, Stichting Applied Piezo, 2013.

[39] A. Kakekhani, S. Ismail-Beigi, E.I. Altman, Ferroelectrics: A pathway to switchable surface chemistry and catalysis, Surf. Sci. 650 (2016) 302–316. https://doi.org/10.1016/j.susc.2015.10.055.

[40] U.O. Matthew, J.S. Kazaure, Chemical polarization effects of electromagnetic field radiation from the novel 5G network deployment at ultra high frequency, Health Technol. (Berl). 11 (2021) 305–317. https://doi.org/10.1007/s12553-020-00501-x.

[41] J.C. Burfoot, Ferroelectrics: an introduction to the physical principles, van Nostrand, 1967.

[42] E.T. Janes, E.T. Jaynes, E.T. Jaynes, M. Physicist, E.T. Jaynes, M. Physicien, Ferroelectricity, Princeton University Press, 1953.

[43] S.J. Blundell, K.M. Blundell, Concepts in thermal physics, Oxford University Press on Demand, 2010.

[44] M.N. Khan, N. Jelani, C. Li, J. Khaliq, Flexible and low cost lead free composites with high dielectric constant, Ceram. Int. 43 (2017) 3923–3926. https://doi.org/10.1016/j.ceramint.2016.12.061.

[45] N.K. Tailor, S. Satapathi, Anisotropy in Perovskite Single Crystals: From Fundamentals to Applications, J. Phys. Chem. C. 126 (2022) 17789–17803.

[46] A.J. Reza Moheimani, S.O.; Fleming, Piezoelectric Transducers for Vibration Control and Damping, Springer, London, 2006. https://doi.org/10.1007/978-3-540-77508-9_1.

[47] E.L. Pradeesh, S. Udhayakumar, M.G. Vasundhara, G.K. Kalavathi, A review on piezoelectric energy harvesting, Springer Berlin Heidelberg, 2022. https://doi.org/10.1007/s00542-022-05334-4.

[48] G. Viola, T. Saunders, X. Wei, K.B. Chong, H. Luo, M.J. Reece, H. Yan, Contribution of piezoelectric effect, electrostriction and ferroelectric/ferroelastic switching to strain-electric field response of dielectrics, J. Adv. Dielectr. 03 (2013) 1350007. https://doi.org/10.1142/s2010135x13500070.

[49] A. American, N. Standard, IEEE Standard on Piezoelectricity: An American National Standard, ANSI/IEEE Std 176-1987. (1988) 8–10. https://doi.org/10.1109/IEEESTD.1988.79638.

[50] S. Priya, H.-C. Song, Y. Zhou, R. Varghese, A. Chopra, S.-G. Kim, I. Kanno, L. Wu, D.S. Ha, J. Ryu, R.G. Polcawich, A Review on Piezoelectric Energy Harvesting: Materials, Methods, and Circuits, Energy Harvest. Syst. 4 (2019) 3–39. https://doi.org/10.1515/ehs-2016-0028.

[51] T. Zheng, J. Wu, D. Xiao, J. Zhu, Recent Development in Lead-Free Perovskite Piezoelectric Bulk Materials, Prog. Mater. Sci. 98 (2018) 552–624. https://doi.org/10.1016/J.PMATSCI.2018.06.002.

[52] X. Gao, M. Zheng, X. Yan, J. Fu, M. Zhu, Y. Hou, The alignment of BCZT particles in PDMS boosts the sensitivity and cycling reliability of a flexible piezoelectric touch sensor, J. Mater. Chem. C. 7 (2019) 961–967. https://doi.org/10.1039/c8tc04741c.

[53] T.R. Shrout, S.J. Zhang, Lead-free Piezoelectric Ceramics: Alternatives for PZT?, J. Electroceramics. 19 (2007) 111–124. https://doi.org/10.1007/s10832-007-9047-0.

[54] D.B. Deutz, N.T. Mascarenhas, J.B.J. Schelen, D.M. de Leeuw, S. van der Zwaag, P. Groen, Flexible Piezoelectric Touch Sensor by Alignment of Lead-Free Alkaline Niobate Microcubes in PDMS, Adv. Funct. Mater. 27 (2017) 1–7. https://doi.org/10.1002/adfm.201700728.

[55] J.F. Tressler, S. Alkoy, R.E. Newnham, Piezoelectric sensors and sensor materials, J. Electroceramics. 2 (1998) 257–272.

[56] G.F.J. and G.S. Schulze, Ferroelectric Crystals. 402 S. Oxford/London/New York/Paris 1962. Pergamon Press. Preis geb. 84 s. net, (1963).

[57] M.E. Lines, A.M. Glass, Principles and applications of ferroelectrics and related materials, Oxford university press, 2001.

[58] G. Liu, S. Zhang, W. Jiang, W. Cao, Losses in ferroelectric materials, Mater. Sci. Eng. RReports. 89 (2015) 1–48. https://doi.org/10.1016/j.mser.2015.01.002.

[59] Y. Wang, Y. Li, L. Wang, Q. Yuan, J. Chen, Y. Niu, X. Xu, Q. Wang, H. Wang, Gradient-layered polymer nanocomposites with significantly improved

insulation performance for dielectric energy storage, Energy Storage Mater. 24 (2020) 626–634. https://doi.org/10.1016/j.ensm.2019.06.013.

[60] Q. Sun, J. Wang, H. Sun, L. He, L. Zhang, P. Mao, X. Zhang, F. Kang, Z. Wang, R. Kang, L. Zhang, Simultaneously enhanced energy density and discharge efficiency of layer-structured nanocomposites by reasonably designing dielectric differences between BaTiO3@SiO2/PVDF layers and BNNSs/PVDF-PMMA layers, Compos. Part A Appl. Sci. Manuf. 149 (2021) 106546. https://doi.org/10.1016/j.compositesa.2021.106546.

[61] Y. Zhang, H. Kim, Q. Wang, W. Jo, A.I. Kingon, S.-H. Kim, C.K. Jeong, Progress in lead-free piezoelectric nanofiller materials and related composite nanogenerator devices, Nanoscale Adv. 2 (2020) 3131–3149.

[62] Y. Xu, Ferroelectric materials and their applications, Elsevier, 2013.

[63] E.A.R. Assirey, Perovskite synthesis, properties and their related biochemical and industrial application, Saudi Pharm. J. 27 (2019) 817–829. https://doi.org/10.1016/j.jsps.2019.05.003.

[64] H.-R. Wenk, A.G. (Andreĭ G. Bulakh, Minerals : their constitution and origin, Cambridge University Press, 2004. https://books.google.co.uk/books?id=mjIji8x-N1MC&pg=PA413&redir_esc=y#v=onepage&q&f=false (accessed April 26, 2019).

[65] M. De Graef, M.E. McHenry, Structure of Materials: An Introduction to Crystallography, Diffraction and Symmetry, Second, Cambridge University Press, 2012.

[66] R.S. Roth, Classification of Perovskite and Other ABO3-Type Compounds, J. Res. Natl. Bur. Stand. (1934). 58 (1957) 75–88. https://doi.org/org/10.6028/jres.058.010.

[67] P. Xu, D. Chang, T. Lu, L. Li, M. Li, W. Lu, Search for ABO 3 type ferroelectric perovskites with targeted multi-properties by machine learning strategies, J. Chem. Inf. Model. 62 (2022) 5038–5049. https://doi.org/10.1021/acs.jcim.1c00566.

[68] E. Taghaddos, M. Hejazi, A. Safari, Lead-free piezoelectric materials and ultrasonic transducers for medical imaging, J. Adv. Dielectr. 5 (2015) 1–15. https://doi.org/10.1142/S2010135X15300029.

[69] H. Wei, H. Wang, Y. Xia, D. Cui, Y. Shi, M. Dong, C. Liu, T. Ding, J. Zhang, Y. Ma, N. Wang, Z. Wang, Y. Sun, R. Wei, Z. Guo, An Overview of Lead-Free Piezoelectric Materials and Devices, J. Mater. Chem. C. (2018) 12446–12467. https://doi.org/10.1039/C8TC04515A.

[70] J. Rödel, W. Jo, K.T.P. Seifert, E.M. Anton, T. Granzow, D. Damjanovic, Perspective on the development of lead-free piezoceramics, J. Am. Ceram. Soc. 92 (2009) 1153–1177. https://doi.org/10.1111/j.1551-2916.2009.03061.x.

[71] H. Wei, H. Wang, Y. Xia, D. Cui, Y. Shi, M. Dong, C. Liu, T. Ding, J. Zhang, Y. Ma, N. Wang, Z. Wang, Y. Sun, R. Wei, Z. Guo, An overview of lead-free piezoelectric materials and devices, J. Mater. Chem. C. 6 (2018) 12446–12467.

https://doi.org/10.1039/c8tc04515a.

[72] F. Hussain, Lead-Free KNN-based Piezoelectric Ceramics, University of Sheffield, 2016.

[73] D.A. Van den Ende, Structured Piezoelectric Composites, University of Delft, 2012.

[74] Y. MATSUO, H. SASAKI, Formation of Lead Zirconate-Lead Titanate Solid Solutions, J. Am. Ceram. Soc. 48 (1965) 289–291. https://doi.org/10.1111/j.1151-2916.1965.tb14743.x.

[75] R. Zuo, L. Li, X. Hu, Z. Gui, Effect of silver dopant on electrical properties of PMN–PNN–PZT piezoelectric ceramics by complex impedance spectroscopy, Mater. Lett. 54 (2002) 185–190. https://doi.org/10.1016/S0167-577X(01)00561-4.

[76] W. Heywang, K. Lubitz, W. Wersing, Piezoelectricity- Evolution and Future of a Technology, Berlin, 2008.

[77] R.C. Turner, P.A. Fuierer, R.E. Newnham, T.R. Shrout, Materials for high temperature acoustic and vibration sensors: A review, Appl. Acoust. 41 (1994) 299–324. https://doi.org/10.1016/0003-682X(94)90091-4.

[78] P. Muralt, Ferroelectric thin films for micro-sensors and actuators: a review, J. Micromechanics Microengineering. 10 (2000) 136.

[79] A.-B.M. A. Ibrahim, R. Murgan, M.K. Abd Rahman, J. Osm, Morphotropic Phase Boundary in Ferroelectric Materials, Ferroelectr. - Phys. Eff. (2012). https://doi.org/10.5772/17206.

[80] T.C. Mike Chung, A. Petchsuk, Polymers, Ferroelectric, in: Encycl. Phys. Sci. Technol., Elsevier, 2003: pp. 659–674. https://doi.org/10.1016/B0-12-227410-5/00594-9.

[81] W. Gong, J.-F. Li, X. Chu, Z. Gui, L. Li, Combined effect of preferential orientation and Zr/Ti atomic ratio on electrical properties of Pb (Zr x Ti 1− x) O 3 thin films, J. Appl. Phys. 96 (2004) 590–595.

[82] M.R. Soares, A.M.R. Senos, P.Q. Mantas, Phase coexistence region and dielectric properties of PZT ceramics, J. Eur. Ceram. Soc. 20 (2000) 321–334.

[83] V. Buscaglia, M.T. Buscaglia, G. Canu, BaTiO3-based ceramics: Fundamentals, properties and applications, in: Encycl. Mater. Tech. Ceram. Glas., 2021: pp. 311–344. https://doi.org/10.1016/B978-0-12-803581-8.12132-0.

[84] P.K. Panda, Environmental friendly lead-free piezoelectric materials, J. Mater. Sci. 44 (2009) 5049–5062.

[85] F. Yan, H. Yang, Y. Lin, T. Wang, Dielectric and Ferroelectric Properties of SrTiO3-Bi0.5Na0.5TiO3-BaAl0.5Nb0.5O3 Lead-Free Ceramics for High-Energy-Storage Applications, Inorg. Chem. 56 (2017) 13510–13516. https://doi.org/10.1021/acs.inorgchem.7b02181.

[86] M.P.C.L.C. Devesa, Susanna; Fernandes Graca, Bismuth - Advanced Applications and Defects Characterization, InTech, 2018.

https://doi.org/10.5772/intechopen.71174.

[87] C. Zhu, Z. Cai, B. Luo, L. Guo, L. Li, X. Wang, High temperature lead-free BNT-based ceramics with stable energy storage and dielectric properties, J. Mater. Chem. A. 8 (2020) 683–692. https://doi.org/10.1039/c9ta10347c.

[88] S.H. Ji, J.H. Cho, Y.H. Jeong, J.-H. Paik, J. Do Yun, J.S. Yun, Flexible lead-free piezoelectric nanofiber composites based on BNT-ST and PVDF for frequency sensor applications, Sensors Actuators A Phys. 247 (2016) 316–322. https://doi.org/10.1016/j.sna.2016.06.011.

[89] X.-Y. Kang, Z.-H. Zhao, Y.-K. Lv, Y. Dai, BNT-based multi-layer ceramic actuator with enhanced temperature stability, J. Alloys Compd. 771 (2019) 541–546. https://doi.org/10.1016/j.jallcom.2018.08.311.

[90] M. Cao, L. Li, W. Bin Hong, S.Y. Wu, X.M. Chen, Greatly enhanced permittivity in BaTiO3-epoxy dielectric composites with improved connectivity of ceramic phase, J. Mater. 7 (2021) 1–7. https://doi.org/10.1016/j.jmat.2020.07.007.

[91] F. Gao, K. Zhang, Y. Guo, J. Xu, M. Szafran, (Ba, Sr)TiO3/polymer dielectric composites–progress and perspective, Prog. Mater. Sci. 121 (2021) 1–39. https://doi.org/10.1016/j.pmatsci.2021.100813.

[92] G. Tselikos, S. Rasul, P. Groen, C. Li, J. Khaliq, In situ printing and functionalization of hybrid polymer-ceramic composites using a commercial 3d printer and dielectrophoresis—a novel conceptual design, Polymers (Basel). 13 (2021). https://doi.org/10.3390/polym13223979.

[93] Y. Huang, F. Li, H. Hao, F. Xia, H. Liu, S. Zhang, (Bi0.51 Na0.47)TiO3 based lead free ceramics with high energy density and efficiency, J. Mater. 5 (2019) 385–393. https://doi.org/10.1016/j.jmat.2019.03.006.

[94] A. Deng, J. Wu, Enhanced strain and electrostrictive properties in lead-free BNT-based ceramics via rare earth doping, J. Mater. 8 (2022) 401–407. https://doi.org/10.1016/j.jmat.2021.08.002.

[95] W.P. Cao, W.L. Li, X.F. Dai, T.D. Zhang, J. Sheng, Y.F. Hou, W.D. Fei, Large electrocaloric response and high energy-storage properties over a broad temperature range in lead-free NBT-ST ceramics, J. Eur. Ceram. Soc. 36 (2016) 593–600. https://doi.org/10.1016/j.jeurceramsoc.2015.10.019.

[96] A. Mishra, B. Majumdar, R. Ranjan, A complex lead-free (Na, Bi, Ba)(Ti, Fe)O 3 single phase perovskite ceramic with a high energy-density and high discharge-efficiency for solid state capacitor applications, J. Eur. Ceram. Soc. 37 (2017) 2379–2384. https://doi.org/10.1016/j.jeurceramsoc.2017.01.036.

[97] Y. Zhao, X. Hao, M. Li, Dielectric properties and energy-storage performance of (Na0.5Bi0.5)TiO3 thick films, J. Alloys Compd. 601 (2014) 112–115. https://doi.org/10.1016/j.jallcom.2014.02.137.

[98] S.B. Vakhrushev, B.G. Ivanitskij, B.E. Kvyatkovskij, A.N. Majstrenko, R.S. Malysheva, N.M. Okuneva, N.M. Parfenova, Neutron-diffraction study on sodium-bismuth titanate, Fiz. Tverd. Tela. 25 (1983) 2613–2616.

[99] S. Gorfman, P.A. Thomas, Evidence for a non-rhombohedral average structure

in the lead-free piezoelectric material Na0. 5Bi0. 5TiO3, J. Appl. Crystallogr. 43 (2010) 1409–1414.

[100] E. Aksel, J.S. Forrester, J.L. Jones, P.A. Thomas, K. Page, M.R. Suchomel, Monoclinic crystal structure of polycrystalline Na0.5Bi0.5TiO3, Appl. Phys. Lett. 98 (2011) 152901. https://doi.org/10.1063/1.3573826.

[101] B.N. Rao, R. Datta, S.S. Chandrashekaran, D.K. Mishra, V. Sathe, A. Senyshyn, R. Ranjan, Local structural disorder and its influence on the average global structure and polar properties in Na0.5Bi0.5TiO3, Phys. Rev. B. 88 (2013) 224103. https://doi.org/10.1103/PhysRevB.88.224103.

[102] H. Lü, S. Wang, X. Wang, The electronic properties and lattice dynamics of (Na0.5Bi 0.5)TiO3: From cubic to tetragonal and rhombohedral phases, J. Appl. Phys. 115 (2014). https://doi.org/10.1063/1.4869733.

[103] R. Cui, K. Tang, D. Zhu, C. Yue, L. Yang, Sm3+-doped KNNS ferroelectric ceramics with enhanced photoluminescence by polarization-field-modulation, J. Mater. Sci. Mater. Electron. 31 (2020) 480–487. https://doi.org/10.1007/s10854-019-02552-x.

[104] B. Malič, J. Koruza, J. Hreščak, J. Bernard, K. Wang, J.G. Fisher, A. Benčan, Sintering of lead-free piezoelectric sodium potassium niobate ceramics, Materials (Basel). 8 (2015) 8117–8146. https://doi.org/10.3390/MA8125449.

[105] M. Węgrzyn, Sodium Potassium Niobate Based Piezoelectric Ceramics, University of Mancheser, 2012. https://www.research.manchester.ac.uk/portal/files/54517402/FULL_TEXT.PDF.

[106] N. Zhang, A.M. Glazer, D. Baker, P.A. Thomas, Structures of K0. 05Na0. 95NbO3 (50–300 K) and K0. 30Na0. 70NbO3 (100–200 K), Acta Crystallogr. Sect. B Struct. Sci. 65 (2009) 291–299.

[107] S. Kumar, N. Thakur, Investigation of Structural, Optical and Electrical Properties of Lead-Free K 0.5 Na 0.5 NbO 3 Ceramics Synthesized by Sol–Gel Reaction Route, J. Electron. Mater. 48 (2019) 6203–6215.

[108] C. Pişkin, Comparison of Powder Synthesis Methods for the Production of Potassium Sodium Niobate (KNN), (2021).

[109] M. Pattanaik, Synthesis and Characterizations of Lead Free KNN Ceramics near Morphotropic Phase Boundaries, (2011).

[110] H. Yang, Y. Lin, F. Wang, H. Luo, Chemical synthesis of K0. 5Na0. 5NbO3 ceramics and their electrical properties, Mater. Manuf. Process. 23 (2008) 489–493.

[111] J.-F. Li, K. Wang, F.-Y. Zhu, L.-Q. Cheng, F.-Z. Yao, (K,Na)NbO 3 -based lead-free piezoceramics: Fundamental aspects, processing technologies, and remaining challenges, J. Am. Ceram. Soc. 96 (2013) 3677–3696. https://doi.org/10.1111/jace.12715.

[112] A.J. Moulson, J.M. Herbert, Electroceramics : materials, properties, applications, Chapman and Hall, 1990. https://www.worldcat.org/title/electroceramics-materials-properties-

applications/oclc/20318593.

[113] D. O'Hare, Hydrothermal Synthesis, Encycl. Mater. Sci. Technol. (2001) 3989–3992. https://doi.org/10.1016/B0-08-043152-6/00701-4.

[114] A.E. Danks, S.R. Hall, Z. Schnepp, The evolution of 'sol–gel'chemistry as a technique for materials synthesis, Mater. Horizons. 3 (2016) 91–112.

[115] A. MAQBOOL, A. HUSSAIN, J.U. RAHMAN, J.K. PARK, T.G. PARK, J.S. SONG, M.H. KIM, Ferroelectric and piezoelectric properties of SrZrO3-modified Bi0.5Na0.5TiO3 lead-free ceramics, Trans. Nonferrous Met. Soc. China. 24 (2014) s146–s151. https://doi.org/10.1016/S1003-6326(14)63302-1.

[116] A. Hussain, A. Maqbool, R.A. Malik, T. Ahmed, S. Lee, M.-H. Kim, Texture performance of lead-free Bi1/2Na1/2TiO3–BaZrO3 ceramics, Ceram. Int. 49 (2023) 10073–10082. https://doi.org/10.1016/j.ceramint.2022.11.188.

[117] H.W. Lee, N.W. Kim, W.H. Nam, Y.S. Lim, Sonochemical activation in aqueous medium for solid-state synthesis of BaTiO3 powders, Ultrason. Sonochem. 82 (2022) 105874. https://doi.org/10.1016/j.ultsonch.2021.105874.

[118] U.S. Schubert, N. Hüsing, Synthesis of inorganic materials, John Wiley & Sons, 2019.

[119] Y. Ben Smida, R. Marzouki, S. Kaya, S. Erkan, M. Faouzi Zid, A. Hichem Hamzaoui, Synthesis Methods in Solid-State Chemistry, in: Synth. Methods Cryst., IntechOpen, 2020. https://doi.org/10.5772/intechopen.93337.

[120] T. Morita, Piezoelectric materials synthesized by the hydrothermal method and their applications, Materials (Basel). 3 (2010) 5236–5245. https://doi.org/10.3390/ma3125236.

[121] M. Shandilya, R. Rai, J. Singh, Review: hydrothermal technology for smart materials, Adv. Appl. Ceram. 115 (2016) 354–376. https://doi.org/10.1080/17436753.2016.1157131.

[122] G. Yang, S.-J. Park, Conventional and microwave hydrothermal synthesis and application of functional materials: A Review, Materials (Basel). 12 (2019) 1177. https://doi.org/10.3390/ma12071177.

[123] D. Segal, Chemical synthesis of ceramic materials, J. Mater. Chem. 7 (1997) 1297–1305. https://doi.org/10.1039/a700881c.

[124] L.-Y. Meng, B. Wang, M.-G. Ma, K.-L. Lin, The progress of microwave-assisted hydrothermal method in the synthesis of functional nanomaterials, Mater. Today Chem. 1–2 (2016) 63–83. https://doi.org/10.1016/j.mtchem.2016.11.003.

[125] A. Hussain, A. Maqbool, J.S. Kim, T.K. Song, M.H. Kim, W.J. Kim, S.S. Kim, Sodium Excess Ta-Modified (K 0.5 Na 0.5)NbO 3 Ceramics Prepared by Reactive Template Grain Growth Method, Int. J. Appl. Ceram. Technol. 12 (2015) 228–234. https://doi.org/10.1111/ijac.12150.

[126] D.S. Chakram, V.R. Reddy, S.N. Kumar, M. Dasari, Capacitive and Resistive Properties of Molten Salt Synthesized Lead-Free K1/2Na1/2NbO3 Ceramic, J. Inorg. Organomet. Polym. Mater. (2023) 1–11.

[127] X.H. Zheng, P.J. Chen, N. Ma, Z.H. Ma, D.P. Tang, Synthesis and dielectric properties of BiFeO 3 derived from molten salt method, J. Mater. Sci. Mater. Electron. 23 (2012) 990–994.

[128] H. Ge, Y. Hou, C. Xia, M. Zhu, H. Wang, H. Yan, Preparation and piezoelectricity of NaNbO3 high-density ceramics by molten salt synthesis, J. Am. Ceram. Soc. 94 (2011) 4329–4334.

[129] L. Liu, Progress on the fabrication of lead-free textured piezoelectric ceramics: perspectives over 25 years, J. Mater. Sci. Mater. Electron. 26 (2015) 4425–4437. https://doi.org/10.1007/s10854-015-2920-8.

[130] L. Liu, F. Gao, Y. Zhang, H. Sun, Dense KSr2Nb5O15 ceramics with uniform grain size prepared by molten salt synthesis, J. Alloys Compd. 616 (2014) 293–299. https://doi.org/10.1016/j.jallcom.2014.07.155.

[131] Y. Ishida, K.-I. Kakimoto, H. Ogawa, M. Aki, Transitional mechanism of particle Sr3Ti2O7 morphology in the molten salt synthesis, Ferroelectrics. 381 (2009) 24–29.

[132] Z. Li, X. Zhang, J. Hou, K. Zhou, Molten salt synthesis of anisometric Sr3Ti2O7 particles, J. Cryst. Growth. 305 (2007) 265–270. https://doi.org/10.1016/j.jcrysgro.2007.04.017.

[133] Y. Yan, D. Liu, W. Zhao, H. Zhou, H. Fang, Topochemical Synthesis of a High-Aspect-Ratio Platelet NaNbO 3 Template, J. Am. Ceram. Soc. 90 (2007) 2399–2403. https://doi.org/10.1111/j.1551-2916.2007.01818.x.

[134] K.H. Yoon, Y.S. Cho, D.H. Kang, Molten salt synthesis of lead-based relaxors, J. Mater. Sci. 33 (1998) 2977–2984.

[135] K. Hyun Yoon, Y. Soo Cho, D. Heon Kangs, Review: Molten salt synthesis of lead-based relaxors, J. Mater. Sci. 33 (1998) 2977–2984. https://link.springer.com/content/pdf/10.1023%2FA%3A1004310931643.pdf.

[136] D.A. Austin, M. Cole, M.C. Stennett, C.L. Corkhill, N.C. Hyatt, A preliminary investigation of the molten salt mediated synthesis of Gd2TiO5 ‘stuffed’ pyrochlore, MRS Adv. 6 (2021) 149–153. https://doi.org/10.1557/s43580-021-00057-6.

[137] Y. Zhang, S. Tong, S. Cao, F. Xing, J. Zhang, Z. Shi, Synthesis and topochemical conversion of plate-like perovskite CaMnO3 microcrystals, Ceram. Int. 49 (2023) 7089–7093.

[138] Y. Saito, H. Takao, K. Wada, Synthesis of platelike CaTiO3 particles by a topochemical microcrystal conversion method and fabrication of textured microwave dielectric ceramics, Ceram. Int. 34 (2008) 745–751.

[139] K. Zhang, F. Gao, J. Xu, M. Fu, L. Wang, Q. Zhang, Y. Ruan, Synthesis of Ba0. 6Sr0. 4TiO3 platelet crystals based on Bi4Ti3O12 precursor by topochemical microcrystal conversion, J. Alloys Compd. 726 (2017) 955–960.

[140] Y. Saito, H. Takao, T. Tani, T. Nonoyama, K. Takatori, T. Homma, T. Nagaya, M. Nakamura, Lead-free Piezoceramics, Nature. 432 (2004) 84–87. https://doi.org/10.1038/nature03028.

[141] D. Liu, Y. Yan, H. Zhou, Synthesis of Micron-Scale Platelet BaTiO 3, J. Am. Ceram. Soc. 90 (2007) 1323–1326. https://doi.org/10.1111/j.1551-2916.2007.01525.x.

[142] J.T. Zeng, K.W. Kwok, W.K. Tam, H.Y. Tian, X.P. Jiang, H.L.W. Chan, Plate-like Na0.5Bi0.5TiO3 template synthesized by a topochemical method, J. Am. Ceram. Soc. 89 (2006) 3850–3853. https://doi.org/10.1111/j.1551-2916.2006.01297.x.

[143] W. Zhao, H. Zhou, Y. Yan, D. Liu, Topochemical Synthesis of Plate-Like Na $_{0.5}$ Bi $_{0.5}$ TiO $_{3}$ from Aurivillius Precursor, J. Am. Ceram. Soc. 91 (2008) 1322–1325. https://doi.org/10.1111/j.1551-2916.2007.02250.x.

[144] L. Li, J. Deng, J. Chen, X. Sun, R. Yu, G. Liu, X. Xing, Wire Structure and Morphology Transformation of Niobium Oxide and Niobates by Molten Salt Synthesis, Chem. Mater. 21 (2009) 1207–1213. https://doi.org/10.1021/cm802776g.

[145] M.K. T, Novel Molten Salt Synthesis of ZrB 2 and ZrC powders and Molten Salt Synthesis of Novel TiC, University of Exeter, 2014. https://core.ac.uk/download/pdf/43094228.pdf (accessed August 28, 2019).

[146] J.P. Zuniga, M. Abdou, S.K. Gupta, Y. Mao, Molten-Salt Synthesis of Complex Metal Oxide Nanoparticles, J. Vis. Exp. (2018) 1–7. https://doi.org/10.3791/58482.

[147] D. Zhang, F. Zheng, X. Yang, L. Feng, X. Huang, H. Liu, M. Cao, Preparation and ferroelectric properties of K0. 5Na0. 5NbO3 thin films derived from non-alcohol niobium salt sol-gel process, Integr. Ferroelectr. 154 (2014) 97–102.

[148] K. Xi, Y. Li, Z. Zheng, L. Zhang, Y. Liu, Y. Mi, Microstructure, dielectric properties, relaxation behavior, and ferroelectric properties of Gd-doped lead-free BZT ceramics by sol–gel process, J. Mater. Sci. Mater. Electron. 31 (2020) 23044–23051.

[149] T. Yu, K.W. Kwok, H.L.W. Chan, Preparation and properties of sol–gel-derived Bi0. 5Na0. 5TiO3 lead-free ferroelectric thin film, Thin Solid Films. 515 (2007) 3563–3566.

[150] I. Chilibon, J.N. Marat-Mendes, Ferroelectric ceramics by sol–gel methods and applications: a review, J. Sol-Gel Sci. Technol. 64 (2012) 571–611.

[151] D. Bokov, A. Turki Jalil, S. Chupradit, W. Suksatan, M. Javed Ansari, I.H. Shewael, G.H. Valiev, E. Kianfar, Nanomaterial by Sol-Gel method: Synthesis and application, Adv. Mater. Sci. Eng. 2021 (2021) 1–21. https://doi.org/10.1155/2021/5102014.

[152] C.B. Carter, M.G. Norton, Sols, gels, and organic chemistry, Ceram. Mater. Sci. Eng. (2007) 400–411.

[153] Z. Ahmad, Polymer Dielectric Materials, in: Dielectr. Mater., InTech, 2012. https://doi.org/10.5772/50638.

[154] J.S. Harrison, Z. Ounaies, Piezoelectric Polymers, 2001. http://citeseerx.ist.psu.edu/viewdoc/download?doi=10.1.1.407.2109&rep=rep1&type=pdf (accessed April 30, 2019).

[155] Y. Wang, L. Zhu, C. Du, Progress in piezoelectric nanogenerators based on PVDF composite films, Micromachines. 12 (2021) 1278. https://doi.org/10.3390/mi12111278.

[156] L. Padurariu, E. Brunengo, G. Canu, L.P. Curecheriu, L. Conzatti, M.T. Buscaglia, P. Stagnaro, L. Mitoseriu, V. Buscaglia, Role of Microstructures in the Dielectric Properties of PVDF-Based Nanocomposites Containing High-Permittivity Fillers for Energy Storage, ACS Appl. Mater. Interfaces. 15 (2023) 13535–13544. https://doi.org/10.1021/acsami.2c23013.

[157] A. Gaur, C. Kumar, R. Shukla, P. Maiti, Induced piezoelectricity in poly (vinylidene fluoride) hybrid as efficient energy harvester, ChemistrySelect. 2 (2017) 8278–8287.

[158] L. Lu, W. Ding, J. Liu, B. Yang, Flexible PVDF based piezoelectric nanogenerators, Nano Energy. 78 (2020) 105251.

[159] S. George, M.T. Sebastian, Three-phase polymer-ceramic-metal composite for embedded capacitor applications, Compos. Sci. Technol. 69 (2009) 1298–1302. https://doi.org/10.1016/j.compscitech.2009.03.003.

[160] R. Li, Z. Zhao, Z. Chen, J. Pei, Novel BaTiO 3 /PVDF composites with enhanced electrical properties modified by calcined BaTiO 3 ceramic powders, Mater. Express. 7 (2017). https://doi.org/10.1166/mex.2017.1393.

[161] I. Babu, Piezoelectric composites : Design , Fabrication and Performance Analysis, Eindhoven University of Technology, 2013. https://doi.org/10.6100/IR760468.

[162] D. Maurya, Y. Yan, S. Priya, Piezoelectric materials for energy harvesting, Adv. Mater. Clean Energy. (2015) 143–178. https://doi.org/10.1201/b18287.

[163] B. Luo, X. Wang, Y. Wang, L. Li, Fabrication, characterization, properties and theoretical analysis of ceramic/PVDF composite flexible films with high dielectric constant and low dielectric loss, Mater. Chem. A. (2014) 510–519. https://doi.org/10.1039/c3ta14107a.

[164] Y. Huan, X. Zhang, J. Song, Y. Zhao, T. Wei, G. Zhang, X. Wang, High-performance piezoelectric composite nanogenerator based on Ag/(K,Na)NbO3heterostructure, Nano Energy. 50 (2018) 62–69. https://doi.org/10.1016/j.nanoen.2018.05.012.

[165] R. Li, H. Wang, P. Wang, H. Liu, J. Pei, Influence of PZT piezoelectric ceramics on the structure and electric properties of piezoelectric lead zirconate titanate/poly(vinylidene fluoride) composites, Mater. Express. 6 (2016) 483–492. https://doi.org/10.1166/mex.2016.1336.

[166] R. Banks, R.L. O'Leary, G. Hayward, Enhancing the bandwidth of piezoelectric composite transducers for air-coupled non-destructive evaluation, Ultrasonics. 75 (2017) 132–144. https://doi.org/10.1016/j.ultras.2016.10.007.

[167] J.A. Gallego-Juarez, Piezoelectric Ceramics and Ultrasonic Transducers, J. Phys. E Sci. Instrum. 22 (1989) 804–816.

[168] L.. Newnham, R.E; Skinner, D.P; Cross, Connectivity and Piezoelectric–Pyroelectric Composite, Mater. Res. Bull. 13 (1978) 525–536.

https://doi.org/10.1016/0025-5408(78)90161-7.

[169] C.R. Bowen, V.Y. Topolov, Y. Zhang, A.A. Panich, 1-3-Type Composites Based on Ferroelectrics: Electromechanical Coupling, Figures of Merit, and Piezotechnical Energy-Harvesting Applications, Energy Technol. 6 (2018) 813–828. https://doi.org/10.1002/ente.201700623.

[170] V.Y. Topolov, C.R. Bowen, A.N. Isaeva, Anisotropy factors and electromechanical coupling in lead-free 1-3-type composites, IEEE Trans. Ultrason. Ferroelectr. Freq. Control. 65 (2018) 1278–1286. https://doi.org/10.1109/TUFFC.2018.2833856.

[171] R. Bao, M. Li, M. Shen, H. Liu, G. Zhang, Y. Zeng, S. Jiang, Enhanced pyroelectric properties of 1–3 nanocomposites achieved by uniaxial stretching, J. Mater. Sci. Mater. Electron. 30 (2019) 6760–6767. https://doi.org/10.1007/s10854-019-00987-w.

[172] C. Zhou, J. Zhang, D. Liu, Z. Zhang, Novel 1–3 (K,Na)NbO3-based ceramic/epoxy composites with large thickness-mode electromechanical coupling coefficient and good temperature stability, Ceram. Int. 3 (2020) 7–11. https://doi.org/10.1016/j.ceramint.2020.10.031.

[173] Y. Zhang, C.K. Jeong, T. Yang, H. Sun, L.Q. Chen, S. Zhang, W. Chen, Q. Wang, Bioinspired elastic piezoelectric composites for high-performance mechanical energy harvesting, J. Mater. Chem. A. 6 (2018) 14546–14552. https://doi.org/10.1039/c8ta03617a.

[174] R. Bao, M. Li, M. Shen, H. Liu, G. Zhang, Y. Zeng, S. Jiang, Enhanced pyroelectric properties of 1–3 nanocomposites achieved by uniaxial stretching, J. Mater. Sci. Mater. Electron. 30 (2019) 6760–6767. https://doi.org/10.1007/s10854-019-00987-w.

[175] N. Chamankar, R. Khajavi, A.A. Yousefi, A. Rashidi, F. Golestanifard, An experimental model for predicting the piezo and dielectric constant of PVDF-PZT nanocomposite fibers with 0–3 and 1–3 connectivity, Ceram. Int. 46 (2020) 23567–23581. https://doi.org/10.1016/j.ceramint.2020.06.128.

[176] P. Eltouby, I. Shyha, C. Li, J. Khaliq, Factors affecting the piezoelectric performance of ceramic-polymer composites: A comprehensive review, Ceram. Int. 47 (2021) 17813–17825. https://doi.org/10.1016/j.ceramint.2021.03.126.

[177] Q. Wang, J. Che, W. Wu, Z. Hu, X. Liu, T. Ren, Y. Chen, J. Zhang, Contributing factors of dielectric properties for polymer matrix composites, Polymers (Basel). 15 (2023) 590. https://doi.org/10.3390/polym15030590.

[178] D.Q. Tan, Review of polymer-based nanodielectric exploration and film scale-up for advanced capacitors, Adv. Funct. Mater. 30 (2020) 1808567.

[179] P.W. Jaschin, R. Bhimireddi, K.B.R. Varma, Enhanced dielectric properties of LaNiO3/BaTiO3/PVDF: A three-phase percolative polymer nanocrystal composite, ACS Appl. Mater. Interfaces. 10 (2018) 27278–27286. https://doi.org/10.1021/acsami.8b07786.

[180] K. Silakaew, E. Swatsitang, P. Thongbai, Novel polymer composites of RuO2@nBaTiO3/PVDF with a high dielectric constant, Ceram. Int. 48 (2022)

18925–18932. https://doi.org/10.1016/j.ceramint.2022.03.173.

[181] R. Pramanik, A. Arockiarajan, Effective properties and nonlinearities in 1-3 piezocomposites: a comprehensive review, Smart Mater. Struct. 28 (2019) 103001. https://doi.org/10.1088/1361-665x/ab350a.

[182] H.J. Lee, S. Zhang, Y. Bar-Cohen, S. Sherrit, High Temperature, High Power Piezoelectric Composite Transducers, Sensors (Switzerland). 14 (2014) 14526–14552. https://doi.org/10.3390/s140814526.

[183] A.A. Jain, P. K. J., A.K. Sharma, A.A. Jain, R. P.N, R.P.. Anjana Jain, Prashanth K. J., Asheesh Kr. Sharma, Arpit Jain, Dielectric and piezoelectric properties of PVDF/PZT composites: A review, Polym. Eng. Sci. 55 (2015) 1589–1616. https://doi.org/10.1002/pen.24088.

[184] S. Schwarzer, A. Roosen, Tape casting of piezo ceramic/polymer composites, J. Eur. Ceram. Soc. 19 (1999) 1007–1010. https://doi.org/10.1016/s0955-2219(98)00363-x.

[185] H. Kim, F. Torres, D. Villagran, C. Stewart, Y. Lin, T.L.B. Tseng, 3D Printing of BaTiO3/PVDF Composites with Electric In Situ Poling for Pressure Sensor Applications, Macromol. Mater. Eng. 302 (2017) 1–6. https://doi.org/10.1002/mame.201700229.

[186] A. Moulart, C. Marrett, J. Colton, Polymeric composites for use in electronic and microwave devices, Polym. Eng. Sci. 44 (2004) 588–597. https://doi.org/10.1002/pen.20053.

[187] H. Kim, J. Johnson, L.A. Chavez, C.A. Garcia Rosales, T.L.B. Tseng, Y. Lin, Enhanced dielectric properties of three phase dielectric MWCNTs/BaTiO3/PVDF nanocomposites for energy storage using fused deposition modeling 3D printing, Ceram. Int. 44 (2018) 9037–9044. https://doi.org/10.1016/j.ceramint.2018.02.107.

[188] I. Cooperstein, E. Sachyani-Keneth, E. Shukrun-Farrell, T. Rosental, X. Wang, A. Kamyshny, S. Magdassi, Hybrid Materials for Functional 3D Printing, Adv. Mater. Interfaces. 5 (2018). https://doi.org/10.1002/admi.201800996.

[189] J. Fu, Y. Hou, M. Zheng, Q. Wei, M. Zhu, H. Yan, Improving Dielectric Properties of PVDF Composites by Employing Surface Modified Strong Polarized BaTiO 3 Particles Derived by Molten Salt Method, ACS Appl. Mater. Interfaces. 7 (2015) 24480–24491. https://doi.org/10.1021/acsami.5b05344.

[190] S. Mahmud, Y. Long, M. Abu Taher, Z. Xiong, R. Zhang, J. Zhu, Toughening polylactide by direct blending of cellulose nanocrystals and epoxidized soybean oil, J. Appl. Polym. Sci. 48221 (2019) 1–13. https://doi.org/10.1002/app.48221.

[191] D.S. Kim, C. Baek, H.J. Ma, D.K. Kim, Enhanced dielectric permittivity of BaTiO3/epoxy resin composites by particle alignment, Ceram. Int. 42 (2016) 7141–7147. https://doi.org/10.1016/j.ceramint.2016.01.103.

[192] D.A. Van Den Ende, B.F. Bory, W.A. Groen, S. Van Der Zwaag, Improving the d33 and g33 properties of 0-3 piezoelectric composites by dielectrophoresis, J. Appl. Phys. 107 (2010) 24107. https://doi.org/10.1063/1.3291131.

[193] H. Khanbareh, S. van der Zwaag, W.A. Groen, In-situ poling and structurization

of piezoelectric particulate composites, J. Intell. Mater. Syst. Struct. 28 (2017) 2467–2472. https://doi.org/10.1177/1045389X17689928.

[194] H.A. Pohl, The Motion and Precipitation of Suspensoids in Divergent Electric Fields, J. Appl. Phys. 22 (1951) 869–871. https://doi.org/10.1063/1.1700065.

[195] H. Khanbareh, S. Van Der Zwaag, W.A. Groen, Effect of dielectrophoretic structuring on piezoelectric and pyroelectric properties of lead titanate-epoxy composites, Smart Mater. Struct. 23 (2014). https://doi.org/10.1088/0964-1726/23/10/105030.

[196] Khaliq, Hoeks, Groen, Fabrication of Piezoelectric Composites Using High-Temperature Dielectrophoresis, J. Manuf. Mater. Process. 3 (2019) 77. https://doi.org/10.3390/jmmp3030077.

[197] N.K. James, D. van den Ende, U. Lafont, S. van der Zwaag, W.A. Groen, Piezoelectric and mechanical properties of structured PZT–epoxy composites, J. Mater. Res. 28 (2013) 635–641. https://doi.org/10.1557/jmr.2012.428.

[198] V. Stuber, D. Deutz, J. Bennett, D. Cannell, D. de Leeuw, S. van der Zwaag, P. Groen, Flexible lead-free Piezoelectric Composite Materials for Energy Harvesting Applications, Energy Technol. 6 (2018) 1–10. https://doi.org/10.1002/ente.201800419.

[199] S.A. Wilson, G.M. Maistros, R.W. Whatmore, Structure modification of 0-3 piezoelectric ceramic/polymer composites through dielectrophoresis, J. Phys. D. Appl. Phys. 38 (2005) 175–182.

[200] D. Deutz, Flexible piezoelectric composites Bridging the gap between materials and applications, Delft University of Technology, 2017. https://doi.org/10.4233/uuid.

[201] T. Yamada, T. Ueda, T. Kitayama, Piezoelectricity of a high-content lead zirconate titanate/polymer composite, J. Appl. Phys. 53 (1982) 4328–4332. https://doi.org/10.1063/1.331211.

[202] H. Khanbareh, Expanding the functionality of piezo-particulate composites, 2016. https://doi.org/10.4233/uuid.

[203] D.A. Van Den Ende, S.E. Van Kempen, X. Wu, W.A. Groen, C.A. Randall, S. Van Der Zwaag, Dielectrophoretically structured piezoelectric composites with high aspect ratio piezoelectric particles inclusions, J. Appl. Phys. 111 (2012) 124107. https://doi.org/10.1063/1.4729814.

[204] S. Dalle Vacche, F. Oliveira, Y. Leterrier, V. Michaud, D. Damjanovic, J.A.E. Månson, The effect of processing conditions on the morphology, thermomechanical, dielectric, and piezoelectric properties of P(VDF-TrFE)/BaTiO 3 composites, J. Mater. Sci. 47 (2012) 4763–4774. https://doi.org/10.1007/s10853-012-6362-x.

[205] G. Sa-Gong, A. Safari, S.J. Jang, R.E. Newnham, Poling flexible piezoelectric composites, Ferroelectr. Lett. Sect. 5 (1986) 131–142. https://doi.org/10.1080/07315178608202472.

[206] R. Kiran, A. Kumar, R. Kumar, R. Vaish, Effect of poling orientation on piezoelectric materials operating in longitudinal mode, Mater. Res. Express. 6

(2019) 0–12. https://doi.org/10.1088/2053-1591/ab0fd0.

[207] H. Khanbareh, S. van der Zwaag, W. Groen, In-situ poling and structurization of piezoelectric particulate composites, J. Intell. Mater. Syst. Struct. 28 (2017) 2467–2472. https://doi.org/10.1177/1045389X17689928.

[208] J. Khaliq, D.B. Deutz, J.A.C. Frescas, P. Vollenberg, T. Hoeks, S. van der Zwaag, P. Groen, Effect of the Piezoelectric Ceramic Filler Dielectric Constant on the Piezoelectric Properties of PZT-Epoxy Composites, Ceram. Int. 43 (2017) 2774–2779. https://doi.org/10.1016/j.ceramint.2016.11.108.

[209] K. Kim, H. Ju, J. Kim, Vertical particle alignment of boron nitride and silicon carbide binary filler system for thermal conductivity enhancement, Compos. Sci. Technol. 123 (2016) 99–105. https://doi.org/10.1016/j.compscitech.2015.12.004.

[210] Y. Zhan, Z. Long, X. Wan, C. Zhan, J. Zhang, Y. He, Enhanced dielectric permittivity and thermal conductivity of hexagonal boron nitride/poly(arylene ether nitrile) composites through magnetic alignment and mussel inspired co-modification, Ceram. Int. 43 (2017) 12109–12119. https://doi.org/10.1016/j.ceramint.2017.06.068.

[211] Y. Ouyang, L. Bai, H. Tian, X. Li, F. Yuan, Recent progress of thermal conductive ploymer composites: Al2O3 fillers, properties and applications, Compos. Part A Appl. Sci. Manuf. 152 (2022) 106685. https://doi.org/10.1016/j.compositesa.2021.106685.

[212] M.C. Araújo, C.M. Costa, S. Lanceros-Méndez, Evaluation of dielectric models for ceramic/polymer composites: Effect of filler size and concentration, J. Non. Cryst. Solids. 387 (2014) 6–15. https://doi.org/10.1016/j.jnoncrysol.2013.12.005.

[213] T. Hu, J. Juuti, H. Jantunen, T. Vilkman, Dielectric properties of BST/polymer composite, J. Eur. Ceram. Soc. 27 (2007) 3997–4001. https://doi.org/10.1016/j.jeurceramsoc.2007.02.082.

[214] M.P. Chun, Effect of particle size of BNT filler on dielectric and mechanical properties of LCP based composite, Appl. Mech. Mater. 483 (2014) 138–141. https://doi.org/10.4028/www.scientific.net/AMM.483.138.

[215] S.Y. Fu, X.Q. Feng, B. Lauke, Y.W. Mai, Effects of particle size, particle/matrix interface adhesion and particle loading on mechanical properties of particulate-polymer composites, Compos. Part B Eng. 39 (2008) 933–961. https://doi.org/10.1016/j.compositesb.2008.01.002.

[216] S.A. Dargham, F. Ponchel, N. Abboud, M. Soueidan, A. Ferri, R. Desfeux, J. Assaad, D. Remiens, D. Zaouk, Synthesis and electrical properties of lead-free piezoelectric Bi0.5Na0.5TiO3 thin films prepared by Sol-Gel method, J. Eur. Ceram. Soc. 38 (2018) 1450–1455. https://doi.org/10.1016/J.JEURCERAMSOC.2017.06.019.

[217] J. Fu, Y. Hou, M. Zheng, M. Zhu, Comparative study of dielectric properties of the PVDF composites filled with spherical and rod-like BaTiO3 derived by molten salt synthesis method, J. Mater. Sci. 53 (2018) 7233–7248. https://doi.org/10.1007/s10853-018-2114-x.

[218] W. Sun, Size effect in barium titanate powders synthesized by different hydrothermal methods, J. Appl. Phys. 100 (2006). https://doi.org/10.1063/1.2358005.

[219] Y. Fu, W. Li, M. Xu, C. Wang, L. Zhang, G. Zhang, Dielectric properties and 3D-printing feasibility of UV-curable resin/micron ceramic filler composites, Adv. Polym. Technol. 2022 (2022) 1–14. https://doi.org/10.1155/2022/9483642.

[220] X. Lu, W. Deng, J. Wei, Y. Zhu, P. Ren, Y. Wan, F. Yan, L. Jin, L. Zhang, Z.-Y. Cheng, Filler size effects on the microstructure and properties of polymer-ceramic nanocomposites using a semicrystalline matrix, J. Mater. Sci. 56 (2021) 19983–19995. https://doi.org/10.1007/s10853-021-06555-0.

[221] D.Q. Tan, The search for enhanced dielectric strength of polymer-based dielectrics: A focused review on polymer nanocomposites, J. Appl. Polym. Sci. 137 (2020) 49379. https://doi.org/10.1002/app.49379.

[222] E.S. Kim, C.J. Jeon, Dependence of dielectric properties on the crystallinity of ceramic/polymer composites, IEEE Trans. Ultrason. Ferroelectr. Freq. Control. 58 (2011) 1939–1946. https://doi.org/10.1109/TUFFC.2011.2034.

[223] P. Han, S. Pang, J. Fan, X. Shen, T. Pan, Highly enhanced piezoelectric properties of PLZT/PVDF composite by tailoring the ceramic Curie temperature, particle size and volume fraction, Sensors Actuators, A Phys. 204 (2013) 74–78. https://doi.org/10.1016/j.sna.2013.10.011.

[224] M. Heidari-Rarani, M. Rafiee-Afarani, A.M. Zahedi, Mechanical characterization of FDM 3D printing of continuous carbon fiber reinforced PLA composites, Compos. Part B Eng. 175 (2019) 107147. https://doi.org/10.1016/j.compositesb.2019.107147.

[225] R. Jayendiran, A. Arockiarajan, Modeling of dielectric and piezoelectric response of 1-3 type piezocomposites, J. Appl. Phys. 112 (2012). https://doi.org/10.1063/1.4748057.

[226] Chitra, A. Khandelwal, R. Gupta, R. Laishram, K.C. Singh, Impact of crystal structure and microstructure on electrical properties of Ho doped lead-free BCST piezoceramics, Ceram. Int. 45 (2019) 10371–10379. https://doi.org/10.1016/j.ceramint.2019.02.095.

[227] D.B. Deutz, N.T. Mascarenhas, S. van der Zwaag, W.A. Groen, Enhancing energy harvesting potential of (K,Na,Li)NbO3-epoxy composites via Li substitution, J. Am. Ceram. Soc. 100 (2017) 1108–1117. https://doi.org/10.1111/jace.14698.

[228] N.A. Shepelin, A.M. Glushenkov, V.C. Lussini, P.J. Fox, G.W. Dicinoski, J.G. Shapter, A. V. Ellis, New developments in composites, copolymer technologies and processing techniques for flexible fluoropolymer piezoelectric generators for efficient energy harvesting, Energy Environ. Sci. 12 (2019) 1143–1176. https://doi.org/10.1039/c8ee03006e.

[229] D.A. Van Den Ende, B.F. Bory, W.A. Groen, S. Van Der Zwaag, Improving the d33 and g33 properties of 0-3 piezoelectric composites by dielectrophoresis, J. Appl. Phys. 107 (2010) 0–8. https://doi.org/10.1063/1.3291131.

[230] H. Ge, Y. Huang, Y. Hou, H. Xiao, M. Zhu, Size dependence of the polarization and dielectric properties of KNbO 3 nanoparticles, RSC Adv. 4 (2014) 23344–23350. https://doi.org/10.1039/c4ra03613a.

[231] K. Yu, S. Hu, W. Yu, J. Tan, Piezoelectric and Dielectric Properties of ((K0.475Na0.495Li0.03)NbO3-0.003ZrO2)/PVDF Composites, J. Electron. Mater. 48 (2019) 2329–2337. https://doi.org/10.1007/s11664-019-06978-1.

[232] S. Dwivedi, T. Pareek, S. Kumar, Structure, dielectric, and piezoelectric properties of K0.5Na0.5NbO3-based lead-free ceramics, RSC Adv. 8 (2018) 24286–24296. https://doi.org/10.1039/c8ra04038a.

[233] Y. Zhang, M. Xie, J. Roscow, C. Bowen, Dielectric and piezoelectric properties of porous lead-free 0.5Ba(Ca0.8Zr0.2)O3-0.5(Ba0.7Ca 0.3)TiO3 ceramics, Mater. Res. Bull. 112 (2019) 426–431. https://doi.org/10.1016/j.materresbull.2018.08.031.

[234] Y. Zhang, M. Xie, J. Roscow, Y. Bao, K. Zhou, D. Zhang, C.R. Bowen, Enhanced pyroelectric and piezoelectric properties of PZT with aligned porosity for energy harvesting applications, J. Mater. Chem. A. 5 (2017) 6569–6580. https://doi.org/10.1039/c7ta00967d.

[235] Y. Zhang, J. Roscow, R. Lewis, H. Khanbareh, V.Y. Topolov, M. Xie, C.R. Bowen, Understanding the effect of porosity on the polarisation-field response of ferroelectric materials, Acta Mater. 154 (2018) 100–112. https://doi.org/10.1016/j.actamat.2018.05.007.

[236] T. Siponkoski, M. Nelo, J. Palosaari, J. Peräntie, M. Sobocinski, J. Juuti, H. Jantunen, Electromechanical properties of PZT/P(VDF-TrFE) composite ink printed on a flexible organic substrate, Compos. Part B Eng. 80 (2015) 217–222. https://doi.org/10.1016/j.compositesb.2015.05.018.

[237] W. Zhao, J. Ya, Y. Xin, L. E, D. Zhao, H. Zhou, Fabrication of Na0.5Bi0.5TiO3–BaTiO3-Textured Ceramics Templated by Plate-Like Na0.5Bi0.5TiO3 Particles, J. Am. Ceram. Soc. 92 (2009) 1607–1609. https://doi.org/10.1111/J.1551-2916.2009.03043.X.

[238] W.K. Tam, K.W. Kwok, J.T. Zeng, H.L.W. Chan, Fabrication of textured BNKLT ceramics by reactive templated grain growth using NBT templates, J. Phys. D. Appl. Phys. 41 (2008) 045402. https://doi.org/10.1088/0022-3727/41/4/045402.

[239] C. Jiang, X. Zhou, K. Zhou, C. Chen, H. Luo, X. Yuan, D. Zhang, Grain oriented Na 0.5 Bi 0.5 TiO 3 -BaTiO 3 ceramics with giant strain response derived from single-crystalline Na 0.5 Bi 0.5 TiO 3 -BaTiO 3 templates, J. Eur. Ceram. Soc. 36 (2016) 1377–1383. https://doi.org/10.1016/j.jeurceramsoc.2015.12.025.

[240] S.N.H. Mohamad Rodzi, H. Zuhailawati, B.K. Dhindaw, Mechanical and degradation behaviour of biodegradable magnesium–zinc/hydroxyapatite composite with different powder mixing techniques, J. Magnes. Alloy. 7 (2019) 566–576. https://doi.org/10.1016/j.jma.2019.11.003.

[241] P. Setasuwon, S. Kijamnajsuk, Synthesis of Na0.5Bi0.5TiO3 anisotropic particles with grain orientation by conversion of Na0.5Bi4.5Ti4O15 crystals,

Sci. Technol. Adv. Mater. 7 (2006) 780–784. https://doi.org/10.1016/j.stam.2006.10.006.

[242] W. Zhou, R. Apkarian, Z.L. Wang, D. Joy, Fundamentals of scanning electron microscopy (SEM), Scanning Microsc. Nanotechnol. Tech. Appl. (2007) 1–40.

[243] N. Tanaka, Scanning transmission electron microscopy of nanomaterials: basics of imaging and analysis, World Scientific, 2014.

[244] E.-C. Stefanaki, Electron microscopy: the basics, Phys. Adv. Mater. Winter Sch. 4 (2008) 1–11.

[245] J. Epp, X-Ray Diffraction (XRD) Techniques for Materials Characterization, Elsevier Ltd, 2016. https://doi.org/10.1016/B978-0-08-100040-3.00004-3.

[246] K. Inaba, S. Kobayashi, K. Uehara, A. Okada, S.L. Reddy, T. Endo, High Resolution X-Ray Diffraction Analyses of (La,Sr)MnO₃/ZnO/Sapphire(0001) Double Heteroepitaxial Films, Adv. Mater. Phys. Chem. 03 (2013) 72–89. https://doi.org/10.4236/ampc.2013.31a010.

[247] J. Xie, Z. Dai, X. Ding, X. Fan, W. Liu, L. Zhang, J. Li, Enhanced energy storage properties of Sr(Sc0.5Nb0.5)O3 modified (Bi0.47La0.03Na0.5)0.94Ba0.06TiO3 lead-free ceramics, J. Mater. Sci. 55 (2020) 13578–13589. https://doi.org/10.1007/s10853-020-04978-9.

[248] Y. Liu, Y. Lu, S. Dai, Hydrothermal synthesis of monosized Bi0.5Na0.5TiO3 spherical particles under low alkaline solution concentration, J. Alloys Compd. 484 (2009) 801–805. https://doi.org/10.1016/j.jallcom.2009.05.033.

[249] S.I.S. Shaharuddin, M.S. Salit, A review of the effect of moulding parameters on the performance of polymeric composite injection moulding, Turkish J. Eng. Environ. Sci. 30 (2006) 23–34.

[250] M. Xie, Y. Zhang, M.J. Kraśny, C. Bowen, H. Khanbareh, N. Gathercole, Flexible and active self-powered pressure, shear sensors based on freeze casting ceramic–polymer composites, Energy Environ. Sci. 11 (2018) 2919–2927. https://doi.org/10.1039/C8EE01551A.

[251] C. Yuan, B. Duan, L. Li, B. Xie, M. Huang, X. Luo, Thermal Conductivity of Polymer-Based Composites with Magnetic Aligned Hexagonal Boron Nitride Platelets, ACS Appl. Mater. Interfaces. 7 (2015) 13000–13006. https://doi.org/10.1021/acsami.5b03007.

[252] D.-H. Kuo, C.-C. Chang, T.-Y. Su, W.-K. Wang, B.-Y. Lin, Dielectric properties of three ceramic/epoxy composites, Mater. Chem. Phys. 85 (2004) 201–206. https://doi.org/10.1016/j.matchemphys.2004.01.003.

[253] J. Huang, P. Fu, W. Li, L. Xiao, J. Chen, X. Nie, Influence of crosslinking density on the mechanical and thermal properties of plant oil-based epoxy resin, RSC Adv. 12 (2022) 23048–23056. https://doi.org/10.1039/D2RA04206A.

[254] C.P. Wong, R.S. Bollampally, Thermal conductivity, elastic modulus, and coefficient of thermal expansion of polymer composites filled with ceramic particles for electronic packaging, J. Appl. Polym. Sci. 74 (1999) 3396–3403. https://doi.org/10.1002/(SICI)1097-4628(19991227)74:14<3396::AID-

APP13>3.0.CO;2-3.

[255] Z. Wu, J. Fan, Y. Zhao, B. Lin, W. Zhou, Q. Zhang, L. Li, Computationally driven design of low dielectric-loss epoxy resin for medium-frequency transformers, J. Phys. D. Appl. Phys. 56 (2023) 184001.

[256] M. Rotan, M. Zhuk, J. Glaum, Activation of ferroelectric implant ceramics by corona discharge poling, J. Eur. Ceram. Soc. 40 (2020) 5402–5409.

[257] E. Nilsson, A. Lund, C. Jonasson, C. Johansson, B. Hagström, Poling and characterization of piezoelectric polymer fibers for use in textile sensors, Sensors Actuators A Phys. 201 (2013) 477–486.

[258] J.A. Giacometti, Radial current-density distributions and sample charge uniformity in a corona triode, J. Phys. D. Appl. Phys. 20 (1987) 675–682. https://doi.org/10.1088/0022-3727/20/6/001.

[259] J.A. Giacometti, S. Fedosov, M.M. Costa, Corona charging of polymers: Recent advances on constant current charging, Brazilian J. Phys. 29 (1999) 269–279. https://doi.org/10.1590/S0103-97331999000200009.

[260] Zepu Wang, J.K. Nelson, Jianjun Miao, R.J. Linhardt, L.S. Schadler, H. Hillborg, Su Zhao, Effect of high aspect ratio filler on dielectric properties of polymer composites: a study on barium titanate fibers and graphene platelets, IEEE Trans. Dielectr. Electr. Insul. 19 (2012) 960–967. https://doi.org/10.1109/TDEI.2012.6215100.

[261] H. Hu, F. Zhang, S. Luo, W. Chang, J. Yue, C.-H. Wang, Recent advances in rational design of polymer nanocomposite dielectrics for energy storage, Nano Energy. 74 (2020) 104844. https://doi.org/10.1016/j.nanoen.2020.104844.

[262] J. Hu, S. Zhang, B. Tang, 2D filler-reinforced polymer nanocomposite dielectrics for high-k dielectric and energy storage applications, Energy Storage Mater. 34 (2021) 260–281.

[263] Z. Feng, Y. Hao, J. Zhang, J. Qin, L. Guo, K. Bi, Dielectric properties of two-dimensional Bi 2 Se 3 hexagonal nanoplates modified PVDF nanocomposites, Adv. Polym. Technol. 2019 (2019).

[264] V. Ramasamy, Y. Subramanian, S. Varadarajan, K. Ramaswamy, K. Kaliappan, D. Arulmozhi, G.R. Srinivasan, R.K. Gubendiran, Influence of process parameters on the optimisation of crystalline phase, size and strain of multiferroic Bismuth Iron Tri Oxide (BiFeO3) nanoceramics: A MCDM based TOPSIS approach, Ceram. Int. 46 (2020) 1457–1471. https://doi.org/10.1016/j.ceramint.2019.09.111.

[265] M.. Salar-García, A. de Ramón-Fernández, V.M. Ortiz-Martínez, D. Ruiz-Fernández, I. Ieropoulos, Towards the optimisation of ceramic-based microbial fuel cells: A three-factor three-level response surface analysis design, Biochem. Eng. J. 144 (2019) 119–124. https://doi.org/10.1016/j.bej.2019.01.015.

[266] M. Sadat-Shojai, M.-T. Khorasani, A. Jamshidi, Hydrothermal processing of hydroxyapatite nanoparticles—A Taguchi experimental design approach, J. Cryst. Growth. 361 (2012) 73–84.

[267] C. Yuangyai, H.B. Nembhard, Design of experiments: a key to innovation in

nanotechnology, in: Emerg. Nanotechnologies Manuf., Elsevier, 2010: pp. 207–234.

[268] S. Khodadoost, A. Hadi, J. Karimi-Sabet, M. Mehdipourghazi, A. Golzary, Optimization of hydrothermal synthesis of Bismuth titanate nanoparticles and application for photocatalytic degradation of Tetracycline, J. Environ. Chem. Eng. 5 (2017) 5369–5380. https://doi.org/10.1016/j.jece.2017.10.006.

[269] L. Aeindartehran, S.S. Ashraf Talesh, Enhanced photocatalytic degradation of Acid Blue 1 using Ni-Decorated ZnO NPs synthesized by sol-gel method: RSM optimization approach, Ceram. Int. 47 (2021) 27294–27304. https://doi.org/10.1016/j.ceramint.2021.06.151.

[270] D.C. Hoaglin, F. Mosteller, J.W. Tukey, Fundamentals of exploratory analysis of variance, John Wiley & Sons, 1991.

[271] P.A. Murtaugh, In defense of P values, Ecology. 95 (2014) 611–617.

[272] S. Greenland, S.J. Senn, K.J. Rothman, J.B. Carlin, C. Poole, S.N. Goodman, D.G. Altman, Statistical tests, P values, confidence intervals, and power: a guide to misinterpretations, Eur. J. Epidemiol. 31 (2016) 337–350.

[273] J. Gill, The insignificance of null hypothesis significance testing, Polit. Res. Q. 52 (1999) 647–674.

[274] D. Laming, Statistics and experimental design in psychology, 1980. https://doi.org/10.1038/283909a0.

[275] A. Di Bucchianico, Coefficient of determination (R 2), Encycl. Stat. Qual. Reliab. (2008).

[276] D. Chicco, M.J. Warrens, G. Jurman, The coefficient of determination R-squared is more informative than SMAPE, MAE, MAPE, MSE and RMSE in regression analysis evaluation, PeerJ Comput. Sci. 7 (2021) e623. https://doi.org/10.7717/peerj-cs.623.

[277] G.M. Ljung, G.E.P. Box, On a measure of lack of fit in time series models, Biometrika. 65 (1978) 297–303.

[278] G.E.P. Box, N.R. Draper, Measures of lack of fit for response surface designs and predictor variable transformations, Technometrics. 24 (1982) 1–8.

[279] S. Lo, S. Andrews, To transform or not to transform: Using generalized linear mixed models to analyse reaction time data, Front. Psychol. 6 (2015) 1171.

[280] J. Pek, O. Wong, A.C. Wong, Data transformations for inference with linear regression: Clarifications and recommendations, Pract. Assessment, Res. Eval. 22 (2017) 9.

[281] J. Osborne, Improving your data transformations: Applying the Box-Cox transformation, Pract. Assessment, Res. Eval. 15 (2010) 12.

[282] D.C. Montgomery, Design and analysis of experiments, John wiley & sons, 2017.

[283] F. Xiangli, W. Wei, Y. Chen, W. Jin, N. Xu, Optimization of preparation conditions for polydimethylsiloxane (PDMS)/ceramic composite pervaporation

membranes using response surface methodology, J. Memb. Sci. 311 (2008) 23–33. https://doi.org/10.1016/j.memsci.2007.11.054.

[284] D.M. D'addona, R. Teti, Genetic algorithm-based optimization of cutting parameters in turning processes, Procedia Cirp. 7 (2013) 323–328.

[285] K.S. Lee, Z.W. Geem, A new meta-heuristic algorithm for continuous engineering optimization: harmony search theory and practice, Comput. Methods Appl. Mech. Eng. 194 (2005) 3902–3933.

[286] I. Veza, M. Spraggon, I.M.R. Fattah, M. Idris, Response surface methodology (RSM) for optimizing engine performance and emissions fueled with biofuel: Review of RSM for sustainability energy transition, Results Eng. 18 (2023) 101213. https://doi.org/10.1016/j.rineng.2023.101213.

[287] S.S. Djimtoingar, N.S.A. Derkyi, F.A. Kuranchie, J.K. Yankyera, A review of response surface methodology for biogas process optimization, Cogent Eng. 9 (2022). https://doi.org/10.1080/23311916.2022.2115283.

[288] J.C. Spall, Factorial design for efficient experimentation, IEEE Control Syst. Mag. 30 (2010) 38–53.

[289] T.-H. Hou, C.-H. Su, W.-L. Liu, Parameters optimization of a nano-particle wet milling process using the Taguchi method, response surface method and genetic algorithm, Powder Technol. 173 (2007) 153–162.

[290] G.E.P. Box, D.W. Behnken, Some new three level designs for the study of quantitative variables, Technometrics. 2 (1960) 455–475.

[291] R.L. Plackett, J.P. Burman, The design of optimum multifactorial experiments, Biometrika. 33 (1946) 305–325.

[292] P.F. de Aguiar, B. Bourguignon, M.S. Khots, D.L. Massart, R. Phan-Than-Luu, D-optimal designs, Chemom. Intell. Lab. Syst. 30 (1995) 199–210. https://doi.org/10.1016/0169-7439(94)00076-X.

[293] S.L.C. Ferreira, M. das G.A. Korn, H.S. Ferreira, E.G.P. da Silva, R.G.O. Araújo, A.S. Souza, S.M. Macedo, D. de C. Lima, R.M. de Jesus, F.A.C. Amorim, J.M. Bosque-Sendra, Application of Multivariate Techniques in Optimization of Spectroanalytical Methods, Appl. Spectrosc. Rev. 42 (2007) 475–491. https://doi.org/10.1080/05704920701551506.

[294] G.E.P. Box, K.B. Wilson, On the experimental attainment of optimum conditions, Break. Stat. Methodol. Distrib. (1992) 270–310.

[295] L. Mousavi, Z. Tamiji, M.R. Khoshayand, Applications and opportunities of experimental design for the dispersive liquid–liquid microextraction method – A review, Talanta. 190 (2018) 335–356. https://doi.org/10.1016/j.talanta.2018.08.002.

[296] P. Setasuwon, S. Kijamnajsuk, Synthesis of $Na_{0.5}Bi_{0.5}TiO_3$ Submicron Particles in Molten Salt, Adv. Mater. Res. 55–57 (2008) 161–164. https://doi.org/10.4028/www.scientific.net/amr.55-57.161.

[297] J. Li, R. Huang, C. Peng, Y. Dai, S. Xiong, C. Cai, H.T. Lin, Low temperature synthesis of plate-like Na0.5Bi0.5TiO3 via molten salt method, Ceram. Int. 46

(2020) 19752–19757. https://doi.org/10.1016/j.ceramint.2020.04.299.

[298] B.R. Li, N.Q. Zhang, H. Bin Chang, Y. Cheng, Bin-Cao, Synthesis and characterization of Bi3NbTiO9 powders prepared by molten salt method, J. Alloys Compd. 505 (2010) 542–548. https://doi.org/10.1016/j.jallcom.2010.04.256.

[299] M. Zhang, H. Fan, L. Chen, C. Yang, Synthesis and formation mechanisms of high aspect ratio platelike NaNbO3 particles by topochemical microcrystal conversion, J. Alloys Compd. 476 (2009) 847–853. https://doi.org/10.1016/j.jallcom.2008.09.124.

[300] C. Jiang, K. Zhou, X. Zhou, Z. Li, D. Zhang, Synthesis and characterization of Na0.5Bi0.5TiO3 platelets with preferred orientation using Aurivillius precursors, Ceram. Int. 41 (2015) 6858–6862. https://doi.org/10.1016/j.ceramint.2015.01.135.

[301] C.M. Riley, W.I. Rose, G.J.S. Bluth, Quantitative shape measurements of distal volcanic ash, J. Geophys. Res. Solid Earth. 108 (2003).

[302] A. Ersoy, M.D. Waller, Textural characterisation of rocks, Eng. Geol. 39 (1995) 123–136.

[303] D. Gantenbein, J. Schoelkopf, G.P. Matthews, P.A.C. Gane, Determining the size distribution-defined aspect ratio of platy particles, Appl. Clay Sci. 53 (2011) 544–552. https://doi.org/10.1016/j.clay.2011.04.020.

[304] S.B. Jones, S.P. Friedman, Particle shape effects on the effective permittivity of anisotropic or isotropic media consisting of aligned or randomly oriented ellipsoidal particles, Water Resour. Res. 36 (2000) 2821–2833. https://doi.org/10.1029/2000WR900198.

[305] H.M. Buckland, J. Saxby, M. Roche, P. Meredith, A.C. Rust, K. V. Cashman, S.L. Engwell, Measuring the size of non-spherical particles and the implications for grain size analysis in volcanology, J. Volcanol. Geotherm. Res. 415 (2021) 107257. https://doi.org/10.1016/j.jvolgeores.2021.107257.

[306] B. Ait-Amir, P. Pougnet, A. El Hami, Meta-Model Development, in: Embed. Mechatron. Syst. 2, Elsevier, 2015: pp. 151–179. https://doi.org/10.1016/B978-1-78548-014-0.50006-2.

[307] W.R. Rice, Analyzing Tables of Statistical Tests, Evolution (N. Y). 43 (1989) 223. https://doi.org/10.2307/2409177.

[308] R.D. Riley, K.I.E. Snell, J. Ensor, D.L. Burke, F.E. Harrell, K.G.M. Moons, G.S. Collins, Minimum sample size for developing a multivariable prediction model: Part I – Continuous outcomes, Stat. Med. 38 (2019) 1262–1275. https://doi.org/10.1002/sim.7993.

[309] M.J. Anderson, P.J. Whitcomb, RSM simplified: optimizing processes using response surface methods for design of experiments, Productivity press, 2016.

[310] C. N. Njoku, S. K. Otisi, Application of Central Composite Design with Design Expert v13 in Process Optimization, in: Response Surf. Methodol. - Res. Adv. Appl., IntechOpen, 2023. https://doi.org/10.5772/intechopen.109704.

[311] M.S. Bartlett, The use of transformations, Biometrics. 3 (1947) 39–52.

[312] S. Foorginezhad, M.M. Zerafat, Microfiltration of cationic dyes using nano-clay membranes, Ceram. Int. 43 (2017) 15146–15159. https://doi.org/10.1016/j.ceramint.2017.08.045.

[313] R. Ghelich, M.R. Jahannama, H. Abdizadeh, F.S. Torknik, M.R. Vaezi, Central composite design (CCD)-Response surface methodology (RSM) of effective electrospinning parameters on PVP-B-Hf hybrid nanofibrous composites for synthesis of HfB2-based composite nanofibers, Compos. Part B Eng. 166 (2019) 527–541. https://doi.org/10.1016/j.compositesb.2019.01.094.

[314] J. Osborne, Notes on the use of data transformations, Pract. Assessment, Res. Eval. 8 (2002) 6.

[315] M.F. Freeman, J.W. Tukey, Transformations related to the angular and the square root, Ann. Math. Stat. (1950) 607–611.

[316] V. Kumar, P. Saharan, A.K. Sharma, A. Umar, I. Kaushal, A. Mittal, Y. Al-Hadeethi, B. Rashad, Silver doped manganese oxide-carbon nanotube nanocomposite for enhanced dye-sequestration: isotherm studies and RSM modelling approach, Ceram. Int. 46 (2020) 10309–10319.

[317] Z.D.I. Sktani, N.A. Rejab, M.M. Ratnam, Z.A. Ahmad, Fabrication of tougher ZTA ceramics with sustainable high hardness through (RSM) optimisation, Int. J. Refract. Met. Hard Mater. 74 (2018) 78–86.

[318] M. Kamankesh, A. Mohammadi, Z. Modarres Tehrani, R. Ferdowsi, H. Hosseini, Dispersive liquid–liquid microextraction followed by high-performance liquid chromatography for determination of benzoate and sorbate in yogurt drinks and method optimization by central composite design, Talanta. 109 (2013) 46–51. https://doi.org/10.1016/j.talanta.2013.01.052.

[319] A. IDRIS, F. KORMIN, M. NOORDIN, Application of response surface methodology in describing the performance of thin film composite membrane, Sep. Purif. Technol. 49 (2006) 271–280. https://doi.org/10.1016/j.seppur.2005.10.010.

[320] M. Elsayed, M. Ghazy, Y. Youssef, K. Essa, Optimization of SLM process parameters for Ti6Al4V medical implants, Rapid Prototyp. J. 25 (2019) 433–447. https://doi.org/10.1108/RPJ-05-2018-0112.

[321] H.-C. Yu, S.-M. Huang, W.-M. Lin, C.-H. Kuo, C.-J. Shieh, Comparison of Artificial Neural Networks and Response Surface Methodology towards an Efficient Ultrasound-Assisted Extraction of Chlorogenic Acid from Lonicera japonica, Molecules. 24 (2019) 2304. https://doi.org/10.3390/molecules24122304.

[322] L. Sthle, S. Wold, Analysis of variance (ANOVA), Chemom. Intell. Lab. Syst. 6 (1989) 259–272. https://doi.org/10.1016/0169-7439(89)80095-4.

[323] S. Pandey, C.L. Bright, What Are Degrees of Freedom?, Soc. Work Res. 32 (2008) 119–128. http://www.jstor.org/stable/42659677.

[324] R.S. Tan, T.A. Tuan Abdullah, A. Abdul Jalil, K. Md Isa, Optimization of hydrogen production from steam reforming of biomass tar over

Ni/dolomite/La2O3 catalysts, J. Energy Inst. 93 (2020) 1177–1186. https://doi.org/10.1016/j.joei.2019.11.001.

[325] F. Mansouri, A. Khavanin, A.J. Jafari, H. Asilian, H.R. Ghomi, S.M. Mousavi, Energy efficiency improvement in nitric oxide reduction by packed DBD plasma: optimization and modeling using response surface methodology(RSM), Environ. Sci. Pollut. Res. 27 (2020) 16100–16109. https://doi.org/10.1007/s11356-020-07870-w.

[326] S. Ebrahimi, C. Stephen Sipaut@ Mohd Nasri, S.E. Bin Arshad, Hydrothermal synthesis of hydroxyapatite powders using Response Surface Methodology (RSM), PLoS One. 16 (2021) e0251009. https://doi.org/10.1371/journal.pone.0251009.

[327] M.M. Ba-Abbad, A.A.H. Kadhum, A.B. Mohamad, M.S. Takriff, K. Sopian, Optimization of process parameters using D-optimal design for synthesis of ZnO nanoparticles via sol–gel technique, J. Ind. Eng. Chem. 19 (2013) 99–105.

[328] H. Xu, F. Wu, M. Li, Z. Liang, Application of response surface methodology for optimization of nano-TiO2 preparation using modified sol-gel method, J. Sol-Gel Sci. Technol. 67 (2013) 394–405. https://doi.org/10.1007/s10971-013-3093-7.

[329] K.C. Bedin, A.L. Cazetta, I.P.A.F. Souza, O. Pezoti, L.S. Souza, P.S.C. Souza, J.T.C. Yokoyama, V.C. Almeida, Porosity enhancement of spherical activated carbon: Influence and optimization of hydrothermal synthesis conditions using response surface methodology, J. Environ. Chem. Eng. 6 (2018) 991–999. https://doi.org/10.1016/j.jece.2017.12.069.

[330] K. Salehi, H. Daraei, P. Teymouri, A. Maleki, Hydrothermal synthesis of surface-modified copper oxide-doped zinc oxide nanoparticles for degradation of acid black 1: Modeling and optimization by response surface methodology, J. Adv. Environ. Heal. Res. 2 (2014) 101–109.

[331] A.A. Bunaciu, E. gabriela Udriştioiu, H.Y. Aboul-Enein, X-Ray Diffraction: Instrumentation and Applications, Crit. Rev. Anal. Chem. 45 (2015) 289–299. https://doi.org/10.1080/10408347.2014.949616.

[332] P. Scherrer, Nachrichten von der Gesellschaft der Wissenschaften zu Göttingen, Math. Klasse. 2 (1918) 98–100.

[333] J. Rivnay, R. Noriega, R.J. Kline, A. Salleo, M.F. Toney, Quantitative analysis of lattice disorder and crystallite size in organic semiconductor thin films, Phys. Rev. B. 84 (2011) 45203.

[334] M. Selvaraj, V. Venkatachalapathy, J. Mayandi, Preparation of meta-stable phases of barium titanate by Sol-hydrothermal method Preparation of meta-stable phases of barium titanate by Sol-hydrothermal method, (2015). https://doi.org/10.1063/1.4935645.

[335] F. Ruf, M.F. Aygüler, N. Giesbrecht, B. Rendenbach, A. Magin, P. Docampo, H. Kalt, M. Hetterich, Temperature-dependent studies of exciton binding energy and phase-transition suppression in (Cs,FA,MA)Pb(I,Br)3 perovskites, APL Mater. 7 (2019). https://doi.org/10.1063/1.5083792.

[336] X. Chao, Z. Wang, Z. Yang, Y. Chang, Z. Liu, Synthesis and morphology of anisotropic NaNbO3 seed crystals, Mater. Chem. Phys. 111 (2008) 195–200. https://doi.org/10.1016/j.matchemphys.2008.04.031.

[337] Z. Zhao, X. Li, H. Ji, M. Deng, Formation Mechanism of Plate-like Bi 4 Ti 3 O 12 Particles in Molten Salt Fluxes, Integr. Ferroelectr. 154 (2014) 154–158. https://doi.org/10.1080/10584587.2014.904705.

[338] B.R. Jennings, K. Parslow, Particle size measurement: the equivalent spherical diameter, Proc. R. Soc. London. A. Math. Phys. Sci. 419 (1988) 137–149.

[339] Y. Ma, H. Xie, Y. Sun, Q. Kou, L. Liu, B. Yang, W. Cao, Y. Chang, F. Li, Topochemical synthesis and structural characteristics of orientation-controlled $(Bi_{0.5}Na_{0.5})_{0.94}Ba_{0.06}TiO_3$ perovskite microplatelets, Topochemical Synth. Struct. Charact. Orientation-Controlled $(Bi_{0.5}Na_{0.5})_{0.94}Ba_{0.06}TiO_3$ Perovskite Microplatelets. 2 (2022) 2022006. https://doi.org/10.20517/microstructures.2021.13.

[340] F. Wen, H. Lou, J. Ye, W. Bai, L. Wang, L. Li, W. Wu, Z. Xu, G. Wang, Z. Zhang, L. Zhang, Preparation and energy storage performance of transparent dielectric films with two-dimensional platelets, Compos. Sci. Technol. 182 (2019) 107759. https://doi.org/10.1016/j.compscitech.2019.107759.

[341] D. Lv, R. Zuo, S. Su, Processing and Morphology of (111) BaTiO3 Crystal Platelets by a Two-Step Molten Salt Method, J. Am. Ceram. Soc. 95 (2012) 1838–1842. https://doi.org/10.1111/j.1551-2916.2012.05124.x.

[342] C.J. Guo, C.S. Zhang, Molten salt synthesis of anisotropic Bi4Ti3O12 particles, Adv. Mater. Res. 284 (2011) 1452–1455.

[343] X. Feng, B. Xu, X. Xu, P. Chen, Z. Wu, D. Teng, J. Xu, F. Gao, Fabrication plate-like BaBi 4 Ti 4 O15 single-crystalline particles by the molten salt synthesis method, J. Adv. Dielectr. 13 (2023). https://doi.org/10.1142/S2010135X22500229.

[344] L. Li, J. Chen, J. Deng, R. Yu, L. Qiao, G. Liu, X. Xing, Topochemical Synthesis of Micron-Platelet (Na 0.5 K 0.5)NbO 3 Particles, Eur. J. Inorg. Chem. 2008 (2008) 2186–2190. https://doi.org/10.1002/ejic.200701263.

[345] S.M. Shahabaz, P. Mehrotra, H. Kalita, S. Sharma, N. Naik, D.J. Noronha, N. Shetty, Effect of Al2O3 and SiC Nano-Fillers on the Mechanical Properties of Carbon Fiber-Reinforced Epoxy Hybrid Composites, J. Compos. Sci. 7 (2023) 133. https://doi.org/10.3390/jcs7040133.

[346] H.B. Kaybal, H. Ulus, O. Demir, Ö.S. Şahin, A. Avcı, Effects of alumina nanoparticles on dynamic impact responses of carbon fiber reinforced epoxy matrix nanocomposites, Eng. Sci. Technol. an Int. J. 21 (2018) 399–407. https://doi.org/10.1016/j.jestch.2018.03.011.

[347] Y. Zare, Study of nanoparticles aggregation/agglomeration in polymer particulate nanocomposites by mechanical properties, Compos. Part A Appl. Sci. Manuf. 84 (2016) 158–164. https://doi.org/10.1016/j.compositesa.2016.01.020.

[348] L.K. Namitha, M.T. Sebastian, High permittivity ceramics loaded silicone

elastomer composites for flexible electronics applications, Ceram. Int. 43 (2017) 2994–3003. https://doi.org/10.1016/j.ceramint.2016.11.080.

[349] N.K. James, Piezoelectric and dielectric properties of polymer-ceramic composites for sensors, Delf Netherlands, 2015.

[350] B. Luo, X. Wang, Y. Wang, L. Li, Fabrication, characterization, properties and theoretical analysis of ceramic/PVDF composite flexible films with high dielectric constant and low dielectric loss, J. Mater. Chem. A. 2 (2014) 510–519.

[351] Y. Hu, Y. Zhang, H. Liu, D. Zhou, Microwave dielectric properties of PTFE/CaTiO3 polymer ceramic composites, Ceram. Int. 37 (2011) 1609–1613.

[352] P. Kum-onsa, P. Thongbai, Improved Dielectric Properties of Poly(vinylidene fluoride) Composites Incorporating Na1/2Y1/2Cu3Ti4O12 Particles, Mater. Today Commun. 25 (2020) 101654. https://doi.org/10.1016/j.mtcomm.2020.101654.

[353] P. Thomas, K.T. Varughese, K. Dwarakanath, K.B.R. Varma, Dielectric properties of Poly(vinylidene fluoride)/CaCu3Ti4O12 composites, Compos. Sci. Technol. 70 (2010) 539–545. https://doi.org/10.1016/j.compscitech.2009.12.014.

[354] P.K. Panda, B. Sahoo, PZT to lead free piezo ceramics: A review, Ferroelectrics. 474 (2015) 128–143. https://doi.org/10.1080/00150193.2015.997146.

[355] A. Watcharapasorn, S. Jiansirisomboon, T. Tunkasiri, Microstructures and mechanical properties of zirconium-doped bismuth sodium titanate ceramics, Chiang Mai J. Sci. 33 (2006) 169–173.

[356] A. Skaliukh, About Mathematical Models of Irreversible Polarization Processes of a Ferroelectric and Ferroelastic Polycrystals, in: Ferroelectr. Their Appl., InTech, 2018. https://doi.org/10.5772/intechopen.78262.

[357] H. Yang, Z. Cai, C. Zhu, P. Feng, X. Wang, Ultra-High Energy Storage Performance in BNT-based Ferroelectric Ceramics with Simultaneously Enhanced Polarization and Breakdown Strength, ACS Sustain. Chem. Eng. 10 (2022) 9176–9183. https://doi.org/10.1021/acssuschemeng.2c02155.

[358] A. Ullah, C.W. Ahn, K.B. Jang, A. Hussain, I.W. Kim, Phase transition and electrical properties of BiAlO3-modified (Bi0.5Na0.5)TiO3 piezoelectric ceramics, Ferroelectrics. 404 (2010) 167–172. https://doi.org/10.1080/00150193.2010.482490.

[359] P. Gowdhaman, V. Annamalai, O.P. Thakur, Piezo, ferro and dielectric properties of ceramic-polymer composites of 0-3 connectivity, Ferroelectrics. 493 (2016) 120–129. https://doi.org/10.1080/00150193.2016.1134028.

[360] M. Xie, Y. Zhang, M.J. Kras´ny, K. Kras´ny, C. Bowen, H. Khanbareh, N. Gathercole, Flexible and active self-powered pressure, shear sensors based on freeze casting ceramic-polymer composites †, Energy Environ. Sci. 11 (2018) 2919. https://doi.org/10.1039/c8ee01551a.

[361] T. Garg, V. Annapureddy, K.C. Sekhar, D.Y. Jeong, N. Dabra, J.S. Hundal,

Modulation in polymer properties in PVDF/BCZT composites with ceramic content and their energy density capabilities, Polym. Compos. 41 (2020) 5305–5316. https://doi.org/10.1002/pc.25795.

[362] S. Saba, G.M. Mustafa, M. Saleem, S.M. Ramay, S. Atiq, Ferroelectric polymer/ceramic nanocomposites with low energy losses, Polym. Compos. 41 (2020) 3271–3281. https://doi.org/10.1002/pc.25618.

[363] S. Yue, B. Wan, H. Li, Y. Liu, Q. Zhang, Enhanced dielectric and energy storage properties of the (200)-oriented plate-like Na 0.5 Bi 0.5 TiO 3 /polyimide composite materials, Int. J. Electrochem. Sci. 14 (2019) 2049–2062. https://doi.org/10.20964/2019.02.78.

[364] H. Luo, J. Roscow, X. Zhou, S. Chen, X. Han, K. Zhou, D. Zhang, C.R. Bowen, Ultra-high discharged energy density capacitor using high aspect ratio Na0.5Bi0.5TiO3 nanofibers, J. Mater. Chem. A. 5 (2017) 7091–7102. https://doi.org/10.1039/c7ta00136c.

[365] Z. Xu, L. Weng, L. Guan, X. Zhang, X. Wang, Z. Wu, Enhanced energy storage performance of PVDF composite films with Na0.5Bi0.5TiO3 particles, J. Mater. Sci. Mater. Electron. 32 (2021) 28129–28143. https://doi.org/10.1007/s10854-021-07191-9.

[366] A. Kumar, A. Kumar, K. Prasad, Evaluation of (Na1/2Bi1/2)TiO3/PVDF Piezocomposites for mechanical energy harvesting, Solid State Sci. 121 (2021) 106729. https://doi.org/10.1016/J.SOLIDSTATESCIENCES.2021.106729.

[367] B. Luo, X. Wang, Q. Zhao, L. Li, Synthesis, characterization and dielectric properties of surface functionalized ferroelectric ceramic/epoxy resin composites with high dielectric permittivity, Compos. Sci. Technol. 112 (2015) 1–7. https://doi.org/10.1016/j.compscitech.2015.02.018.

[368] X. Zhang, M. Le, O. Zahhaf, J. Capsal, P. Cottinet, L. Petit, Enhancing dielectric and piezoelectric properties of micro-ZnO / PDMS composite-based dielectrophoresis, Mater. Des. 192 (2020) 108783. https://doi.org/10.1016/j.matdes.2020.108783.

[369] Y. Zhan, Z. Long, X. Wan, C. Zhan, J. Zhang, Y. He, Enhanced dielectric permittivity and thermal conductivity of hexagonal boron nitride / poly (arylene ether nitrile) composites through magnetic alignment and mussel inspired co-modi fi cation, 43 (2017) 12109–12119. https://doi.org/10.1016/j.ceramint.2017.06.068.

[370] S. Jin, X. Qiu, B. Huang, L. Wang, Q. Zhang, Z. Fu, Dielectric properties of modified BNT/PTFE composites for microwave RF antenna applications, J. Mater. Sci. Mater. Electron. 27 (2016) 8378–8383. https://doi.org/10.1007/s10854-016-4849-y.

[371] S. Hajra, S. Sahoo, R.N.P. Choudhary, Fabrication and electrical characterization of (Bi0.49Na0.49Ba0.02)TiO3-PVDF thin film composites., J. Polym. Res. 26 (2019) 1. http://10.0.3.239/s10965-018-1673-5%0Ahttp://proxy.libraries.smu.edu/login?url=http://search.ebscohost.com/login.aspx?direct=true&db=a9h&AN=134208390&site=ehost-live&scope=site.

[372] S.D. Cho, S.Y. Lee, J.G. Hyun, K.W. Paik, Comparison of theoretical

predictions and experimental values of the dielectric constant of epoxy/BaTiO3 composite embedded capacitor films, J. Mater. Sci. Mater. Electron. 16 (2005) 77–84. https://doi.org/10.1007/s10854-005-6454-3.

[373] Lynell J. Gilbert; Thomas P. Shuman; Faith Dogan, Dielectric Powder/Polymer composites for high energy density capacitators, Adv. Electron. Electrochem. Ceram. 179 (2005) 227. https://www.wiley.com/en-us/Advances+in+Electronic+and+Electrochemical+Ceramics%3A+Proceedings+of+the+107th+Annual+Meeting+of+The+American+Ceramic+Society%2C+Baltimore%2C+Maryland%2C+USA+2005-p-9781574982626 (accessed May 5, 2023).

[374] L. Ren, X. Zeng, X. Zhang, R. Sun, X. Tian, Y. Zeng, J. Bin Xu, C.P. Wong, Silver nanoparticle-modified alumina microsphere hybrid composites for enhanced energy density and thermal conductivity, Compos. Part A Appl. Sci. Manuf. 119 (2019) 299–309. https://doi.org/10.1016/j.compositesa.2019.02.004.

[375] S.P.P. Sadhu, S. Siddabattuni, B. Ponraj, M. Molli, V. Sai Muthukumar, K.B.R. Varma, Enhanced dielectric properties and energy storage density of interface controlled ferroelectric BCZT-epoxy nanocomposites, Compos. Interfaces. 24 (2017) 663–675. https://doi.org/10.1080/09276440.2017.1262665.

[376] H. Tang, Y. Lin, H.A. Sodano, Enhanced Energy Storage in Nanocomposite Capacitors through Aligned PZT Nanowires by Uniaxial Strain Assembly, Adv. Energy Mater. 2 (2012) 469–476. https://doi.org/10.1002/aenm.201100543.

[377] A. Choudhury, Dielectric and piezoelectric properties of polyetherimide/BaTiO3 nanocomposites, Mater. Chem. Phys. 121 (2010) 280–285. https://doi.org/10.1016/J.MATCHEMPHYS.2010.01.035.

[378] D. Sun, J. Yin, Y. Liu, X. Liu, The electrical and thermal properties of polyimide/boron nitride nanocomposite films, J. Polym. Res. 23 (2016) 2–9. https://doi.org/10.1007/s10965-016-1151-x.

[379] M. Mikolajek, T. Reinheimer, N. Bohn, C. Kohler, M.J. Hoffmann, J.R. Binder, Fabrication and Characterization of Fully Inkjet Printed Capacitors Based on Ceramic/Polymer Composite Dielectrics on Flexible Substrates, Sci. Rep. 9 (2019) 1–13. https://doi.org/10.1038/s41598-019-49639-3.

[380] Y. Liu, W. Liu, Y. Zhou, J. Chen, Z. Wang, W. Du, J. Wen, J. Cao, D. Zhang, Enhanced dielectric constant and breakdown strength in dielectric composites using TiO2@HfO2 nanowires with gradient dielectric constant, Ceram. Int. 48 (2022) 12483–12489. https://doi.org/10.1016/j.ceramint.2022.01.114.

[381] L. Variar, M.N. Muralidharan, S.K. Narayanankutty, S. Ansari, High dielectric constant, flexible and easy-processable calcium copper titanate/thermoplastic polyurethane (CCTO/TPU) composites through simple casting method, J. Mater. Sci. Mater. Electron. 32 (2021) 5908–5919. https://doi.org/10.1007/s10854-021-05311-z.

[382] Y. Zhang, M. Wang, C. Yang, Y. Shao, X. Qi, J. Yang, Y. Wang, Heterogeneous BaTiO3@Ag core-shell fibers as fillers for polymer dielectric composites with simultaneously improved dielectric constant and breakdown

strength, Compos. Commun. 27 (2021) 100874. https://doi.org/10.1016/j.coco.2021.100874.

[383] S. Liu, Y. Guo, G. Hu, S. Wu, J. Xu, J. Chen, W. Bulejak, H. Baxter, B. Yang, J. Kong, M. Szafran, F. Gao, (Ba0.6Sr0.4)TiO3/PEEK composites modified by polyethersulfone with low dielectric constant and high dielectric tunability under DC bias, Compos. Sci. Technol. 233 (2023) 109929. https://doi.org/10.1016/j.compscitech.2023.109929.

[384] P. Mallick, R. Patra, D. Mohanty, S.K.U. Satpathy, Development and characterization of copper doped perovskite- polymer composite through high-temperature technique, Sādhanā. 134 (2022) (2022). https://doi.org/10.1007/s12046-022-01904-4.

[385] P. Singh, H. Borkar, B.P. Singh, V.N. Singh, A. Kumar, Ferroelectric polymer-ceramic composite thick films for energy storage applications, AIP Adv. 4 (2014) 087117. https://doi.org/10.1063/1.4892961.

[386] T. Kim, H. Lim, Y. Lee, B.J. Kim, Synthesis of BaTiO3nanoparticles as shape modified filler for high dielectric constant ceramic-polymer composite, RSC Adv. 10 (2020) 29278–29286. https://doi.org/10.1039/d0ra04196c.

[387] Y. Zeng, C. Xiong, J. Li, Z. Huang, G. Du, Z. Fan, N. Chen, Structural, dielectric and mechanical behaviors of (La, Nb) Co-doped TiO2/Silicone rubber composites, Ceram. Int. 47 (2021) 22365–22372. https://doi.org/10.1016/j.ceramint.2021.04.245.

[388] Y. Guo, S. Liu, S. Wu, J. Xu, E. Pawlikowska, W. Bulejak, M. Szafran, A. Rydosz, F. Gao, Enhanced tunable dielectric properties of Ba0.6Sr0.4TiO3/PVDF composites through dual-gradient structural engineering, J. Alloys Compd. 920 (2022). https://doi.org/10.1016/j.jallcom.2022.166034.

[389] I. Babu, D.A. van den Ende, G. de With, Processing and characterization of piezoelectric 0-3 PZT/LCT/PA composites, J. Phys. D. Appl. Phys. 43 (2010) 425402. https://doi.org/10.1088/0022-3727/43/42/425402.

[390] I. Babu, G. de With, Highly flexible piezoelectric 0-3 PZT-PDMS composites with high filler content, Compos. Sci. Technol. 91 (2014) 91–97. https://doi.org/10.1016/j.compscitech.2013.11.027.

[391] H. Peng, H. Ren, M. Dang, Y. Zhang, X. Yao, H. Lin, Novel high dielectric constant and low loss PTFE / CNT composites, Ceram. Int. 44 (2018) 16556–16560. https://doi.org/10.1016/j.ceramint.2018.06.077.

[392] C. Chen, L. Wang, X. Liu, W. Yang, J. Lin, G. Chen, X. Yang, K0.5Na0.5NbO3-SrTiO3/PVDF Polymer Composite Film with Low Remnant Polarization and High Discharge Energy Storage Density, Polym. 2019, Vol. 11, Page 310. 11 (2019) 310. https://doi.org/10.3390/POLYM11020310.

[393] N.B. Mahmood, E.K. Al-Shakarchi, Simulation and Experimental Data of P-E Hysteresis Loop in BNT and BKT, J. Mod. Phys. 08 (2017) 844–851. https://doi.org/10.4236/jmp.2017.85053.

[394] F. Aslam, Z. Li, G. Qu, Y. Feng, S. Li, S. Li, H. Mao, Improvement of DC

Breakdown Strength of the Epoxy/POSS Nanocomposite by Tailoring Interfacial Electron Trap Characteristics, Materials (Basel). 14 (2021) 1298. https://doi.org/10.3390/ma14051298.

[395] R. Guo, J.I. Roscow, C.R. Bowen, H. Luo, Y. Huang, Y. Ma, K. Zhou, D. Zhang, Significantly enhanced permittivity and energy density in dielectric composites with aligned BaTiO3 lamellar structures, J. Mater. Chem. A. 8 (2020) 3135–3144. https://doi.org/10.1039/c9ta11360f.

[396] G. Jian, Y. Jiao, Q. Meng, Z. Wei, J. Zhang, C. Yan, K.S. Moon, C.P. Wong, Enhanced dielectric constant and energy density in a BaTiO3/polymer-matrix composite sponge, Commun. Mater. 1 (2020) 1–12. https://doi.org/10.1038/s43246-020-00092-0.

[397] S. Luo, Y. Shen, S. Yu, Y. Wan, W.-H. Liao, R. Sun, C.-P. Wong, Construction of a 3D-BaTiO 3 network leading to significantly enhanced dielectric permittivity and energy storage density of polymer composites, Energy Environ. Sci. 10 (2017) 137–144. https://doi.org/10.1039/C6EE03190K.

[398] Z. Zhang, Y. Gu, J. Bi, S. Wang, M. Li, Z. Zhang, Tunable BT@SiO2 core@shell filler reinforced polymer composite with high breakdown strength and release energy density, Compos. Part A Appl. Sci. Manuf. 85 (2016) 172–180. https://doi.org/10.1016/j.compositesa.2016.03.025.

[399] S. Adireddy, V.S. Puli, T.J. Lou, R. Elupula, S.C. Sklare, B.C. Riggs, D.B. Chrisey, Polymer-ceramic nanocomposites for high energy density applications, J. Sol-Gel Sci. Technol. 73 (2015) 641–646. https://doi.org/10.1007/s10971-014-3573-4.

[400] J. Shang, Y. Zhang, L. Yu, X. Luan, B. Shen, Z. Zhang, F. Lv, P.K. Chu, Fabrication and enhanced dielectric properties of graphene–polyvinylidene fluoride functional hybrid films with a polyaniline interlayer, J. Mater. Chem. A. 1 (2013) 884–890. https://doi.org/10.1039/C2TA00602B.

List of Publications

1. P. Eltouby, I. Shyha, C. Li, J. Khaliq, Factors affecting the piezoelectric performance of ceramic-polymer composites: A comprehensive review, Ceramics International 47 (2021) 17813-17825. https://doi.org/10.1016/j.ceramint.2021.03.126.
2. P. Eltouby, F. Elfakhri, H. M. Eldessouky, C. Li, L. E. Dodd, J. Khaliq, Predictive modeling and optimisation of two-dimensional particle shape and size in molten salt synthesis for enhanced dielectric performance using a response surface methodology approach, Journal of Advanced Powder Materials (APM) (Under Review)
3. P. Eltouby, F. Elfakhri, H. M. Eldessouky, J. Khaliq, Exploring the influence of mechanical alignment technique on dielectric properties and energy storage potential in ceramic/polymer composites (Under Preparation)

Appendix A

DOE – ANOVA Tests

The parameters resulting from applying an ANOVA test for a general RSM design with n replicates is described briefly in this appendix. The table below shows the general form of an ANOVA analysis for a 2^k factorial design.

Source of Variation		SS	dF	MS	F_o
K main effects	A	SS_A	a-1	$MS_A = \frac{SS_A}{a-1}$	$\frac{MS_A}{MS_E}$
	B	SS_B	b-1	$MS_B = \frac{SS_B}{b-1}$	$\frac{MS_B}{MS_E}$
	⋮	⋮	⋮	⋮	
	K	SS_K	k-1	$MS_B = \frac{SS_K}{k-1}$	$\frac{MS_K}{MS_E}$
Two-Factor Interaction	AB	SS_{AB}	(a-1)(b-1)	$MS_{AB} = \frac{SS_{AB}}{(a-1)(b-1)}$	$\frac{MS_{AB}}{MS_E}$
	AC	SS_{AC}	(a-1)(c-1)	$MS_{AB} = \frac{SS_{AC}}{(a-1)(c-1)}$	$\frac{MS_{AC}}{MS_E}$
	⋮	⋮	⋮	⋮	
	JK	SS_{JK}	(j-1)(k-1)	$MS_{JK} = \frac{SS_{JK}}{(j-1)(k-1)}$	$\frac{MS_{JK}}{MS_E}$
***k*-Factor Interaction**	ABC… K	$SS_{ABC....K}$	(a-1)(b-1)(c-1)....(k-1)	$MS_{ABC...K} = \frac{SS_{ABC....K}}{(a-1)(b-1)(c-1)....(}$	$\frac{MS_{ABC...}}{MS_E}$
ERROR		SS_E	$2^k(n-1)$	$MS_E = \frac{SS_E}{2^k(n-1)}$	
TOTAL		SS_T	$n2^k - 1$	$MS_T = \frac{SS_T}{n2^k - 1}$	

The parameters used for an ANOVA test found in the previous table are described as follows:

- There are a levels of factor A, b levels of factor B, c levels of factor C and so on, arranged in a factorial order, whereas *n* represents the number of replicates of the complete experiment.

$$\boldsymbol{i = 1, 2, \ldots, a}$$
$$\mathbf{j = 1, 2, \ldots, b}$$
$$\boldsymbol{k = 1, 2, \ldots, c}$$

- Degree of freedom (dF) is calculated for each main factor by subtracting the levels by one, and for the combination of factors as the product of the degree of freedoms of the corresponding main factors.

- Sum of Squares (SS) is a measure of variation or deviation of a factor from the mean. In order to calculate the sum of squares, the average of experiments replications for each effect must be calculated. The formula below presents generally the grand average ($\bar{y}_{\ldots}$) calculated upon the grand total ($y_{\ldots}$). The average is calculated for each of the corresponding ith, jth and

$$\boldsymbol{y_{\ldots} = \sum_{i=1}^{a} \sum_{j=1}^{b} \sum_{k=1}^{c} y_{ijk} \quad \bar{y}_{\ldots} = \frac{y_{\ldots}}{abk}}$$

- Once the averages are calculated, the variance of these averages are required. The case presented in this theses considers a three factor analysis of variance and thus the sum of squares for the main effects, in this case, a are computed from the totals of the factors A($\boldsymbol{y_{i\ldots}}$) , **B**($\boldsymbol{y_{.j.}}$) , $\boldsymbol{C}(\boldsymbol{y_{..k}})$ as shown in the equation below.

$$\boldsymbol{SS_A = \frac{1}{bcn} \sum_{i=1}^{a} y^2{}_{i\ldots} - \frac{y^2{}_{\ldots}}{abcn}}$$

$$\boldsymbol{SS_B = \frac{1}{bcn} \sum_{j=1}^{b} y^2{}_{.j.} - \frac{y^2{}_{\ldots}}{abcn}}$$

$$\boldsymbol{SS_C = \frac{1}{abn} \sum_{k=1}^{c} y^2{}_{..k} - \frac{y^2{}_{\ldots}}{abcn}}$$

- For the computation of the two-factor interaction sums of squares, the totals for the A x B, A x C and B x C cells are needed. The formula for one of the interacted effect is shown below:

$$SS_{AB} = \frac{1}{cn}\sum_{i=1}^{a}\sum_{j=1}^{b} y^2{}_{ij..} - \frac{y^2{}_{...}}{abcn} - SS_A - SS_B$$

$$= SS_{Subtotal(AB)} - SS_A - SS_B$$

- The total of the sum of squares is:

$$SS_T = \sum_{i=1}^{a}\sum_{j=1}^{b}\sum_{k=1}^{c}\sum_{l=1}^{n} y^2{}_{ijkl} - \frac{y^2{}_{...}}{abcn}$$

- The error sum of squares is computed by subtracting the sum of squares for each main effect and interaction from the total sum of squares.
- Mean Square (MS) is mean of the SS stated above and is calculated by dividing the SS by the dF and calculated for all factors and their interactions.
- F_o is the means by which the significance of a factor is decided. F_o is the ratio of that part of the sum of squares attributed to a factor to that attributed to the error. That error is already assumed as a normal variable. Therefore, as F_o tends to unity or near to unity, that variation of the response due to that factor could be considered as random and hence the effect is not significant.
- The P-Value is based on an F-distribution. If this value is less than 0.0001, then the factor has a significant effect on the response, otherwise less than 0.05 is considered marginally significant.

Appendix B

- Distribution plots depicting the variation in the measured area of the particles across the 17 samples:

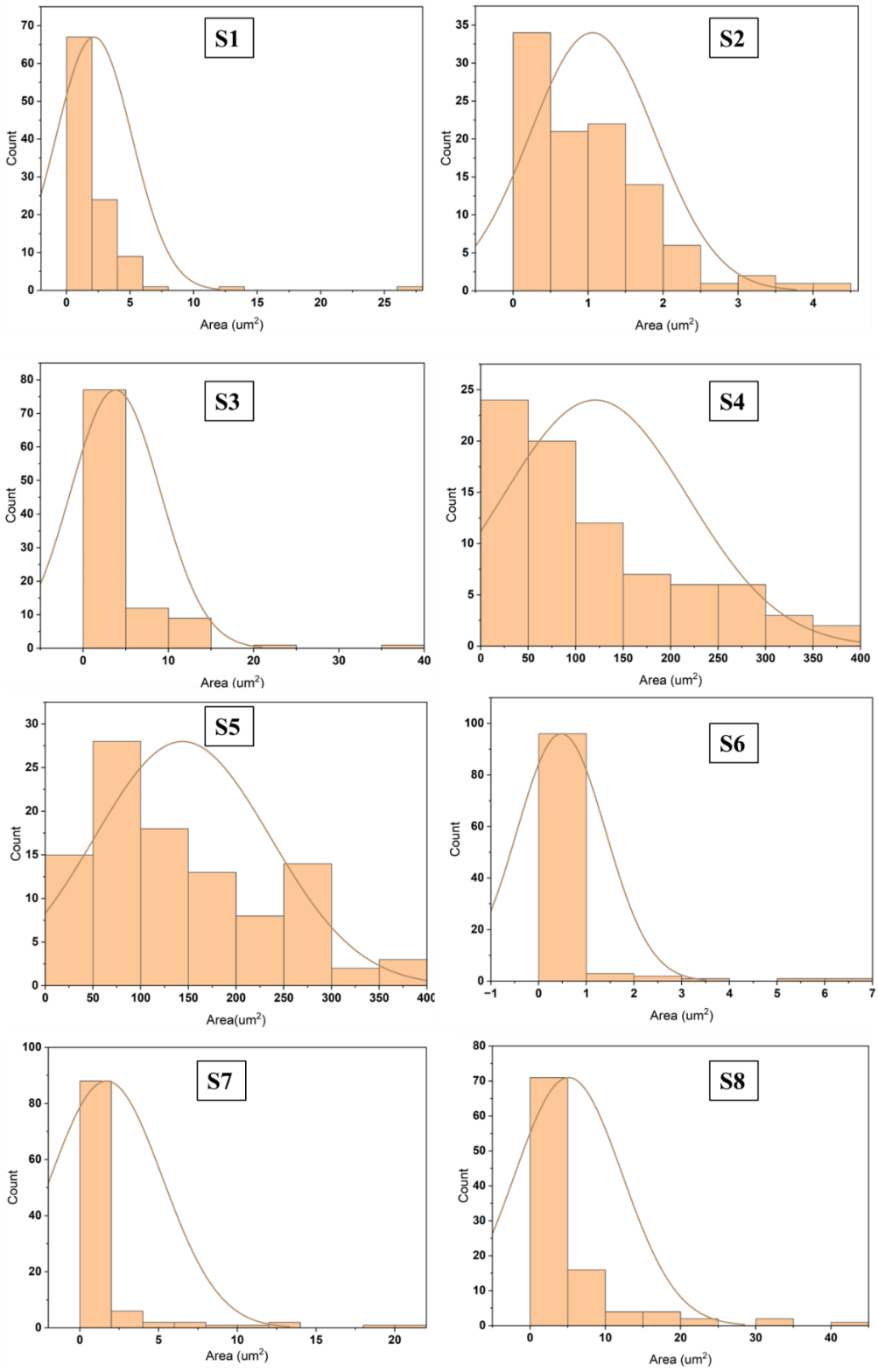

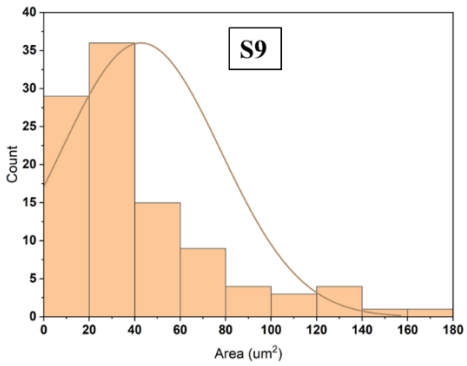
S9
Count
Area (um²)

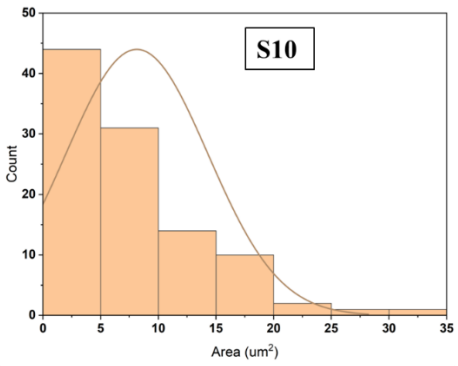
S10
Count
Area (um²)

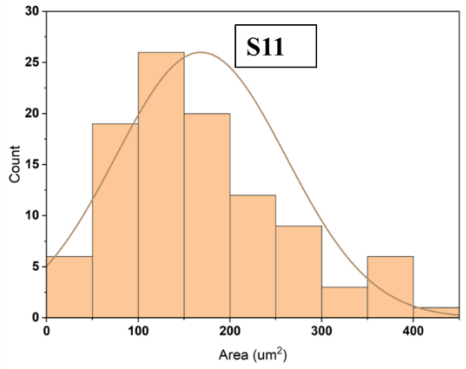
S11
Count
Area (um²)

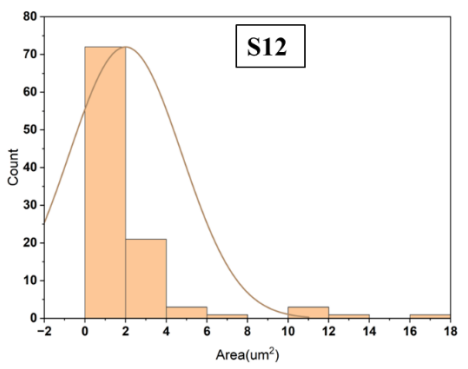
S12
Count
Area(um²)

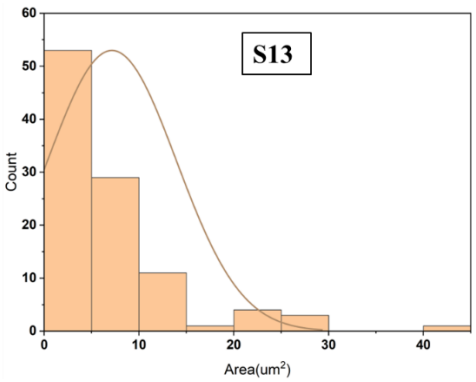
S13
Count
Area(um²)

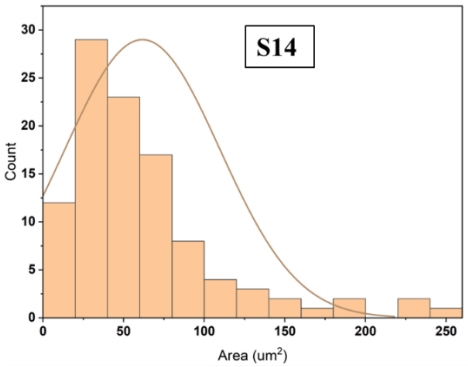
S14
Count
Area (um²)

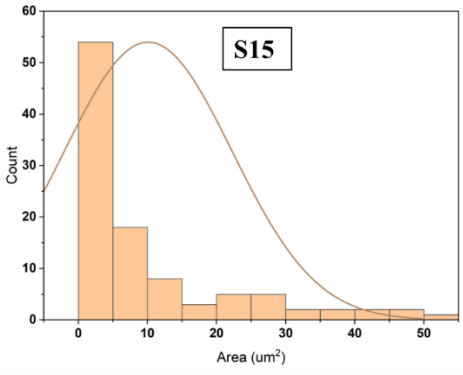
S15
Count
Area (um²)

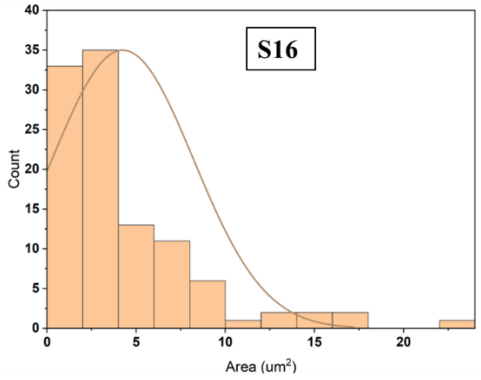
S16
Count
Area (um²)

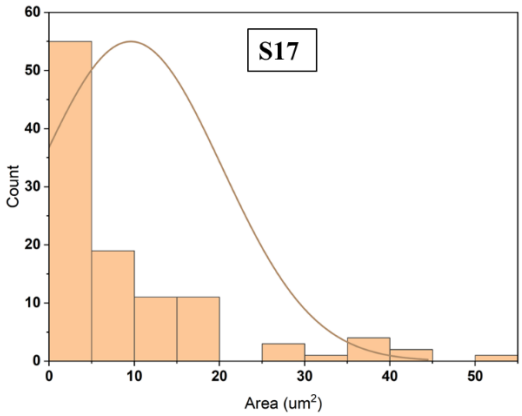
S17
Count
Area (um²)

- Distribution plots depicting the variation in the measured thickness of the particles across the 17 samples:

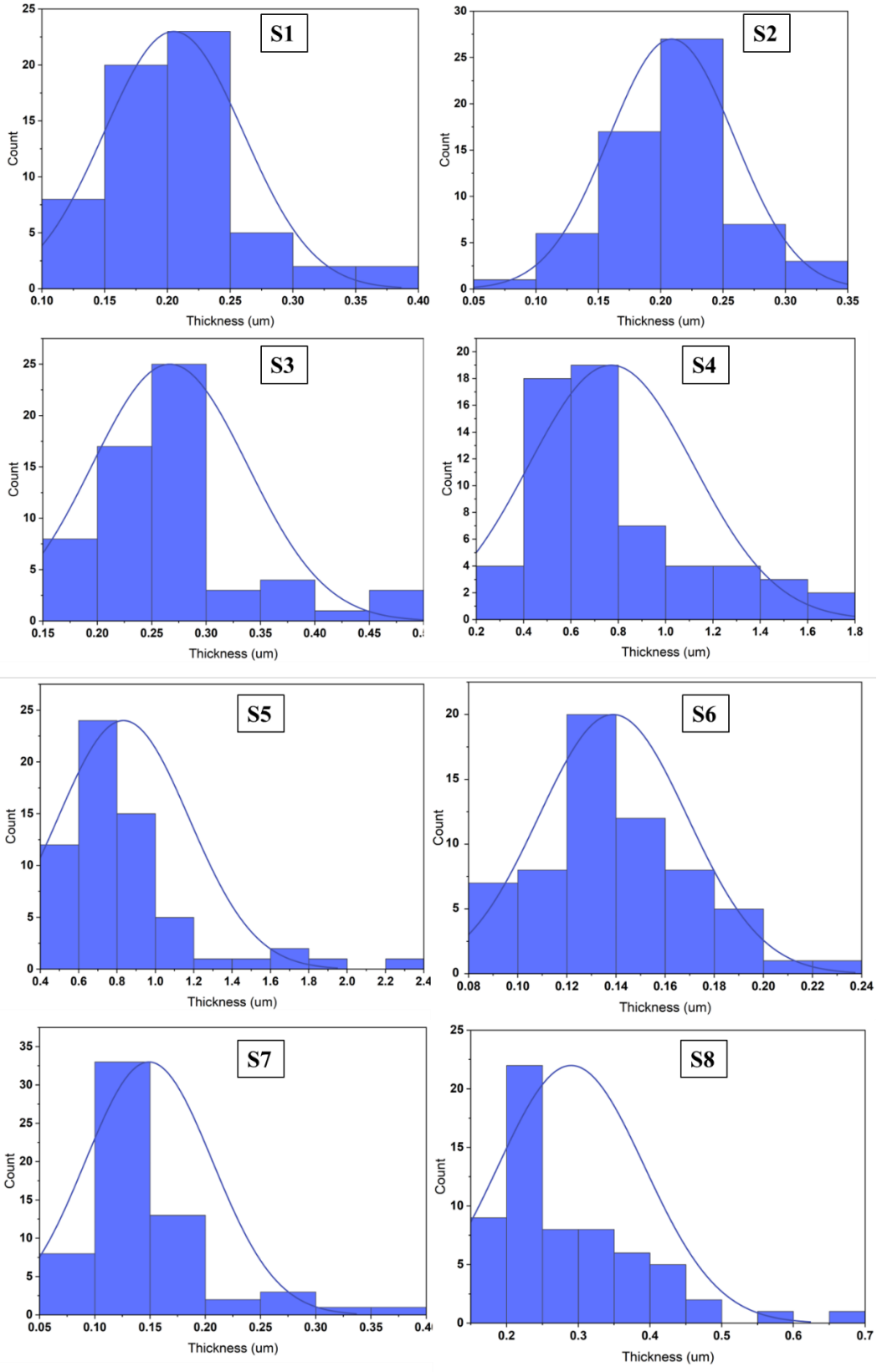

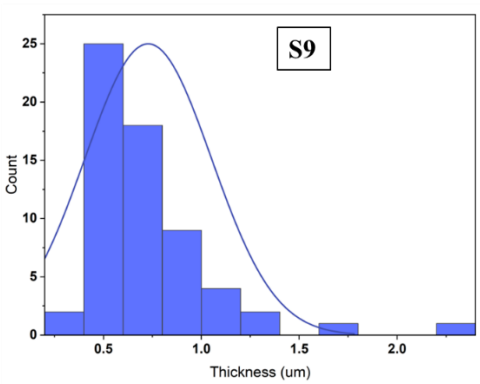
S9
Count
Thickness (um)

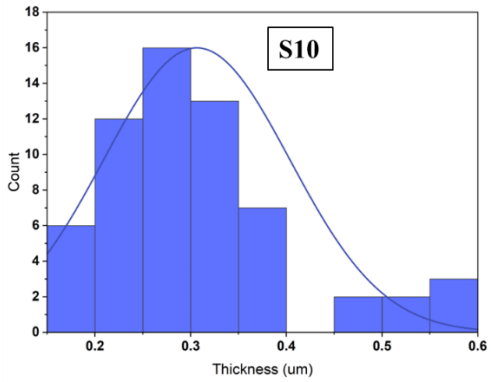
S10
Count
Thickness (um)

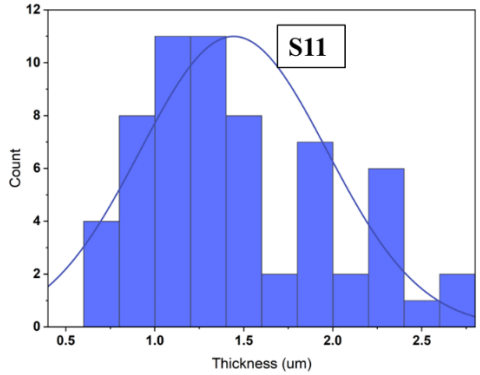
S11
Count
Thickness (um)

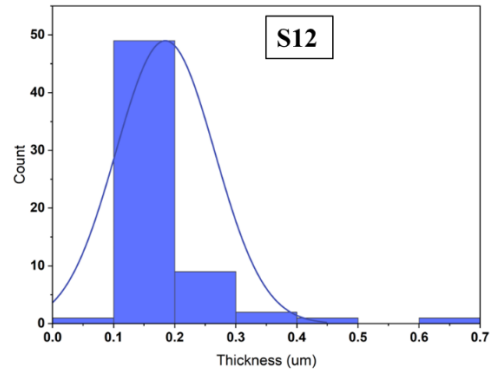
S12
Count
Thickness (um)

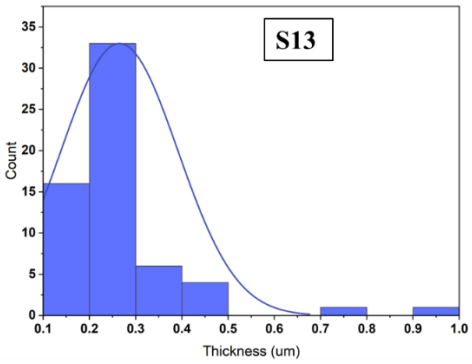
S13
Count
Thickness (um)

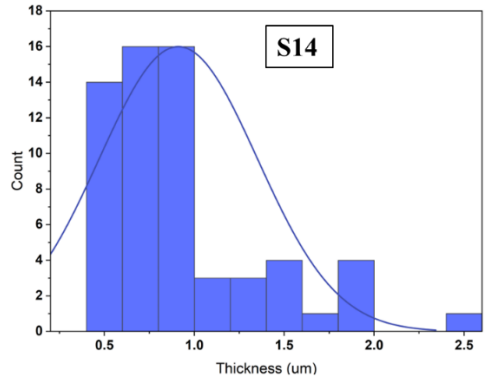
S14
Count
Thickness (um)

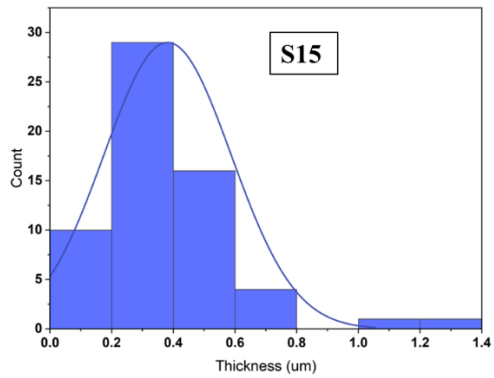
S15
Count
Thickness (um)

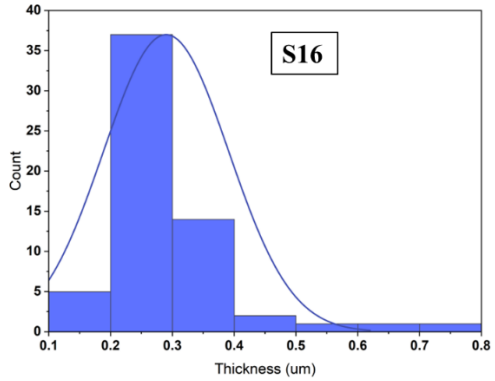
S16
Count
Thickness (um)

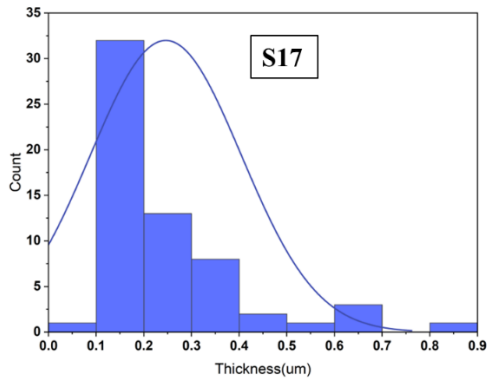
S17
Count
Thickness(um)

- Distribution plots depicting the variation in the measured Feret's diameter of the particles across the 17 samples:

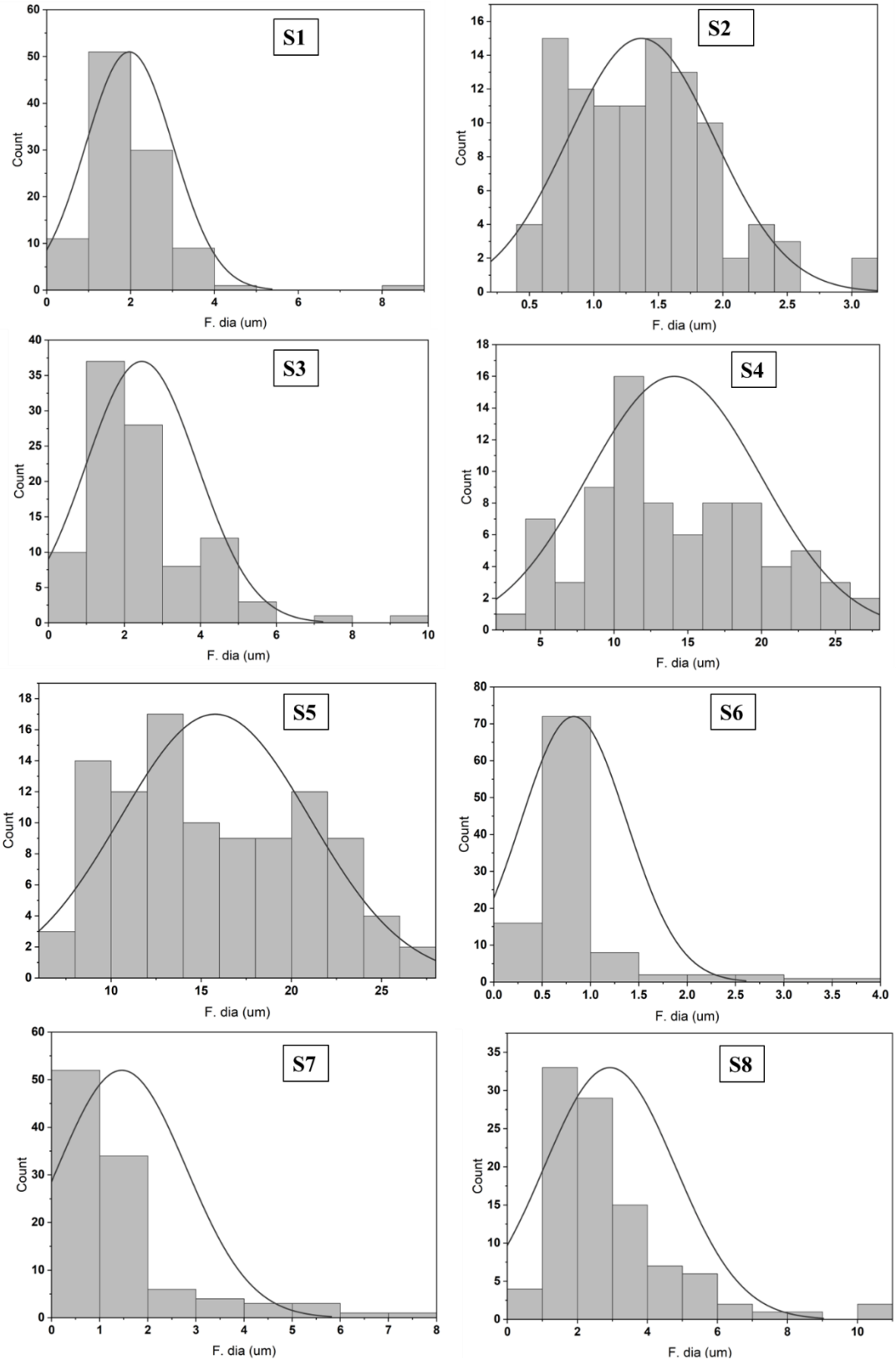

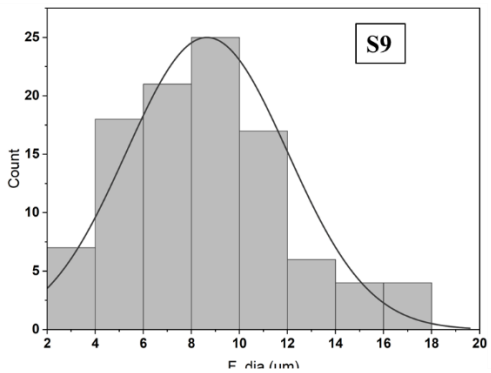
S9
Count
F. dia (um)

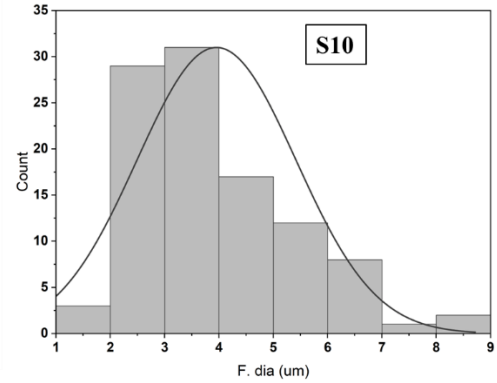
S10
Count
F. dia (um)

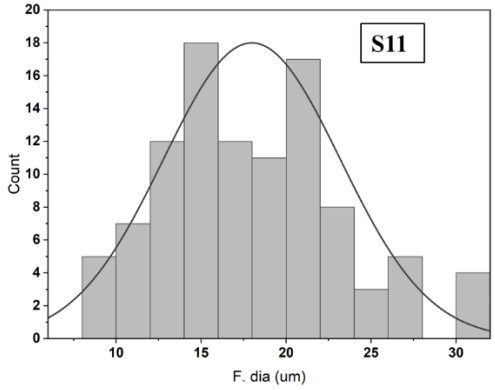
S11
Count
F. dia (um)

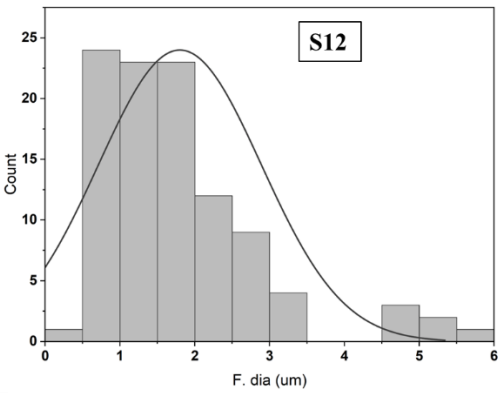
S12
Count
F. dia (um)

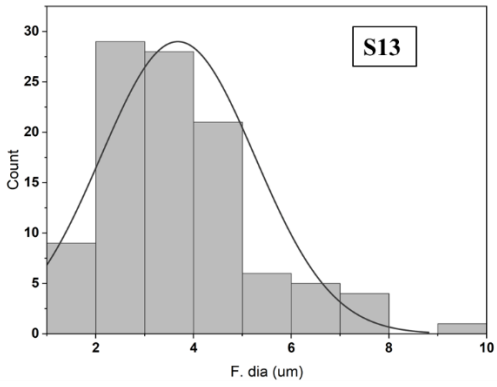
S13
Count
F. dia (um)

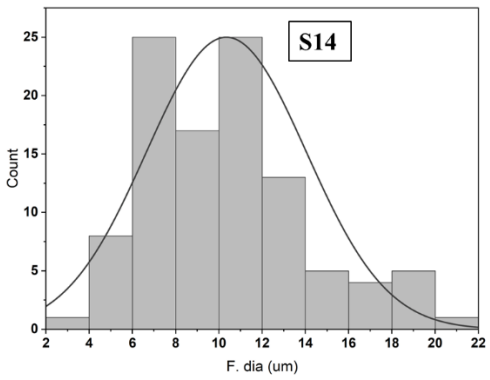
S14
Count
F. dia (um)

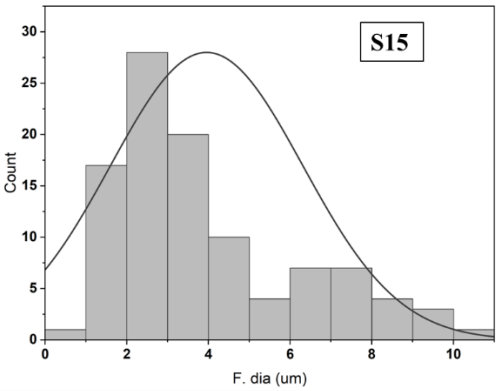
S15
Count
F. dia (um)

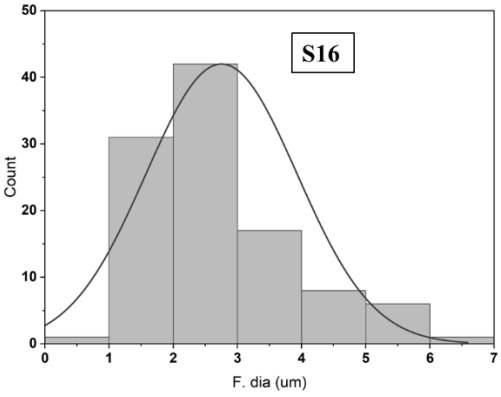
S16
Count
F. dia (um)

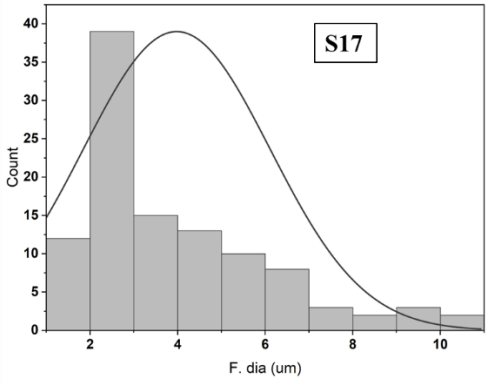
S17
Count
F. dia (um)

Appendix C

This Appendix presents the detailed ANOVA outcomes during the initial statistical analysis stage which was **before** the data transformation.

- ANOVA results for the average area of the particles (R1):

ANOVA for Response Surface Quadratic Model						
Analysis of variance table [Partial sum of squares - Type III]						
Source	Sum of Squares	df	Mean Square	F Value	p-value Prob > F	
Model	47438.2	9	5270.911	23.80571	0.0002	significant
A-Temperature	27938.66	1	27938.66	126.183	< 0.0001	
B-Holding Time	4251.778	1	4251.778	19.20286	0.0032	
C-Heat Rate	8.883728	1	8.883728	0.040123	0.8469	
AB	5393.572	1	5393.572	24.35969	0.0017	
AC	2.588214	1	2.588214	0.011689	0.9169	
BC	219.8951	1	219.8951	0.993141	0.3522	
A^2	6994.471	1	6994.471	31.59004	0.0008	
B^2	4.603942	1	4.603942	0.020793	0.8894	
C^2	52.16174	1	52.16174	0.235585	0.6422	
Residual	1549.896	7	221.4138			
Lack of Fit	1546.096	5	309.2192	162.7181	0.0061	significant
Pure Error	3.800672	2	1.900336			
Cor Total	48988.1	16				

R-Squared	0.968362
Adj R-Squared	0.927684
Pred R-Squared	0.7

Model:

Area = 8.022056 + 52.85704 * A + 20.61984 * B + 0.942535 * C + 25.96529 * A * B + 0.568794 * A * C + 5.242794 * B * C + 51.09415 * A^2 - 1.31087 * B^2 - 4.41235 * C^2

- ANOVA results for the average thickness of the particles (R2):

ANOVA for Response Surface Quadratic Model						
Analysis of variance table [Partial sum of squares - Type III]						
Source	Sum of Squares	df	Mean Square	F Value	p-value Prob > F	
Model	1.96079	9	0.217866	12.28485	0.0016	significant
A-Temperature	1.442156	1	1.442156	81.31931	< 0.0001	
B-Holding Time	0.032594	1	0.032594	1.837882	0.2173	
C-Heat Rate	0.014987	1	0.014987	0.845098	0.3885	
AB	0.072721	1	0.072721	4.100564	0.0825	
AC	0.024189	1	0.024189	1.363943	0.2811	
BC	0.077047	1	0.077047	4.34445	0.0756	
A^2	0.144453	1	0.144453	8.145343	0.0245	
B^2	0.002613	1	0.002613	0.147346	0.7125	
C^2	0.002799	1	0.002799	0.157813	0.7030	
Residual	0.124141	7	0.017734			
Lack of Fit	0.116837	5	0.023367	6.398515	0.1407	not significant
Pure Error	0.007304	2	0.003652			
Cor Total	2.084931	16				

R-Squared	0.940458
Adj R-Squared	0.91
Pred R-Squared	0.5321

Model:

Thickness = 0.273910594 + 0.379757352 * A + 0.057091063 * B + 0.038713538 * C + 0.095342411 * A * B + 0.054987308 * A * C + 0.098136766 * B * C + 0.232197635 * A^2 + 0.031230032 * B^2 + 0.032320196 * C^2

- ANOVA results for the average Feret's diameter of the particles (R3):

ANOVA for Response Surface Quadratic Model						
Analysis of variance table [Partial sum of squares - Type III]						
Source	Sum of Squares	df	Mean Square	F Value	p-value Prob > F	
Model	471.6929	9	52.41032	35.01067	< 0.0001	significant
A-Temperature	352.7334	1	352.7334	235.6298	< 0.0001	
B-Holding Time	18.71792	1	18.71792	12.50378	0.0095	
C-Heat Rate	0.200325	1	0.200325	0.133819	0.7253	
AB	31.21433	1	31.21433	20.85152	0.0026	
AC	0.038138	1	0.038138	0.025477	0.8777	
BC	0.896703	1	0.896703	0.599008	0.4643	
A^2	47.16447	1	47.16447	31.50639	0.0008	
B^2	0.131662	1	0.131662	0.087951	0.7754	
C^2	0.747867	1	0.747867	0.499584	0.5025	
Residual	10.47887	7	1.496981			
Lack of Fit	9.302346	5	1.860469	3.162658	0.2575	not significant
Pure Error	1.176523	2	0.588261			
Cor Total	482.1718	16				

R-Squared	0.978267
Adj R-Squared	0.950325
Pred R-Squared	0.739844

Model:

Feret's dia = 3.473189071 + 5.939136275 * A + 1.368134405 * B + 0.141536275 * C + 1.975295343 * A * B + 0.069045343 * A * C + 0.334795343 * B * C + 4.195669126 * A^2 + 0.221678472 * B^2 - 0.528330874 * C^2

- ANOVA results for the average aspect ratio of the particles (R4):

ANOVA for Response Surface Quadratic Model						
Analysis of variance table [Partial sum of squares - Type III]						
Source	Sum of Squares	df	Mean Square	F Value	p-value Prob > F	
Model	147.8024	9	16.42249	1.88157	0.2084	not significant
A-Temperature	97.64149	1	97.64149	11.18705	0.0123	
B-Holding Time	2.025535	1	2.025535	0.232071	0.6447	
C-Heat Rate	0.540722	1	0.540722	0.061952	0.8106	
AB	9.108541	1	9.108541	1.043591	0.3410	
AC	3.297739	1	3.297739	0.377831	0.5582	
BC	24.03688	1	24.03688	2.753972	0.1410	
A^2	0.279504	1	0.279504	0.032023	0.8630	
B^2	1.877081	1	1.877081	0.215062	0.6569	
C^2	10.76098	1	10.76098	1.232916	0.3035	
Residual	61.09655	7	8.728079			
Lack of Fit	60.35145	5	12.07029	32.3989	0.0302	significant
Pure Error	0.745105	2	0.372552			
Cor Total	208.899	16				

R-Squared	0.707531
Adj R-Squared	0.331499
Pred R-Squared	-0.71035

Model:

AR = 12.06894324 + 3.124763759 * A + 0.450059489 * B - 0.232534256 * C + 1.06703682 * A * B - 0.642041535 * A * C - 1.73338119 * B * C + 0.322988751 * A^2 + 0.837018933 * B^2 - 2.004101688 * C^2

- ANOVA results for the particle size (R5):

ANOVA for Response Surface Quadratic Model						
Analysis of variance table [Partial sum of squares - Type III]						
Source	Sum of Squares	df	Mean Square	F Value	p-value Prob > F	
Model	3665.18	9	407.2423	4.379368	0.064	not significant
A-Temperature	0.007723	1	0.007723	8.31E-05	0.9930	
B-Holding Time	694.0781	1	694.0781	7.46392	0.0293	
C-Heat Rate	256.0693	1	256.0693	2.753697	0.1410	
AB	774.0013	1	774.0013	8.323392	0.0235	
AC	653.508	1	653.508	7.027641	0.0329	
BC	605.7795	1	605.7795	6.514381	0.0380	
A^2	48.41024	1	48.41024	0.52059	0.4940	
B^2	375.3463	1	375.3463	4.036369	0.0845	
C^2	30.32301	1	30.32301	0.326085	0.5858	
Residual	650.9377	7	92.99109			
Lack of Fit	647.1937	5	129.4387	69.14636	0.0143	significant
Pure Error	3.743907	2	1.871953			
Cor Total	4316.118	16				

R-Squared	0.849184
Adj R-Squared	0.655279
Pred R-Squared	-1.33761

Model:

Particle size = 9.424444214 - 0.027790435 * A - 8.331134959 * B + 5.06032866 * C + 9.836166038 * A * B - 9.03816902 * A * C - 8.70186371 * B * C + 4.250718745 * A^2 + 11.83613364 * B^2 - 3.364185128 * C^2